Fault-tolerant feature-based estimation of space debris motion and inertial properties

ScuDo

Scuola di Dottorato ~ Doctoral School

WHAT YOU ARE, TAKES YOU FAR

Doctoral Dissertation

Doctoral Program in Mechanical Engineering (29^{th}cycle)

Fault-tolerant feature-based estimation of space debris motion and inertial properties

By

Gabriele Biondi

******

Supervisor(s):

Prof. Stefano Mauro, Supervisor

Prof. Stefano Pastorelli, Co-Supervisor

Doctoral Examination Committee:

Prof. G. Avanzini, Referee, Università del Salento

Prof. P. B. Zobel, Referee, Università dell'Aquila

Politecnico di Torino

2017

Declaration

I hereby declare that, the contents and organization of this dissertation constitute my own original work and does not compromise in any way the rights of third parties, including those relating to the security of personal data.

Gabriele Biondi

2017

* This dissertation is presented in partial fulfillment of the requirements for **Ph.D. degree** in the Graduate School of Politecnico di Torino (ScuDo).

They are more desirable than gold
yes, than much fine gold.
Sweeter also than honey
and the drippings of the honeycomb.

Abstract

The exponential increase of the needs of people in the modern society and the contextual development of the space technologies have led to a significant use of the lower Earth's orbits for placing artificial satellites. The current overpopulation of these orbits also increased the interest of the major space agencies in technologies for the removal of at least the biggest spacecraft that have reached their end-life or have failed their mission.

One of the key functionalities required in a mission for removing a non-cooperative spacecraft is the assessment of its kinematics and inertial properties. In a few cases, this information can be approximated by ground observations. However, a re-assessment after the rendezvous phase is of critical importance for refining the capture strategies preventing accidents. The CADET program (CApture and DE-orbiting Technologies), funded by Regione Piemonte and led by Aviospace s.r.l., involved Politecnico di Torino in the research for solutions to the above issue.

This dissertation proposes methods and algorithms for estimating the location of the center of mass, the angular rate, and the moments of inertia of a passive object. These methods require that the chaser spacecraft be capable of tracking several features of the target through passive vision sensors. Because of harsh lighting conditions in the space environment, feature-based methods should tolerate temporary failures in detecting features. The principal works on this topic do not consider this important aspect, making it a characteristic trait of the proposed methods. Compared to typical

treatments of the estimation problem, the proposed techniques do not depend solely on state observers. However, methods for recovering missing information, like compressive sampling techniques, are used for preprocessing input data to support the efficient usage of state observers. Simulation results showed accuracy properties that are comparable to those of the best-known methods already proposed in the literature.

The developed algorithms were tested in the laboratory staged by Aviospace s.r.l., whose name is CADETLab. The results of the experimental tests suggested the practical applicability of such algorithms for supporting a real active removal mission.

Contents

List of Figures ix

List of Tables xviii

Introduction 1

1 Simulation of feature tracking 9

1.1 Kinematic and dynamic equations for satellites 10

1.2 Models for the production of simulated datasets 15

1.2.1 Feature selection and tracking 17

1.2.2 Uncertainties on trajectories of the features 27

2 Localization of the center of mass 32

2.1 A new estimator in absence of uncertainties 35

2.1.1 Estimation without missing data 35

2.1.2 Estimation with missing data 49

2.2 Regularizing noise by Procrustes analysis 55

2.3 Estimation in realistic conditions 61

3 Estimation of attitude, angular rate and inertia ratios 72

3.1 Theory of observers for stochastic systems 73

3.1.1 Kalman filter 77

3.1.2 Unscented Kalman filter 85

3.2 Compressive sampling for signal recovery 92

3.2.1 Theoretical basis 96

3.2.2 Split augmented Lagrangian shrinkage algorithm 103

3.3 Original estimation algorithms and results 108

3.3.1 First approach: few known features 109

3.3.2 Second approach: no shape information 124

4 Experimental tests 140

4.1 The CADETLab facility 142

4.2 Algorithms for laboratory conditions 152

4.3 Tests results 160

4.3.1 Data from infrared camera 162

4.3.2 Data from stereo-rig system 168

Conclusions 177

Bibliography 181

Appendix A Basics of orbital dynamics **187**

A.1 Kepler's laws 188

A.2 Parametrization for orbits 196

A.3 Relative dynamics for two satellites 202

Appendix B Basics of attitude dynamics **206**

B.1 Attitude kinematics and parameterizations 207

B.2 Rotational dynamics in torque-free conditions 216

List of Figures

1.1 Flowchart showing the approach for validating the developed algorithms by mathematical simulations. 16

1.2 Third stage of Ariane 4, H10. 17

1.3 H10 model with features ${}^{B}\boldsymbol{d}_3$ (on the left) and ${}^{B}\boldsymbol{d}_1$ (on the right) 18

1.4 H10 model with features ${}^{B}\boldsymbol{d}_4$ (on the left), ${}^{B}\boldsymbol{d}_2$ (middle point) and ${}^{B}\boldsymbol{d}_5$ (on the right) 19

1.5 H10 model with features ${}^{B}\boldsymbol{d}_4$, ${}^{B}\boldsymbol{d}_3$ and ${}^{B}\boldsymbol{d}_5$ 19

1.6 Position of the 44 unlabeled complementary features 20

1.7 Reference frames: body, chaser, sensor, and features 22

1.8 Trajectories of features with respect to the chaser reference frame C. The considered time interval starts from zero to one target orbital period . . 24

1.9 Backface culling technique. The surface normal in the hidden feature (case b) form an angle with the feature position which is bigger than 90 degrees. 25

1.10 Euclidean coordinates of the point $\boldsymbol{\rho}_1$ after the application of the Backface culling technique in a short time interval. $\boldsymbol{\rho}_{1_i}$ is the i-th coordinate of the point $\boldsymbol{\rho}_1$ 25

1.11 Second approach for the dataset production: simulation time is divided in intervals, and in some of these ones there are no data available. That corresponds to the introduction of artificial occlusion periods. 26

1.12 Stereo rig system. 28

1.13 Histogram of the errors on the trajectory after the inverse projection, $\sigma = 10^{-4}$ 29

1.14 Histogram of the errors on the trajectory after the inverse projection, $\sigma = 10^{-5}$ 30

2.1 Application of the Releaux method. 35

2.2 Application of the Releaux method in an infinitesimal time interval. . . 36

2.3 Plane individuation and axis localization. 39

2.4 Center of mass localization if there is no relative dynamics between chaser and target. In (b) the trajectories of the five features in Eq. (1.17) are shown, while in (a) the projections of the rotation axes on the C^1C^2 plane are illustrated. 41

2.5 Pseudo-intersection of successive axes of rotation. 43

2.6 Axes distances d_e (upper charts) and estimation errors δ_g for two different attitude dynamics: a) axisymmetric ${}^B\boldsymbol{J}$; b) generic ${}^B\boldsymbol{J}$ 44

2.7 Axes distances d_e (upper charts) and estimation errors δ_g after changing initial relative conditions 45

2.8 Axes distances d_e (upper chart) and estimation errors δ_g with a near-circular orbit 47

2.9 magnitude of the normal-to-axis component of the relative velocity between the centers of mass of the target and the chaser: case a) is relevant to Fig. 2.7; case b) is relevant to Fig. 2.8 48

2.10 Result of the selection method, eccentric orbit (Tab. 1.1).The circles indicate the found relative maxima 50

2.11 Global estimation of the center of mass location, eccentric orbit (Tab. 2.1). 51

2.12 Distribution of the estimation error for the second coordinate of the CoM, eccentric orbit (Tab. 2.1). 52

2.13 Result of the selection method, near-circular orbit (Tab. 2.1) 53

2.14 Global estimation of the center of mass location, eccentric orbit (table 2.1). 53

2.15 Distribution of the estimation error for the second coordinate of the CoM, eccentric orbit (table 2.1). 54

2.16 GPA procedure: all the *configurations* are linearly transformed for comparison. The mean *configuration* is assumed to be optimal. 59

2.17 Appearing and disappearing features from the FOV of the vision-based sensors. Note that features 1, 2 and 3 are exactly the same of 11, 12 and 13, but no algorithm is exploited to recognize this fact. 61

2.18 Raw (solid line) and filtered (dashed line) screw axis and pole of rotation. An occlusion period interrupts data. 63

2.19 Representation of the three estimated coordinates of the center of mass (CoM) in the chaser-fixed reference frame C. The standard deviation of the measurement noise is equal for each coordinate to 10 mm. 64

2.20 Final estimation error in the CoM trajectory. The standard deviation of the measurement noise is equal for each coordinate to 10 mm. 65

2.21 Representation of the three estimated coordinates of the center of mass (CoM) in the chaser-fixed reference frame C. The standard deviation of the measurement noise is equal for each coordinate to 10 mm. 67

2.22 Final estimation error in the CoM trajectory. The standard deviation of the measurement noise is equal for each coordinate to 10 mm. 67

2.23 Representation of the three estimated coordinates of the center of mass (CoM) in the chaser-fixed reference frame C. The standard deviation of the measurement noise is equal for each coordinate to 10 mm. 69

2.24 Final estimation error in the CoM trajectory. The standard deviation of the measurement noise is equal for each coordinate to 10 mm. 69

2.25 Representation of the three estimated coordinates of the center of mass (CoM) in the chaser-fixed reference frame C. The standard deviation of the measurement noise is equal for each coordinate to 10 mm. 71

2.26 Final estimation error in the CoM trajectory. The standard deviation of the measurement noise is equal for each coordinate to 10 mm. 71

3.1 Example of raw attitude information $\left({}^{\mathcal{F}}q_I\right)$. The amplitude of the noise on the coordinates of the features has been set to 30 mm for each coordinate. 94

3.2 Illustration of the different implications on the proposed estimation algorithms according to the characteristics of the available set of data. If the features have correspondence with the one of a CAD model of the target, the attitude of one particular body-fixed frame is always monitored. Otherwise, other motion descriptions must be found. 110

3.3 Example of raw attitude information $\left({}^{\mathcal{F}}q_I\right)$. The amplitude of the noise on the coordinates of the features has been set to 30 mm for each coordinate. 111

3.4 Two possible sequences of same attitude information. The signal marked with 0000 consists of the first five pieces of ${}^{\mathcal{F}}q_{I0}$ in Fig 3.3. The label 1001 indicates that the second and the last pieces have inverted signs. . 112

3.5 Preliminary phase, $N'_p = 5$: raw data (crosses) and recovered signal (red line). 114

3.6 Values of penalty scores, as defined in Eq.(3.96); best recoveries in blue correspond to 1111 and 1100 label sets. 114

3.7 Introduction of a new piece of quaternion: the component is added to the best recovered signals with opposite sign. 115

3.8 Final best recovery of the quaternion ${}^{F}q_I$: raw data (blue crosses) and recovered signal (red line). 115

3.9 Attitude recovery performed for different target conditions (see Tab. 3.1). 116

3.10 Final estimation of the angular rate after Kalman filtering the recovered quaternions in fig 3.9. Reference values of the angular rate components are represented by dashed lines. 121

3.11 Final estimation of the relative values of the principal moments of inertia after Kalman filtering the recovered quaternions in fig 3.9. Reference values are represented by dashed lines. 121

3.12 Mean and maximum estimation error for each angular rate component; the UKF converges at about 1000 seconds 123

3.13 Appearing and disappearing features typical of the second approach. Features 4 and 5 coincides with 6 and 7. The same holds for 1,2 and 3, which are the same of 13, 14 and 15. However, no algorithm is exploited to recognize this fact. Occlusions contributes to this problem. 124

3.14 Flow-chart describing the second estimation approach of the target rotational dynamics 125

3.15 Raw $\boldsymbol{\Omega}$ from trajectories of features. A local zoom on the time axis reveals the periodicity and the sparsity of the signal 130

3.16 Recovered $\boldsymbol{\Omega}$: the amplitude of the signal is slightly decreased due to the reduction of the noise power. The signal does not present missing samples. 131

3.17 Prediction scheme of ${}^{I}\boldsymbol{\Omega}_{k+1}$. 133

3.18 Final estimation of the angular rate after Kalman filtering the recovered Gibbs representation $\boldsymbol{\Omega}$ of the successive finite rotations. Reference values of the angular rate components are represented by dashed lines. . 135

3.19 Final estimation of the relative values of the principal moments of inertia after Kalman filtering the recovered Gibbs representation $\boldsymbol{\Omega}$ of the successive finite rotations. Reference values are represented by dashed lines. 136

3.20 Mean and maximum estimation error for each angular rate component; the UKF converges at about 1000 seconds 138

4.1 Scaled physical model of the H10 upper stage. The cylindrical part is approximately 1.2 m long and have a diameter of 330 mm. The texture formed by the external insulation layer is reproduced with decorative paper 142

4.2 Mechanism for the simulation of the spinning motion of the mock-up. The mechanism is mounted inside the mock-up. A stepper motor allows the external structure rotating around its symmetry axis. Ball bearings support the rotating structure with respect to the frame of the motor. . . 143

4.3 Mechanism for rotating the mock-up around a fixed axis in the inertial space. In the left image, one of the extremes of the visible cylindrical arm is hinged to a fixed platform welded to the base. The other extreme is hidden by a black panel. The right image shows the connection to the mock-up 144

4.4 Scheme of the rotational degrees of freedom of the target mock-up. Note that θ_{sp} identifies the spin motion of an axisymmetric torque-free body. 145

4.5 A detail of the dolly platform and of the linear slider that constraints the motion of the platform 146

4.6 A photo of the 5 DOF Kawasaki RS05N robot. The end-effector is equipped with a plenty of sensors for the observation of the target mock-up. 147

4.7 Characteristic dimensions and workspace of the Kawasaki RS05N robot. 148

4.8 A photo of the CADETLab. 149

4.9 3DOne assembly and the case for tests 149

4.10 Xenics uncooled silicon microbolometer with its case to form the monocular IR camera used for tests in CADETLab. 150

4.11 3D renedring of the object contour detected by Blue Engineering s.r.l. by Xenics IR camera. 152

4.12 Raw ${}^{I}\boldsymbol{\Omega}$ from simulated trajectories of features in laboratory conditions. 157

4.13 Attitude quaternions ${}^{\mathcal{F}}q_I$ from ${}^{I}\boldsymbol{\Omega}$ in Fig. 4.12 by means of Eq. (4.12). . 158

4.14 Layout of the CADETLab control room and reference coordinate system for input data 161

4.15 Trajectories of the three fictitious features from the elaboration of the data from the IR camera. The dimensions are expressed in m. 162

4.16 Estimated angular rate $\boldsymbol{\omega}$ of the mock-up in the camera-fixed frame shown in Fig.4.14. Notice the steadiness of the first component, which corresponds to the sum of the pseudo-tumbling rate $\dot{\gamma}$ and the constant component of the spin rate $\dot{\theta}_{sp}$ on the first axis 163

4.17 Estimated counterclockwise spin rate $\dot{\theta}_{sp}$ of the mock-up. The mean value is represented with a thick line 165

4.18 Estimated counterclockwise pseudo-tumbling rate $\dot{\gamma}$ of the mock-up. The mean value is represented with a thick line 165

4.19 Estimated spin rate $\dot{\theta}_{sp}$ of the mock-up, and estimated pseudo-tumbling rate in camera frame. Notice the tiny differences between the mean values and the estimated signals 166

4.20 Localization of the intersection point of the spin axis with the pseudo-tumbling axis. The distance between this point and the camera was constant 168

4.21 Tracked points from stereo-vision system by Eurix s.r.l. A total number of 3923 points were tracked with a 5 Hz frequency. A detail of the figure is offered to increase readability. No relationships can be extracted between the features and a CAD model of the mock-up. 169

4.22 Number of time samples in which the features are continuously tracked. The horizontal axis shows the number of points associated to a specific tracking duration (in number of time samples) 170

4.23 Estimated angular rate $\boldsymbol{\omega}$ of the mock-up in the camera-fixed frame shown in Fig.4.14. Notice the steadiness of the first component, which corresponds to the sum of the pseudo-tumbling rate $\dot{\gamma}$ and the constant component of the spin rate $\dot{\theta}_{sp}$ on the first axis 171

4.24 Estimated counterclockwise spin rate $\dot{\theta}_{sp}$ of the mock-up. The mean value is represented with a thick line 172

4.25 Estimated counterclockwise pseudo-tumbling rate $\dot{\gamma}$ of the mock-up. The mean value is represented with a thick line 172

4.26 Estimated spin rate $\dot{\theta}_{sp}$ of the mock-up, and estimated pseudo-tumbling rate in camera frame. Notice that the quality of the estimation is not too bad. 173

4.27 Localization of the intersection point of the spin axis with the pseudo-tumbling axis. The distance between this point and the camera was constant 175

A.1 Areas spanned by the moving vector ${}^{I}\boldsymbol{r}$. P' is the displaced point P and P'' is the projection of P on ${}^{I}\boldsymbol{r}$ after the displacement. 190

A.2 Characteristic parameters of an ellipse 194

A.3 Representation of the orbital parameters 198

A.4 Definition of the LVLH coordinate system of the target 203

B.1 Intersection of momentum and energy ellipsoid. The tip of the angular rate vector lies on the intersection curve, which is called Polhode 220

B.2 The angular rate vector traces in the inertial frame an open curve, which is called Herpoloid. The energy ellipsoid rolls without sliding on the plane normal to the angular momentum vector 221

List of Tables

1.1 Keplerian parameters used in the simulation 23

2.1 Keplerian elements of a near-circular orbit 46

3.1 Attitude error for different dynamic conditions of the target (algorithm's output in fig. 3.9); the standard deviation of the measurement noise is equal for each coordinate to 50 mm. 117

3.2 Attitude error for different dynamic conditions of the target; the standard deviation of the measurement noise is equal for each coordinate to 50 mm. 118

3.3 Angular rate and attitude estimation error after Kalman filtering; standard deviation of the measurement noise is equal for each coordinate to 50 mm. 122

3.4 Nominal normalized principal moments of inertia and difference beetwen nominal value and estimation after convergence 123

3.5 Angular rate estimation error after Kalman filtering; standard deviation of the measurement noise is equal for each coordinate to 10 mm. 137

3.6 Nominal normalized principal moments of inertia and difference beetwen nominal value and estimation after convergence 138

Introduction

Since the launch of Sputnik, the first artificial satellite, by the USSR in 1957, a significant number of satellites have been launched into space by several countries, for different purposes. In particular, from the second half of the twentieth century up to the present, the number of artificial satellites in low-Earth orbit has increased considerably, a few of which are currently inactive and uncontrolled. As the number of failed spacecraft increases significantly every year, so does the risk of dangerous collisions between relatively large space objects. A well-known accident that happened in 2009 between Cosmos 2251 and Iridium 33 caused an environmental disaster because of the fragmentation of the two bodies [1].

In this context, major space agencies such as NASA and ESA are interested in the possibility of removing relatively large space objects. As a result, several concepts of active removal systems were developed. Many methods for enabling space debris capturing and removal were proposed in the past decade, and several approaches were tested on the ground or in parabolic flight experiments [2].

In particular, although some possible contact-less techniques have been investigated [3], it is an established idea to dock and guide passive spacecraft with active chaser spacecraft. A few of the pioneering techniques involve, for example, the use of nets or electrodynamic tethers [4]. However, no one has removed any space debris yet.

The operation presents several challenges that are related to the typical non-cooperativeness of these objects. In particular, space debris can have a large variety of dimensions, shapes, and motion conditions. However, these characteristics are often partially or even completely unknown.

Evidently, for planning the docking between spacecraft and the successive target removal, it is important to estimate the whole relative dynamic state between the chaser and the target. If there is a lack of such information, or if it is inaccurate, the contact between spacecraft during capturing and removal may lead to compromise the stability of the entire system.

Some authors made a significant effort for determining the complete dynamic state of passive objects from astrometric and photometric data [5], [6]. In both works, the fusion of angles data together with the information contained in light curves lead to the goal. The second work, in particular, proposes an approach for estimating the mass of the object. The accuracy of the relative position estimation is on the order of ten meters; this makes the method efficient for planning rendezvous with the objects. However, the estimation accuracy is not sufficient for the docking of the object.

A relatively precise orbit determination can also be obtained by laser ranging from ground stations [7]. It is achieved in this case a high precision in measuring the distances of space debris from the station (0.7 m RMS). However, this information, which is necessary to reach the target, is still insufficient for predicting the dynamic response of the chaser during capture maneuvers. Thus, for the success of the capturing, there is a need to consider an in-situ refinement of these estimates

In particular, an accurate estimation of the location of the center of mass (CoM) of the target leads to the prediction of the potential torques caused by the interaction between spacecraft. At the same time, it is necessary to predict the direction of the

angular acceleration of the target for assessing its mass distribution. For this purpose, it is important to estimate a normalized form of the inertia tensor of the target.

The mentioned relative state estimation is not completely trivial even when the chaser and the target are fully cooperative. In particular, examples can be found in [8], [9], and [10]. When the spacecraft are non-cooperative, the estimation becomes more difficult as the absence of suitable sensors results in a loss of most of the information about the motion of the target spacecraft.

Hence, to collect sufficient information for the state estimation, it is necessary to track the passive target by using appropriate vision sensors on the chaser that is designated to capture the object. This phase should follow the rendezvous and precede the capture maneuver.

The most high-performance techniques findable in the literature involve the exploitation of active sensors, such as laser range finders. Lichter and Dubowsky [11] proposed an architecture for the estimation of the dynamic state of non-cooperative spacecraft. This instrumentation primarily consists of 3D laser sensors, which are suitable for use in harsh lighting conditions. Aghili *et al.* [12] presented a method for pose estimation of passive space bodies using a laser 3D scanner. Their method also considers the possibility of failures during the scanning procedure without compromising the estimation. On the other hand, this method requires a CAD model of the object.

The use of active sensors, although they are relatively reliable, could nevertheless be less appealing than obtaining the same information using passive sensors, because of the possibility of saving energy. Besides, secondarily, even costs result inferior. A survey of the most common tracking techniques based with stereo-vision is in [13]. In [14] and [15], two different methods are presented to maintain a target space body in the field of view (FOV) of cameras on a chaser spacecraft after the rendezvous phase. In these

studies, the estimation of the angular rate is not present. Both of the methods seem to be applicable over a relatively extended period.

The key aspect of diffidence regards the reliability of these techniques: occlusions, critical reflections, and poor lighting conditions contribute to probable tracking failures. Though in an incomplete way, some researchers have taken this aspect into consideration.

In [16], the prediction of the velocities of its features allows the tracking of a target body. This prediction depends on a kinematic model of the object. This article considers the problem of recovering the pose and the angular rate of the body during occlusions; however, it does not show any results in the case in which no features are detectable. Moreover, when the number of detected features decreases, the precision of the estimation significantly decreases. The paper states, however, that the prediction is useful for re-initializing the tracking.

The work presented in [17] considers the determination of the relative pose between a chaser and a larger target that are cooperative. This work is interesting for two reasons: tracking is performed using stereo-vision cameras, and when occlusions occur, despite the missing attitude information, the position of the body is predicted using a mathematical model of the body itself. The tracking can then continue after the occlusion intervals; however, the pose of the object is not obtained in these periods. An important assumption underlying the cooperativeness between the spacecraft is that the positions of certain artificial features on the target (in the case considered, LEDs) are known a-priori.

Other authors decided instead to ignore the problem proposing, on the other hand, very efficient estimation methods. In [18] a 3D-model-matching technique, as used in [12], is combined with stereo-vision sensors. Notwithstanding, the considered method requires a large number of detected features and a very detailed model of the failed satellite.

The work of Segal et al. [19] illustrates a method that is based only on tracking features. The measured locations of several extracted features are used to make the estimation by employing the iterated extended Kalman filter. However, they excluded the possibility of sudden interruptions of the tracking. This assumption implies that this method is infeasible in the case of occlusions, or when the features disappear temporarily from the FOV of cameras.

Ultimately, the current state of the art appears to be missing of fault-tolerant methods for target state estimation from features detected using stereo cameras or, generally, passive sensors.

The purpose of this dissertation is to propose two estimation methods: the first for locating the CoM of a target debris, the second for estimating its rotational state, which is composed of the angular rate and the inertia tensor.

The method proposed in this work offers the possibility of recovering the dynamic conditions of a non-cooperative space body such as a failed spacecraft, even if the continuity of the feature tracking is missing. Thus, the method can recover the object poses when momentary failures in feature detection occur. This last aspect is probably one of the most novel elements of this dissertation.

Hence, the developed techniques are into the category of the feature-based methods: characteristic points of the target spacecraft are tracked in-situ for understanding the high-level motion of the entire object. The methods belonging to this category have the reputation of being not reliable. That holds because, typically, they are not robust to the several challenges due to the harsh lighting conditions of the space environment. Instead, the proposed techniques are fault-tolerant, meaning that temporary defections of the tracking sensors do not compromise the quality of the motion understanding.

The difficulty in obtaining real data to be processed led to the necessity of simulating them with the scope of assessing the proposed approach to the problem.

A virtual simulation environment was implemented in MATLAB-Simulink to evaluate trajectories of points belonging to a rigid body. The motion of this rigid body was according to the classic dynamics of an Earth's orbiting satellite. The chaser spacecraft was simulated as a reference system on which expressing the trajectories. Moreover, uncertainties were added to these trajectories. Besides, the data were further corrupted by introducing losses of data to enhance the realism of the dataset.

The work described in this paper has been developed within the CADET research program [20], which is co-funded by Regione Piemonte. CADET, which is also mentioned in [2], aims at the functional development of technologies for the capture and removal of space debris. In CADET, the Team of Politecnico di Torino is in charge to determine both the actual motion parameters and the inertial properties of the target.

The program leader was Aviospace s.r.l.: they built a laboratory named CADETLab to simulate the various phases of a removal mission. The methodologies that are proposed in this work were tested in this lab with the help of other project partners, who extracted feature trajectories from the vision sensors that equip the laboratory.

This work produced some original contributions to the state of the art (see [21], [22], [23], [24], [25]). The contents of these publications will be presented with greater detail in this dissertation.

The following dissertation is mainly divided into four chapters. Each of the chapters contains both original and theoretical sections. Although the latter parts do not significantly contribute by themselves to increase the scientific knowledge, they are essential for a full comprehension of the newly developed techniques. Moreover, all the original parts of the chapters have backgrounds that are afferent to very different areas of Engineering. In particular, they include celestial and applied mechanics, controls, statistics, and signal processing.

Thus, in this multidisciplinary context, it seemed convenient to give to the reader coming from one of the mentioned areas the keys for a full understanding of all the sections of this work.

The first chapter treats the virtual simulation of two close Earth's orbiting satellites. It concludes giving the instruments for obtaining two different sets of simulated data, both consisting of partial and corrupted trajectories of features belonging to the simulated target debris. The first section synthesizes the classic laws for modeling the orbital and the attitude dynamics of Earth's orbiting satellites. The second section introduces the implemented simulation environment, based on the mentioned principles. Moreover, the ways used for corrupting the simulated datasets are discussed as a function of the selected models of the considered sensors.

The second chapter illustrates an original alternative method for localizing the CoM of the target. In particular, the first section introduces an estimator that is based only on kinematic considerations. While the estimator is tested in this section on ideal data, the other two sections treat methods for enhancing the robustness of the proposed estimator: the second section shows the principle of the statistical shape analysis, while the third section illustrates a proper application of these concepts for estimating the CoM position from corrupted data.

The third chapter concerns the estimation of the angular rate and inertia moments of the target. One of the most interesting aspects of this chapter is that the presented methods come from the original combined application of two modern techniques: compressive sampling and Kalman filtering. The first technique has been useful for several purposes like image coding/decoding, pattern recognition, and prognostic. The second approach belongs to the world of the Bayesian state observers, and it has been extensively used for modern feedback controls. In this work, these techniques cooperate for recovering attitude and angular rate of a space object. The first two sections are dedicated to

the theory of these approaches. The third section illustrates two possible estimation procedures.

Finally, the last chapter presents the tests of the methods in the CADETLab environment. In particular, two different tests were performed. In the first test the data came from a monocular infrared camera; in the second one, the data came from a classic 3D stereo-rig system. The first section of the chapter presents the laboratory environment. The second section provides an adaptation of the developed algorithms to the particular conditions of the laboratory. Finally, the third section shows the test results.

Chapter 1

Simulation of feature tracking

This work presents methods and algorithms to estimate in-situ the motion conditions and the mechanical properties of uncontrolled satellites. The data required to feed the estimation algorithms consist of the Euclidean coordinates of some natural features of the target satellite.

Despite the interest of the principal space agencies and organizations, no active removal missions have been completed today. Thus, the unavailability of real data has led to validate the developed methods by testing them on simulated data. The observation phase of the removal mission can be reproduced physically in a laboratory environment or by mathematically modeling the dynamics of both the target and the chaser spacecraft. This chapter illustrates the equations to simulate numerically the acquisition of an appropriate input dataset to test the algorithms

1.1 Kinematic and dynamic equations for satellites

The purpose of this section is the introduction of the fundamental equations for the simulation of relative motion between the target and the chaser. Those equations are derived from the classic principles of the celestial mechanics.

Since the underlying concepts have been firmly established for very long time, it seemed appropriate to list only the essential expressions that will be sometimes recalled in the remainder of this dissertation. Moreover, this section introduces the notation used in this work. For the interested reader, Appendix A and Appendix B illustrate the basics of the orbital and attitude mechanics of satellites.

The first introduced equations are the ones for simulating the relative orbital motion between the chaser and the target:

$$
{}^{\ell}\begin{bmatrix} \ddot{\rho}_1 \\ \ddot{\rho}_2 \\ \ddot{\rho}_3 \end{bmatrix} = {}^{\ell}\begin{bmatrix} 2\dot{\vartheta}\dot{\rho}_2 + \ddot{\vartheta}\rho_2 + \dot{\vartheta}^2\rho_1 - \frac{\mu(r+\rho_1)}{\left[(r+\rho_1)^2+(\rho_2)^2+(\rho_3)^2\right]^{3/2}} + \frac{\mu}{r^2} \\ -2\dot{\vartheta}\dot{\rho}_1 - \ddot{\vartheta}\rho_1 + \dot{\vartheta}^2\rho_2 - \frac{\mu\rho_2}{\left[(r+\rho_1)^2+(\rho_2)^2+(\rho_3)^2\right]^{3/2}} \\ -\frac{\mu\rho_3}{\left[(r+\rho_1)^2+(\rho_2)^2+(\rho_3)^2\right]^{3/2}} \end{bmatrix} \tag{1.1}
$$

In Eq. (1.1) $\boldsymbol{\rho}$ is the position of the center of gravity of the chaser from the one of the target, r is the magnitude of the position $\boldsymbol{r}$ of the target from the Earth's center, ϑ is the true anomaly of target, and μ is the planetary constant.

In the whole dissertation the left superscript indicates the coordinate system about which the relevant vector is expressed. In particular, the symbol ℓ indicates the *local vertical-local horizontal* (LVLH) triad of the target.

The following equation expresses the orientation of such reference triad about the axes of the *Earth-centered inertial* (ECI) coordinate frame I:

$$ {}^{I}A_{\ell} = \left[\begin{array}{ccc} {}^{I}\hat{\boldsymbol{r}} & -{}^{I}\hat{\boldsymbol{r}} \times \frac{{}^{I}\boldsymbol{r} \times {}^{I}\dot{\boldsymbol{r}}}{\left| {}^{I}\boldsymbol{r} \times {}^{I}\dot{\boldsymbol{r}} \right|} & \frac{{}^{I}\boldsymbol{r} \times {}^{I}\dot{\boldsymbol{r}}_{1}}{\left| {}^{I}\boldsymbol{r} \times {}^{I}\dot{\boldsymbol{r}} \right|} \end{array} \right] \tag{1.2} $$

where ${}^{I}A_{\ell}$ is the *direction cosines matrix* (DCM) from frame ℓ to frame I. In the whole dissertation, the symbol $\hat{\boldsymbol{\zeta}}$ indicates the unit vector corresponding to $\boldsymbol{\zeta}$.

Introducing the principal body-fixed frame B of the target, it is possible to write the equation of the attitude kinematics of the target, known as Darboux's equation:

$$ {}^{B}\dot{A}_{I} = -{}^{B}\boldsymbol{\omega}^{\times}\,{}^{B}A_{I} \tag{1.3} $$

where $\boldsymbol{\omega}$ is the angular rate of the target. The notation $\boldsymbol{\zeta}^{\times}$ indicates the following skew-symmetric matrix:

$$ \boldsymbol{\zeta}^{\times} = \left[\begin{array}{ccc} 0 & -\zeta_3 & \zeta_2 \\ \zeta_3 & 0 & -\zeta_1 \\ -\zeta_2 & \zeta_1 & 0 \end{array} \right] \tag{1.4} $$

Different kinematic equations can be obtained from Eq. (1.3) if the DCM is substituted by other kinds of attitude parameters. For instance, choosing the 321 Euler angle sequence it holds:

$$ \left[\begin{array}{c} \dot{\phi} \\ \dot{\theta} \\ \dot{\psi} \end{array} \right] = \frac{1}{\cos\theta} \left[\begin{array}{ccc} \cos\theta & \sin\phi\sin\theta & \cos\phi\sin\theta \\ 0 & \cos\phi\cos\theta & -\sin\phi\cos\theta \\ 0 & \sin\phi & \cos\phi \end{array} \right] {}^{B}\boldsymbol{\omega} \tag{1.5} $$

Otherwise, the choice of *quaternions* leads to the following equation:

$$ {}^{B}\dot{q}_I = \frac{1}{2} \begin{bmatrix} 0 & -\omega_1 & -\omega_2 & -\omega_3 \\ \omega_1 & 0 & \omega_3 & -\omega_2 \\ \omega_2 & -\omega_3 & 0 & \omega_1 \\ \omega_3 & \omega_2 & -\omega_1 & 0 \end{bmatrix}^{B} {}^{B}q_I = \frac{1}{2} {}^{B}W \, {}^{B}q_I \tag{1.6} $$

Quaternions can be obtained from a DCM by using one of the following four equivalences:

$$ \begin{cases} {}^{B}q_{0I} = \pm\frac{1}{2}\sqrt{1+A_{11}+A_{22}+A_{33}} \\ {}^{B}q_{1I} = \frac{1}{4\,{}^{B}q_{0I}}(A_{23}-A_{32}) \\ {}^{B}q_{2I} = \frac{1}{4\,{}^{B}q_{0I}}(A_{31}-A_{13}) \\ {}^{B}q_{3I} = \frac{1}{4\,{}^{B}q_{0I}}(A_{12}-A_{21}) \end{cases} \quad \begin{cases} {}^{B}q_{0I} = \frac{1}{4\,{}^{B}q_{1I}}(A_{23}-A_{32}) \\ {}^{B}q_{1I} = \pm\sqrt{1+A_{11}-A_{22}-A_{33}} \\ {}^{B}q_{2I} = \frac{1}{4\,{}^{B}q_{1I}}(A_{12}+A_{21}) \\ {}^{B}q_{3I} = \frac{1}{4\,{}^{B}q_{1I}}(A_{13}+A_{31}) \end{cases} \tag{1.7} $$

$$ \begin{cases} {}^{B}q_{0I} = \frac{1}{4\,{}^{B}q_{2I}}(A_{31}-A_{13}) \\ {}^{B}q_{1I} = \frac{1}{4\,{}^{B}q_{2I}}(A_{12}+A_{21}) \\ {}^{B}q_{2I} = \pm\sqrt{1-A_{11}+A_{22}-A_{33}} \\ {}^{B}q_{3I} = \frac{1}{4\,{}^{B}q_{2I}}(A_{23}+A_{32}) \end{cases} \quad \begin{cases} {}^{B}q_{0I} = \frac{1}{4\,{}^{B}q_{3I}}(A_{12}-A_{21}) \\ {}^{B}q_{1I} = \frac{1}{4\,{}^{B}q_{3I}}(A_{13}+A_{31}) \\ {}^{B}q_{2I} = \frac{1}{4\,{}^{B}q_{3I}}(A_{23}+A_{32}) \\ {}^{B}q_{3I} = \pm\sqrt{1-A_{11}-A_{22}+A_{33}} \end{cases} $$

The Eq. (1.6) can be recast for obtaining the angular rate as a function of the attitude variation [26]:

$$ {}^{B}\boldsymbol{\omega} = 2\left({}^{B}q_{0I}\,{}^{B}\dot{\boldsymbol{q}}_I - {}^{B}\boldsymbol{q}_I\,{}^{B}\dot{q}_{0I}\right) - 2\,{}^{B}\boldsymbol{q}_I \times {}^{B}\dot{\boldsymbol{q}}_I \tag{1.8} $$

Equation (1.7) shows that besides choosing one of the possible four ways for the conversion, it is also necessary to choose the sign of the obtained quaternion. Although this choice does not affect the attitude information carried out by the quaternion, it may reveal important if this conversion is made for different time samples during a motion simulation. Indeed, to have a convenient representation of the whole body kinematics, one would like to interpolate the multiple quaternions with four continuous smooth curves. A powerful conversion algorithm that guarantees this possibility is Stanley's algorithm [27], of which a brief description is given:

1. calculate four quaternion components as a function of the elements of the principal diagonal of ${}^{B}A_I(t_k)$ (e.g. ${}^{B}q_{0I}$ in the first system of eq. 1.7);
2. evaluate the maximum value q_{max}, and then, calculate ${}^{B}q_I(t_k)$ according to ${}^{B}q_{hI} = q_{max}$ (a good example is again given by eq. 1.7 with ${}^{B}q_{hI} = {}^{B}q_{0I} = q_{max}$);
3. apply the following rule to guarantee continuity (except when $k = 0$):

$$ \text{if} \qquad {}^{B}q_{hI}(t_{k-1}) < 0 \qquad \text{then} \qquad {}^{B}q_I(t_k) \leftarrow -{}^{B}q_I(t_k) $$

Note that this kind of algorithm fails when the time step is not constant; therefore, if there is any lack of information at some time instant regarding the attitude of the body, the continuity of the quaternions cannot be guaranteed.

Attitude dynamics of spacecraft is governed by the *Euler's equation*. Both the environmental perturbation torques and the distance between the center of gravity and

the CoM of the target are neglected in this work. This assumption is acceptable if the dynamics of the target is studied for short time periods [11]. Hence:

$$ {}^{B}J\,{}^{B}\dot{\boldsymbol{\omega}} + {}^{B}\boldsymbol{\omega} \times \left({}^{B}J\,{}^{B}\boldsymbol{\omega}\right) = \mathbf{0} \tag{1.9} $$

Notice that the solution of this system does not change if the principal inertia moments vector

$$ {}^{B}\boldsymbol{J} = \begin{bmatrix} {}^{B}J_1 & {}^{B}J_2 & {}^{B}J_3 \end{bmatrix}^{T} \tag{1.10} $$

is multiplied by a positive scalar k. Thus, in the following ${}^{B}\boldsymbol{J}$ will always be considered a unitary norm vector.

For a generic body, the analytic solution of Eq. (1.9) with $J_1 > J_2 > J_3$ was found by Jacobi [28]:

$$ \begin{aligned} {}^{B}\omega_1 &= \mathcal{P}\, cn[\Xi, \Theta] \\ {}^{B}\omega_2 &= \mathcal{Q}\, sn[\Xi, \Theta] \\ {}^{B}\omega_3 &= \mathcal{R}\, dn[\Xi, \Theta] \end{aligned} \tag{1.11} $$

$\mathcal{P}$, $\mathcal{Q}$, $\mathcal{R}$, and Θ are constants that depend on both the initial angular rate and the inertia tensor; Ξ is a linear function of time; and cn, sn, and dn are the Jacobi elliptic functions. Despite the fact that this formula does not contain sines and cosines, it is worth to notice that the solution is periodic.

Jacobi elliptic functions are known to be expandable as Lambert series, i.e. is of the form

$$ \sum_{n=1}^{\infty} a_n \frac{\mathfrak{q}^n}{1-\mathfrak{q}^n} \tag{1.12} $$

where a_n is a trigonometric function, and $\mathfrak{q}$, called *nome*, is a function of the arguments of the elliptic function. It holds that $0 < \mathfrak{q} < 1$, so the series is convergent.

1.2 Models for the production of simulated datasets

The theoretical aspects of the kinematics and dynamics of satellites orbiting the Earth introduce the possibility of simulating the motion of a chaser spacecraft meeting a non-cooperative tumbling object. The simulation consists of the numerical integration of the dynamic and kinematic equations shown in the previous section. In particular, MATLAB-Simulink has been the software chosen for this simulation. These bodies have been synthetically represented by their CoM, assumed coincident with the center of gravity, and by a principal body-fixed coordinate system for the target.

This simulation permits to compute a dataset of Euclidean coordinates of a set of characteristic points or features, which are fixed to the target-fixed reference frame and expressed in a proper coordinate system whose origin belongs to the chaser.

Then, it is necessary to obtain equations for the trajectories of the features in this last coordinate system.

These trajectories, which are representative of the target-chaser relative state, will be used as inputs for the algorithms proposed in this work.

Figure 1.1 provides the flowchart representing this approach. Note the importance of some preprocessing steps between the outputs of the mathematical simulation and the realistic inputs for the algorithm.

First of all, features are not always detectable in realistic conditions. In general, a particular feature cannot be tracked continuously; typically, the body to which the feature belongs has not transparencies. So, the feature may be hidden to the detecting sensor

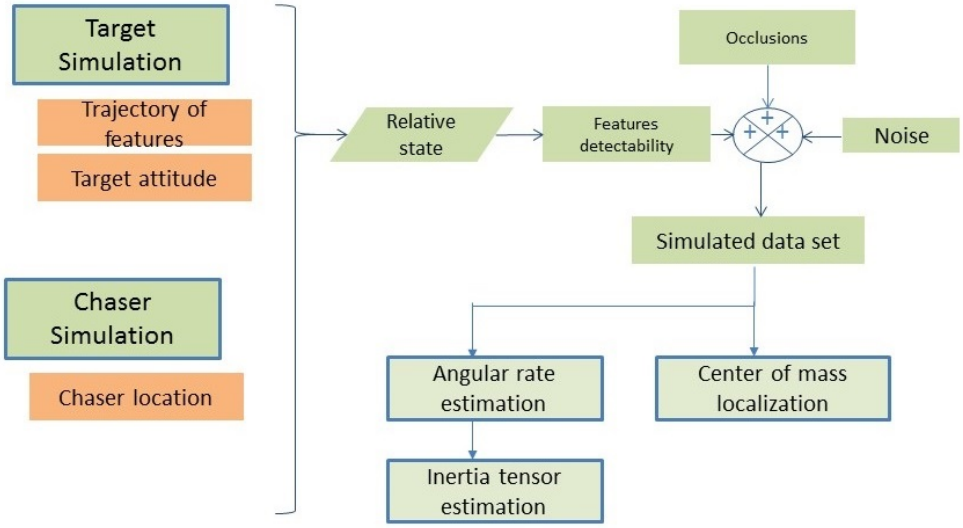

Figure 1.1 Flowchart showing the approach for validating the developed algorithms by mathematical simulations.

by the body itself in some instances. This last aspect, considered in the input dataset simulation, corresponds to the concept of feature detectability in Fig. 1.1.

Moreover, although the algorithms contained in this work are capable of treating data coming from many types of sensors, they are particularly suitable for exploiting data from passive sensors like cameras. Thus, it is also needed to consider possible failed detections and corresponding temporary lacks of input data. Occlusions are relevant examples.

Finally, it is necessary to introduce uncertainties on the data about the mentioned trajectories. This noise adding step is shown in Fig. 1.1. The entity of these uncertainties has to be coherent with at least an approximate model of the sensor that is assumed to be capable of tracking the features of the target.

1.2.1 Feature selection and tracking

The first necessary step consists in the choice of a mock-up of the target; the realistic perspective target chosen is the third stage, H10, of the expendable launch system Ariane 4 [29] (see figure 1.2). This object is 11.53m high, 2.66m in diameter, and 12000kg in gross mass.

It is worth to notice that an observer will always see one part of the target due to its rotation; the other parts of the target will always be hidden to the observer, so it is possible to consider two different approaches. In the first approach, each feature has a label that identifies its position in the body-fixed coordinate system; the observer knows these labels and it can always recognize the point once it appears after being hidden. According to the first approach, the observer needs prior information about the shape of the target; in particular, the observer requires the possession of a model of the target.

According to the second approach, the observer considers an appearing feature as it would never have been observed before. The following part of this section will show

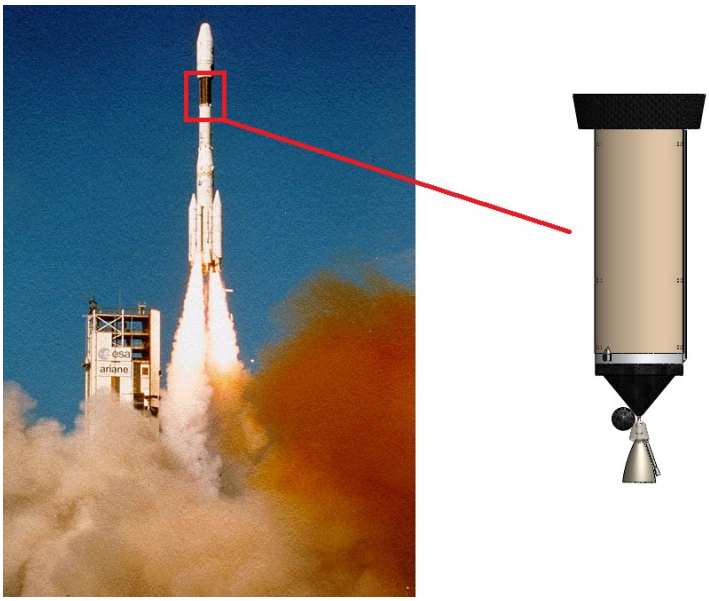

Figure 1.2 Third stage of Ariane 4, H10.

more details about the two sets of data used, which correspond to the two mentioned approaches respectively.

Considering the first approach, the following five peculiar features have been chosen. In particular, their positions are expressed in B.

$$\begin{aligned}
{}^{B}\boldsymbol{d}_1 &= [4,0,0]\,m \\
{}^{B}\boldsymbol{d}_2 &= [-5,71,0,-0,81]\,m \\
{}^{B}\boldsymbol{d}_3 &= [-3,91,0,1,42]\,m \\
{}^{B}\boldsymbol{d}_4 &= [-3,97,1,02,-1,02]\,m \\
{}^{B}\boldsymbol{d}_5 &= [-7,61,0,0]\,m
\end{aligned} \tag{1.13}$$

Figures 1.3, 1.4, and 1.5 show the presented features.

Considering the second approach, the lack of a-priori information about the shape of the body is compensated by a greater number of points tracked. Fig. 1.6 shows the

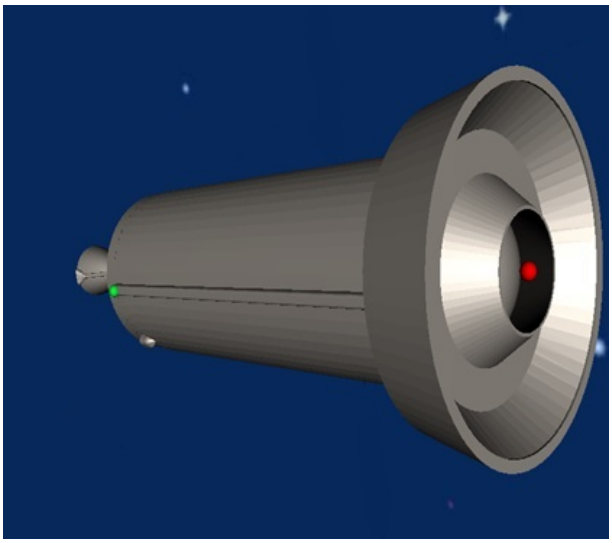

Figure 1.3 H10 model with features ${}^{B}\boldsymbol{d}_3$ (on the left) and ${}^{B}\boldsymbol{d}_1$ (on the right)

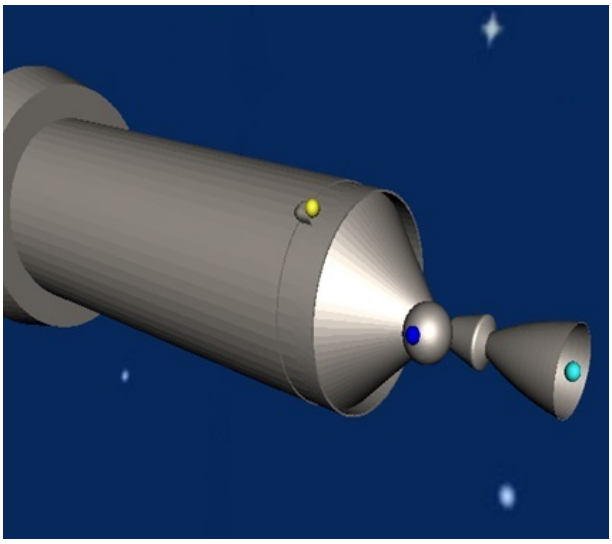

Figure 1.4 H10 model with features ${}^{B}\boldsymbol{d}_4$ (on the left), ${}^{B}\boldsymbol{d}_2$ (middle point) and ${}^{B}\boldsymbol{d}_5$ (on the right)

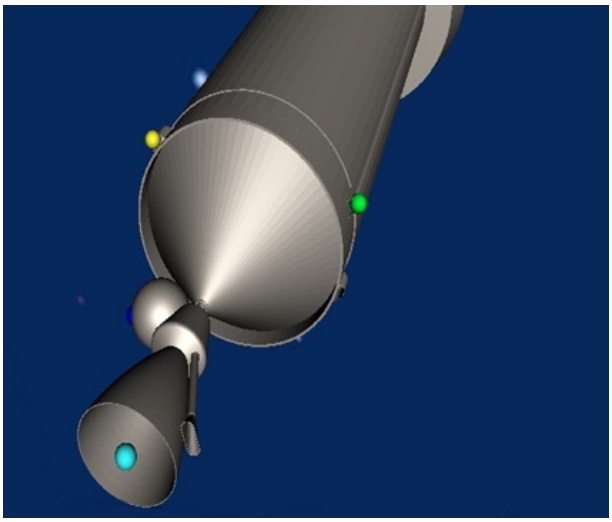

Figure 1.5 H10 model with features ${}^{B}\boldsymbol{d}_4$, ${}^{B}\boldsymbol{d}_3$ and ${}^{B}\boldsymbol{d}_5$

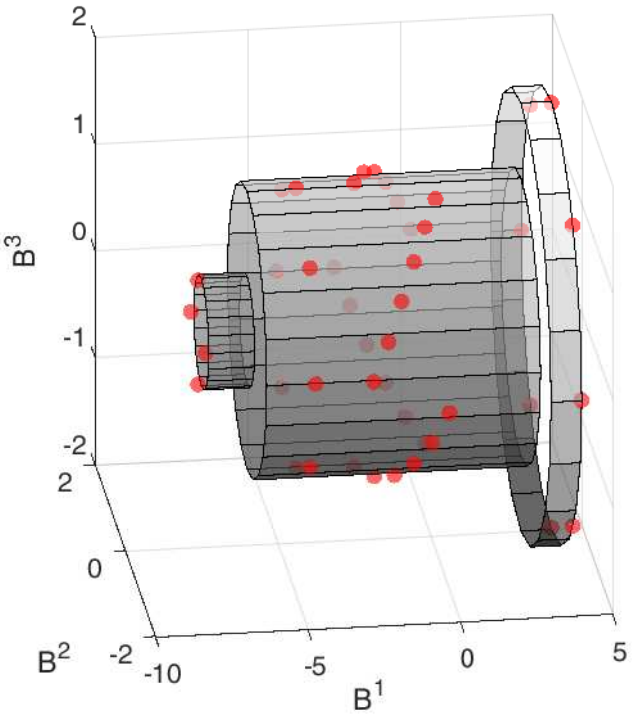

Figure 1.6 Position of the 44 unlabeled complementary features

position of the chosen features. The total number of considered features on the body surface is 44: 20 of those points are placed along three circular sections of H10, while the rest are placed along spirals.

Once the features have been placed on the body, they will move according to the target attitude dynamics, expressed by Eq. (1.9). It is important to observe the trajectory of the features from a proper reference frame. In particular, a convenient coordinate system in which expressing the position of the features has the same orientation of the inertial coordinate system I. The attitude dynamics of the chaser should be considered known, since it is a controlled spacecraft. In particular, it is equipped with sensors capable of accurately observe its own motion.

Thus, it is possible to define a coordinate system C whose origin coincides with the CoM of the chaser, and whose axes are oriented as the ones of the system I. Hence, it holds:

$$ {}^{I}A_{C} = I_{3} \tag{1.14} $$

The characteristic coordinate system of the tracking sensor is referred as S, which is different from C in orientation and origin. In particular, the position of its origin is ${}^{C}\boldsymbol{s}$, while its orientation is given by the matrix ${}^{C}A_{S}$.

Both these two quantities are time dependent, according to the controlled attitude dynamics of the chaser. However, the coordinates of the features that are measured in S can be transformed by

$$ {}^{C}\boldsymbol{\rho}_{i} = {}^{C}\boldsymbol{s} + {}^{C}A_{S}\,{}^{S}\boldsymbol{\rho}_{S_i} \tag{1.15} $$

The vector ${}^{C}\boldsymbol{s}$ and the matrix ${}^{C}A_{S}$ are considered known. So, this calculation could be avoided. Moreover, it is not necessary to simulate the attitude dynamics of the chaser, but only its orbital one, which is relative to the system ℓ of the target using Eq.(1.1). Thus, the computation of the coordinates of the features will be performed directly in C. Figure 1.7 shows the defined reference frames.

The position of the target CoM in C comes from:

$$ {}^{C}\boldsymbol{\rho} = -{}^{I}A_{C}^{T}\,{}^{I}A_{\ell}\,{}^{\ell}\boldsymbol{\rho} \tag{1.16} $$

where ${}^{I}A_{\ell}$ is defined by Eq.(1.2).

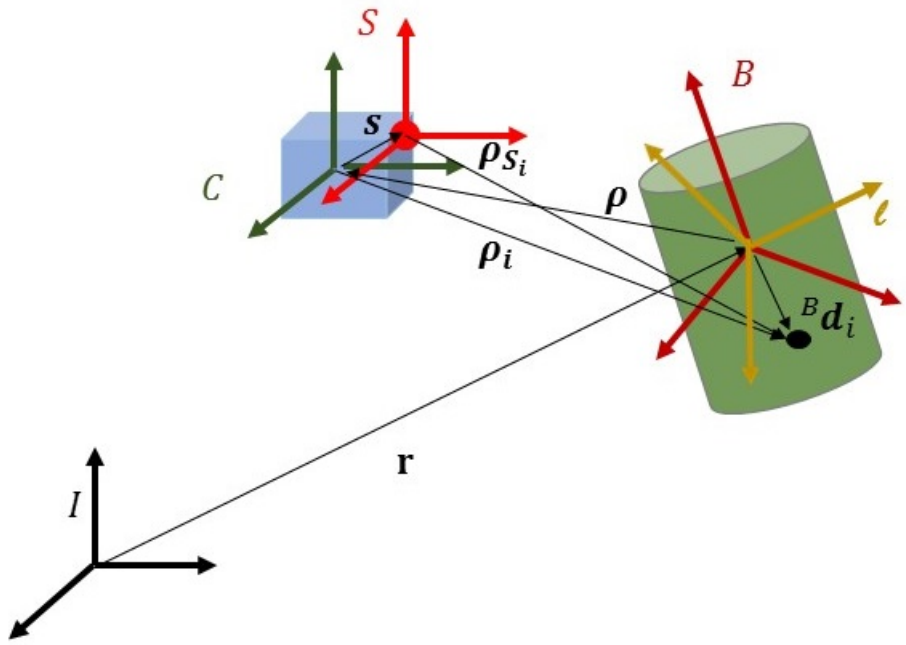

Figure 1.7 Reference frames: body, chaser, sensor, and features

The position of a generic i-th feature of the target with respect to the frame C is obtained from the knowledge of the constant position ${}^B\boldsymbol{d}_i$ in the body-fixed frame B:

$$ {}^C\boldsymbol{\rho}_i = {}^C\boldsymbol{\rho} + {}^I A_C^T \, {}^B A_I^T \, {}^B\boldsymbol{d}_i \tag{1.17} $$

${}^B A_I$ is obtained by solving the differential equation system deriving from Eq.(1.3) and Eq.(1.9).

Equation (1.17) is used to obtain the final result of the simulation.

To give an example of the computed trajectories, it is necessary to define the following initial conditions of the target and the chaser:

- orbit of the target, defined by orbital parameters. An example is given in Tab. 1.1. The considered orbit is strongly eccentric.

- the initial conditions of the relative translational dynamics between target and chaser. In this first example, to solve Eq. (1.1), ${}^{\ell}\boldsymbol{\rho}_0$ and ${}^{\ell}\dot{\boldsymbol{\rho}}_{\mathbf{0}}$ are chosen as follows:

$$ {}^{\ell}\boldsymbol{\rho}_0 = \left[\begin{array}{c} -0.22, -92.86, 0 \end{array} \right]^T \text{m} $$

$$ {}^{\ell}\dot{\boldsymbol{\rho}}_0 = \left[\begin{array}{c} -0.044, 0.004, 0 \end{array} \right]^T \text{m/s} $$

- the principal inertia moment ${}^{B}\boldsymbol{J} = [0.7014, 0.5762, 0.4196]$
- the initial absolute angular rate ${}^{B}\boldsymbol{\omega}_0 = [10.2 \quad 0.72 \quad -17.1]$ deg/s

ephemeris	$e = 0.55$
	$i_n = 6.93^\circ$
	$\omega_p = 146.4^\circ$
	$\Omega_{an} = 132.2^\circ$
	$a = 15371\ km$
	$\vartheta_0 = 349.9^\circ$

Table 1.1 Keplerian parameters used in the simulation

The trajectories of the features defined in Eq. (1.13) are shown in Fig. 1.8; note that the curves wrap around the trajectory of the center of mass of the target.

It has been mentioned that most of the target surface is hidden to the observer. For that reason, the data obtained through Eq. (1.17) can not be directly exploited, but some of the data have to be discarded. Indeed, it is practically impossible that a feature always remains visible to the observer. That can occur just if the chaser is guided such to point always toward the specific feature. This last condition is tough to be achieved. Obviously, if some feature is belonging to the hidden parts in one generic instant of time, its position should be eliminated from the simulated data in that instant. Thus, a certain feature is

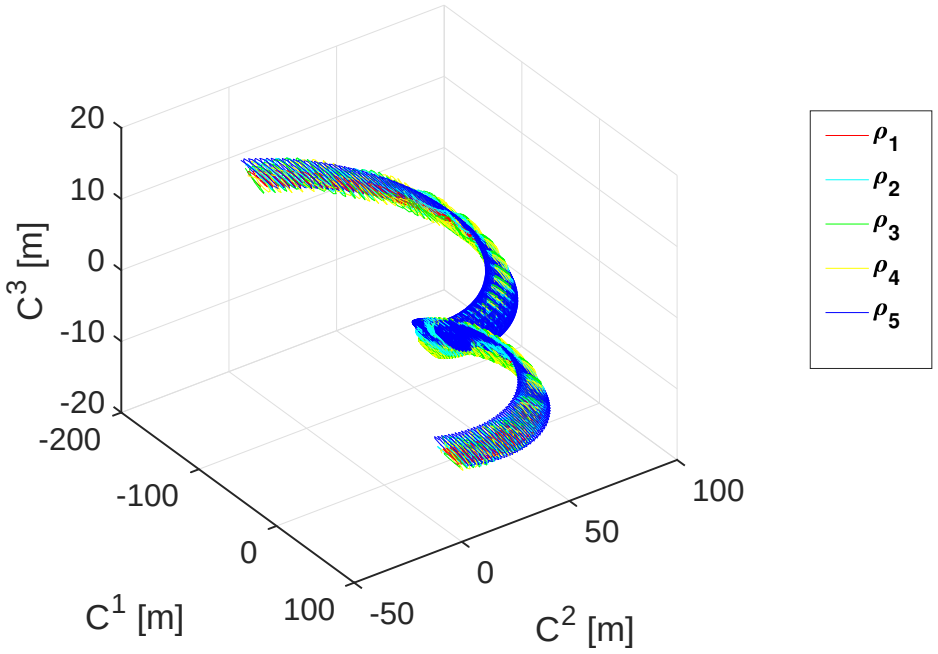

Figure 1.8 Trajectories of features with respect to the chaser reference frame C. The considered time interval starts from zero to one target orbital period

subjected to appear and disappear repeatedly from the observer, and it is necessary a method to determine which features are visible at every instant of time.

There are many techniques for hidden surface determination; in this work the backface culling technique has been used [30]: the direction of the normal to the examined surface has been evaluated and then, if the scalar product between the normal vector and the view direction is negative, then the surface and its points are visible (see Fig. 1.9 and Eq. (1.18)).

An example of the elimination of tracking data after backface culling is given in Fig. 1.10 where the piece-wise position signal related to the feature $\boldsymbol{\rho}_1$ of the Fig. 1.8 is shown for a short interval of time.

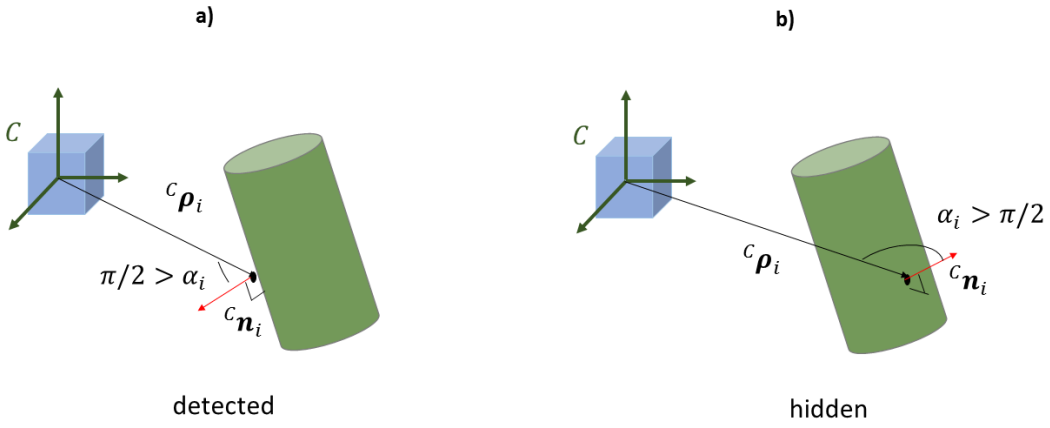

Figure 1.9 Backface culling technique. The surface normal in the hidden feature (case b) form an angle with the feature position which is bigger than 90 degrees.

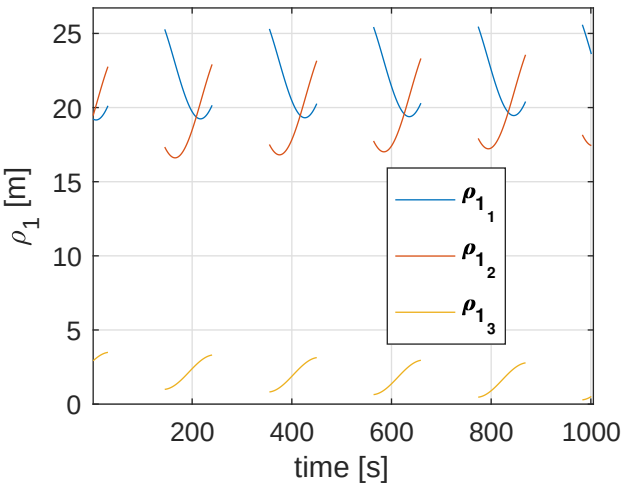

Figure 1.10 Euclidean coordinates of the point $\boldsymbol{\rho}_1$ after the application of the Backface culling technique in a short time interval. $\boldsymbol{\rho}_{1_i}$ is the i-th coordinate of the point $\boldsymbol{\rho}_1$

$$\frac{^C\boldsymbol{\rho}_i \cdot {}^C\boldsymbol{n}_i}{||^C\boldsymbol{\rho}_i||} = \cos\alpha_i > 0 \implies \text{feature } i \tag{1.18}$$

This simple technique is perfectly valid only if the body to which the surface belongs is convex (i.e. cylinders, cubes). Otherwise, it produces some errors. So for complex bodies backface culling has to be followed by other techniques (*e.g.* z-buffer) [30]. However, this is beyond the purpose of this work, in which a coarse determination of the hidden surfaces is more than sufficient.

Using the above algorithm, one can create a Boolean array χ_i for the generic point i containing the visibility information.

When few features are considered the non-visibility condition frequently occurs. Notice that by using few features (first approach) all of them can be hidden at the same time. As this would happen frequently, this condition simulates *de-facto* several global losses of measured data. The second approach, on the contrary, considers a higher number of features. This would guarantee that some points are visible at every instant. However, it is proper to consider that some temporary interruptions in data acquisition can occur, e.g. occlusions. In this case, provisional lacks of data may occur, so there is the need of robust algorithms that can deal with lacks of input data; to provide the

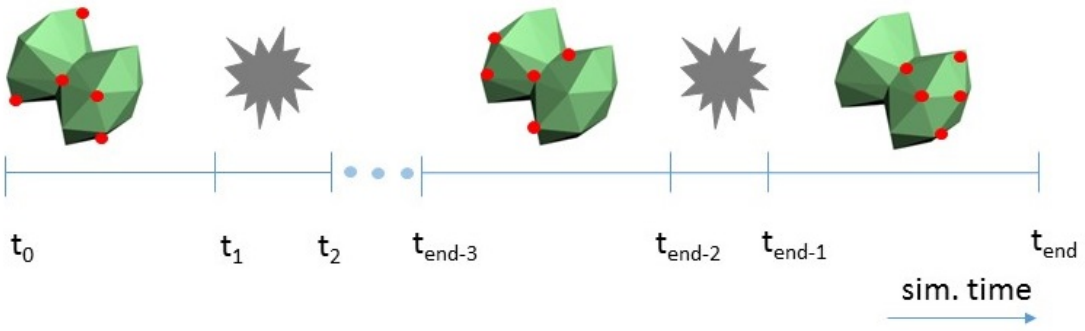

Figure 1.11 Second approach for the dataset production: simulation time is divided in intervals, and in some of these ones there are no data available. That corresponds to the introduction of artificial occlusion periods.

robustness of the proposed algorithm, artificial occlusions have been introduced (see Fig. 1.11).

1.2.2 Uncertainties on trajectories of the features

At this step of the production of the data, the trajectories of the features are available. As underlined before, many parts of these trajectories are not available for several intervals of time. That holds due to the visibility issue or to the artificial occlusions added. To better simulate the acquisition of the trajectories, it is necessary to add some noise, which should be characteristic of the considered acquisition process. This noise is proper of the sensor, so it is needed to consider a particular sensor model to identify its characteristics.

The algorithms proposed in this work have been thought to be exploited with different kinds of sensors. Among these, stereo cameras can be considered the most affected by errors, so their model is used to create noisy data and test the algorithms in the worst case.

In the following, stereo cameras observation model is described, with particular attention to noise. Then, it is described the procedure to create noisy data from trajectories.

Assume that a stereo rig, composed of two parallel cameras, is mounted rigidly on the chaser. A coordinate system S originating at the center of mass of the chaser is defined. Referring to Fig. 1.12, the axis S^1 points from the center of projection of the left camera COP_{S_l} to the one of the right camera COP_{S_r}, S^3 is vertical and positive upward, and S^2 follows the right-hand rule.

The right camera's center of projection COP_{S_r} is located on the CoM of the chaser, and the left one is located at a distance b_S from COP_{S_r}.

$$^S\boldsymbol{COP}_{S_r} = [0,0,0]^T, ^S\boldsymbol{COP}_{S_l} = [-b_S,0,0]^T \tag{1.19}$$

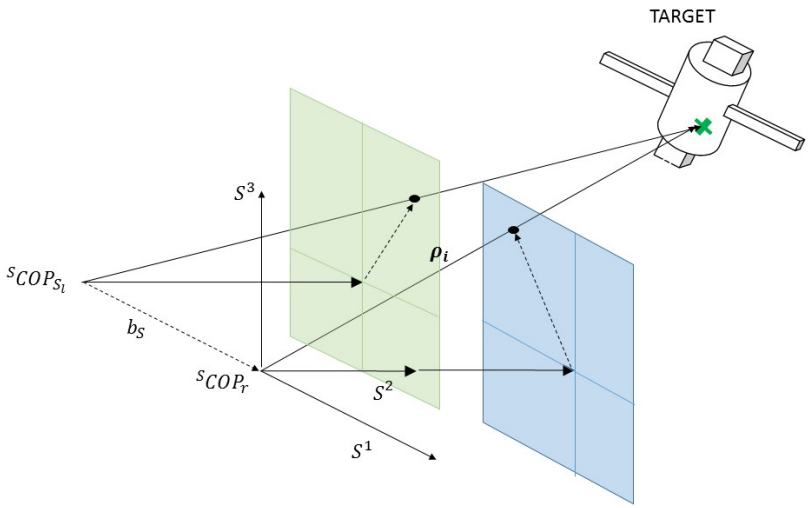

Figure 1.12 Stereo rig system.

In this framework, the perspective projection model [31] can be used to describe the visual observation of the features by the stereo rig. Feature points are transformed onto the image plane according to the function π:

$$\pi({}^{S}\rho_i) = \left[\frac{{}^{S}\rho_{i_1}}{{}^{S}\rho_{i_2}}, \frac{{}^{S}\rho_{i_3}}{{}^{S}\rho_{i_2}}\right]^T \tag{1.20}$$

Therefore, the observations corresponding to the i-th feature point are:

$$\varepsilon_i^r = \pi({}^{S}\boldsymbol{\rho}_i), \varepsilon_i^l = \pi({}^{S}\boldsymbol{\rho}_i + {}^{S}\boldsymbol{b}_S) \tag{1.21}$$

where ${}^{S}\boldsymbol{b}_S = [b_S, 0, 0]$ is the baseline vector.

To understand how the noise added at the image plane level affects the Euclidean coordinates of the features, we considered 10^6 points that we distributed uniformly inside a 3m$\times$10m$\times$3m box. This box was placed at $[0 \quad 25 \quad 0]$ m in the frame S. Then, the two

projections $\pi({}^S\boldsymbol{\rho}_i)$ and $\pi({}^S\boldsymbol{\rho}_i + {}^S\boldsymbol{b}_S)$ were applied. Adding a zero-mean Gaussian noise to the projected points and after an inverse projection, the error distribution at coordinate level is obtained. Two extremal noise conditions have been examined, so these steps were repeated for two cases. In particular, the standard deviation of the Gaussian noise was set to 10^{-4} in the first instance and 10^{-5} in the second. The latter value is consistent with the usage of a medium-high end camera. For example, a 8 megapixel camera with a 3296x2472 pixel array, 5.5 μm pixel pitch, and 70 mm of focal length [1].

Fig. 1.13 and Fig. 1.14 show that, in both cases, the greatest error affects the depth coordinate (${}^S\rho_2$).

[1] https://www.thorlabs.com/newgrouppage9.cfm?objectgroup_id=7566

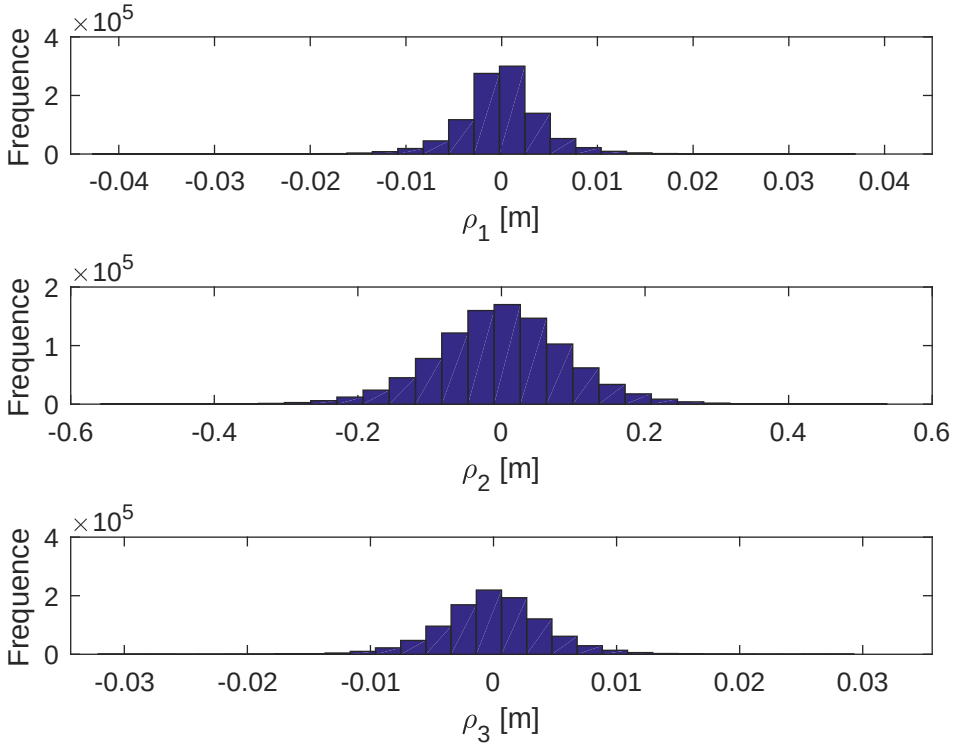

Figure 1.13 Histogram of the errors on the trajectory after the inverse projection, $\sigma = 10^{-4}$

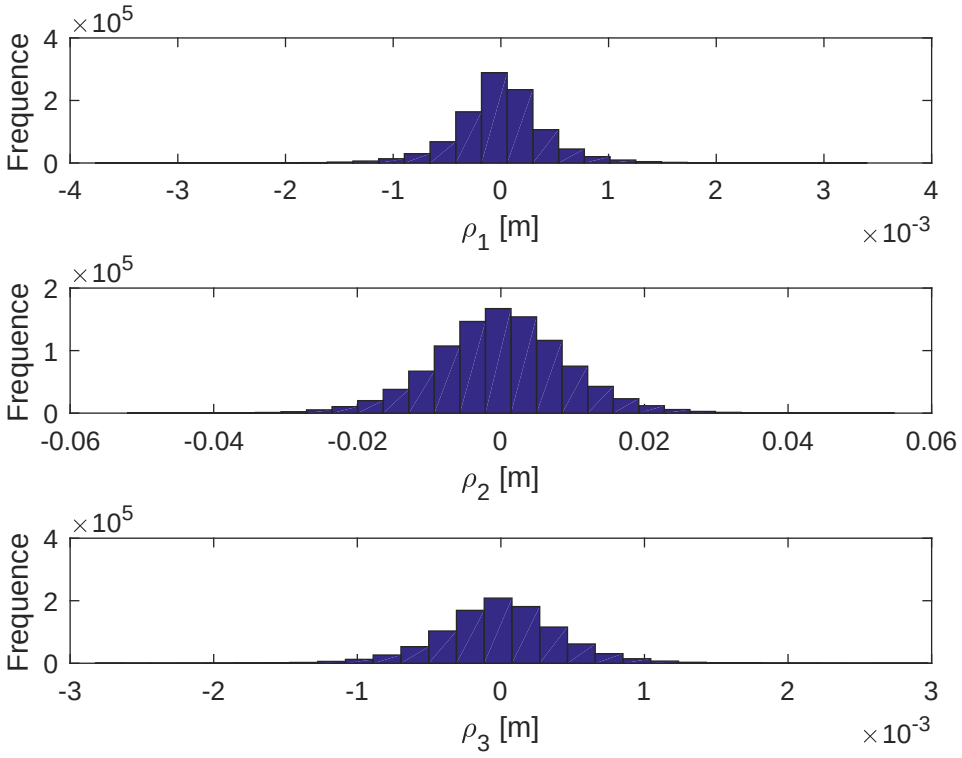

Figure 1.14 Histogram of the errors on the trajectory after the inverse projection, $\sigma = 10^{-5}$

In both cases, the distribution of the errors on the three components of the position of the points is similar to the zero-mean Gaussian. In the first case, in particular, the empirical standard deviations of the first and the third components are both 0.0042 m, while 0.0927 m is the standard deviation of the second component. In the second case, the empirical standard deviations for the first and the third components are both 0.0004 m, while 0.0093 m is the standard deviation of the second component.

Notice that these values have been derived in the *S* framework, which is the original framework of the sensor. However, the simulated dataset contains coordinates of features of the target in the *C* framework. Eq. (1.15) expresses the mapping between positions in

C and S. Since the considered system S has its origin in the CoM of the chaser, it holds ${}^{C}\boldsymbol{s} = 0$.

Moreover, the matrix ${}^{C}A_S$ is orthonormal. Thus, the amplitude of the noise on each component of ${}^{C}\boldsymbol{\rho}_i$ should not be greater than the one of the depth coordinate of ${}^{S}\boldsymbol{\rho}_i$. As ${}^{C}A_S$ is not known a-priori, the worst case has been considered: the noise added to the each component of ${}^{S}\boldsymbol{\rho}_i$ has a standard deviation equal to the biggest found in ${}^{S}\boldsymbol{\rho}_i$. Therefore, the range for the standard deviation of the noise on each component of detected features can vary from 10 mm to 100 mm.

These last remarks complete the data simulation phase (see Fig. 1.1). The final dataset obtained can be sufficiently realistic for a first validation of the methods presented in the following.

Chapter 2

Localization of the center of mass

The most explored methods for active removal of space debris require the contact between the chaser spacecraft and the target. When the mechanical parts of the docking mechanism come in touch with some natural interfaces on the target surface, they exert forces and torques on the tumbling object. These actions have to be accurately controlled to prevent the loss of the chaser control. In particular, to predict the torques exerted on the target, it is necessary to have at least an approximate knowledge of the location of the CoM of the object.

The rotation of a tumbling space object is about its CoM since it is completely unconstrained. Thus, the problem of identifying the location of the CoM is equivalent to the research of the point about which the body rotates. Hence, the identification of a dynamic property of the target reduces to a problem of kinematic nature.

However, from an analysis of state of the art, this kinematic approach is typically avoided. That probably holds due to the difficulties in finding reliable information about the body rotation from corrupted measurements of feature positions. Approaches that exploit statistical state observers are more common due to their powerful capabilities of indirectly estimating unknown quantities from corrupted measurements of related

quantities and the knowledge of a reliable mathematical model of the dynamics of the observed system. Indeed, by simply assuming the coincidence of the CoM with the center of gravity of the satellite, it is considerable that this point moves according to the Kepler's laws whose treatment can be found in Appendix A.1.

Nevertheless, also this kind of approaches present drawbacks linked to the assumptions needed for their application. As it will be described in the next chapter with greater detail, the measurements required to feed the observer have to be taken at regular time steps for many samples. If interruptions of this depicted sequence occur, then the observer loses the capability of estimating the unknown quantities of interest. Moreover, all the measured samples must always refer to the same quantities.

Approaches that rely on state observer use the positions of the features as the mentioned sequence of measurements. Thus, they are forced to assume that the tracked features are always the same for the whole observation period. Moreover, failures in the feature detection have to be excluded (for instance, see [19] or [32]). However, for the considerations exposed in section 1.2, these assumptions appear to be quite restrictive.

For those reasons, in this work, it has made an attempt in developing a complete estimation approach based on kinematic considerations only.

Two poses of the object, represented by the same set of homologous features in two different time samples, underlie a finite motion represented by a rotation about an axis and a translation along the same axis. This statement is the result of the Mozzi-Chasles' theorem [33].

The first arising problem is that this representation depends only on the initial and final configuration of the body, and it does not take into account the actual motion during the considered interval of time. Thus, a correct description of the motion needs that the mentioned time interval is infinitesimal.

A second issue is that if the body does not move in a plane, there is an infinite set of points having the same velocity, which all belong to the same axis whose direction aligns to those velocities. This axis is the *instantaneous screw axis*. Thus, it is not clear how to discriminate the CoM from the infinite points belonging to that axis until no information comes from the motion analysis during more intervals of time.

This chapter will show that an approximate identification is possible if the relative velocity between the target and the chaser becomes very low at a certain moment of the observation. This unique but fundamental assumption for the effectiveness of the presented method turns practically in the closeness of the orbits of the two objects. However, that condition seems unavoidable for having a close rendezvous, which is necessary for considering the capture of the target.

The first part of this chapter dedicates to the characterization of an estimator of the location of the CoM of the target from the positions of homologous features at three adjacent time samples. For a better discussion of the properties of this estimator, a first subsection treats the estimation problem neglecting issues about detectability of the features or uncertainties on measurements (see section 1.2). A second subsection introduces the possibility of missing input data still without the addition of the noise. This subsection also proposes the estimation in a body-fixed frame.

Then, to apply the developed estimator on corrupted data, it is necessary to exploit filtering techniques to regularize the uncertainties. The second part of this chapter will describe such techniques. Finally, the final accuracy of the estimation is discussed through some application examples.

2.1 A new estimator in absence of uncertainties

2.1.1 Estimation without missing data

The knowledge of the Euclidean coordinates of some points of a rigid body in different instants of time could be used to perform the so-called kinematic registration of the body. This term means essentially to determinate axes and poles of the finite rotations of the body.

In 1985, Franz Reuleaux [34] proposed a general graphical rule for evaluating the position of the pole of the rotation underlying a planar rigid displacement of a body. This rule starts from the knowledge of the position of two points of the body after and before the movement, i.e. two couples of homologous points. Then, the method individuates the pole U of the displacement finding the intersection point of bisecting lines that connects the corresponding homologous points (see Fig.2.1).

Implicitly, the usage of this rule corresponds to represent the finite motion of a body with one simple rotation around a pole. However, the movement of an unconstrained rigid body on a plane can be seen instantaneously as the combination of a translational motion,

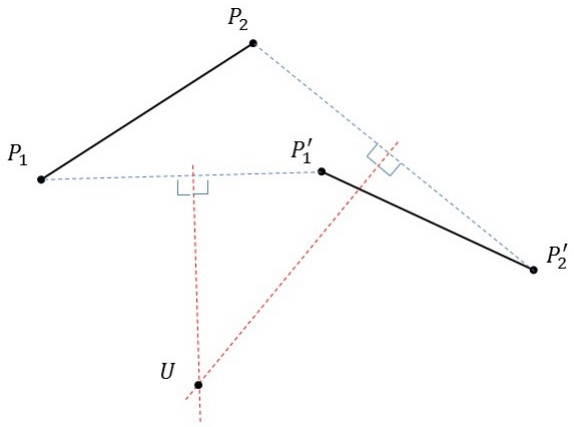

Figure 2.1 Application of the Releaux method.

characterized by the velocity of its CoM, and of a rotational motion, characterized by an angular velocity around the same CoM.

Thus, the application of the Reuleaux rule does not provide information about the actual motion of the object, but it provides only a synthetic representation of the final configuration of the body as a function of the initial one. Indeed, the found pole of the rotation is not coincident, in general, with the CoM of the body, nor it is a point belonging to the body itself.

Even considering an infinitesimal time interval, the application of the Releaux rule identifies an instantaneous center of rotation that is not, in general, coincident with the CoM. In particular, the distance between this instantaneous center of rotation and the CoM is proportional to the rate between the magnitudes of the CoM velocity and the angular rate (v_G/ω). As a consequence, if the motion is a pure rotation, the Reuleaux rule is useful to find exactly the CoM of the body.

Demonstration of this statement follows (see Fig.2.2):

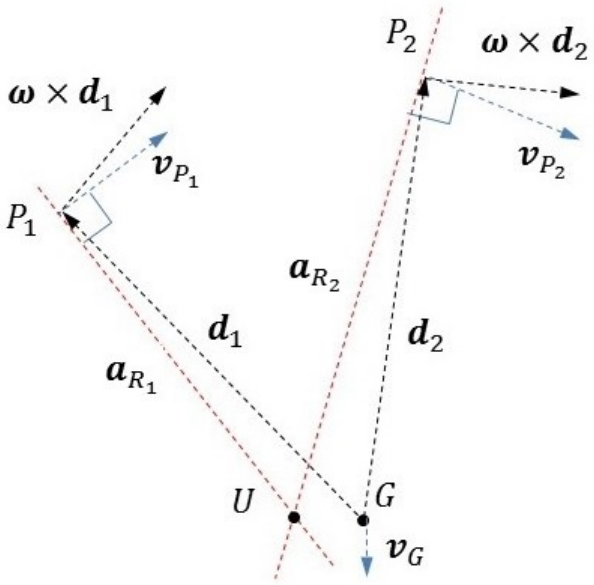

Figure 2.2 Application of the Releaux method in an infinitesimal time interval.

Let P_1 and P_2 two points of the rigid body, whose CoM is G. Due to the fact that the body is rigid, it holds

$$\boldsymbol{v}_{P_i} = \boldsymbol{v}_G + \boldsymbol{\omega} \times \boldsymbol{d}_i \qquad i = 1,2 \tag{2.1}$$

where $\boldsymbol{d}_i$ is the distance between P_i and the CoM. According to the Releaux method, the pole U of the displacement is the intersection point of bisecting lines that connects the corresponding homologous points. It holds that

$$P_i' = P_i + \Delta t \; \boldsymbol{v}_{P_i} \qquad i = 1,2 \tag{2.2}$$

The axis of the line connecting the two points is normal to v_{P_i}. If the time interval is infinitesimal, then homologous points tends to coincide ($P_i' \to P_i$), and the bisecting line defined by the Releaux rule would be the axis $\boldsymbol{a}_{R_i}$ passing for P_i and normal to $\boldsymbol{v}_{P_i}$.

A generic point of a_{R_i} is of the form:

$$U_i = P_i + \lambda_i \begin{bmatrix} 0 & -1 \\ 1 & 0 \end{bmatrix} \boldsymbol{v}_{P_i} \qquad i = 1,2 \tag{2.3}$$

Hence, to find the pole of the rotation, the intersection between a_{R_1} and a_{R_2} has to be computed. Thus, the constraint $U_1 = U_2$ is imposed and the system of linear equation represented by Eq.(2.3) is solved in (λ_1, λ_2). It is found that $\lambda_1 = \lambda_2 = -\frac{1}{\omega}$, and

$$U = U_1 = U_2 = P_1 - \frac{1}{\omega} \begin{bmatrix} 0 & -1 \\ 1 & 0 \end{bmatrix} (\boldsymbol{v}_G + \boldsymbol{\omega} \times \boldsymbol{d}_1) \tag{2.4}$$

Finally, the distance between U and G is computed; it holds that:

$$|U-G| = \frac{v_G}{|\omega|} \tag{2.5}$$

Eq. (2.5) shows that, if a translation occurs, the pole computed by the Releaux method is different from the exact CoM of the body even if an infinitesimal time interval dt is considered. Clearly, the error will increase with the interval duration.

Reuleaux rule is not suitable when it is necessary to characterize the motion of a body in the three-dimensional space. Different works regarding the parameterization of 3D rigid body motions have been published: Some reliable methods are, for instance, in [35] or in [36]. In [37] it is possible to find a complete theoretical treatment of the parameterization of a 3D rigid motion with compact dual orthonormal tensors.

However, the parametrization method chosen in this work is the one provided by Eberharter and Ravani [38]. This choice has been made due to the simplicity and effectiveness of the proposed method. In particular, the method is an efficient generalization of the two-dimensional Reuleaux rule. It exploits the knowledge of the coordinates of three couples of homologous points to find a rotation axis and a point belonging to this axis.

Given three vectors $\boldsymbol{g}_i$ connecting as many couples of homologous points (P_i and P_i'), the vectors $\boldsymbol{c}_1 = \boldsymbol{g}_2 - \boldsymbol{g}_1$ and $\boldsymbol{c}_2 = \boldsymbol{g}_3 - \boldsymbol{g}_1$, span a plane which is perpendicular to the finite screw axis $\hat{\boldsymbol{e}}$ [39]. Then, from the family of planes that are normal to $\hat{\boldsymbol{e}}$, it is considered the one passing through the origin of the reference frame in which points are expressed, namely ε (see Fig. 2.3).

The components of the axis $\hat{\boldsymbol{e}}$ can be evaluated through the subsequent formula:

$$\hat{\boldsymbol{e}} = \frac{\boldsymbol{c}_1 \times \boldsymbol{c}_2}{||\boldsymbol{c}_1 \times \boldsymbol{c}_2||} \tag{2.6}$$

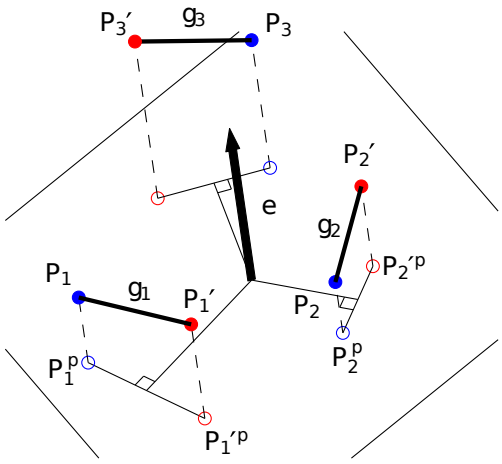

Figure 2.3 Plane individuation and axis localization.

After the identification of the direction of the screw axis $\hat{\boldsymbol{e}}$, for continuing with the kinematic registration, it is necessary to localize a point that belongs to that axis. To make that, one can project only two couples of homologous points on the found plane ε. The Reuleaux rule can be then applied to find the location of a pole of the rotation of the body.

The calculation of the translational displacement and the rotation angle of the body completes the kinematic registration. The translational displacement t_e is simply the dot product between $\hat{\boldsymbol{e}}$ and one of the $\boldsymbol{g}_i$ vectors. The rotation angle α is the angle formed by line segments connecting U to two projected homologous points. However, for the purpose of this work, only the localization of the screw axis is sufficient.

As well as for the simple Reuleaux rule, the method does not provide information about the actual motion of the considered body, but it provides only a relationship between the initial and final poses of the body. The found screw axis does not pass, in general, through the CoM of the body. However, if the motion of the body is a pure rotation, then the found axis will pass through the CoM of the body. If one would extend

the above concepts from planar motions to 3D motions, the error made assuming that the center of mass belongs to the found axis is proportional to the rate between the magnitudes of the in-plain (normal to the rotation axis) component of the CoM velocity and the angular rate ($v_{g\perp}/\omega$)

If the chaser were capable of perfectly following the trajectory of the center of gravity of the target, which will be considered coincident with its CoM, the following elementary equation would substitute the Eq. (1.1) for simulating relative orbital dynamics between the chaser and the target:

$$^{C}\dot{\boldsymbol{\rho}} = \begin{bmatrix} 0 & 0 & 0 \end{bmatrix}^{T} \tag{2.7}$$

For instance, imposing the initial condition

$$^{C}\boldsymbol{\rho}_{0} = \begin{bmatrix} 14 & 10 & 0 \end{bmatrix}^{T} \text{m},$$

and considering the five features of the target in Eq. (1.13), the dataset computed from Eq. (1.17) would be such that the direct application of the method in [38] provides results illustrated by Fig. 2.4. All the computed axes intersect exactly in the CoM of the simulated target. Note that the backface culling technique for eliminating the hidden features were not applied, so all the features were always detectable.

In real conditions, the relative distance between the two objects can vary significantly, or also diverge as a function of the initial conditions chosen for solving Eq. (1.1). It is assumed, however, that the orbits of the two objects are close enough so that two conditions are guaranteed. The first one is that the objects remain sufficiently close, at least for a short interval of time, so that the features can be detected accurately with vision based sensors. The second one is that there is, at least, one instant in which the relative velocity between the two object tends to zero. For instance, the initial conditions

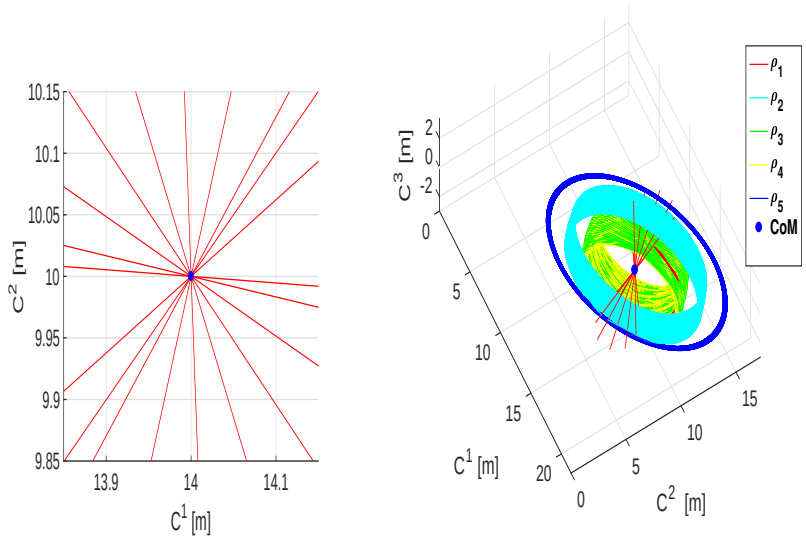

Figure 2.4 Center of mass localization if there is no relative dynamics between chaser and target. In (b) the trajectories of the five features in Eq. (1.17) are shown, while in (a) the projections of the rotation axes on the C^1C^2 plane are illustrated.

proposed is subsection 1.2.1 for obtaining the trajectories in Fig. 1.8 are such that the mentioned conditions are satisfied.

Let us consider three separated time instants $t-1$, t and $t+1$, being t a generic time index. Given the locations of three features at the instant $t-1$ and t in the frame C, the screw axis direction ${}^C\hat{\boldsymbol{e}}_{t-1,t}$ comes from Eq. (2.6); moreover, also a point of this axis $U_{t-1,t}$ comes from the 3D extension of the classic Reuleaux rule. In the same way, a second screw axis direction ${}^C\hat{\boldsymbol{e}}_{t,t+1}$ and a point $U_{t,t+1}$ are obtainable from other three features at the instants t and $t+1$.

As a relative translation between the chaser and the target occurs, two successive screw axes do not intersect as they are non-coplanar. So, in this condition, it is not possible to find the CoM via a rigorous axes intersection. Nevertheless, it is still possible to determine approximately the location of this point.

If the sample time is very much lower than the orbital period of the target (sampling frequency in the order of 1 Hz), the distance between two successive screw axes will be tiny. Hence, a possible estimator of the location of the CoM could consist, for instance, of the following set of linear operations. Being V and T two parametric points of the two screw axes in the unknown parameters λ_T and μ_V, it holds:

$$\begin{aligned} T(\lambda_T) &= \lambda_T \, {}^C\hat{\boldsymbol{e}}_{t-1,t} + U_{t-1,t} \\ V(\mu_V) &= \mu_V \, {}^C\hat{\boldsymbol{e}}_{t,t+1} + U_{t,t+1} \end{aligned} \tag{2.8}$$

Then it can be imposed the orthogonality between the line segment $T - V$ and the screw axes:

$$\begin{aligned} [T-V]^T \, {}^C\hat{\boldsymbol{e}}_{t-1,t} &= \mathbf{0} \\ [T-V]^T \, {}^C\hat{\boldsymbol{e}}_{t,t+1} &= \mathbf{0} \end{aligned} \tag{2.9}$$

that leads to the following linear system in the parameters λ_T and μ_V:

$$\Gamma \begin{bmatrix} \lambda_T \\ \mu_V \end{bmatrix} = \xi \implies \begin{bmatrix} \lambda_T \\ \mu_V \end{bmatrix} = \Gamma^{-1} \xi \tag{2.10}$$

The solution of the system always exists if the two screw axes are non-coplanar. Moreover, it is unique. The 2×2 matrix Γ depends only on the directions of the axes, while the column matrix ξ also contains the information related to the axes location. Then, after the elimination of the parameters, the location of the CoM can be finally estimated at the instant t as:

$${}^C\bar{\boldsymbol{\rho}}_t = \frac{1}{2}[T+V] \tag{2.11}$$

Moreover, the distance between the two screw axes is evaluable as:

$$d_{e_t} = |T - V| \tag{2.12}$$

An illustration of this kind of estimation via *pseudo*-intersection of the screw axes is in Fig.2.5.

The properties of this kind of estimator will be now discussed with the aid of two examples of application. Two different orbits of the simulated target will be considered. The first considered orbit is strongly eccentric; the related Keplerian parameters are in Tab. 1.1. The initial dynamic conditions of the target are those listed in subsection 1.2.1. For a better understanding of how the attitude dynamics influences the proposed estimator, another simulation ran with the normalized principal inertia moments equal to

$${}^{B}\boldsymbol{J} = \begin{bmatrix} 0.075 & 0.705 & 0.705 \end{bmatrix}^{T},$$

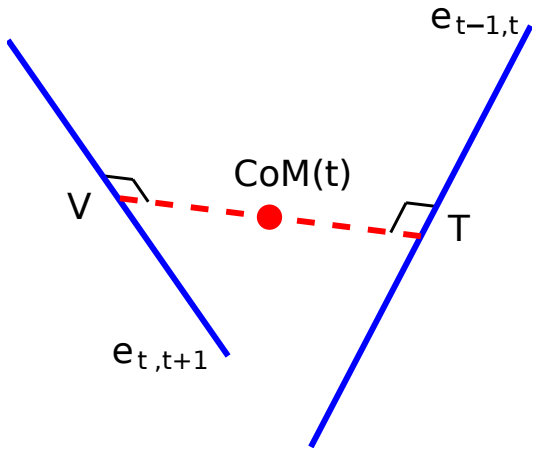

Figure 2.5 Pseudo-intersection of successive axes of rotation.

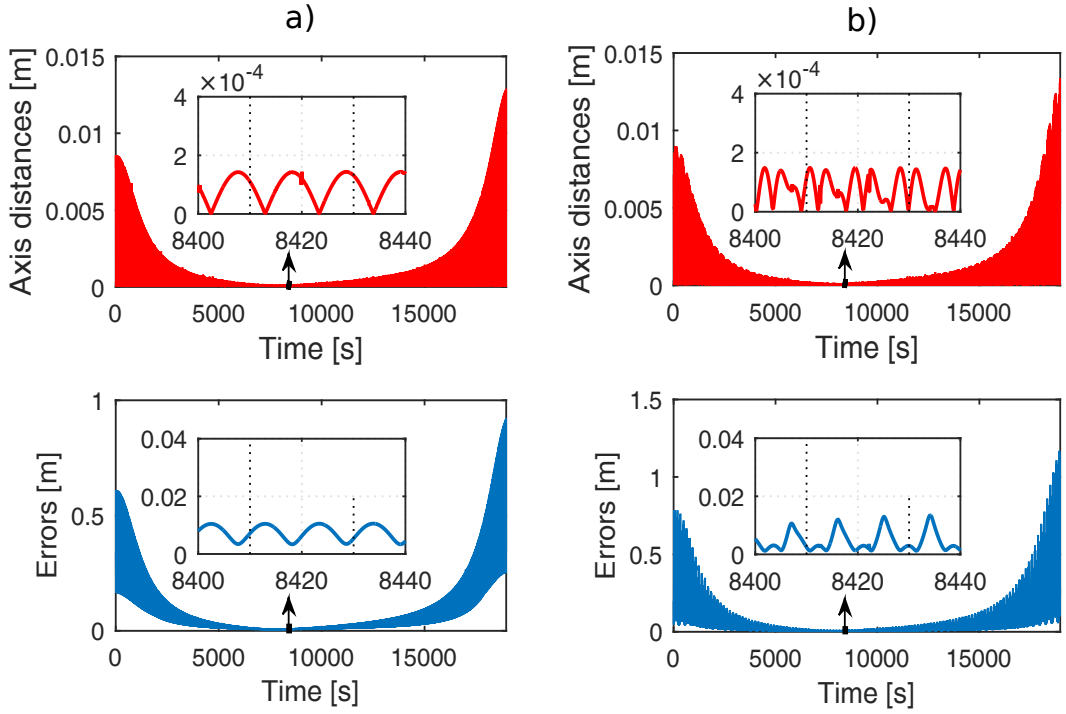

Figure 2.6 Axes distances d_e (upper charts) and estimation errors δ_g for two different attitude dynamics: a) axisymmetric ${}^B\boldsymbol{J}$; b) generic ${}^B\boldsymbol{J}$

so the distribution of the target mass was axisymmetric.

The results that comes out from the estimation via Eq. (2.11) and Eq. (2.12) (see Fig. 2.6) are illustrated by the quantities d_e and

$$\delta_g = ||{}^C\bar{\boldsymbol{\rho}} - {}^C\boldsymbol{\rho}||_2,$$

which rigorously is the distance between the localized CoM and the center of gravity of the target. Assuming negligible the difference between center of gravity and CoM, δ_g represents a localization error.

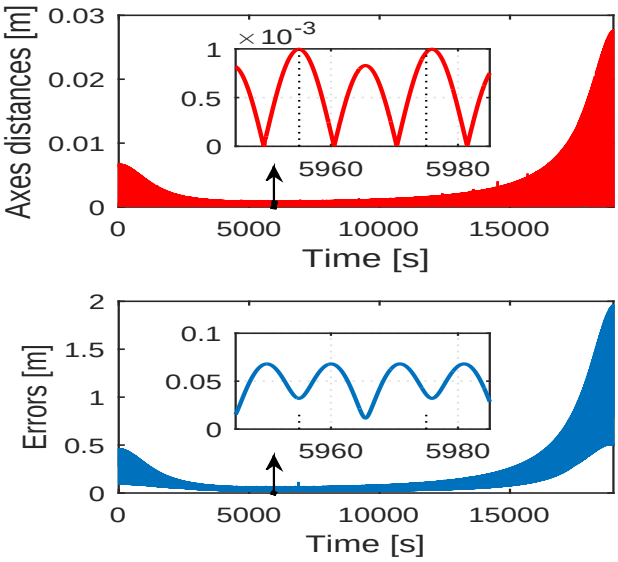

Figure 2.7 Axes distances d_e (upper charts) and estimation errors δ_g after changing initial relative conditions

Changing the relative initial conditions to:

$$
\begin{aligned}
{}^{\ell}\boldsymbol{\rho}_0 &= \begin{bmatrix} -2 & -85 & -1.5 \end{bmatrix}^T \text{m} \\
{}^{\ell}\dot{\boldsymbol{\rho}}_0 &= \begin{bmatrix} -0.045 & 0.01 & 0.025 \end{bmatrix}^T \text{m/s}
\end{aligned}
$$

leads to the results shown in Fig. 2.7. Only the axisymmetric model of the target is considered.

Before commenting these results, to have a global view of its performances, the method is tested also for a completely different kind of target orbit. In this case, a near-circular orbit with a smaller semi-major axis is considered. The Keplerian parameters for this orbit are shown in Tab. 2.1

The initial conditions for the simulation model in this new configuration are here resumed:

ephemeris	$e = 0.0011$
	$i_n = 48.45°$
	$\omega_p = 228.11°$
	$\Omega_{an} = 285.11°$
	$a = 6795\ km$
	$\vartheta_0 = 270°$

Table 2.1 Keplerian elements of a near-circular orbit

$$^{\ell}\boldsymbol{\rho}_0 = \begin{bmatrix} -9 & -64 & 6 \end{bmatrix}^T \text{m} \tag{2.13}$$

$$^{\ell}\dot{\boldsymbol{\rho}}_0 = \begin{bmatrix} -0.005 & 0.013 & -0.03 \end{bmatrix}^T \text{m/s} \tag{2.14}$$

$$^{B}\boldsymbol{\omega}_0 = \begin{bmatrix} 7.2 & 0.96 & -7.74 \end{bmatrix}^T \text{deg/s} \tag{2.15}$$

The inertia moments are the one of the axisymmetric case. The results relative to this last case are given another time under the form of charts. These charts are shown in Fig. 2.8

In all the studied cases the estimation error δ_g appears to be strongly correlated with the distances d_e. In particular, note that whenever d_e has a relative maximum, δ_g has a relative minimum (see Fig. 2.6, Fig. 2.7 and Fig. 2.8). This property holds whatever are the initial conditions of the simulation and the inertia tensor of the target. This result is because both the quantities d_e and δ_g are influenced by the relative motion between the two considered objects. For instance, for the axisymmetric target, both the quantities present a period between two relative maxima that is the half of the one of the angular rate vector, whose tip traces the polhode (see Appendix B.2).

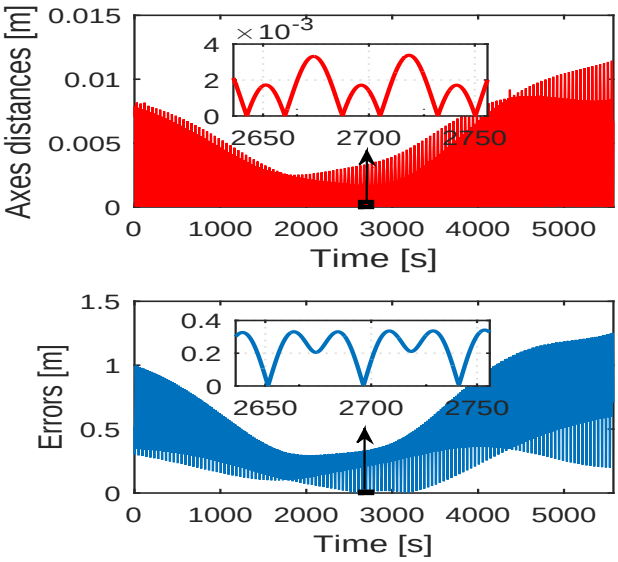

Figure 2.8 Axes distances d_e (upper chart) and estimation errors δ_g with a near-circular orbit

Looking at the instantaneous relative motion, the importance of the direction of the instantaneous screw axis arises immediately: the vertical component of the velocity to the rotation axis depends obviously on the axis direction. The time behavior of the magnitude of this component is shown in Fig. 2.9 for the two different target-chaser conditions relevant to Fig. 2.7 and Fig. 2.8.

The curves in Fig. 2.9 are very similarly shaped to the appropriate error curves. Indeed, the existence of velocity components that do not align with the rotation axis is the main source of error of the proposed estimator. In the studied cases two successive finite rotations of the target are parametrized with two non-coplanar axes whose distance is slight (see Fig. 2.7 and Fig. 2.8). However, the biggest problem is that they do not pass through the CoM of the body, as they were found using a 3D generalization of the Reuleaux rule. It is useful to remind that the module of the angular rate influences this kind of error. However, this magnitude is constant due to the conservation of the kinetic energy of the target, which is an unperturbed body in space.

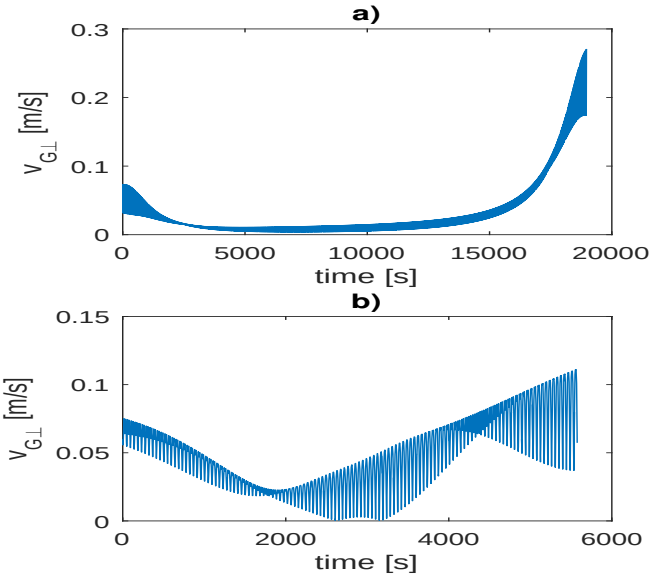

Figure 2.9 magnitude of the normal-to-axis component of the relative velocity between the centers of mass of the target and the chaser: case a) is relevant to Fig. 2.7; case b) is relevant to Fig. 2.8

It is evident that the curves in Fig. 2.9 are not available until the CoM of the target is localized, but on the other hand the time behavior of d_e, which comes from measured data, is also influenced by the shape of those curves.

Then, it approximately reveals the time behavior of δ_g. It is important to underline that the values of both d_e and δ_g depend marginally on the sample time of the dataset simulation. On the contrary, they strongly rely on the relative instantaneous motion between the chaser and the target. Notwithstanding, the sample time should be at least a tenth of the time interval between the relative maxima of d_e. Otherwise, the signals will be down-sampled, and no information may be extracted from them.

From these examples, it is possible to conclude that the proposed estimator is biased. However, the magnitude of the error does not diverge if the component of the relative velocity, which is normal to the rotation axis, remains bounded. Moreover, when the distance between two successive screw axes has a maximum, the corresponding estimation error has a minimum.

Note that in this subsection, the features of the target have been assumed to be always detectable. Thus, no algorithms removed information about hidden parts of the target surface. This choice was made for allowing a better characterization of the proposed estimator regarding the approximation level. Actually, the estimation is repeatedly performed using data about three successive time samples. So, the presence of missing data for a certain number of time samples does not prevent the estimation at other time samples for which data are available.

2.1.2 Estimation with missing data

When the application of the backface culling technique (see subsection 1.2.1) reduces the available data, there will be several instants in which the finite screw axis is not determinable. Considering the detectability of only five features, such as the ones in Eq. (1.17), the function d_e will show several missing samples. Indeed, there are many time samples in which three of the features are hidden. Remember that the locations of three couples of homologous features at two instants are necessary for applying the presented 3D generalization of the Reuleaux's rule.

Notwithstanding, making the numerical derivative (whenever possible) of d_e is useful to find its relative maxima. Moreover, the mean of the available values of d_e is obtainable in different short time intervals. This mean serves to determine the intervals in which it is the lowest one. These intervals are the ones in which the estimator's bias should be the lowest possible.

In Fig. 2.10 the results of a searching algorithm, which relies on the latest considerations, are displayed. The algorithm provides the time samples in which the proposed estimator of the CoM location produces the most accurate results. Figure 2.10 is referred to the considered eccentric orbit (Tab. 1.1).

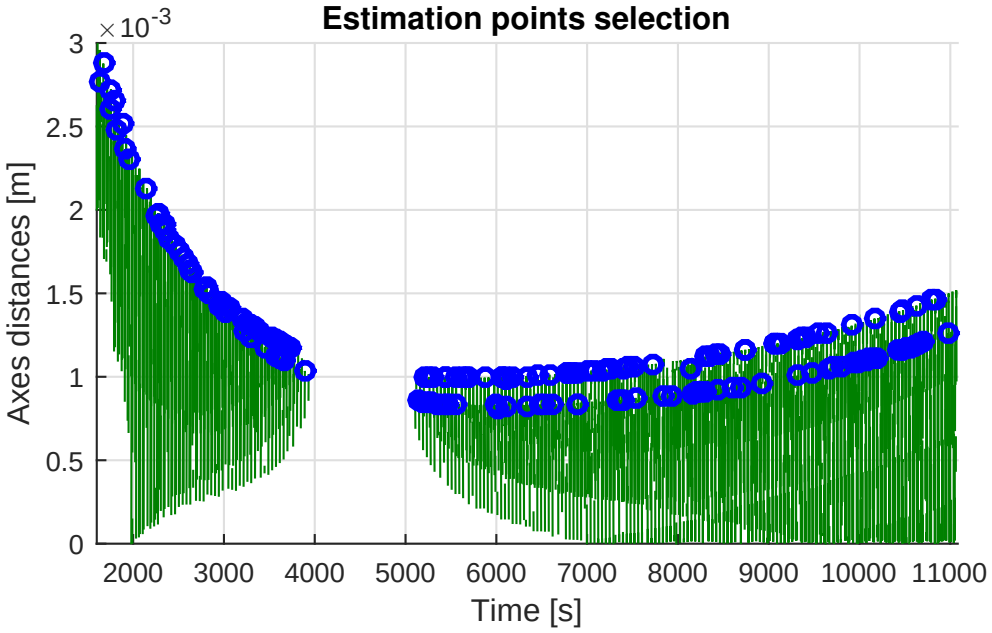

Figure 2.10 Result of the selection method, eccentric orbit (Tab. 1.1).The circles indicate the found relative maxima

A collection of several estimates of the position of the CoM in a body-fixed frame can be useful for analyzing the error distribution. Given the positions of three features (e.g. ${}^{C}\boldsymbol{\rho}_1$, ${}^{C}\boldsymbol{\rho}_2$, and ${}^{C}\boldsymbol{\rho}_4$), a body-fixed frame can be built through the following sample procedure:

- evaluate first axis through ${}^{C}\boldsymbol{\nu}_i = \frac{{}^{C}\boldsymbol{\rho}_2 - {}^{C}\boldsymbol{\rho}_1}{||{}^{C}\boldsymbol{\rho}_2 - {}^{C}\boldsymbol{\rho}_1||}$
- evaluate second axis through ${}^{C}\boldsymbol{\nu}_j = \frac{{}^{C}\boldsymbol{\nu}_i \times ({}^{C}\boldsymbol{\rho}_4 - {}^{C}\boldsymbol{\rho}_1)}{||{}^{C}\boldsymbol{\nu}_i \times ({}^{C}\boldsymbol{\rho}_4 - {}^{C}\boldsymbol{\rho}_1)||}$
- evaluate third axis through ${}^{C}\boldsymbol{\nu}_k = {}^{C}\boldsymbol{\nu}_i \times {}^{C}\boldsymbol{\nu}_j$

Once the estimates are expressed in the built body-fixed frame, they will be distributed around the true center of mass of the body. Then the expected value of the position of the center of mass can be obtained by meaning all the estimates. In Fig. 2.11 it is shown the application of this procedure to the eccentric orbit case.

In the case represented by Fig. 2.11, the true location of the CoM in the built body-fixed reference frame (namely $\mathcal{F}$) is:

$$^{\mathcal{F}}\boldsymbol{\rho}_g = \begin{bmatrix} 3.9862 & -0.3141 & 0.1090 \end{bmatrix}^T m \tag{2.16}$$

The expected value of the center of mass is instead:

$$E(^{\mathcal{F}}\boldsymbol{\rho}_g) = \begin{bmatrix} 3.9852 & -0.3209 & 0.1153 \end{bmatrix}^T m \tag{2.17}$$

So the difference is:

$$\Delta_{ecc} = \begin{bmatrix} -0.001 & -0.006 & 0.006 \end{bmatrix}^T m \tag{2.18}$$

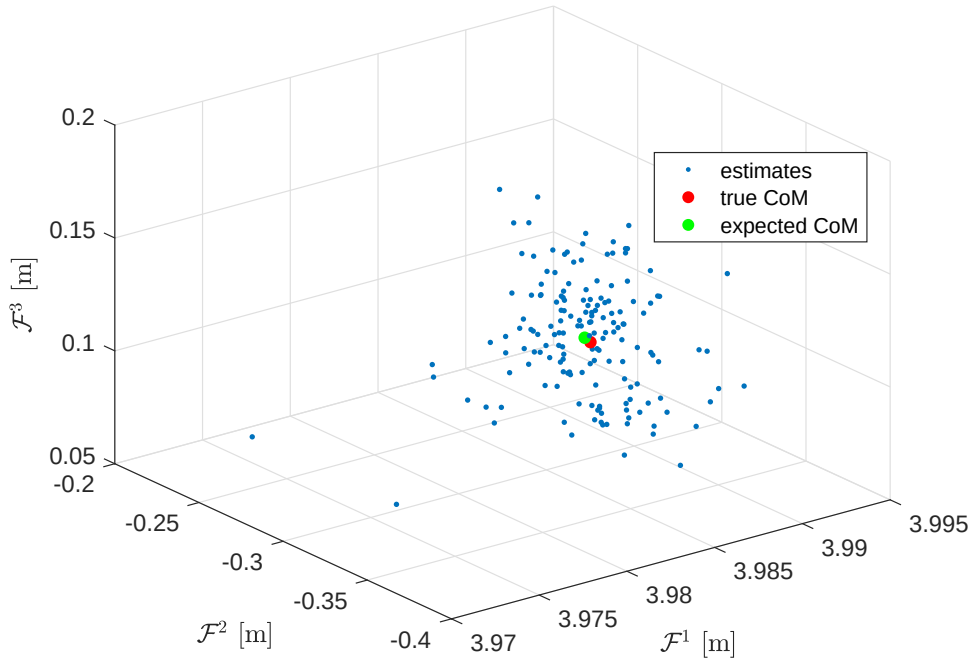

Figure 2.11 Global estimation of the center of mass location, eccentric orbit (Tab. 2.1).

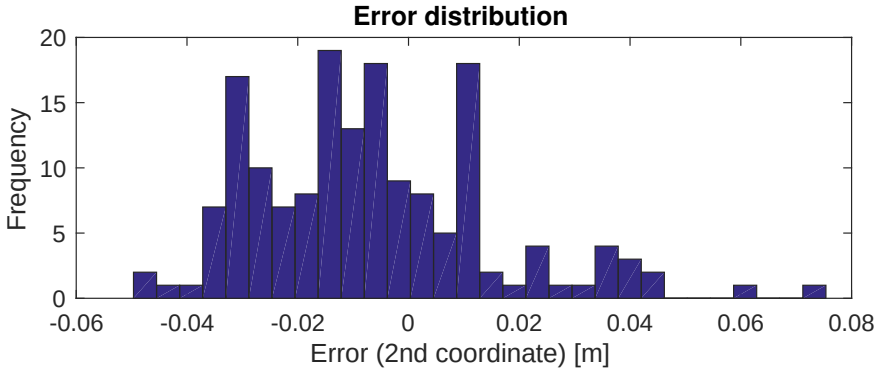

Figure 2.12 Distribution of the estimation error for the second coordinate of the CoM, eccentric orbit (Tab. 2.1).

Then, the error between the expected position of the target's center of mass and the true one is equal in magnitude to 9 *mm*. The distribution of the error for the second coordinate of the CoM is in Fig. 2.12; the distributions for the other coordinates have a quite similar shape, so they are omitted. The latter figure shows that residuals are almost centered. Moreover, their distribution is light tailed. However, it seems not rigorous to fit any canonical probability density function to the residuals.

The same methodology can also be applied to the near-circular orbit case (Tab. 2.1): Fig. 2.13 shows the results of the same searching algorithm used for the previous case. Fig. 2.14 illustrates the collected estimates expressed in the body-fixed frame $\mathcal{F}$. The true position of the CoM in this body-fixed frame is equal to the one shown in Eq. (2.16). The expected value of the CoM position is in this case:

$$E({}^{\mathcal{F}}\rho_g) = \begin{bmatrix} 3.9876 & -0.2888 & 0.1553 \end{bmatrix}^T m \tag{2.19}$$

Then, the difference is:

$$\Delta_{circ} = \begin{bmatrix} 0.001 & -0.025 & 0.046 \end{bmatrix}^T m \tag{2.20}$$

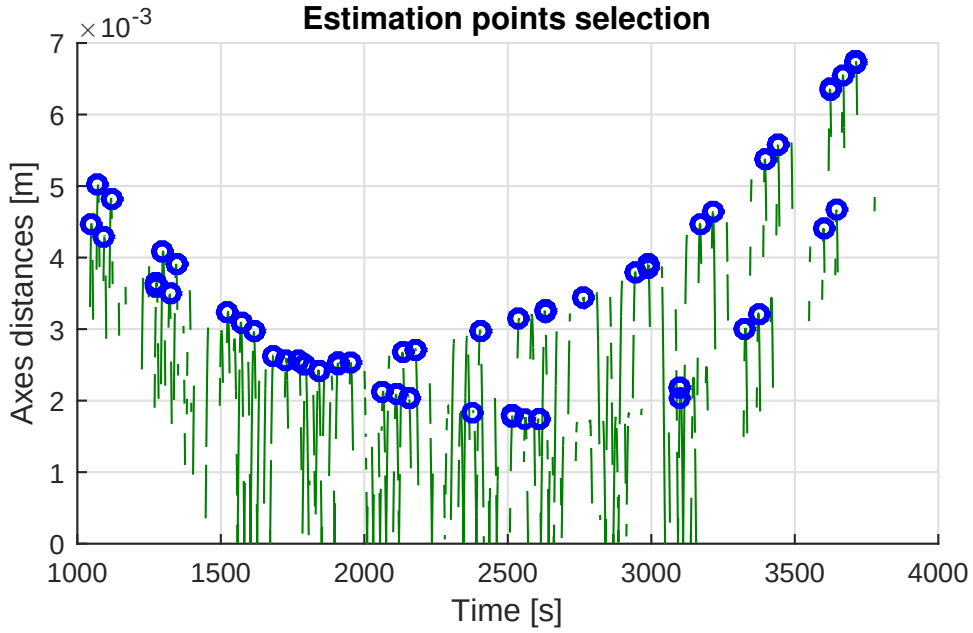

Figure 2.13 Result of the selection method, near-circular orbit (Tab. 2.1) .

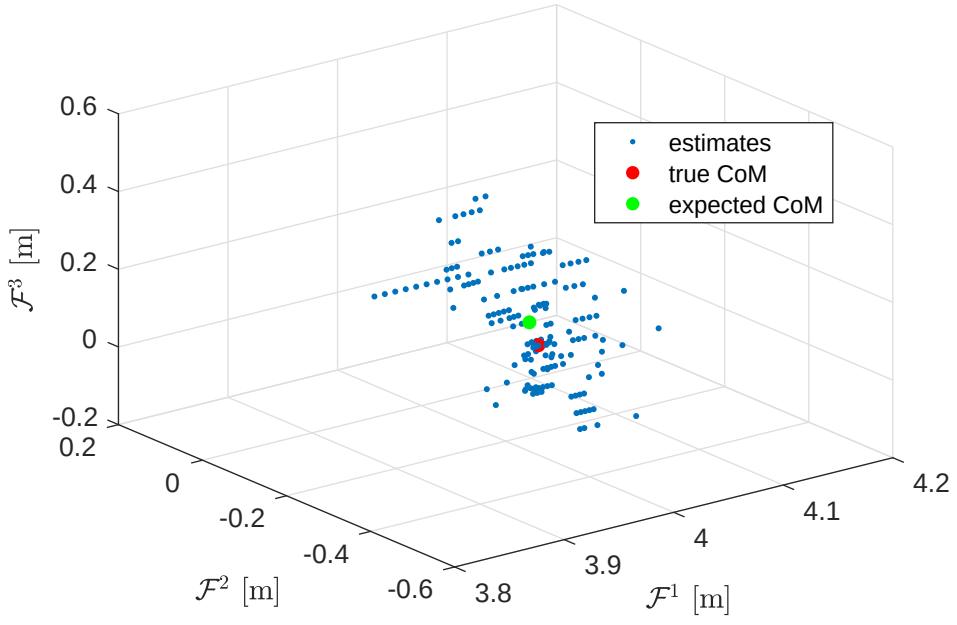

Figure 2.14 Global estimation of the center of mass location, eccentric orbit (table 2.1).

The error between the expected position of the target's CoM and the actual one is equal this time to 52*mm* in magnitude. The distribution of the error for the second coordinate of the CoM is in Fig. 2.15; the distributions for the other coordinates have quite similar shapes, so they are omitted. In comparison to the case of Fig. 2.12, here the residuals are more spread, although a significant part of them are concentrated around the mean. No elementary probability density function fits the residuals, neither coarsely.

From these two scenarios it is possible to conclude that although the distribution of the estimates around the true CoM is not strictly traceable to standard distributions, the mean of the estimates remains sufficiently near to the nominal position of the CoM. This result holds because, in general, the error made by the proposed estimator is bounded and directly correlated to the magnitude of the velocity of the target about the chaser. Thus, the more the relative dynamics between the two objects is slow, the less will be the difference between the mean of the estimates and the actual position of the CoM in a body fixed-frame.

If the orbits of the two objects are such that it exists an interval of time in which the distance between the objects variates slowly (e.g. few meters in five minutes), then the

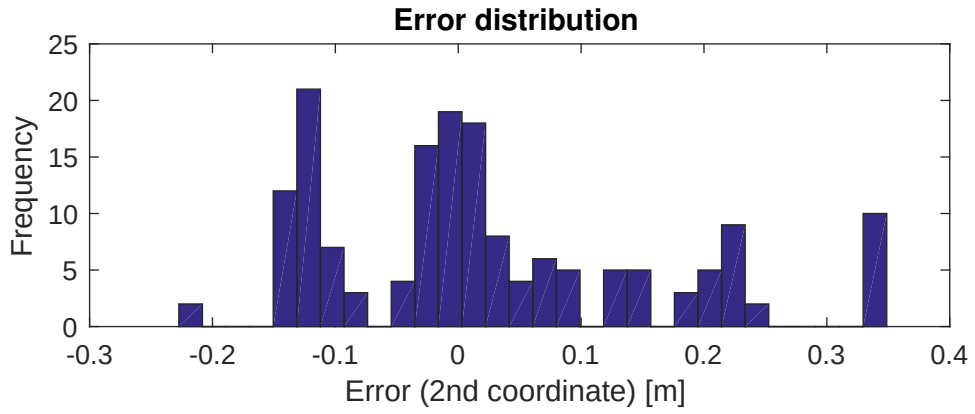

Figure 2.15 Distribution of the estimation error for the second coordinate of the CoM, eccentric orbit (table 2.1).

proposed estimator will show fair properties in that interval (see Fig. 2.9, Fig. 2.6, and Fig. 2.8).

The mentioned slow relative dynamics is a standard requirement for starting the capture maneuver (e.g. see [40]). Hence, this hypothesis is not particularly restrictive. The localization errors are sufficiently high to justify the assumed equivalence between the CoM and the center of gravity. So, in conclusion, the proposed estimator appears to be compliant for the application. Its robustness in case of corrupted data will be proved in the next sections of this chapter.

2.2 Regularizing noise by Procrustes analysis

The presence of large uncertainties on the actual location of the detected features from vision sensors prevent the direct application of the estimation technique that was illustrated in the previous section. However, a significant part of this uncertainty may be filtered out by exploiting some reasonable assumptions about the target body and its motion. Then, if a quite accurate representation of the movement of the body is obtainable through finite screw axes, it is possible to exploit the fine properties of the presented estimator to obtain many rough estimates that are reasonably distributed about the actual CoM. In fact, a single estimate could also be extremely far from the real value, but the fundamental aspect is that the mean of the error is almost zero.

The fundamental assumption to be considered regards the rigidity of the tracked target. The detected features must maintain through the time a constant relative distance. Screw axes are representations for the rigid displacement of a body between two different poses. The accuracy of this representation is greatly affected by the violation of the rigidity constraint. Moreover, neglecting the presence of moving appendages (that is

beyond the purpose of this work), the only significant reason for this violation consists of errors in detecting the actual location of the features.

Indeed, the first noticeable effect of the presence of noise on the coordinates of the features is that the tracked body does not appear rigid. The size of the target can also change due to thermal expansions or shrinkages, but these size variations have a too slow dynamics for being compared to the effect of the noise on the coordinates.

The mentioned noise acts as a source of distortion of the actual geometry of the considered target. The theory of *statistical shape analysis* specifically addresses the problem of distinguishing this distortion from the original contour of a body. In particular, the Generalized Procrustes Analysis (GPA) [41] is the considered technique in this work to address this problem.

According to the terminology of statistical shape analysis, a *shape* is defined as the set of all the geometric information that remains when location, scaling, and rotational effects are filtered out from an object. A finite number of features on the outline of the body can be a synthetic description of the defined *shape*.

Within a certain time interval, because of the motion of the body, these homologous features take different positions, setting the pose of the body. A *configuration* is here defined as the disposition in $\mathbb{R}_3$ of the homologous features at a given instant of the considered time interval. The main purpose of GPA is the alignment of different *configurations* to recover the original *shape* of the body.

GPA is an iterative procedure that starts by assuming that the first *configuration* in chronological order is the best representative of the original *shape*. Then, all the *configurations* need to be aligned with the first.

Mathematically, the Euclidean coordinates of the features of the i-th *configuration* are included in a *configuration matrix* X_i, which has 3 rows and n_c columns, n_c being the

number of homologous features. The relationship between X_i and the initial *configuration matrix*, i.e., X_0, is as follows:

$$X_i = R_i X_0 + T_i + \eta_{ci} \tag{2.21}$$

The optimization variables R_i and T_i represent the i-th rotation matrix and a translation matrix whose columns are equal to the i-th optimal translation vector $\boldsymbol{t}_i$, respectively. Matrix η_{ci} represents the unknown inaccuracy.

To align the *configurations* with respect to the location, the centroids are computed. Then, the optimal $\bar{\boldsymbol{t}}_i$ consists of the vector connecting the centroids. Position information is filtered out by subtracting the resulting optimal $\bar{T}_i$ to the configuration matrix X_i:

$$X_{Ci} = X_i - \bar{T}_i \tag{2.22}$$

Thus, the centered *configuration matrix* X_{Ci} and X_0, can be compared to find the optimal rotation matrix. That corresponds to solve the so-called *orthogonal Procrustes problem*: given the matrices X_{Ci} and X_0, it is needed to search for the orthogonal matrix $\bar{R}_i$ that most closely maps X_{Ci} to X_0:

$$\bar{R}_i = \arg\min_R \|RX_{Ci} - X_0\|_2 \qquad \text{subject to} \qquad RR^T = I_3 \tag{2.23}$$

Note that this problem is equivalent to find a matrix that is most closely orthogonal to the product $X_0 X_{Ci}^T$. The latter matrix can be factorized through the singular value decomposition (SVD):

$$X_0 X_{Ci}^T = \Sigma \nabla D^T \tag{2.24}$$

where ∇ is a diagonal matrix, while Σ and D are both orthogonal matrices. It is proved that the problem in Eq. (2.23) has a closed-form solution [42]:

$$\bar{R}_i = D\Sigma^T \tag{2.25}$$

The result in Eq. (2.24) has both a physical and a statistical meaning. From the physical point of view, the three terms of the SVD represent two pure rotations through the orthogonal matrices, plus a scaling of the set of features through the diagonal matrix. Thus, only the composition of rotations is taken to find the optimal rotation matrix $\bar{R}_i$. The scaling part is filtered out instead. From a statistical point of view the matrix $\bar{R}_i$, obtained through Eq. (2.25), is the one that maximizes the correlation between the two matrices X_{Ci} and X_0.

Following this logic of finding for each i-th *configuration* the optimal translation vector and the optimal rotation matrix from the 0-th *configuration*, it is possible to bring all the available j_c *configurations* to the initial time, making them comparable. This procedure is illustrated in Fig. 2.16. The number, j_c, of estimates, $\bar{X}_0^i$, can be obtained through

$$\bar{X}_0^i = \bar{R}_i^T \left(X_i - \bar{T}_i\right) \qquad \forall i = 1, 2 \ldots j_c \tag{2.26}$$

Then, the original *shape* of the body is estimated by averaging the transformed *configurations*. The *Procrustes mean* is obtained as follows:

$$\bar{X}_{PM} = \sum_{i=0}^{j_c} \frac{\bar{X}_0^i}{j_c} \tag{2.27}$$

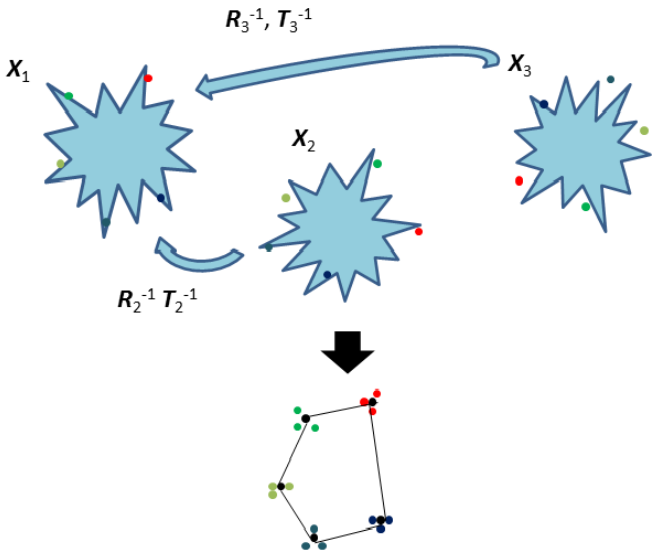

Figure 2.16 GPA procedure: all the *configurations* are linearly transformed for comparison. The mean *configuration* is assumed to be optimal.

All the described procedure can be iteratively repeated by aligning the j_c *configurations* to the current *Procrustes mean*. The procedure stops when the *Procrustes mean* does not change significantly. This requirement often occurs at the second iteration; thus, the procedure is not computationally expensive [43].

At the end of the GPA, applying the optimal inverse similarity transformations on the mean *configuration* generates a set of filtered data. After this procedure, the relative distances between features become equal at each sample time. Hence, the tracked body behaves as a rigid body.

It is worth mentioning that the problem in Eq. (2.21) leads to an overdetermined linear system that consists of 12 unknowns, which are subject to 6 nonlinear constraints. Several numerical techniques are available in the literature for this type of problems. The proposed solution scheme ensures numerical stability and excellent capability of dealing with nearly-singular conditions. Since the sampling frequency of vision-based sensors is

much higher (from 30 Hz up to 100 Hz) than natural frequencies of space debris attitude kinematics (quite less than 1 Hz), numerical stability is a fundamental aspect.

As it will be shown in the next section, on the other hand, since the dimension of *configurations* to obtain acceptable results is low (15 is appropriate), the reduced dimensionality of the problem makes any possible gain negligible in terms of computational efficiency.

Considering the two kinds of datasets that were discussed in subsection 1.2.1, while there is a high confidence about the quality of GPA results on the dataset based on the features of Fig. 1.6, the GPA is not fairly applicable on the other dataset, which contains the trajectories of the five features in Eq. 1.17. In fact, after the application of the backface culling technique for the elimination of undetectable parts of trajectories, for too many time samples there are only three tracked features, or even less.

Hence, for the estimation of the CoM location from corrupted data, only the dataset with 44 unlabeled features is exploited (see Fig. 1.6). This aspect cannot be considered a problem for the method. Indeed, it is easier to track a huge number of features than recognizing on-board few particular points of the target surface on a CAD drawing of it. Moreover, this last recognition procedure requires obviously the possession of such CAD model of the object. As discussed in subsection 1.2.1 this assumption could be restrictive for certain removal scenarios.

Clearly, the considered 44 features are not all detectable at a particular instant of time. Moreover, once they disappear from the FOV of sensors they are definitively lost in the sense that they reappear after some time as new features. Fig. 2.17 provides an illustration of that concept.

Since *configurations* consists of a fixed set of features with different poses, the simulation time was split into several intervals such that, for each of them, a reasonably large set of homologous features is tracked without interruptions. In particular, the

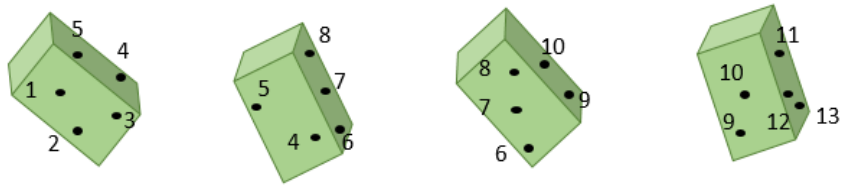

Figure 2.17 Appearing and disappearing features from the FOV of the vision-based sensors. Note that features 1, 2 and 3 are exactly the same of 11, 12 and 13, but no algorithm is exploited to recognize this fact.

minimum dimension obtained for the *configurations* was equal to 9, while the maximum one was equal to 21. As mentioned in subsection 1.2.1 with Fig. 1.11, some of the considered intervals are useful to simulate occlusions or rather temporary losses of measured data. When occlusions occur, the GPA is not applicable. It will be shown in the next section as this problem does not compromise the final estimation of the entire trajectory of the CoM.

2.3 Estimation in realistic conditions

The GPA were first applied to the dataset obtained with the following initial conditions for the relative orbital dynamics:

- Keplerian parameters of the target in Tab.1.1, here resumed:

ephemeris	$e = 0.55$
	$i_n = 6.93°$
	$\omega_p = 146.4°$
	$\Omega_{an} = 132.2°$
	$a = 15371\ km$
	$\vartheta_0 = 349.9°$

- initial relative position and velocity:

$$^{\ell}\boldsymbol{\rho}_0 = \begin{bmatrix} -0.22 & -92.86 & 0 \end{bmatrix}^T \text{m}$$

$$^{\ell}\dot{\boldsymbol{\rho}}_0 = \begin{bmatrix} -0.044 & 0.004 & 0 \end{bmatrix}^T \text{m/s}$$

- the principal inertia moment $^{B}\boldsymbol{J} = \begin{bmatrix} 0.7014 & 0.5762 & 0.4196 \end{bmatrix}$
- the initial absolute angular rate $^{B}\boldsymbol{\omega}_0 = \begin{bmatrix} 10.2 & 0.72 & -17.1 \end{bmatrix}$ deg/s

Then, after the imposition of the rigidity condition to the features, the 3D extension of the Reuleaux's rule is applied to the filtered dataset. According to the average accuracy of existing stereo-vision systems (see subsection 1.2.2 for details) a 10 mm noise amplitude was considered for being added to the coordinate of the features. Moreover, the artificial occlusion intervals had a duration of 120 s.

The successive screw axes representing the target pose evolution are described by a 6-th dimensional signal in time domain. The first three dimensions are the direction cosines of the screw axes, while the last three ones are the coordinates of one point of those axes. This signal is illustrated in Fig. 2.18.

Note from Fig. 2.18 that the signal above is still corrupted by an high-frequency noise that is not coherent with the underlying motion of the target. However, the application of the GPA allowed the noise to have a small amplitude. The estimation of the CoM location should follow through the pseudo-intersection of Fig. 2.5, whose properties were illustrated in section 2.1. However, the pseudo-intersection procedure involves an amplification of the noise amplitude. The amplification holds because the resulting position of the CoM is the product of the combination of information regarding successive time samples. Therefore, the pseudo-intersection behaves as a noise amplifier like the numerical derivative.

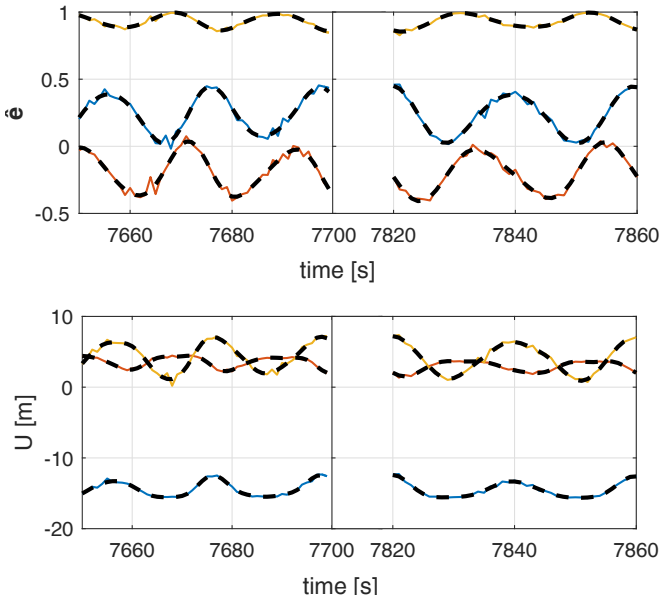

Figure 2.18 Raw (solid line) and filtered (dashed line) screw axis and pole of rotation. An occlusion period interrupts data.

For those reasons, a preliminary filtering of the signal in Fig. 2.18 is necessary to obtain meaningful estimates of the CoM location. For recovering the original information, we applied a low-pass filter to all parts of the signal. The recommended cutoff frequency is 1 Hz, which is reasonably high for preserving information related to the typical slow motion of a tumbling target. To avoid signal distortion, we considered zero-phase filtering using a high order Butterworth filter. The filter transfer function has the following form:

$$|H(j\omega)|^2 = \frac{G_0^2}{1+\left(\frac{\omega}{\omega_c}\right)^{2n_f}} \tag{2.28}$$

where G_0 is the gain at zero frequency, ω_c is the cut-off frequency, and n_f is the filter order (we set it to 22). The unique limitation on the choice of n_f is given by the minimum number of samples within the periods in which occlusions do not occur. In particular,

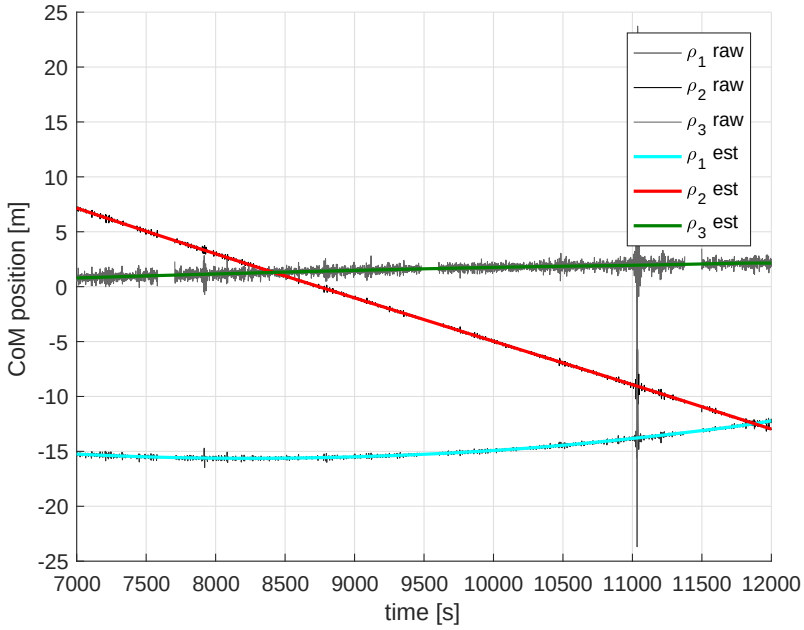

Figure 2.19 Representation of the three estimated coordinates of the center of mass (CoM) in the chaser-fixed reference frame C. The standard deviation of the measurement noise is equal for each coordinate to 10 mm.

this number must be more than three times the filter order. The filtered signal is also shown in Fig. 2.18 together with the relevant raw signal.

After these operations, the pseudo-intersection of the screw axes leads to the estimated coordinates of the CoM. The procedure output is shown in Fig. 2.19. Clearly, the presence of occlusion periods leads to missing samples in the estimated trajectory of the CoM. Moreover, as expected, the estimation errors are significantly high due to the noise amplification produced by the proposed estimator.

However, Fig. 2.19 shows that although the noise has a high power, its mean appear shaped like the actual trajectory of the CoM. This result is something expected due to the properties of the proposed estimator, discussed in section 2.1. Thus, the original trajectory can be restored even by simply fitting the data through appropriate polynomials.

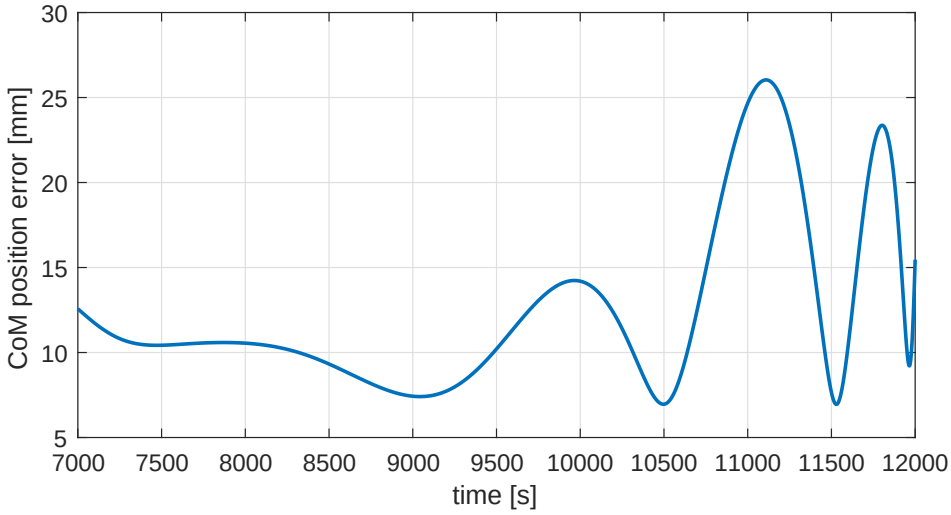

Figure 2.20 Final estimation error in the CoM trajectory. The standard deviation of the measurement noise is equal for each coordinate to 10 mm.

In fact, the last estimated trajectory of the CoM, from the chaser point of view, is recovered by fitting the coordinates with a tenth order polynomial. In Fig. 2.19, the resulting curves are overlaid on the corrupted components of the trajectory of the CoM. In particular, these curves also cover the missing information regarding the artificially introduced occlusion intervals.

Finally, the norm of the absolute estimation error for the considered example is shown in Fig. 2.20. The mean error is approximately under 30 mm, which is a relatively low value. Indeed, the accuracy level reached with the proposed method is comparable to that of the best-known methods (e.g., in [19] 40 mm RMSE was obtained). However, differently from state-of-the-art methods, the proposed method is robust to occlusions and does not require the continuous detection of a particular fixed set of features. This result holds because the proposed method does not rely on state-observers as mentioned at the beginning of this chapter.

The GPA were secondly applied to the dataset obtained with the following initial conditions for the relative orbital dynamics:

- Keplerian parameters of the target in Tab.2.1, here resumed:

ephemeris	$e = 0.0011$
	$i_n = 48.4°$
	$\omega_p = 228.1°$
	$\Omega_{an} = 285.1°$
	$a = 6795\ km$
	$\vartheta_0 = 270°$

- initial relative position and velocity:

$$^{\ell}\boldsymbol{\rho}_0 = \begin{bmatrix} -9.00 & -63.99 & 5.99 \end{bmatrix}^T \text{m}$$

$$^{\ell}\dot{\boldsymbol{\rho}}_0 = \begin{bmatrix} -0.003 & 0.011 & -0.030 \end{bmatrix}^T \text{m/s}$$

- the principal inertia moment $^{B}\boldsymbol{J} = \begin{bmatrix} 0.5978 & 0.7399 & 0.3085 \end{bmatrix}$
- the initial absolute angular rate $^{B}\boldsymbol{\omega}_0 = \begin{bmatrix} 0.14 & 0.14 & -0.09 \end{bmatrix}$ deg/s

Then, as in the first case, we applied the 3D extension of the Reuleaux's rule to the filtered dataset, considering also noise and artificial occlusions. The pseudo-intersection of the screw axes leads to the estimated coordinates of the CoM. The procedure output is shown in Fig. 2.21.

The original trajectory can be restored by simply fitting the data through appropriate polynomials, see Fig. 2.21.

In Fig. 2.21, the fitted coordinates are overlaid on the corrupted components of the trajectory of the CoM.

Finally, the norm of the absolute estimation error for the considered example is shown in Fig. 2.22. The mean error is approximately under 20 mm. Again, the accuracy level reached with the proposed method is comparable to that of the best-known methods.

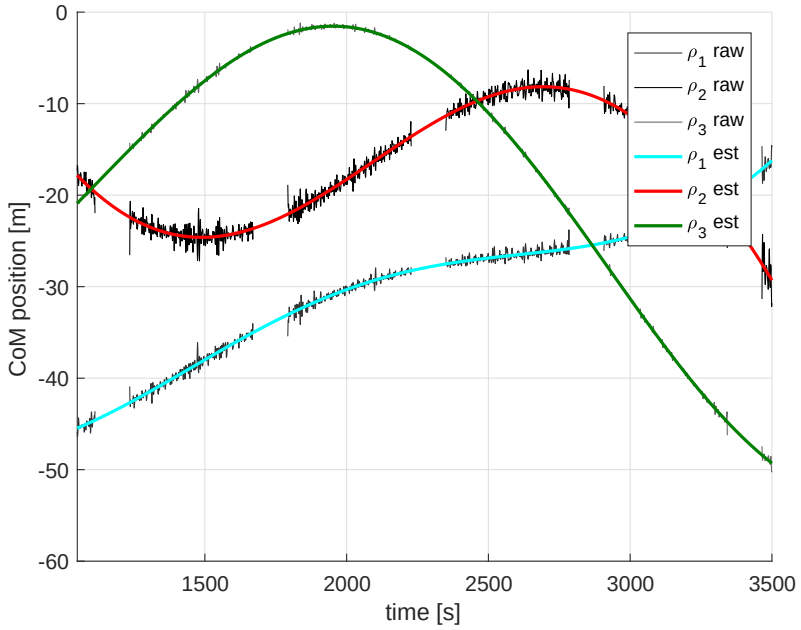

Figure 2.21 Representation of the three estimated coordinates of the center of mass (CoM) in the chaser-fixed reference frame C. The standard deviation of the measurement noise is equal for each coordinate to 10 mm.

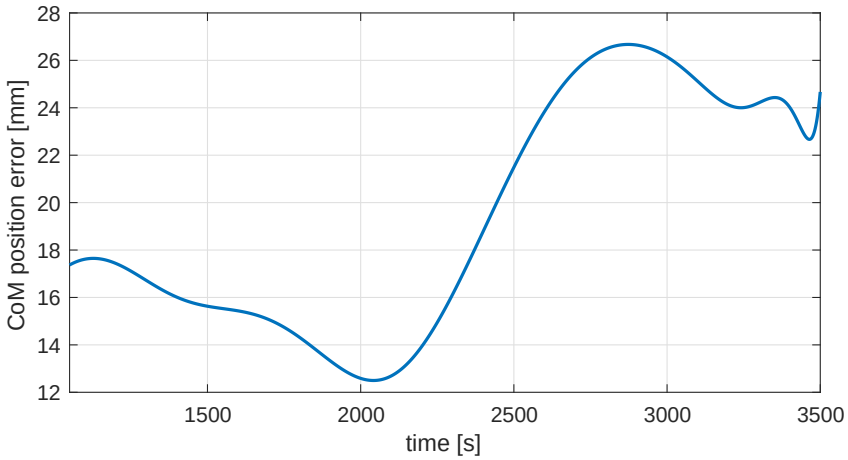

Figure 2.22 Final estimation error in the CoM trajectory. The standard deviation of the measurement noise is equal for each coordinate to 10 mm.

In a third example, the GPA were applied to the dataset obtained with the following initial conditions for the relative orbital dynamics:

- Keplerian parameters of the target here resumed:

ephemeris	$e = 0.34$ $i_n = 89.4°$ $\omega_p = 45.8°$ $\Omega_{an} = 12.7°$ $a = 10359\ km$ $\vartheta_0 = 11.7°$

- initial relative position and velocity:

$$^{\ell}\boldsymbol{\rho}_0 = \begin{bmatrix} -5.72 & -68.37 & 0 \end{bmatrix}^T \text{m}$$

$$^{\ell}\dot{\boldsymbol{\rho}}_0 = \begin{bmatrix} -0.022 & 0.009 & 0 \end{bmatrix}^T \text{m/s}$$

- the principal inertia moment $^{B}\boldsymbol{J} = \begin{bmatrix} 0.5978 & 0.7399 & 0.3085 \end{bmatrix}$
- the initial absolute angular rate $^{B}\boldsymbol{\omega}_0 = \begin{bmatrix} 0.14 & 0.14 & -0.09 \end{bmatrix}$ deg/s

As usual, the 3D extension of the Reuleaux's rule is applied to the filtered dataset. The estimated coordinates of the CoM are shown in Fig. 2.23.

Again, the original trajectory are restored fitting the data through appropriate polynomials, see Fig. 2.23.

In Fig. 2.23, the fitted coordinates are overlaid on the corrupted components of the trajectory of the CoM.

Finally, the norm of the absolute estimation error for the considered example is shown in fig. 2.24. The mean error is approximately 30 mm.

The GPA were finally applied to the dataset obtained with the following initial conditions for the relative orbital dynamics:

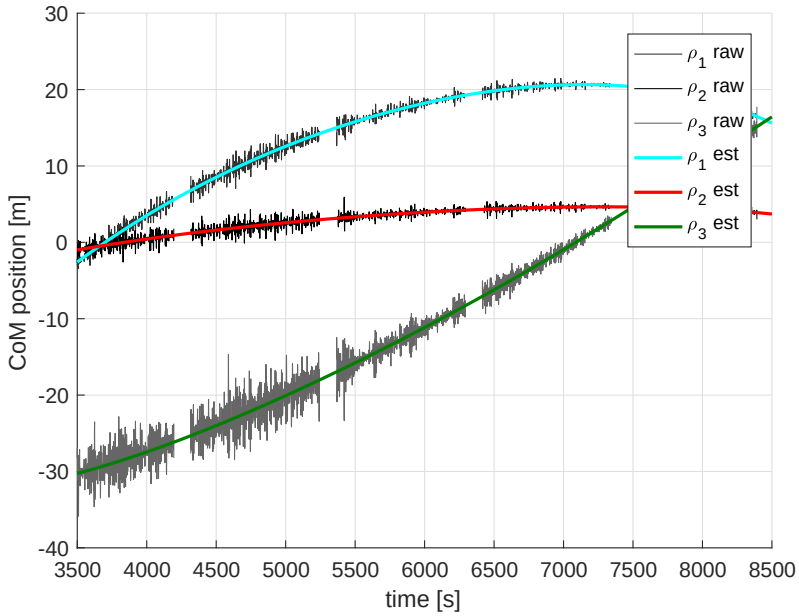

Figure 2.23 Representation of the three estimated coordinates of the center of mass (CoM) in the chaser-fixed reference frame C. The standard deviation of the measurement noise is equal for each coordinate to 10 mm.

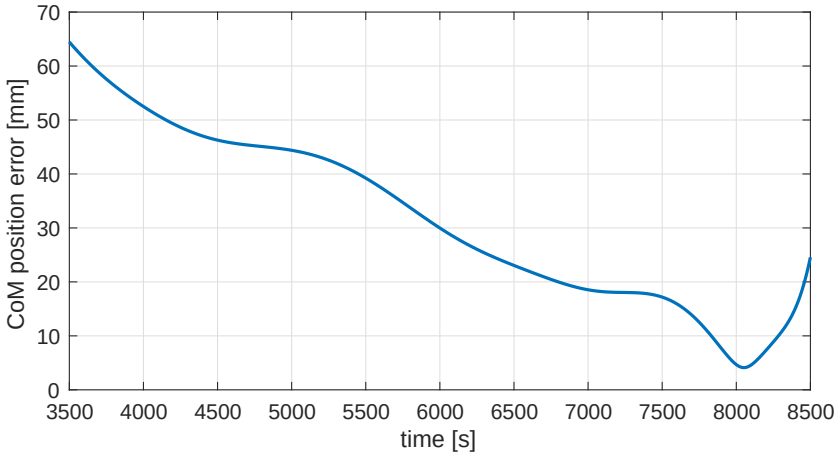

Figure 2.24 Final estimation error in the CoM trajectory. The standard deviation of the measurement noise is equal for each coordinate to 10 mm.

- Keplerian parameters of the target here resumed:

ephemeris	$e = 0.17$
	$i_n = 234.8°$
	$\omega_p = 94.2°$
	$\Omega_{an} = 66°$
	$a = 8559\ km$
	$\vartheta_0 = 102.10°$

- initial relative position and velocity:

$$^{\ell}\boldsymbol{\rho}_0 = \begin{bmatrix} -4.63 & -24.07 & 0 \end{bmatrix}^T \text{m}$$

$$^{\ell}\dot{\boldsymbol{\rho}}_0 = \begin{bmatrix} 0.0007 & 0.0038 & 0 \end{bmatrix}^T \text{m/s}$$

- the principal inertia moment $^{B}\boldsymbol{J} = \begin{bmatrix} 0.4915 & 0.4915 & 0.7189 \end{bmatrix}$
- the initial absolute angular rate $^{B}\boldsymbol{\omega}_0 = \begin{bmatrix} -0.18 & -0.16 & 0.19 \end{bmatrix}$ deg/s

The coordinates of the CoM obtained by the pseudo-intersection of the screw axes are shown in Fig. 2.25.

The original trajectory is then restored fitting the data through appropriate polynomials.

In Fig. 2.25, the fitted coordinates are overlaid on the corrupted components of the trajectory of the CoM.

The norm of the absolute estimation error for the considered example is shown in Fig. 2.26. The mean error is approximately under 60 mm.

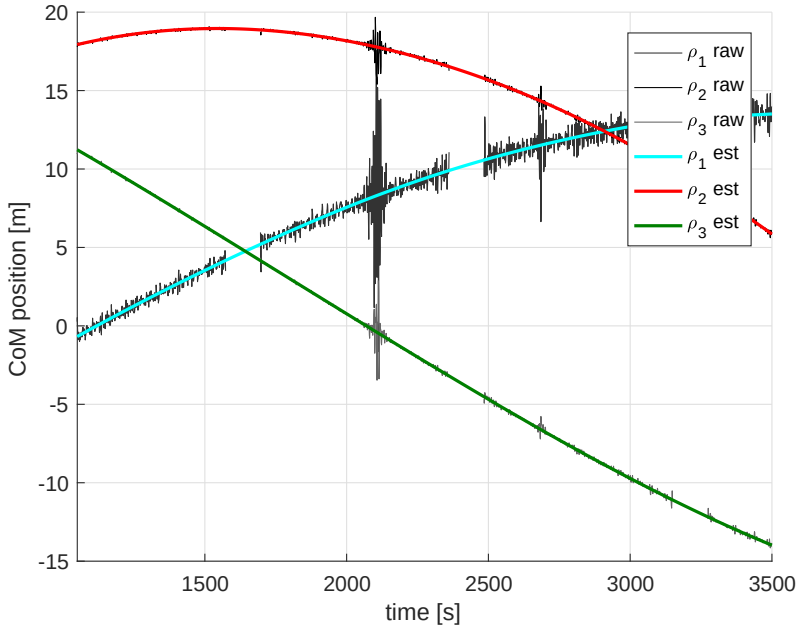

Figure 2.25 Representation of the three estimated coordinates of the center of mass (CoM) in the chaser-fixed reference frame C. The standard deviation of the measurement noise is equal for each coordinate to 10 mm.

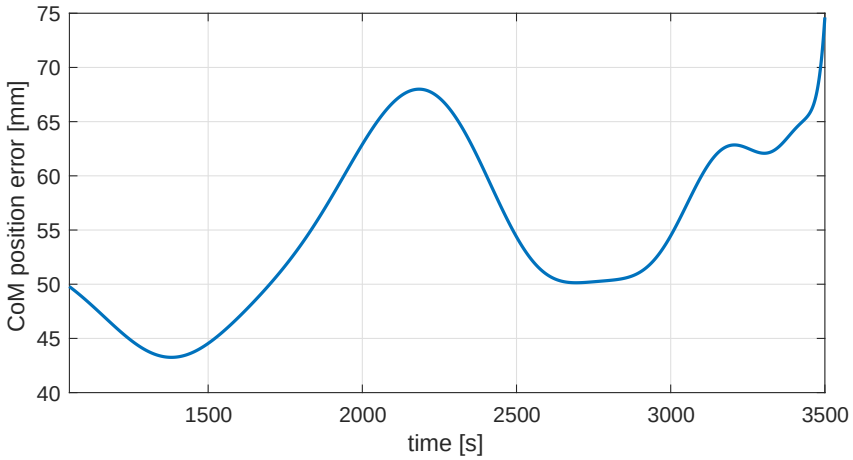

Figure 2.26 Final estimation error in the CoM trajectory. The standard deviation of the measurement noise is equal for each coordinate to 10 mm.

Chapter 3

Estimation of attitude, angular rate and inertia ratios

The accurate knowledge of the attitude dynamics of the target is of critical importance to the success of the capture maneuver, especially if the capture system rely on tentacles or robotic arms. To approach the target without having abrupt impacts, both the capture system and the chaser spacecraft have to cooperate during the approach phase to reduce the relative angular rate between the parts that should become in contact.

Thus, the estimation of the actual angular rate of the passive object is fundamental. A typical estimation approach consists of achieving information on the pose of the object in different time samples to derive the actual dynamics of the target from a state-space model of it.

The main difficulties are related to the intrinsic complexity in representing the attitude, and to the non-linearity of the dynamic equations. However, the possibility of assuming the principal moments of inertia of the target as constants gives an important help in solving the task. Moreover, the estimation of the dynamic rotational state of the target

is further hampered by the fact that the sensors for achieving the pose of the object are subject to momentary failures.

If there are interruptions in the acquisition of the pose information, the common state observers used for the estimation start to learn a wrong time behavior of the state without having the possibility of correcting it through the measurements. Then, when the measures become available again, the state observer need to employ several samples to re-learn the actual state, hoping that new data interruptions will not occur.

This chapter presents the basic theory of stochastic state observers and the determined ways to support their employment in case of sudden losses of measured data. Different applications of the developed methods are presented as a function of the typology of acquired data: few tracked features and prior information on the target shape, and a greater number of features without that a-priori information.

3.1 Theory of observers for stochastic systems

The observation of any dynamic system has necessarily to start from the measurement of some physical quantities that are influenced by the dynamics that should be observed. In the language of the systems theory, these measurable quantities are often denoted as the *outputs* of the system, typically contained in a column vector y. Clearly, one or more sensors are necessary to have an estimate of these quantities. In particular, all the measurements are collected in a column vector z such that the following *measurement equations* hold for any instant k:

$$z_k = y_k + v_k \tag{3.1}$$

The *measurement noise* v_k is the uncertainty due to the imperfection of the sensors used for measuring y_k. The sensors behave as a simple estimator of the outputs of the system; the error made by this estimator is evidently equal to v_k, which is a random variable whose distribution is completely dependent by the characteristic of the sensors. Based on the particular application, the accuracy of this estimator is sometimes not sufficient so, to obtain better estimates, it arise the necessity of defining mathematical procedures that are based on some prior knowledge about the dynamics of the system.

Moreover, the directly measurable quantities are not usually sufficient for a complete description of the system behavior. The quantities that completely represent the dynamics of the system are collected into a column vector x that is called *state vector*. In the most general case the outputs are linked to the state variable by a function h, so that the measurement equations become:

$$z_k = h(x_k) + v_k \tag{3.2}$$

An appropriate way of mathematically representing the actual dynamics of the system is the statement of the *state equations*, which can be a system of finite difference equations. For instance, it holds:

$$x_{k+1} = f(x_k) + w_k \tag{3.3}$$

where w_k is the so-called *process noise*. The introduction of the random variable w_k represent the fact that, evidently, the actual dynamics of the system is not perfectly known. Moreover, the process noise takes into account also of the inherent inaccuracy of a discrete representation of a typical continuous-time process.

Since they contribute to the knowledge of information about the system behavior, state equations are very useful to identify an estimator of the state vector. Both the measurement equations and the state equations are not deterministic due to the presence of the random variable v_k and w_k. Thus, the uncertainties in the system description should be described by the probability theory. The time behavior of the measurement reflects its joint probability function; assuming there is no correlation between the values of v_k at two different instants, it holds:

$$p(v^N) = p(v_0, v_1, ..., v_n) = p(v_0)p(v_1)...p(v_N) \tag{3.4}$$

The same applies for the process noise, which is also assumed to be a white noise.

By sampling from the assumed joint probability distribution of the process noise, Eq. (3.3) gives the opportunity of estimating the state vector from the mathematical model of the considered system. However, at the same time the acquired measurements produce more information about the state of the system through Eq. (3.2), in which also the measurement noise have to be sampled from its joint probability distribution.

Formally, the combination of this information in terms of probability density function is expressed by the Bayes formula for conditional probability:

$$p\left(x_k \mid z^k\right) = \frac{p\left(z_k \mid x_k\right) p\left(x_k \mid z^{k-1}\right)}{p\left(z_k \mid z^{k-1}\right)} \tag{3.5}$$

where $p\left(x_k \mid z^k\right)$ is the conditional probability of x_k given the entire history of the measurements of the system output, which is represented by the joint probability function $p(z^k)$. $p\left(z_k \mid x_k\right)$ is the conditional probability of the current measurement z_k given the actual outcome of the state x_k. Evidently, this last probability density function is directly influenced by the distribution of the measurement noise $p(v_k)$ through Eq. (3.2).

$p\left(x_k \mid z^{k-1}\right)$ represents the predicted probability density function of x_k given all the past measurements but not the current one. Thus, this can be obtained using only Eq. (3.3) and the probability distribution of the process noise $p(w_{k-1})$. In particular, it holds:

$$p\left(x_k \mid z^{k-1}\right) = \int p\left(x_k \mid x_{k-1}\right) p\left(x_{k-1} \mid z^{k-1}\right) dx_{k-1} \tag{3.6}$$

where $p\left(x_k \mid x_{k-1}\right)$ is the transition probability density function.

Finally, the normalizing constant $p\left(z_k \mid z^{k-1}\right)$ can be obtained from the following convolution:

$$p\left(z_k \mid z^{k-1}\right) = \int p\left(z_k \mid x_k\right) p\left(x_k \mid z^{k-1}\right) dx_k \tag{3.7}$$

Equations (3.5) and (3.6) defines the general formulation for a *Bayesian filter*. Note that the latter is not properly a filter because it does not perform any signal processing or transformation. Instead, it performs the estimation of the time behavior of the probability distribution of the state variables. Thus, it is an observer of the state treated as a random variable.

The estimation is mainly composed of two operations. The first is the prediction, represented by Eq. 3.6, in which the assumed state-space model of the system reveals a-priori information about the probability distribution of the future state, before the acquisition of any measure of the system outputs. Then, once the distribution of the relative measurements is available, the a-priori estimated distribution of the state is updated via Eq. 3.5. That justify the use of the word filter.

From assumptions and algorithms, simpler observers then the general Bayesian filter can be obtained. For instance, one common assumption is that the process represented by Eq. (3.3) is a Markov chain. A process is Markov [44] if it holds:

$$p\left(x_k \mid x^{k-1}\right) = p\left(x_k \mid x_{k-1}\right) \tag{3.8}$$

Equation (3.8) states that the probability density function of the state at k is influenced only by the state at the precedent instant $k-1$. Monte Carlo sampling the function $p\left(x_{k-1} \mid z^{k-1}\right)$, it is possible to propagate the outcomes through the assumed generic nonlinear model of the system to estimate $p\left(x_k \mid z^{k-1}\right)$. A genetic treatment of the predicted outcomes, that are called *particles*, lead to the updating phase of the *particle filter* [45].

Assuming the linearity and Gaussianity of both process and measurements, it is possible to derive the formula for one of the most appreciated observers: the *Kalman filter*. The latter will be used in this work together with its adaptations for treating nonlinear systems. The reason for its usage in many applications consists of its simplicity, effectiveness and robustness.

3.1.1 Kalman filter

The assumption of the linearity of the system leads to the following state-space representation:

$$x_{k+1} = F_k x_k + w_k \tag{3.9}$$

$$z_k = H_k x_k + v_k \tag{3.10}$$

where F_k is a square matrix with dimension n_x, and H_k is a $n_z \times n_x$ dimensional matrix.

Moreover, the following assumptions hold:

$$E\left[w_k w_l^T\right] = E\left[w_k\right] E\left[w_l^T\right] \tag{3.11}$$

$$E\left[v_k v_l^T\right] = E\left[v_k\right] E\left[v_l^T\right] \tag{3.12}$$

Thus, the noises at instant k are both white noises. Moreover it holds:

$$E\left[w_k w_l^T\right] = 0 \qquad l \neq k \tag{3.13}$$

$$E\left[v_k v_l^T\right] = 0 \qquad l \neq k \tag{3.14}$$

Hence, both the process and the measurement noise at instant k have not correlation with themselves at other instants. Then they are Gaussian noises with zero mean. If $k = l$, their covariance matrices will be indicated as Q_k and R_k respectively. Besides, the process and the measurement noise are not mutually dependent:

$$E\left[w_k v_l^T\right] = 0 \tag{3.15}$$

Finally, it is assumed that the state equations represent a Markov chain and that the state at instant k is a Gaussian random variable with mean $\bar{x}_k$ and covariance P_k.

The updating phase of the Kalman filter have to be derived from the Bayes formula in Eq. (3.5). The calculation requires the knowledge of the a-priori probability density function of the state given the past measurements:

$$p\left(x_k \mid z^{k-1}\right) = \mathcal{N}\left(x_k : \bar{x}_k^-, P_k^-\right) \tag{3.16}$$

Equation (3.16) states that the a-priori distribution of the random variable x_k is a Gaussian characterized by a mean $\bar{x}_k^-$ and a covariance P_k^-. Thus, the superscript "$-$" indicate an estimation that is only based on the assumed model of the actual system. The notation $\mathcal{N}$ introduces a multivariate Gaussian with a certain mean and covariance.

It is straightforward to verify that the measurement probability density function can be characterized through Eq. (3.10) as follows:

$$p\left(z_k \mid x_k\right) = \mathcal{N}\left(z_k : H_k x_k, R_k\right) \tag{3.17}$$

Finally, from Eq. (3.16) and from Eq. (3.17) the normalization constant has to be:

$$p\left(z_k \mid z^{k-1}\right) = \mathcal{N}\left(z_k : H_k \bar{x}_k^-, H_k P_k^- H_k^T + R_k\right) \tag{3.18}$$

The Bayes formula gives then:

$$p\left(x_k \mid z^k\right) = \frac{\mathcal{N}\left(z_k : H_k x_k, R_k\right) \mathcal{N}\left(x_k : \bar{x}_k^-, P_k^-\right)}{\mathcal{N}\left(z_k : H_k \bar{x}_k^-, H_k P_k^- H_k^T + R_k\right)} \tag{3.19}$$

The updated probability density function of the state have to be Gaussian. It can be demonstrated that if the measurement probability density function is Gaussian, the fact that the prior distribution is Gaussian ensure that also the posterior one is Gaussian [46]. The prior and the posterior distribution are then called *conjugate distributions*.

Hence, the posterior distribution is characterized as follows:

$$p\left(x_k \mid z^k\right) = \mathcal{N}\left(x_k : \bar{x}_k^+, P_k^+\right) \tag{3.20}$$

where the superscript "+" indicates that the estimated statistics of the state are updated. By the definition of multivariate Gaussian probability density function, it holds:

$$\mathcal{N}\left(x_k : \bar{x}_k^+, P_k^+\right) = \frac{(2\pi)^{\frac{n_x}{2}}}{|P_k|^{\frac{1}{2}}} \exp\left[-\frac{1}{2}\left(x_k - \bar{x}_k^+\right)^T \left(P_k^+\right)^{-1}\left(x_k - \bar{x}_k^+\right)\right] \tag{3.21}$$

In the same way, Eq. (3.19) can be appropriately rewritten by exploiting the properties of exponential functions:

$$\begin{aligned}\mathcal{N}\left(x_k : \bar{x}_k^+, P_k^+\right) = \\ k_p \exp\Bigg\{-\frac{1}{2}\Big[{\delta_z}^T \left(R_k\right)^{-1} \delta_z + \\ + {\delta_x^-}^T \left(P_k^-\right)^{-1} \delta_x^- - {\delta_z^-}^T \left(H_k^T P_k^- H_k + R_k\right)^{-1} \delta_z^-\Big]\Bigg\}\end{aligned} \tag{3.22}$$

where k_p is an appropriate constant, and the symbol δ indicates the deviation between the outcome and the expected value.

From the expansion and comparison of Eq. (3.21) and Eq. (3.22), it is possible to obtain two important relationships:

$$P_k^{+-1} = H_k^T R^{-1} H_k + P_k^{--1} \tag{3.23}$$

$$P_k^{+-1}\bar{x}_k^+ = H_k^T R_k^{-1} z_k + P_k^{--1}\bar{x}_k^- \tag{3.24}$$

Deriving $\bar{x}_k^+$ from Eq. (3.24), substituting $P_k^{-\,-1}$ with the expression obtainable from Eq. (3.23), and applying the following matrix inversion lemma on the second member of Eq. (3.23):

$$\left(H_k^T R^{-1} H_k + P_k^{-\,-1}\right)^{-1} = P_k^- - P_k^- H_k^T \left(H_k P_k^- H_k^T + R_k\right)^{-1} H_k P_k^- \tag{3.25}$$

it is possible to obtain also the following expression:

$$\bar{x}_k^+ = \bar{x}_k^- + P_k^- H_k^T \left(H_k P_k^- H_k^T + R_k\right)^{-1} \left(z_k - H_k \bar{x}_k^-\right) \tag{3.26}$$

Rewriting and collecting the last two expressions, it holds:

$$K_k = P_k^- H_k^T \left(H_k P_k^- H_k^T + R_k\right)^{-1} \tag{3.27}$$

$$\bar{x}_k^+ = \bar{x}_k^- + K_k \left(z_k - H_k \bar{x}_k^-\right) \tag{3.28}$$

$$P_k^+ = P_k^- - K_k H_k P_k^- \tag{3.29}$$

where the matrix K_k is known as the *Kalman gain*. Equations from Eq. (3.27) to Eq. (3.29) constitutes the updating or filtering stage of the Kalman filter.

For deriving the prediction scheme it is necessary to rely on the explicit computation of the integral in Eq. (3.6):

$$\mathcal{N}\left(x_{k+1} : \bar{x}_{k+1}^-, P_{k+1}^-\right) = \int \mathcal{N}\left(x_k : \bar{x}_k^+, P_k^+\right) \mathcal{N}\left(x_{k+1} : F x_k, Q_k\right) dx_k \tag{3.30}$$

It is verifiable that the integral in Eq. (3.30) have the following result:

$$k'_p \exp\left[b_p^T \left(P_k^{+-1} + F_k^T Q_k^{-1} F_k\right) b_p - \bar{x}_k^{+T} P_k^{+-1} \bar{x}_k + x_{k+1}^T Q_k^{-1} x_{k+1}\right] \tag{3.31}$$

where

$$b_p = P_k^{+-1} \bar{x}_k^+ + F_k^T Q_k^{-1} x_{k+1}$$

and k'_p is an appropriate constant.

As the prior distribution is Gaussian, it holds:

$$\mathcal{N}\left(x_{k+1} : \bar{x}_{k+1}^- P_{k+1}^-\right) = k'_p \exp\left[-\frac{1}{2}\left(x_{k+1} - \bar{x}_{k+1}^-\right)^T \left(P_{k+1}^-\right)^{-1} \left(x_{k+1} - \bar{x}_{k+1}^-\right)\right] \tag{3.32}$$

The expansion and comparison of Eq. (3.30) and Eq. (3.22) leads to two fundamental relationships:

$$\bar{x}_{k+1}^- = F_k \bar{x}_k^+ \tag{3.33}$$

$$P_{k+1}^- = F_k P_k^+ F_k^T + Q_k \tag{3.34}$$

Equation (3.33) and Eq. (3.34) constitute the prediction stage of the Kalman filter. An alternative way for expressing the equations useful for the updating stage of the Kalman filter exploits the following theorem [47]: If x_k and z_k are two random variables, distributed according to a multivariate Gaussian distribution, then the distribution of x_k conditional on z_k is multivariate normal with the following mean and covariance matrix:

$$\bar{x}_k^+ = \bar{x}_k^- + P_{xz_k} P_{zz_k}^{-1} \left(z_k - \bar{z}_k\right) \tag{3.35}$$

$$P_k^+ = P_k^- - P_{xz_k} P_{zz_k}^{-1} P_{zx_k} \tag{3.36}$$

where it holds:

$$P_{xz_k} = E\left[\left[x_k - \bar{x}_k^-\right]\left[z_k - \bar{z}_k\right]^T\right] \tag{3.37}$$

$$P_{zx_k} = E\left[\left[z_k - \bar{z}_k\right]\left[x_k - \bar{x}_k^-\right]^T\right] \tag{3.38}$$

$$P_{zz_k} = E\left[\left[z_k - \bar{z}_k\right]\left[z_k - \bar{z}_k\right]^T\right] \tag{3.39}$$

The developed observer requires the satisfaction of several assumptions. Other assumptions that emerge from the theoretical development regard the knowledge of the distribution of the process noise and the measurement one for each considered time sample. Moreover, the initial prior distribution of the state has to be guessed. Notwithstanding, the broad usage of this observer for many applications has revealed its very high robustness to slight alterations of the nominal conditions for which the filter is optimal. This statement holds especially with regards to the Gaussianity, whiteness and mutually independence of the process and measurement noises. Their covariance matrices, which should be known for a correct state estimation, are often chosen efficiently after a manual tuning.

However, if the observed system has an actual nonlinear behavior, the usage of the Kalman filter is highly discouraged. Nevertheless, it is quite evident that also a nonlinear dynamics is approximable by a linear model for a certain amount of time depending on

the local slope of the function that describes the actual nonlinear dynamics. In particular, if the sampling frequency is sufficiently high such that the numerical derivative of that function remains almost constant, then an accurate state-space model as in Eq. (3.2) and in Eq. (3.3) is efficiently approximated by:

$$x_{k+1} \simeq f(\bar{x}_k^+) + F_k\left(x_k - \bar{x}_k^+\right) \tag{3.40}$$

$$z_k \simeq h(\bar{x}_k^-) + H_k\left(x_k - \bar{x}_k^-\right) \tag{3.41}$$

where now it holds:

$$F_k = \left.\frac{\partial f}{\partial x_k}\right|_{x_k=\bar{x}_k^+} \tag{3.42}$$

$$H_k = \left.\frac{\partial h}{\partial x_k}\right|_{x_k=\bar{x}_k^-} \tag{3.43}$$

Thus, it is easy to verify that the usage of the Bayes formula leads to filter equations that are formally identical to the ones shown from Eq. (3.27) to Eq. (3.29), and Eq. (3.33) together with Eq. (3.34). The set of these formula constitutes the so-called *extended Kalman filter* (EKF), which is probably the most used state observer in practice. With the EKF, the nonlinear state-space model of the system is approximated to the first order of its Taylor's series expansion. Thus, also in the case in which all the other basic assumptions of the Kalman filter are satisfied, the accuracy of the final estimation will suffer from that approximation.

If the observed system is highly nonlinear, the first order approximation could not be sufficient to assure the filter stability or satisfactory results concerning accuracy.

In that case, it is possible to consider higher orders of the above Taylor's series expansion. However, this kind of approach is rare. Indeed, this way requires the explicit computation of at least the Hessians of the functions f and h. For that reason, approaches that involve the usage of the *unscented transform* [48] are typically preferable.

3.1.2 Unscented Kalman filter

Referring to the idea of Monte Carlo sampling the posterior distribution of the state variables, the availability of a high number of predicted values of the state can lead to a decent approximation of the actual prior distribution at the immediately future instant. Indeed, a famous statement indicates that it is much more easier to approximate a probability distribution than a nonlinear transformation [49].

A set of deterministic samples of the state is chosen to represent its posterior distribution. Thus, also a set of weights should be considered to obtain that the sample mean and covariance of these samples, called *sigma points*, coincide with the posterior mean and covariance of the state. To avoid biased estimates it is necessary that the sum of the weights be equal to one:

$$\sum_{i=0}^{N_\sigma} W_{\sigma_i} = 1 \tag{3.44}$$

where $W_{\sigma i}$ is the i-th sigma point and N_σ is the number of sigma points. One $2n_x$-dimensional set that respect the above condition is the following one:

$$\begin{aligned}
\chi_i &= \bar{x} + \left(\sqrt{n_x P}\right)_i \\
W_{\sigma_i} &= n_x/2 \\
\chi_{n_x+i} &= \bar{x} - \left(\sqrt{n_x P}\right)_{n_x+i} \\
W_{\sigma_{n_x+i}} &= n_x/2
\end{aligned} \tag{3.45}$$

where the notation $\left(\sqrt{n_x P}\right)_i$ indicates the i-th column of the matrix $\sqrt{n_x P}$

Sigma points belonging to this set have the same weight and are symmetrically distributed on the covariance contour. If the moments of the set are the same of the ones of the represented distribution they are optimal, otherwise they will represent an approximate distribution. For instance, in [50] it is shown that the fourth-order moment of the set of symmetric sigma points in Eq. (3.45) is equal to $n_x P^2$, while for Gaussian distributions is equal to $3P^2$. Thus, the symmetric set of sigma points is capable of approximately representing a Gaussian distribution. To capture the fourth-order moment it is possible to introduce one additional sigma point. For instance, it is feasible to consider the following set:

$$
\begin{aligned}
\chi_0 &= \bar{x} \\
W_{\sigma_0} &= W_{\sigma_0} \\
\chi_i &= \bar{x} + \left(\sqrt{\frac{n_x}{1-W_{\sigma_0}}P}\right)_i \\
W_{\sigma_i} &= \frac{1-W_{\sigma_0}}{n_x} \\
\chi_{n_x+i} &= \bar{x} - \left(\sqrt{\frac{n_x}{1-W_{\sigma_0}}P}\right)_{n_x+i} \\
W_{\sigma_{n_x+i}} &= \frac{1-W_{\sigma_0}}{n_x}
\end{aligned}
\tag{3.46}
$$

If W_{σ_0} is set equal to $(1-n_x/3)$, the fourth-order moment of the set becomes identical to the one of the Gaussian distribution. Thus, at least from a theoretical point of view, it is possible to represent any distribution by the appropriate choice of the sigma point set.

The weight W_{σ_0} in Eq. (3.46) can be set arbitrarily to increment or decrement the spread of the sigma points about the expected value of the state. Note that also negative values are selectable because the sigma points represent a probability density function but, clearly, they are not.

Another possible set of sigma points is findable in [51]:

$$
\begin{aligned}
\chi_0 &= \bar{x} \\
W_{\sigma_0} &= \frac{\alpha_W^2 - 1}{\alpha_W^2} + 1 - \alpha_W^2 + \beta_W \\
\chi_i &= \bar{x} + \left(\sqrt{\alpha_W^2 n_x P}\right)_i \\
W_{\sigma_i} &= \frac{1}{2\alpha_W^2 n_x} \\
\chi_{n_x+i} &= \bar{x} - \left(\sqrt{\alpha_W^2 n_x P}\right)_{n_x+i} \\
W_{\sigma_{n_x+i}} &= \frac{1}{2\alpha_W^2 n_x}
\end{aligned}
\tag{3.47}
$$

where α_W is the spreading parameter, and β_W is a scaling parameter used to appropriately match some of the higher order moments of the actual distribution. The values for α_W should be between 1×10^{-4} and 1, while the optimal β_W for Gaussian distributions is equal to 2.

For reducing the number of involved sigma points without affecting the accuracy of the distribution representation, [52] presents an algorithm for sampling $n_x + 1$ sigma points that lie on a hypersphere centered in the mean value of the state:

1. Choose W_{σ_0} between 0 and 1
2. Choose a weight sequence:
$$W_{\sigma_i} = \frac{1 - W_{\sigma_0}}{n_x + 1} \tag{3.48}$$
3. Initialize vector sequence as:
$$\chi_0^1 = [0], \qquad \chi_1^1 = \left[-\frac{1}{\sqrt{2W_{\sigma_1}}}\right], \qquad \chi_2^1 = \left[-\frac{1}{\sqrt{2W_{\sigma_1}}}\right] \tag{3.49}$$

4. Expand vector sequence for $j = 2,3,...,n_x$ according to

$$\chi_i^j = \begin{cases} \begin{bmatrix} \chi_0^{j-1} \\ 0 \end{bmatrix} & \text{for } i = 0 \\ \begin{bmatrix} \chi_i^{j-1} \\ -\frac{1}{\sqrt{j(j+1)W_1}} \end{bmatrix} & \text{for } i = 1,...,j \\ \begin{bmatrix} \mathbf{0}_{j-1} \\ -\frac{1}{\sqrt{j(j+1)W_1}} \end{bmatrix} & \text{for } i = j+1 \end{cases} \tag{3.50}$$

Note that each sigma point except the $0-th$ has the same weight and lies on the hypersphere of radius $\sqrt{n}/(1-W_0)$. Clearly, the complete sigma points are obtained at any sample time k summing χ_i^j to the current mean of the state

The selected set of sigma points is subjected to a non linear transformation, that could be represented by the function f or by the function h in Eq. (3.3) and in Eq. (3.2). Thus, the mean and the covariance of the transformed sigma points is calculated to approximate the distribution of the corresponding transformed random variable. This process is referred as *unscented transform*.

To realize the approximation level of this operation, the Taylor series expansion of the mean $\bar{z}$ as a function of the state x is given below:

$$\bar{z} = E[h(\bar{x}+e)] = h(\bar{x}) + E\left[D_e^{(1)}h + \frac{D_e^{(2)}h}{2!} + \frac{D_e^{(3)}h}{3!} + ...\right] \tag{3.51}$$

It is straightforward to verify that, truncating the series to the second order, it holds

$$\bar{z} = h(\bar{x}) + \bar{x}D_e^{(1)}h + PD_e^{(2)}h \tag{3.52}$$

Thus, it is necessary to have correct information about the first two moments of the distribution of x to obtain a second order approximation of $\bar{z}$.

A similar relation holds for the covariance:

$$\begin{aligned}\mathbf{\Sigma}_z =& H(x)\mathbf{\Sigma}_x H^T(x) + E\left[\frac{D_e^{(1)}h(D_e^{(3)}h)^T}{3!} + \frac{D_e^{(2)}h(D_e^{(2)}h)^T}{2\times 2!} + \frac{D_e^{(3)}h(D_e^{(1)}h)^T}{3!}\right] + \\ & - E\left[\frac{D_e^{(2)}h}{2}\right] E\left[\frac{D_e^{(2)}h}{2}\right]^T + \ldots\end{aligned} \tag{3.53}$$

Here, it is necessary to have correct information about the first four moments of the distribution of x to obtain a second order approximation of $\mathbf{\Sigma}_z$.

Sigma points are chosen to match the first two moments of the x distribution, and in some case can even match the first four moments.

The unscented transform involves the knowledge of the entire transforming nonlinear function, and of at least two moments of the transforming variable distribution. Thus, a filter based on the unscented transform guarantees an accuracy of the second order for the state mean, and of the first order for the state covariance.

The scheme of the filter is the following:

1. calculate the sigma points set χ_k^+ from a-posteriori estimate of the state mean $\bar{x}_k^+$, according to one of the Equations (3.45), (3.46), (3.47), and (3.50)

2. propagate sigma points through the non-linear dynamics of the system:

$$\chi_{k+1}^- = f(\chi_k^+) \tag{3.54}$$

3. calculate mean and covariance of the propagated sigma point

$$\bar{x}_{k+1}^{-} = \sum_{i=0}^{L} W_{\sigma_i} \chi_{i_{k+1}}^{-} \tag{3.55}$$

$$P_{k+1}^{-} = \sum_{i=0}^{L} W_{\sigma_i} \left(\chi_{i_{k+1}}^{-} - \bar{x}_{k+1}^{-} \right) \left(\chi_{i_k+1}^{-} - \bar{x}_{k+1}^{-} \right)^T + R_{k+1} \tag{3.56}$$

where $L-1$ is the cardinality of χ_k^+;

4. recalculate the sigma points set χ_{k+1}^{-} from a-priori estimate of the state mean $\bar{x}_{k+1}^{-}$

5. calculate the so-called *innovations*:

$$\mathcal{Z}_{k+1}^{-} = h\left(\chi_{k+1}^{-}\right) \tag{3.57}$$

6. calculate innovation mean and covariance, and cross-covariance with the state x_{k+1}^{-}:

$$z_{k+1}^{-} = \sum_{i=0}^{L} W_{\sigma_i} \mathcal{Z}_{i_{k+1}}^{-} \tag{3.58}$$

$$P_{zz_{k+1}} = \sum_{i=0}^{L} W_{\sigma_i} \left(\mathcal{Z}_{i_{k+1}}^{-} - z_{i_{k+1}}^{-} \right) \left(\mathcal{Z}_{i_{k+1}}^{-} - z_{i_{k+1}}^{-} \right)^T \tag{3.59}$$

$$P_{zx_{k+1}} = \sum_{i=0}^{L} W_{\sigma_i} \left(\mathcal{Z}_{i_{k+1}}^{-} - z_{i_{k+1}}^{-} \right) \left(\chi_{k+1}^{-} - \bar{x}_{k+1}^{-} \right)^T \tag{3.60}$$

$$P_{xz_{k+1}} = \sum_{i=0}^{L} W_{\sigma_i} \left(\chi_{k+1}^{-} - \bar{x}_{k+1}^{-} \right) \left(\mathcal{Z}_{i_{k+1}}^{-} - z_{i_{k+1}}^{-} \right)^T \tag{3.61}$$

7. update the estimates of mean and covariance:

$$\bar{x}_{k+1}^{+} = \bar{x}_{k}^{-} + P_{xz_{k+1}} P_{zz_{k+1}}^{-1} \left(z_{k+1} - \bar{z}_{k+1} \right) \tag{3.62}$$

$$P_{k+1}^{+} = P_{k+1}^{-} - P_{xz_{k+1}} P_{zz_{k+1}}^{-1} P_{zx_{k+1}} \tag{3.63}$$

The steps above describe the so-called *unscented Kalman filter*. From the computational point of view, the critical step is the computation of the sigma points, in which the covariance matrix P appears within square root. Thus, P has to be semidefinite positive; Cholesky decomposition, meaning finding V such that

$$P = VV^T \tag{3.64}$$

is the most used technique to compute $\sqrt{P}$ in unscented Kalman filter applications. Evidently, the computation complexity increases with the dimension of the state vector and, thus, with the number of sigma points that need to be propagated.

3.2 Compressive sampling for signal recovery

State observers have very interesting properties of optimality in the estimation of the system dynamics. These properties are essentially related to the combination of the information contained into a mathematical approximate model of the real system, and into a set of sequential measurements of sensitive quantities depending on the dynamics. In particular, with regard to Kalman filters, it has been shown that all the history of the measurements contributes to the state learning by sequentially updating information coming from a Markov process like the state equations.

Sudden interruptions of the measurement availability influence negatively this optimal chain of prediction and updating operations. From a practical point of view, the estimation error starts to diverge until new measurements are available. However, if the error have a slow convergence to zero, for instance because of the non strict Gaussianity of the process and measurement noises, the global quality of the estimation becomes insufficient.

For instance, it is possible to consider the data in Fig. 1.8 after the application of the backface culling technique; raw attitude information can be achieved from the detectable features at any time sample in which three or more characteristic points are visible.

As mentioned in the previous chapter, given the positions of three different features at a given sample time k in the frame C, one can define two connecting vectors, ${}^{C}\boldsymbol{v}_i$ and ${}^{C}\boldsymbol{v}_u$, whose cross product is the vector ${}^{C}\boldsymbol{v}_j$, which is perpendicular to both. A third column vector, ${}^{C}\boldsymbol{v}_k$, can be simply obtained through another cross product between ${}^{C}\boldsymbol{v}_i$ and ${}^{C}\boldsymbol{v}_j$. Then, the orientation of a body-fixed reference frame $\mathcal{F}$, which (in general) is different from the principal reference frame B, with respect to the inertial frame I, is given by the following expression:

$$ {}^{I}A_{C_k}\,{}^{C}A_{\mathcal{F}_k} = {}^{I}A_{\mathcal{F}_k} = \left[\begin{array}{ccc} {}^{C}\hat{\boldsymbol{v}}_i & {}^{C}\hat{\boldsymbol{v}}_j & {}^{C}\hat{\boldsymbol{v}}_k \end{array} \right] \in SO(3) \tag{3.65} $$

A similar expression can be found in Eq. (1.2). Vectors ${}^{C}\hat{\boldsymbol{v}}_i$, ${}^{C}\hat{\boldsymbol{v}}_j$, and ${}^{C}\hat{\boldsymbol{v}}_k$ are the unit vectors corresponding to ${}^{C}\boldsymbol{v}_i$, ${}^{C}\boldsymbol{v}_j$, and ${}^{C}\boldsymbol{v}_k$, respectively. Moreover, it is reminded that Eq. (1.14) holds; hence, C and I have the same orientation by construction.

A non-singular mapping between an element of the $SO(3)$ group and a unit quaternion always exists (see Appendix B.1). This mapping has been shown in Eq. (1.7) for the orientation of I relative to B. However, the aforementioned mapping is valid for any considered reference frames.

At a new instant, e.g. $k+1$, the visible features can be different from the ones visible at k. Thus, the vectors connecting the features define a new coordinate system $\mathcal{F}'$. However, assuming the knowledge of a model of the target, and thus of the relative positions of all the detectable features (first approach in subsection 1.2.1), it is possible to evaluate the orientation of $\mathcal{F}$ by exploiting the knowledge of matrix ${}^{\mathcal{F}}A_{\mathcal{F}'}$. The latter matrix is constant and depends only on the layout of the features on the target surface.

The resulting attitude quaternions ${}^{\mathcal{F}}q_I$ associated to ${}^{I}A_{\mathcal{F}}^{T}$ are shown in Fig. 3.1. The reference frame $\mathcal{F}$ has been defined at the initial sample time by the first, third, and fourth feature defined in Eq. (1.13).

The fourth dimensional signal shown in Fig. 3.1 presents many missing samples because in the relevant time samples three of the five considered features are hidden to the observer on the chaser. The Stanley's algorithm depicted in the subsection 1.1 have been applied for any part of the signal. However, the sign of the first quaternion sample

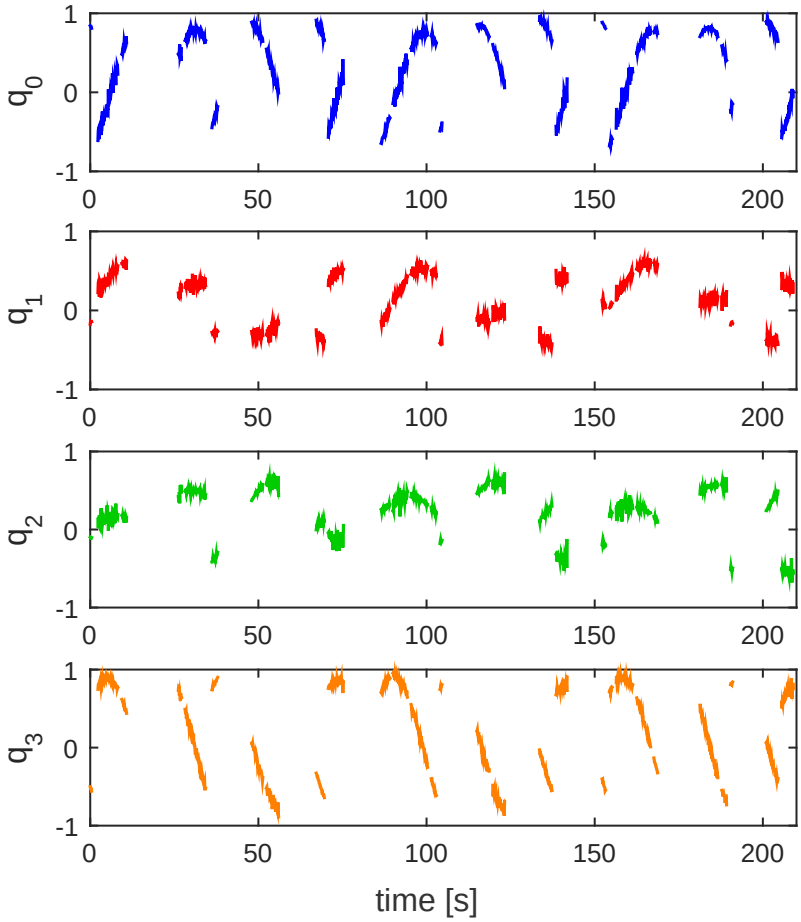

Figure 3.1 Example of raw attitude information $\left({}^{\mathcal{F}}q_I\right)$. The amplitude of the noise on the coordinates of the features has been set to 30 mm for each coordinate.

for each part had to be chosen randomly. This aspect will imply considerations that will be further discussed in the next sections. The amplitude of the noise on the coordinates of the features has been set to 30 mm for each coordinate, according to the actual accuracy of existing stereo-vision systems (see subsection 1.2.2 for details).

The attitude of the target is absolutely sufficient for observing its angular rate because of the direct correlation between the two quantities. However, the presence of so many missing samples prevent from the usage of the signal as a set of measurements for feeding Kalman filters. Thus, the preliminary recovery of the missing attitude information has a fundamental importance for the further estimation of the global rotational state of the target. However, some assumptions on the nature of this attitude signal have to be made to perform the recovery.

An extensive treatment of attitude dynamics can be found in Appendix B.2; however, from Eq. (1.11) it can be deduced that the angular rate of a torque-free body is a continuous, differentiable, and periodic function of time. Moreover, its Lambert's series expansion, shown in Eq. (1.12), is convergent. Approximating the function by truncating the series at the n_{or}-th order, with n_{or} positive and finite, the angular rate is approximately a linear combination of trigonometric functions.

Thus, the frequency spectra of the components of the angular rate vector are approximately *sparse*. Alternatively, it is possible to state that the angular rate signal is approximately sparse in the frequency domain.

The attitude of the target is obtainable from the integration of Eq. (1.6). Altought it is very difficult to find a closed form solution of this differential equation, there are not evident contraindications in assuming that also quaternions are approximately sparse in frequency domain. Indeed, the numerical integration of Eq. (1.6) with an explicit method like the Euler's one leads to evidence that each component of the quaternion at the future time sample ${}^{B}q_{I_{k+1}}$ is approximately a linear combination of trigonometric functions,

whose coefficients are proportional to the components of the current quaternion sample ${}^{B}q_{I_k}$. In addiction to the aforementioned theoretical evidences, the assumption of *sparsity* of attitude signals in the frequency domain is also supported by simulation results [53].

The recovery of sparse signals affected by noise is a well known task in the field of image processing and telecommunications. The developed methods are covered by the so-called *compressive sampling* (CS) theory, whose basics will be discussed in the next subsection for illustrating their application for attitude recovery. In the next subsections of this chapter, each component of the chosen attitude parameterization for the target will be considered as a separated mono-dimensional signal that have to be recovered.

3.2.1 Theoretical basis

In general, a noisy measured signal with missing samples $s \in \mathbb{R}^{p_s}$ can be modeled as:

$$s = \mathcal{S}\sigma + \eta_s \tag{3.66}$$

where $\sigma \in \mathbb{R}^{m_s}$ represents the unknown original signal, η_s represents the noise, and $\mathcal{S}$ is a $p_s \times m_s$ matrix that can be defined using the following expression:

$$\mathcal{S}^T\mathcal{S} = \text{diag}(\tau) \tag{3.67}$$

where τ is an array whose elements τ_j, $j = 1,2...,m_s$ are equal to zero when a lack of attitude information is associated with the time instant t_j. Otherwise, τ_j is equal to one. Using these definitions, one can find that $\mathcal{S}$ must be a matrix whose columns are null when the column index corresponds to a time instant with a lack of attitude information. Additionally, it is easy to verify that the following equation holds, $\mathcal{S}\mathcal{S}^T = I_{p_s}$, where I_{p_s} is the $p_s \times p_s$ identity matrix.

The theory of CS addresses the problem of recovering a signal that is approximately decomposable into a linear combination of a small number of elementary functions of time. When a sufficient number of measurements of the signal is available, it is possible to assume the parametric forms (at least) of the functions that compose the signal. This result leads to the definition of an arbitrary-but-finite number of unit-norm signals that might contribute to the signal to be recovered. Finding the most relevant elementary signals, which are also called *atoms*, corresponds to the statement and solution of an optimization problem. In particular, it is desirable to find the smallest possible number of atoms whose linear combination optimally fits the available measurements.

All of the atoms are grouped into a set that is called a *dictionary*, whose properties can be easily examined via the associated synthesis matrix. The dictionary synthesis matrix Φ is defined as a representation of the linear mapping between certain complex coefficients $c \in \mathbb{C}^{n_s}$ and the original signal σ. An interesting dictionary is the so-called *Fourier dictionary*; the synthesis matrix Φ of this dictionary is given by the following formula:

$$\sigma_k = \sum_{u=0}^{n_s-1} \frac{c(u)}{\sqrt{n_s}} e^{i\frac{2\pi}{n_s}uk} \qquad \forall k = 0,1,...,m_s-1 \tag{3.68}$$

$$\Phi_{k,u} = \frac{1}{\sqrt{n_s}} e^{i\frac{2\pi}{n_s}uk} \quad \forall k = 0,1,...,m-1 \quad \wedge \quad \forall u = 0,1,...,n_s-1 \tag{3.69}$$

When m_s is equal to n_s, the linear mapping $\Phi : \mathbb{C}^{n_s} \to \mathbb{R}^{m_s}$ becomes the so-called inverse discrete Fourier transform (IDFT) multiplied by the normalization constant n_s. Additionally, it is possible to define the dictionary analysis matrix Φ^* as the conjugate-transpose of Φ, showing that when $m_s = n_s$ the linear mapping $\Phi^* : \mathbb{R}^{m_s} \to \mathbb{C}^{n_s}$ becomes the so-called discrete Fourier transform (DFT). This property holds because of the orthogonality of the matrix Φ. It is defined the *coherence* parameter as follows:

$$\vartheta_c = \max_{\iota \neq \kappa} \left| \sum_{k=0}^{m_s-1} \Phi_{k,\iota} \Phi_{k,\kappa} \right| \tag{3.70}$$

where the Fourier dictionary is found to be completely incoherent ($\vartheta_c = 0$), which is, in general, a very useful property for a dictionary because the atoms are linearly independent. This result implies that it is easier to find the atoms that compose the original signal. On the contrary, if two atoms are very similar, it is harder to determine the separate contributions of each of them. Note that in the common case of $n_s > m_s$, the dictionary has a null coherence because of the well-known orthogonality of sine and cosine waves.

Based on these definitions, Eq. (3.66) can be conveniently rewritten as:

$$s = \mathcal{S}\Phi c + \eta_s = \tilde{\Phi} c + \eta_s \tag{3.71}$$

Equation (3.71) proposes the problem of estimating the coefficient vector c from a noisy signal with missing samples s. This problem is obviously ill-posed; a naive attempt to solve it could be formulated as follows:

$$\arg\min_c \|c\|_2^2 \qquad \text{subject to} \qquad s = \tilde{\Phi} c \tag{3.72}$$

The problem formulated in Eq. (3.72) could be solved, for example, using the common Gauss method; however, for signal recovery pursuit, the solution is certainly inaccurate. For example, adopting the Fourier dictionary and obtaining $\Phi\Phi^* = n_s I_{n_s}$, the solution to the problem in Eq. (3.72) becomes:

$$c = \frac{1}{n_s} \Phi^* \mathcal{S}^T s \tag{3.73}$$

from which it is easy to show that the product $\mathcal{S}^T s$ produces a signal with missing samples substituted by zero values. Furthermore, because the solution is not (in general) *sparse*, *i.e.*, most of the coefficient values are far from zero, one obtains only another representation of a disguised noisy signal. Thus, a clever approach will introduce some regularizer that can induce sparsity in the coefficient vector. Therefore, a problem that is optimal could be stated as follows:

$$\arg\min_{c} \|c\|_0 \qquad \text{subject to} \qquad \|s - \tilde{\Phi} c\|_2 \leq \varepsilon_0 \tag{3.74}$$

where ε_0 is a reasonable tolerance of the estimation error and the $l0$-norm is defined as the number of non-zero elements of the argument. Unfortunately, obtaining a solution to this problem requires searching for a solution among all possible combinations of the non-zero elements of c. For this reason, it is appropriate to use a relaxation of the problem, which leads to the following problem:

$$\arg\min_{c} \|c\|_1 \qquad \text{subject to} \qquad \|s - \tilde{\Phi} c\|_2 \leq \varepsilon_1 \tag{3.75}$$

where ε_1 depends on ε_0 and the $l1$-norm is defined as the sum of the elements of the argument.

The problem in Eq. (3.75) is equivalent to the one in Eq. (3.74) under certain restrictions that are synthesized by the so-called *restricted isometry property* (RIP) [54]. This last condition can be stated as: let $\tilde{\Phi}_s$ a matrix composed by $s_s < n_s$ columns of $\tilde{\Phi}$, a positive constant $\delta_s < 1$ exists such that for every sub-matrix $\tilde{\Phi}_s$ and for every sparse c with only s_s non-null elements, it holds:

$$(1-\delta_s)\,\|c_s\|_2^2 \leq \|\tilde{\Phi}_s c_s\|_2^2 \leq (1+\delta_s)\,\|c_s\|_2^2 \tag{3.76}$$

where c_s is the vector of the actual non-null elements of c. From a practical point of view the property in Eq. (3.76) requires that if the vector to be reconstructed has actually s_s non-null elements, all the possible sub-matrices of $\tilde{\Phi}$ with s_s columns should have a $l2$-norm that is not too far from one. This means, in other words, that the columns of $\tilde{\Phi}$ should not be too similar.

Evidently, for a completely incoherent dictionary like the Fourier one, the RIP is satisfied for δ_s equal to zero. Thus, if the $l2$-norm of any appropriate sub-matrix of $\tilde{\Phi}$ is equal to one, the relaxed problem in Eq. (3.75) is capable of recovering the sparse vector c with errors bounded by ε_1. Using the Fourier dictionary, this occur if there are not missing samples on measurements s, because $\mathcal{S}$ becomes an identity matrix.

If missing samples occur, the presence of null columns on $\mathcal{S}$ leads to a slight reduction of the $l2$-norm of the sub-matrices of $\tilde{\Phi}$. Clearly, the entity of this reduction depends mainly on the number the percentage of missing samples contained into the signal.

For instance, considering that the 50% of the samples are missing, which is a very high percentage, the $l2$-norm of a sub-matrix of $\tilde{\Phi}$ with only three columns is coarsely 0.75, which is a sufficiently high value for the satisfaction of the RIP. If the number of considered columns increases, then also the $l2$-norm of the sub-matrix grows.

Note that the problem in Eq. (3.75) is convex; thus, it has only one suitable solution, if a solution exists. However, a more convenient method to solve this problem is to write it in its Lagrangian form:

$$\arg\min_{c} \frac{1}{2}\|\tilde{\Phi}c - s\|_2^2 + \lambda\,\|c\|_1 \tag{3.77}$$

The regularization parameter λ is defined as a *penalization parameter*: when λ is equal to zero, the solution of the problem is a coefficient vector that accurately represents the signal s; however, the entire noise vector is preserved and contained in the coefficients. When $\lambda \to +\infty$ the only coefficient vector that can solve the problem is $c \to 0$, which represents a null constant signal. In other words, for higher values of λ, the signal will be smoother but the recovery will be less accurate.

The problem stated in Eq. 3.75 is known as the *basis pursuit denoising* problem; several algorithms have been created to solve it. The problem stated in Eq. (3.77) is known as the *lasso* problem; it directly descends from the basis pursuit problem.

To better understand the capabilities of lasso for recovering sparse signals including noise, one can consider a dictionary synthesis matrix whose columns have a unitary $l2$-norm. Unfortunately, the matrix $\tilde{\Phi}$ does not have this property, because the matrix $\mathcal{S}$ presents (in general) null columns. However, without any loss of generality, one can re-normalize the column of the matrix $\tilde{\Phi}$, contextually multiplying the norms of the columns by the relevant coefficients contained in c. After re-normalization of the columns, the dictionary associated with the synthesis matrix $\tilde{\Phi}$ has a non-null coherence ϑ_c. However, the condition of having a null coherence is not mandatory: as stated in [55], the fundamental condition that assures that an exactly sparse signal can be optimally recovered with most of the existing algorithms is that a subset Λ of linearly independent atoms in the dictionary that multiplies the *support* of the *unique minimizer* of the problem stated in Eq. (3.77) should exist. In other words, all of the non-zero elements of the optimal c, should be multiplied by only the mentioned subset of linearly independent atoms Λ. This condition is met, at least for a sufficiently large value of λ, if the following fundamental relationship holds [55]:

$$\|\tilde{\Phi}^*(s - a_\Lambda)\|_\infty \leq \lambda \left[1 - \max_{\gamma \notin \Lambda} \|(\tilde{\Phi}_\Lambda^* \tilde{\Phi}_\Lambda)^{-1} \tilde{\Phi}_\Lambda^* \tilde{\Phi}_\gamma\|_1\right] \tag{3.78}$$

where matrix $\tilde{\Phi}_\Lambda$ is the sub-matrix of $\tilde{\Phi}$ that is composed by atoms belonging to the set Λ, $\tilde{\Phi}_\gamma$ is the generic γ-th column of $\tilde{\Phi}$ that is not contained in $\tilde{\Phi}_\Lambda$, and

$$a_\Lambda = \tilde{\Phi}_\Lambda (\tilde{\Phi}_\Lambda^* \tilde{\Phi}_\Lambda)^{-1} \tilde{\Phi}_\Lambda^* s$$

is intended as the best approximation of the signal using only the atoms contained in Λ. Note that a_Λ is obtained by multiplying $\tilde{\Phi}_\Lambda$ to its Moore pseudo-inverse, and then to the measured signal s with missing samples.

In Eq. (3.78) the quantity included in square brackets can be defined as the *Exact recovery coefficient ERC*. Note that the relationship in Eq. (3.78) holds for some positive λ if *ERC* is greater than zero. Note also that when λ is arbitrarily large, the estimated signal becomes the null vector.

The *ERC* defines the extent to which a subset of linearly independent atoms in a dictionary is different from any other subset in it. For example, in an entirely incoherent dictionary (such as the Fourier dictionary), $ERC = 1$ holds. Therefore, to guarantee a satisfying solution, the value of λ could be quite small. However, note that, although the coherence of the dictionary is not null, it is sufficient that the signal to be estimated can be represented as a combination of linearly independent atoms that are not too similar to others in the dictionary. This situation can also occur if the coherence value ϑ_c is a strictly positive value.

After all, this requirement of having different atoms is necessary also to the satisfaction of the RIP. Hence, if the RIP is satisfied, it is reasonable to assume that also the condition in Eq. (3.78) is respected for relatively low values of the penalization parameter λ

Signal recovery via basis pursuit is a very powerful tool for estimating the quantities that directly depend on the corrupted measured signals; however, finding a fast algorithm capable of accurately identifying the minimizer of the function in Eq. (3.77) can be tough. Various algorithms base their strength on avoiding the high computation and storage of dictionary synthesis matrix, which means that they include fast transformation algorithms that map coefficients to signals and vice-versa. This process is inevitably reflected in the choice of a suitable dictionary. For example, the Fourier dictionary is very convenient because it is well-known that direct and inverse fast Fourier transform algorithms can easily be implemented within the main algorithm.

The chosen algorithm is an alternative version of the iterative SALSA, the acronym of split augmented Lagrangian shrinkage algorithm [56]. The reasons for this choose reside in the speed, computational efficiency, and ease of implementation.

3.2.2 Split augmented Lagrangian shrinkage algorithm

The two most important theoretical contributions to the selected algorithm are so-called variable splitting and the use of the augmented Lagrangian function. Variable splitting is a method for solving a problem of the following form:

$$\min_{u_f} \quad f_1(u_f) + f_2(g(u_f)) \tag{3.79}$$

where f_1, f_2, and g are real functions. Defining $g(u) = v$, the previous problem becomes:

$$\min_{u_f, v_f} f_1(u_f) + f_2(v_f) \qquad \text{subject to} \qquad g(u_f) = v_f \tag{3.80}$$

Thus, this first contribution consists of introducing a new variable in the optimization problem. The second contribution of SALSA can be applied, for example, to the following general constrained optimization problem:

$$\min_{z_a} E_a(z_a) \qquad \text{subject to} \qquad W_a z_a - b_a = 0 \tag{3.81}$$

The augmented Lagrangian function for this problem can be defined as follows:

$$E_a(z_a) + \psi_a^T (b_a - W_a z_a) + \frac{\mu_a}{2} \|W_a z_a - b_a\|_2^2 \tag{3.82}$$

where ψ_a is the Lagrange multiplier's array and $\mu_a \geq 0$ is another penalization parameter. Minimizing the function in Eq. (3.82) corresponds to giving the constraint in Eq. (3.81) extra weighting.

Note that the quantity in Eq. (3.82) can be recast in the following form:

$$E_a(z_a) + \frac{\mu_a}{2} \|W_a z_a - l\|_2^2 \tag{3.83}$$

Now, the described contributions can be applied to Eq. (3.77). The result of variable splitting is as follows:

$$\arg\min_{c, v_f} \frac{1}{2} \|\tilde{\Phi} c - s\|_2^2 + \lambda \|v_f\|_1 \qquad \text{subject to} \qquad c - v_f = 0 \tag{3.84}$$

where, by substituting c in the $l1$-norm, we obtain the new variable v_f, which is constrained to have values equal to those of c. The function to be minimized appears to be a function of the vector $z = \begin{bmatrix} c & v_f \end{bmatrix}^T$; comparing this definition to the problem in Eq

(3.81), it is possible to find that $W_a = [I_{n_s} \; -I_{n_s}]$ and $b_a = 0$. Thus, recasting the problem using the augmented Lagrangian function, the following is obtained:

$$\arg\min_{c,v_f} \frac{1}{2}\|\tilde{\Phi}c - s\|_2^2 + \lambda\|v_f\|_1 + \frac{\mu_a}{2}\|c - v_f - l\|_2^2 \tag{3.85}$$

In this formulation of the problem, the high value of the parameter μ_a forces the equality of c and v_f, compensating for the introduction of a new auxiliary variable.

However, the problem in Eq. (3.85) is difficult to solve because both variables, c and v_f, are in the norm. One way to address this issue is to minimize the function for only one variable while holding the other fixed; this is repeated alternately for the two variables for a fixed number of iterations.

This algorithm is the proposed SALSA algorithm. The algorithm consists of the following operations once λ, μ_a, and some arbitrary initial guesses v_{f_0} and l_0 are chosen:

- $c_{\nu+1} = \arg\min_c \|\tilde{\Phi}c - s\|_2^2 + \mu_a\|c - v_{f_\nu} - l_\nu\|_2^2$
- $v_{f_{\nu+1}} = \arg\min_{v_f} \lambda\|v_f\|_1 + \frac{\mu_a}{2}\|c_{\nu+1} - v_f - l_\nu\|_2^2$
- $l_{\nu+1} = l_\nu - (c_{\nu+1} - v_{f_{\nu+1}})$
- $\nu \leftarrow \nu + 1$

These basic steps can be solved in a closed form: the first step represents a classic constrained least-squares optimization problem, as the function to be minimized is a strictly convex quadratic function. The solution is as follows:

$$c_{\nu+1} = (\tilde{\Phi}^*\tilde{\Phi} + \mu_a I_{n_s})^{-1}[\tilde{\Phi}^* s + \mu_a(v_{f_\nu} + l_\nu)] \tag{3.86}$$

The second step is minimization of a function that is a pure denoising function, meaning that the parameter λ is the regularizer of the equivalence condition between a known vector $c_{v+1} - l_v$ and the variable v_f: if $\lambda = 0$, $v_f = c_{v+1} - l_v$; if λ is bigger than zero, it induces sparsity in v_f.

The closed-form solution to this kind of problem is well known [57]. Specifically, when the regularizer is applied to the $l1$-norm, the solution is the so-called *soft-thresholding function*.

This non-linear function is defined for every component of the argument array Δ:

$$\text{soft}(\Delta_i, L) = \text{sign}(\Delta_i) \max\{|\Delta_i| - L, 0\} \tag{3.87}$$

Then, the solution to the second step is:

$$v_{f_{v+1}} = \text{soft}\left(c_{v+1} - l_v, \frac{\lambda}{\mu_a}\right) \tag{3.88}$$

To obtain a simpler algorithm, this method can be slightly modified, according to [58], by changing the variables $u_{f_v} = v_{f_v} + l_v$. Thus, Eq. (3.86) can be written as follows:

$$c_{v+1} = (\tilde{\Phi}^* \tilde{\Phi} + \mu_a I_{n_s})^{-1} (\tilde{\Phi}^* s + \mu_a u_{f_v}) \tag{3.89}$$

Using the matrix-inverse lemma, the matrix inversion above can be simplified:

$$(\tilde{\Phi}^* \tilde{\Phi} + \mu_a I_{n_a})^{-1} = \frac{1}{\mu_a} I_{n_s} - \frac{1}{\mu_a} \tilde{\Phi}^* (\mu_a I_{p_s} + \tilde{\Phi} \tilde{\Phi}^*)^{-1} \tilde{\Phi} \tag{3.90}$$

Then, because the following equations hold (as in the case of using the Fourier dictionary):

$$\mathcal{S}\mathcal{S}^T = I_{p_s} \tag{3.91}$$

$$\tilde{\Phi}\tilde{\Phi}^* = n_s I_{p_s} \tag{3.92}$$

the expression can be turned into

$$(\tilde{\Phi}^*\tilde{\Phi} + \mu_a I_{n_s})^{-1} = \frac{1}{\mu_a} I_{n_s} - \frac{1}{\mu_a(\mu_a + n_s)}\tilde{\Phi}^*\tilde{\Phi} \tag{3.93}$$

and thus

$$c_{\nu+1} = \left(\frac{1}{\mu_a} I_{n_s} - \frac{1}{\mu_a(\mu_a + n_s)}\tilde{\Phi}^*\tilde{\Phi}\right)(\tilde{\Phi}^* s + \mu_a u_{f_\nu}) = u_{f_\nu} + \frac{1}{\mu_a + n_s}\tilde{\Phi}^*(s - \tilde{\Phi} u_\nu), \tag{3.94}$$

which leads to:

$$c_{\nu+1} = u_{f_\nu} + \frac{1}{\mu_a + n_s}\Phi^*[\mathcal{S}^T s - \text{diag}(\tau)\Phi u_\nu] \tag{3.95}$$

Equation (3.95) shows that because a fast transform that maps coefficients to signals and vice-versa exists (*i.e.*, the direct and inverse fast Fourier transform), the explicit computation of Φ and Φ^* can be avoided, which allows the algorithm to be very fast and efficient.

Then, the final algorithm obtained (gathering all of the equations presented in this section) is as follows:

- $u_{f_{\nu+1}} = \text{soft}(c_\nu - l_\nu, \lambda/\mu_a) + l_\nu$
- $c_{\nu+1} = (\tilde{\Phi}^*\tilde{\Phi} + \mu I_{n_s})^{-1}(\tilde{\Phi}^* s + \mu_a u_{f_\nu})$
- $l_{\nu+1} = u_{f_{\nu+1}} - c_{\nu+1}$
- $\nu \leftarrow \nu + 1$

To implement the algorithm, it is still necessary to choose values for λ and μ_a, and to specify the initial guesses for c_0 and l_0.

The presented algorithm has been used to recover the attitude of the target. In the following it will be described the direct application of the theory for estimating the rotational dynamics of the target.

3.3 Original estimation algorithms and results

The theoretic sections about state observers and compressive sampling techniques serve as the basic background for the description of algorithms for the identification of the rotational dynamics of the target from trajectories of its tracked points. As shown in the section 1.2.1 two complementary datasets have been simulated. In particular, they correspond to two different estimation conditions: in a first instance, few features of the target are matched to a model of the shape of the object; in a second condition no prior information is available about the target surface, but a larger number of features are detectable. The same fundamental problem unites both the conditions, that is the impossibility of having continuity in the input data. Some temporary lacks of data must be taken into account. For instance, for the first tracking condition, the evaluation of a raw attitude signal has been possible. An example of the result of this assessment is in Fig. 3.1. However, it is evident the presence of relatively large time intervals in which no

information is available. The condition of unavailability of data is indicated in this work as occlusion.

Regardless of the tracking conditions considered, the missing attitude information will be recovered by using compressive sampling techniques, then the estimated attitude will be exploited for feeding unscented Kalman filters for the estimation of the angular rate and mass distribution of the target.

What it changes between the two different approach is the way of evaluating the raw attitude signal. Indeed, if no prior information about the shape of the target is available, it is impossible to obtain the quaternions in Fig. 3.1. This statement holds because the values of the quaternions depend on the particular considered body-fixed coordinate system, which is attached to three particular features of the target. Thus, once the tracking of these features is lost, it is also lost the information about the orientation of the system attached to them. On the contrary, in the first tracking condition, this information is obtained by the detected position of new features due to their known disposal relatively to the hidden features. These concepts are schematically illustrated in Fig. 3.2

Hence, it must be found a parameter that describes the rotation of the body, which should be independent of the particular set of considered features, but also should be computable from their trajectories. Then, the state-space model of the target dynamics has to be modified such that the relevant state observer can be fed with the new indirectly measured attitude information.

3.3.1 First approach: few known features

Equation (1.7) shows that the two opposite quaternions represent the same attitude of a body. Therefore, CS techniques described in the previous section are not directly applicable to recovery of quaternion signals (such as those represented in Fig. 3.3).

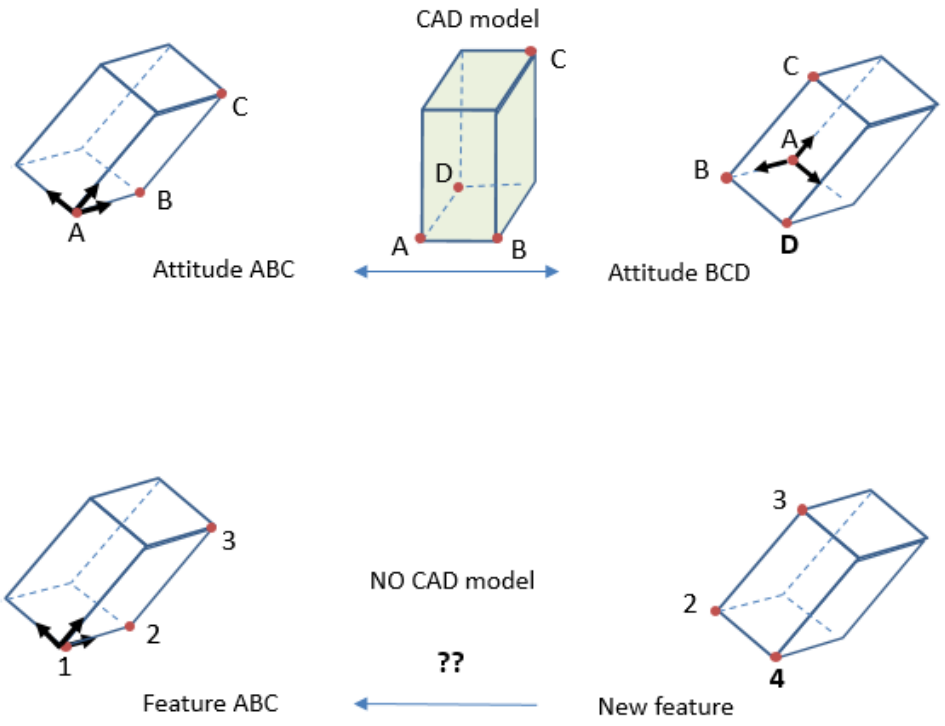

Figure 3.2 Illustration of the different implications on the proposed estimation algorithms according to the characteristics of the available set of data. If the features have correspondence with the one of a CAD model of the target, the attitude of one particular body-fixed frame is always monitored. Otherwise, other motion descriptions must be found.

Actually, the recovery of the missing samples for these kinds of signals does not, in general, lead to the restoration of a continuous attitude signal. In fact, once the sign of the first value of the quaternions is chosen, the signs of the other (subsequent) values are not freely selectable: when the signs are randomly selected, the attitude signal, in general, presents abrupt changes. However, having fixed the sign for the first value, a unique sequence of choices that leads to a smooth signal exists. In other words, the assumption concerning the sparsity of the quaternions is valid only if the sign of each value of the quaternions is properly selected. This selection is often made by exploiting known algorithms, an example of which is Stanley's algorithm that was presented in

subsection 1.1. Unfortunately, these algorithms are not applicable when the quaternions have missing samples.

The chosen approach to this problem consists of recovering all possible signals produced by all possible choices of value signs of the signals. This principle relies on the hypothesis of finding some criterion to identify the individual smooth signal that represents the body attitude.

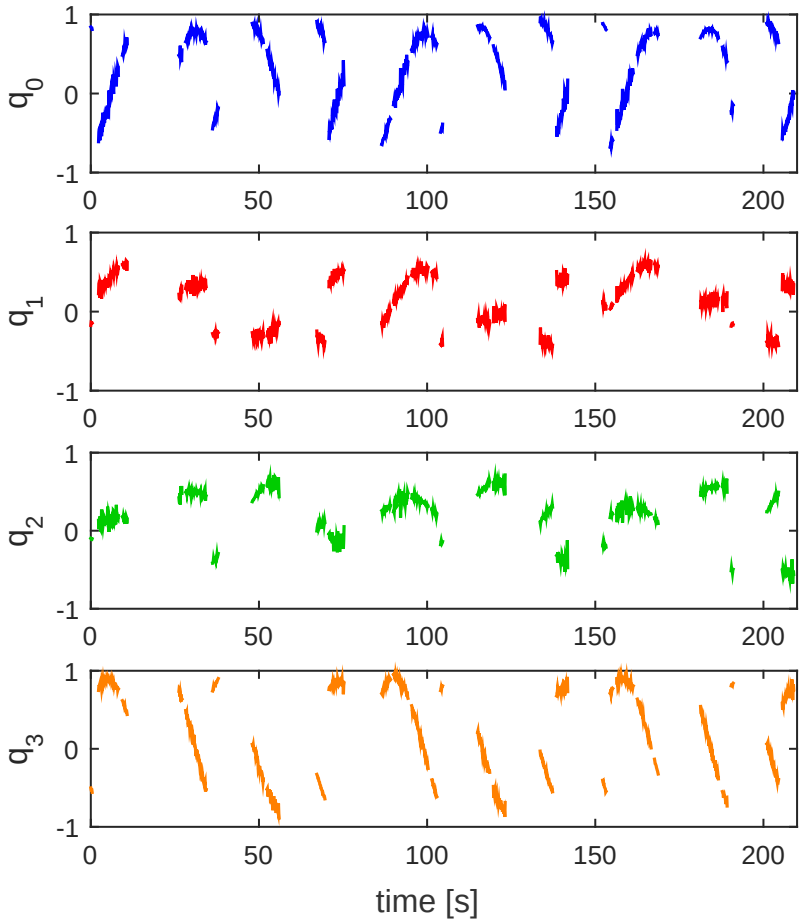

Figure 3.3 Example of raw attitude information $\left({}^{\mathcal{F}}q_I\right)$. The amplitude of the noise on the coordinates of the features has been set to 30 mm for each coordinate.

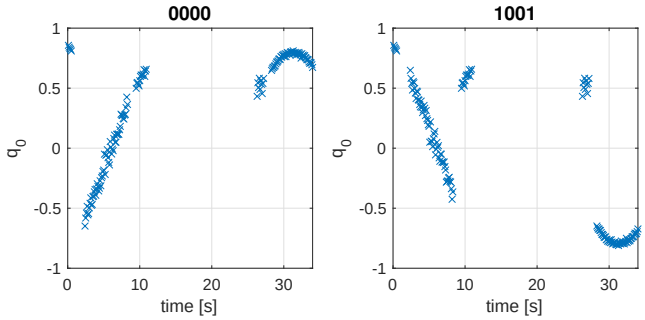

Figure 3.4 Two possible sequences of same attitude information. The signal marked with 0000 consists of the first five pieces of ${}^{\mathcal{F}}q_{I0}$ in Fig 3.3. The label 1001 indicates that the second and the last pieces have inverted signs.

The quaternion signals that have missing samples can be considered a set of N_p pieces. Excluding the first piece, all of the other pieces may be marked with a Boolean label. If no changes have been made to the sign of the values of the input pieces, all of the labels are set to zero. On the contrary, whenever a sign change affects the values of a specific piece, the Boolean label switches to one. Thus, by sorting all the $N_p - 1$ digits, a set of labels that uniquely characterizes the relationship between a general sequence and the original input sequence can be composed. An example of this labeling technique is in Fig. 3.4, where the first five pieces of ${}^{\mathcal{F}}q_{I0}$ in Fig. 3.3 are considered. The first piece has not to be taken into account. Then, in Fig. 3.4 the signal marked with 0000 is the original sequence, while the one marked with 1001 presents the second and the fifth pieces with changed signs.

Based on these considerations, note that the number of all possible different signals must be 2^{N_p-1}. These signals contain the same piece of information regarding the attitude of the body.

Once all of the signals have been recovered, we must determine which criterion can be used to identify the correct one.

For example, it can be assumed that the searched signal is the *sparsest* signal from among the recovered signals.

This assumption is supported by numerical simulations and by theoretical considerations that were discussed at the beginning of the section 3.2. Furthermore, it is intuitive that signals with abrupt variations have a more complex frequency spectrum than smooth signals. Clearly, if these variations occur because the noise has a large amplitude, the quaternions are not more sparse; however, in this case, it seems impossible to separate the attitude information from the noise using any method.

The sparsity of the h-th signal can be quantified using, for example, a penalty score calculated as follows:

$$PS = const_1 \|c_h\|_0 + const_2 \|c_h\|_1 \tag{3.96}$$

where $const_1$ and $const_2$ are two steady gains, and c_h is the vector of the coefficients of the Fourier transform of the recovered h-th signal. Any reasonable score can be used to make classifications of the signals. The score used herein has been proven to be valid using numerical simulations.

Using this principle, one can find that if the number N_p of pieces of quaternions is large, the total number of piece-wise signals that should be recovered will increase exponentially, which would make the explained idea inapplicable. For example, the quaternions shown in Fig. 3.3 present $N_p = 28$ pieces for each element, which means that the overall number of signals that should be recovered would be roughly one hundred million.

A suitable method for making the recovery procedure feasible consists of preliminarily considering a relatively small number $N'_p << N_p$ of pieces, and then, recovering all of the resulting $2^{N'_p-1}$ signals. This technique allows us to make a preliminary selection of the best signals. Once one or more signals are selected using the score in Eq. (3.96), the complete recovery is performed by adding new pieces considering both possible signs.

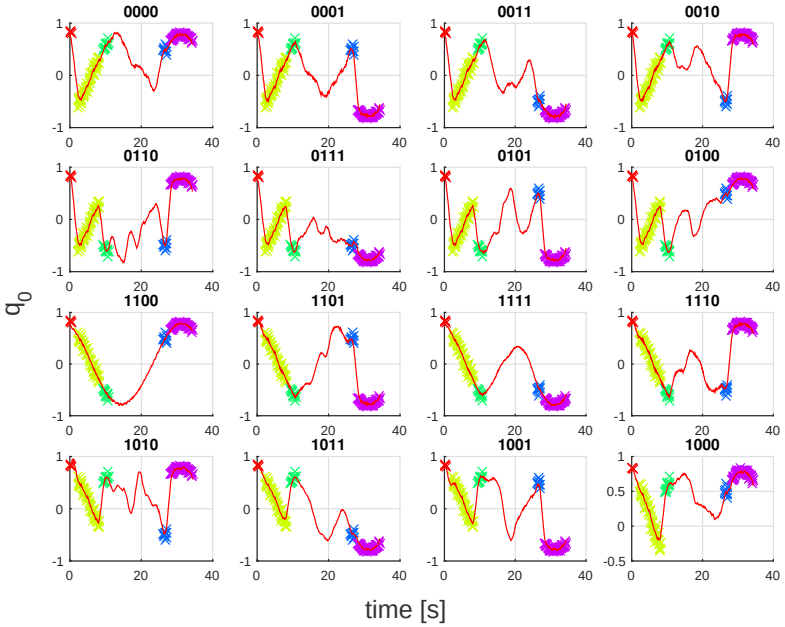

Figure 3.5 Preliminary phase, $N'_p = 5$: raw data (crosses) and recovered signal (red line).

Specifically, every intermediate recovery is followed by discarding the worst recovered signals. At the end of this procedure, only the best signal remains.

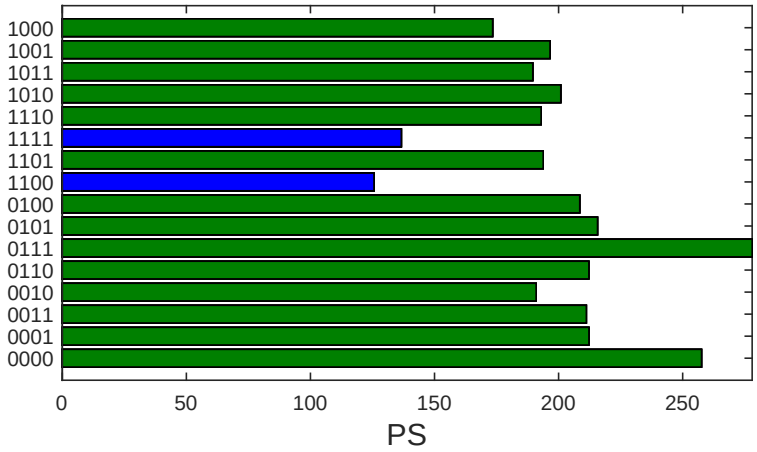

Figure 3.6 Values of penalty scores, as defined in Eq.(3.96); best recoveries in blue correspond to 1111 and 1100 label sets.

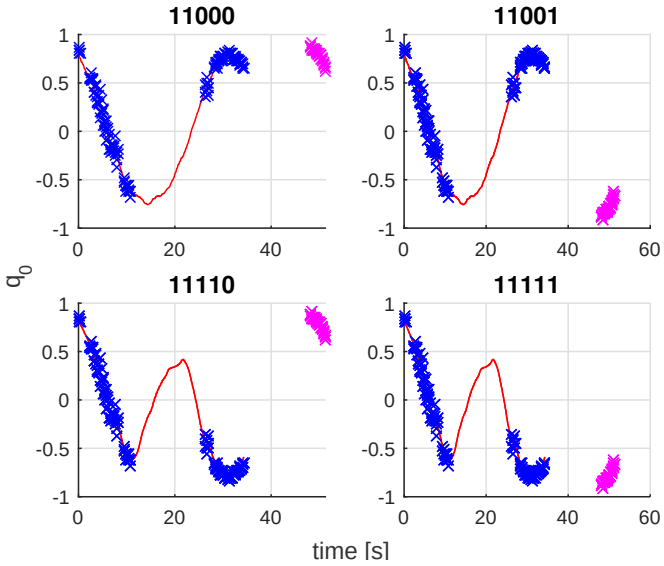

Figure 3.7 Introduction of a new piece of quaternion: the component is added to the best recovered signals with opposite sign.

Considering the quaternions shown in Fig. 3.3, a number $N'_p = 5$ pieces of ${}^{\mathcal{F}}q_{0I}$ is considered. Note that the number N'_p cannot be excessively low because insufficient information concerning measurements leads to poor preliminary recovery. In Fig. 3.5 recovery for sixteen signals is shown. Each signal is characterized by a set of boolean labels that specifies the relationship between the signal itself and the original input, marked with 0000.

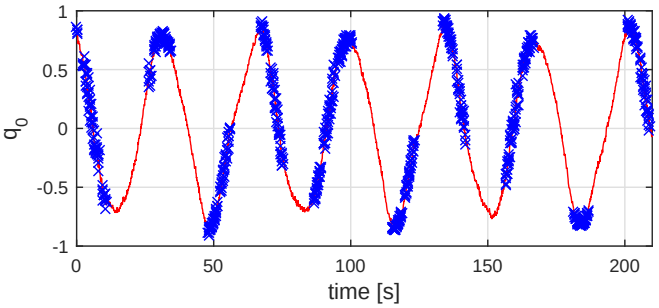

Figure 3.8 Final best recovery of the quaternion ${}^{F}q_I$: raw data (blue crosses) and recovered signal (red line).

In Fig. 3.6, a bar chart showing the penalty scores for the recovered signals is presented. Intuitively, the sparsest recovered signals are those marked with 1100 and 1111 (see also Fig. 3.5). However, it was challenging to predict which of the two signals was actually the best. Therefore, they are both preserved for the next phase, in which the 6-th piece of ${}^{\mathcal{F}}q_{0I}$ is added to the two best-recovered signals (see Fig. 3.7 for example).

The new signals could be recovered using the same method as employed in the preliminary phase. Therefore, a new score calculated using Eq. (3.96) can be associated with each recovered sequence so as to eliminate the worst cases. This process can be stopped when all of the available input data are exploited. The complete recovered ${}^{\mathcal{F}}q_{0I}$ signal is shown in Fig. 3.8. Notice that the recovery is completely automated and doesn't need any external supervision.

Figure 3.9 depicts the complete recovery of four different quaternion signals derived from distinct sets of initial angular rates and inertial properties of the benchmark space-

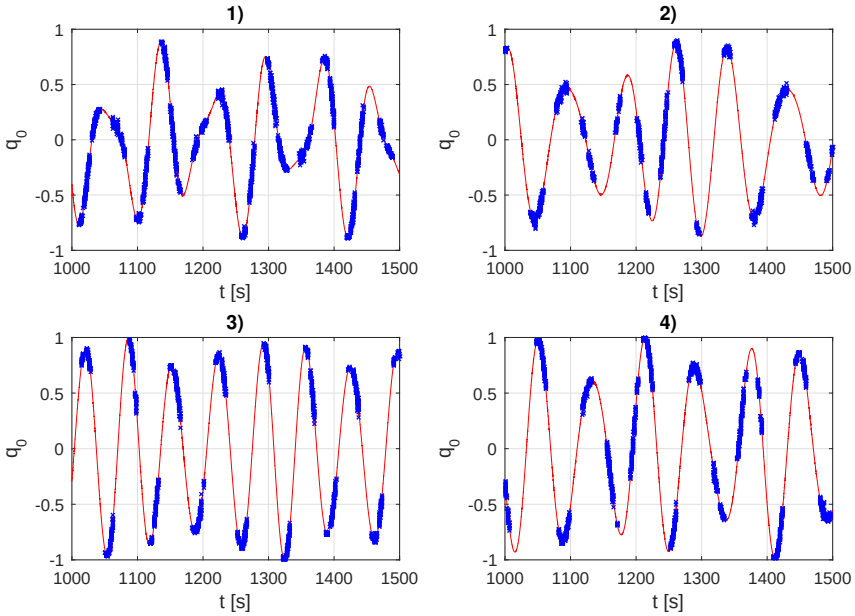

Figure 3.9 Attitude recovery performed for different target conditions (see Tab. 3.1).

CaseID	${}^{B}J_1$	${}^{B}J_2$	${}^{B}J_3$	${}^{B}\omega_{01}$	${}^{B}\omega_{02}$	${}^{B}\omega_{03}$	ε_θ
1)	0.618	0.707	0.345	7.200	5.525	-1.624	0.503
2)	0.601	0.446	0.664	8.400	-0.263	2.860	0.508
3)	0.657	0.489	0.574	7.200	5.914	6.023	0.585
4)	0.518	0.461	0.720	6.000	6.600	4.440	0.591
M. unit:	[-]	[-]	[-]	[deg/s]	[deg/s]	[deg/s]	[deg]

Table 3.1 Attitude error for different dynamic conditions of the target (algorithm's output in fig. 3.9); the standard deviation of the measurement noise is equal for each coordinate to 50 mm.

craft. Each simulation ran for 1500 s. Only the final parts of the signals are shown for better illustrating the output quality. For these cases, the standard deviation of the noise added to the feature coordinates increased to 50 mm for assessing the robustness of the algorithm.

Parameters that characterize each of the cases are in Tab. 3.1. The latter table presents also root-mean-square errors ε_θ (RMSE) for each attitude recovery. The attitude estimation error e_θ was defined by the following expressions:

$$\delta q = q \otimes \hat{q}^{-1} \tag{3.97}$$

$$e_\theta = 2\cos^{-1}(\delta q_0) \tag{3.98}$$

where $\hat{q}$ is the estimated quaternion, and $\otimes$ is the symbol employed to identify quaternion multiplication (see Appendix B.1). Due to the complete generality of Eq. (3.97), no indications about coordinate systems are given.

Table. 3.2 illustrates the RMSE for other six different recoveries. The graphical outputs regarding these last scenarios are not shown since they do not provide remarkable information for a deeper understanding of the algorithm capabilities.

CaseID	${}^{B}J_1$	${}^{B}J_2$	${}^{B}J_3$	${}^{B}\omega_{01}$	${}^{B}\omega_{02}$	${}^{B}\omega_{03}$	ε_θ
5)	0.295	0.781	0.551	7.200	0.253	-13.198	0.565
6)	0.531	0.473	0.703	8.400	0.545	0.458	0.577
7)	0.719	0.658	0.224	6.600	1.296	9.557	0.470
8)	0.745	0.512	0.427	6.000	-7.620	12.000	0.482
9)	0.742	0.521	0.421	-3.000	4.800	-2.700	0.686
10)	0.371	0.743	0.557	3.000	-4.800	-2.100	0.555
M. unit:	[-]	[-]	[-]	[deg/s]	[deg/s]	[deg/s]	[deg]

Table 3.2 Attitude error for different dynamic conditions of the target; the standard deviation of the measurement noise is equal for each coordinate to 50 mm.

From a brief analysis of the data presented in Tab. 3.1 and in Tab. 3.2 it appears that attitude estimation errors are in the order of $5 \cdot 10^{-1}$ deg. In particular, the mean value of RMSE in the considered cases is equal to 0.552 deg, while the error range is from 0.470 deg to 0.686 deg

Making, for instance, a comparison with the method presented in [19] that, although is a very effective method, is not fault-tolerant, the errors made in estimating attitude are comparable. In [19], the noise on the feature coordinates is dependent on the relative position between chaser and target. Indeed, the noise is added at the camera's image plane level. Two extremal noise conditions were examined. In particular, they considered noise standard deviations equal to 10^{-4} and 10^{-5}. As seen in Fig. 1.14 and in Fig. 1.13, these two values correspond approximately to standard deviations equal to 100 mm and 10 mm for the depth coordinate, which is the most affected by noise. With the first condition, the obtained attitude errors have been under 2.5 deg, while with the second one, the errors have decreased to 2×10^{-1} deg.

On the other hand, the attitude recovery method proposed in this work provides, before making use of state observers, attitude errors that are in the order of 5×10^{-1} deg, having 50 mm of noise amplitude at coordinate level. After a comparison with the

current state of the art, this result is quite encouraging to future practical applications of this method.

Finally, certain considerations regarding the sample period should be made: the value strictly depends on the type of sensor chosen for tracking the features of the body. The recovery is reliable if the sampling frequency is sufficiently higher than the highest significant frequency in the quaternion signal. Most torque-free space bodies have a slowly oscillating attitude; thus, tracking sensors such as simple cameras often have a high acquisition frequency. For example, a sampling frequency equal to 1 Hz is considered sufficient, while a point tracking system can operate even up to $30-50$ Hz.

The estimation of the rate from attitude information, *i.e.*, from Eq. (1.8), requires the evaluation of the quaternion's derivative. Numerically performing the derivative of the estimated signal produces unacceptable results because the recovered attitude signal still contains high-frequency noise, which is drastically amplified in the numeric derivative. For solving this issue, an unscented Kalman filter was implemented. The discrete-time nonlinear dynamic system,

$$x_{k+1} = f(x_k) + w_k = x_k + \Delta t \begin{bmatrix} \frac{1}{2}\,{}^{B}W_k\left({}^{B}\boldsymbol{\omega}_k\right){}^{B}q_{Ik} \\ 0_{4\times 1} \\ \operatorname{diag}\left({}^{B}\boldsymbol{J}_k\right)^{-1}\left[{}^{B}\boldsymbol{\omega}_k \times \left(\operatorname{diag}\left({}^{B}\boldsymbol{J}_k\right){}^{B}\boldsymbol{\omega}_k\right)\right] \\ 0_{3\times 1} \end{bmatrix} + w_k \tag{3.99}$$

$$z_k = h(x_k) + v_k = {}^{\mathcal{F}}q_{Bk} \otimes {}^{B}q_{Ik} + v_k \tag{3.100}$$

served as framework for the UKF. In Eq. (3.99) the state vector

$$x_k = \begin{bmatrix} {}^{B}q_{Ik} & {}^{\mathcal{F}}q_{Bk} & {}^{B}\boldsymbol{\omega}_k & {}^{B}\boldsymbol{J}_k \end{bmatrix}^T$$

contains: the unit quaternion ${}^{B}q_{Ik}$ that describes the relative attitude between the principal body frame B and the inertial frame I; the offset quaternion ${}^{B}q_{\mathcal{F}k}$ that describes the relative

attitude between the body frame $\mathcal{F}$ attached to the features and B; the angular velocity ${}^{B}\boldsymbol{\omega}$ of the body frame with respect to B; the column array ${}^{B}\boldsymbol{J}$ which entries are the normalized principal moments of inertia of the target body. Moreover, Δt indicates the time step, and w_k is the process noise.

The state equations for the UKF have been derived from Eq. (1.6), Eq. (1.9), and the conservation of the principal inertia moments. Clearly, also the offset quaternion must be constant.

Regarding Eq. (3.100), $z_k = {}^{\mathcal{F}}q_{Ik}$ is the measurement vector (the recovered quaternions), the operator $\otimes$ represents the quaternion multiplication, and v_k is the measurement noise.

The prediction and updating scheme of the UKF were detailedly described in section 3.1.2. In particular the chosen set of sigma points is the one in Eq. (3.50). Thus the spherical simplex unscented transform was employed.

Note that because of the chosen state-space model of the system, at each completion of the updating phase, the principal moments of inertia are normalized as well as the quaternions involved. This *brute-force* operation for preserving quaternion norm is not the most elegant approach but is proven to work generally well [59], [60].

An example of the final result of Kalman filtering the surrogate quaternion measurements is depicted in Fig. 3.10: the components of the estimated angular rate are compared to the ones obtained via simulation of the target attitude dynamics (see Appendix B.2). The four results refer to the scenarios listed in Tab. 3.1. The estimated values of the normalized inertia moments are shown in Fig. 3.11. The latter part of the figure puts in evidence the simulated time needed by the observer to approximately learn the actual inertia ratios. The estimation error is directly reflected into the accuracy in identifying the angular rate and attitude. Notice that the mentioned time is different in each case, and goes from 250 s (case 4) to 550 s (case 3, which seems to be the worst).

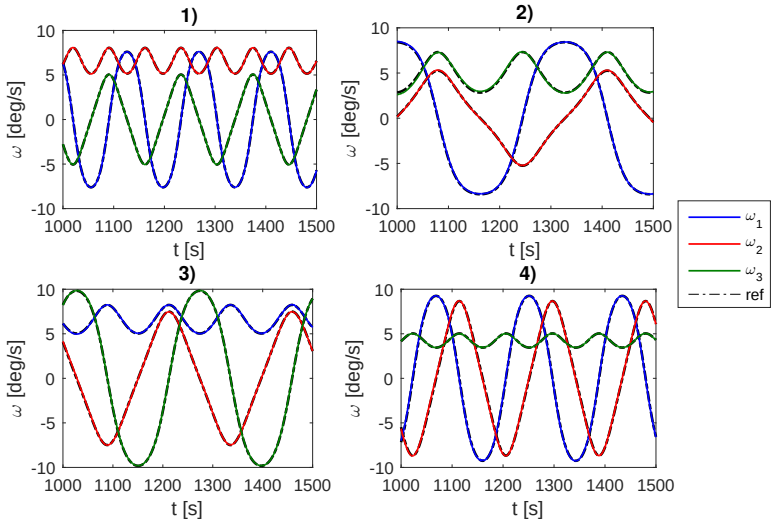

Figure 3.10 Final estimation of the angular rate after Kalman filtering the recovered quaternions in fig 3.9. Reference values of the angular rate components are represented by dashed lines.

.

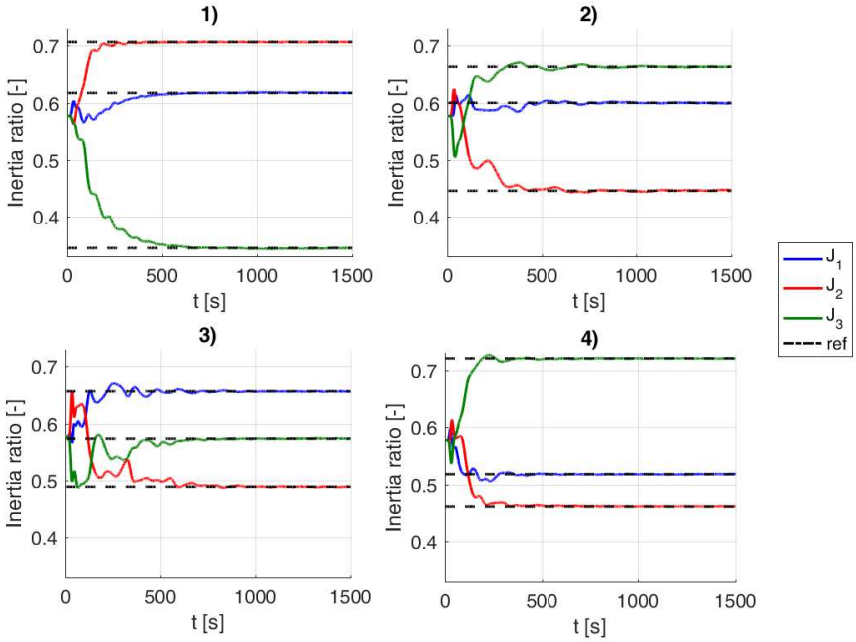

Figure 3.11 Final estimation of the relative values of the principal moments of inertia after Kalman filtering the recovered quaternions in fig 3.9. Reference values are represented by dashed lines.

CaseID	ε_{ω_1}	ε_{ω_2}	ε_{ω_3}	ε_{θ}
1)	0.029	0.015	0.019	0.187
2)	0.080	0.036	0.098	0.203
3)	0.032	0.045	0.036	0.275
4)	0.093	0.085	0.016	0.139
5)	0.048	0.092	0.118	0.363
6)	0.053	0.099	0.036	0.398
7)	0.016	0.015	0.048	0.181
8)	0.017	0.041	0.051	0.171
9)	0.030	0.038	0.041	0.406
10)	0.008	0.016	0.065	0.176
M. unit:	[deg/s]	[deg/s]	[deg/s]	[deg]

Table 3.3 Angular rate and attitude estimation error after Kalman filtering; standard deviation of the measurement noise is equal for each coordinate to 50 mm.

The estimation algorithm was also applied to the other recovered quaternions corresponding to scenarios listed in Tab. 3.2. To show the performances of the whole approach, the final RMSE concerning the estimated attitude and each component of the estimated rate, are listed in Tab. 3.3. These values were evaluated after the Kalman filter convergence.

Analyzing the data shown in Tab. 3.3 it appears that the errors in the angular rate estimation are approximately between 10^{-2} deg/s and 10^{-1} deg/s. Thus, the results obtained with the presented algorithm are again comparable with the results obtained in [19]. In such work, the angular rate estimation error was assessed between 10^{-2} deg/s and 10^{-1} deg/s. However, these values have been obtained starting from data affected by the minimum considered noise amplitude (10^{-5}). In the presented work a 50 mm noise amplitude was taken into account at coordinate level.

From Tab. 3.3, a new mean value of the attitude error was evaluated (0.3 deg). As expected, the attitude estimation accuracy has been further improved after the non-linear Kalman filtering stage.

CaseID	${}^{B}J_1$	${}^{B}J_2$	${}^{B}J_3$	$\Delta {}^{B}\bar{J}_1$	$\Delta {}^{B}\bar{J}_2$	$\Delta {}^{B}\bar{J}_3$
1)	0.6177	0.7068	0.3448	0.0000	0.0000	-0.0001
2)	0.6005	0.4462	0.6635	-0.0008	0.0013	-0.0001
3)	0.6570	0.4890	0.5738	-0.0001	-0.0001	0.0002
4)	0.5180	0.4614	0.7203	0.0000	0.0002	-0.0001
5)	0.2952	0.7806	0.5510	0.0016	-0.0026	0.0028
6)	0.5309	0.4729	0.7032	0.0004	0.0011	-0.0010
7)	0.7195	0.6575	0.2237	0.0030	-0.0029	0.0006
8)	0.7452	0.5123	0.4269	0.0002	-0.0001	-0.0003
9)	0.7421	0.5215	0.4212	-0.0003	-0.0013	0.0022
10)	0.3714	0.7428	0.5571	0.0032	0.0000	-0.0022
M. unit:	[-]	[-]	[-]	[-]	[-]	[-]

Table 3.4 Nominal normalized principal moments of inertia and difference beetwen nominal value and estimation after convergence

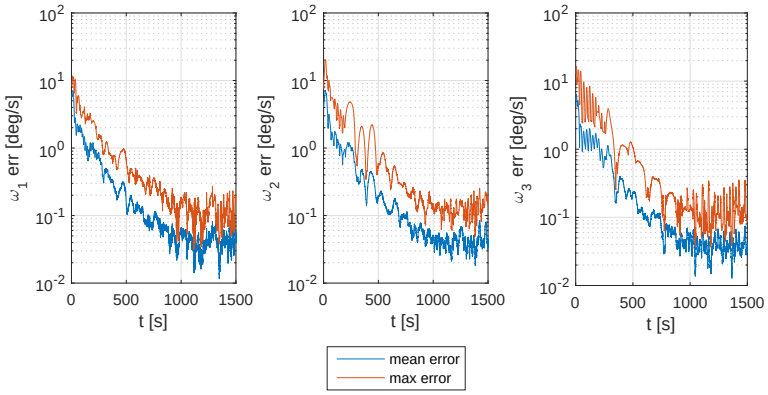

Figure 3.12 Mean and maximum estimation error for each angular rate component; the UKF converges at about 1000 seconds

.

The mean estimated normalized principal moments of inertia after convergence $\bar{\boldsymbol{J}}$ are compared to the reference values in table 3.4. The error in the inertia moment estimation varies from 10^{-5} to 3.2×10^{-3}. The mean error equals 9.6×10^{-4}.

Finally, to show the convergence properties of the designed unscented Kalman filter, the time behavior of mean and maximum angular rate estimation error in the considered

scenarios is illustrated in Fig. 3.12. From the latter figure it can be noted that the error level stabilizes at about 1000 s.

3.3.2 Second approach: no shape information

The assumption of having a model of the target object, for instance, a CAD (Computer aided design) drawing, is realistic for certain cases. When the objects of interest are fragmentation debris or foreign failed satellites, the mentioned knowledge must be excluded. Moreover, mapping the in-situ detected features with the ones of the model requires non-straightforward algorithms subjected to errors whose final effect is an increase of the uncertainties on input data.

For those reasons, the development of a more general methodology remains a pressing demand. As seen in the previous subsection, the knowledge of shape information regarding the target allowed for the indirect measurement of the orientation of one particular coordinate system that remains fixed to the body (see Fig. 3.2). This attitude information is fundamental for the estimation of the dynamic rotational state of the object.

The second approach discussed in subsection 1.2.1 consists in considering the 44 features in Fig. 1.6. However, all of them are not visible at the same instant. In particular,

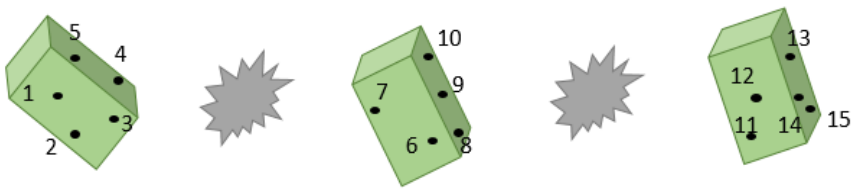

Figure 3.13 Appearing and disappearing features typical of the second approach. Features 4 and 5 coincides with 6 and 7. The same holds for 1,2 and 3, which are the same of 13, 14 and 15. However, no algorithm is exploited to recognize this fact. Occlusions contributes to this problem.

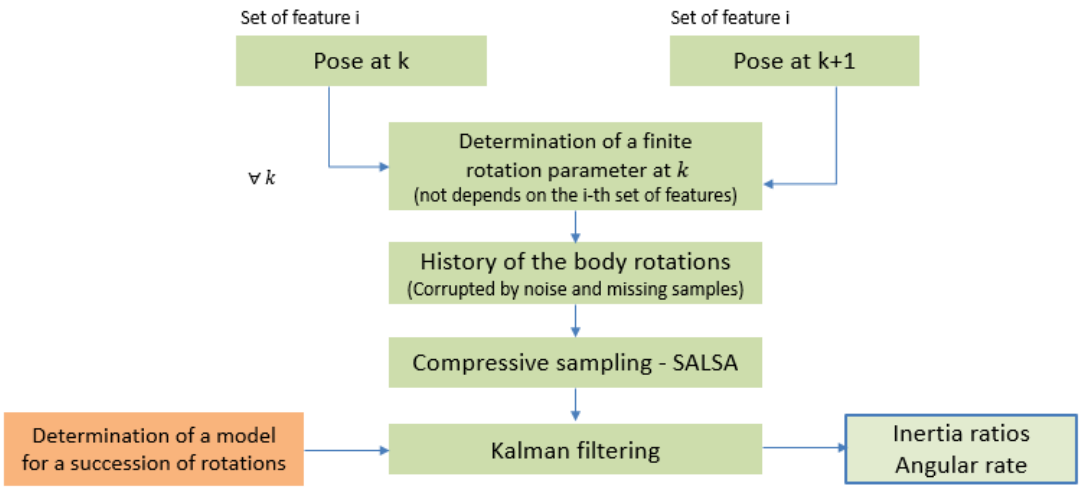

Figure 3.14 Flow-chart describing the second estimation approach of the target rotational dynamics

every time a feature appears in the field of view of the observer, the feature is marked as a new one (see Fig. 3.13).

Then, once prior information regarding the target shape is not available, it arises the necessity of a more global description of the finite rotations of the body. These rotations occur between the poses that the target takes at each sample of the observation time. Once an appropriate parameter is found, this should be evaluated from the detected trajectories of features. At the same time, evidently, the parameter must be independent by the considered set of features for its evaluation. Moreover, the evaluated parameter will be necessarily corrupted by noise and missing samples. Thus, if it is sparse, the evaluated parameter should be preprocessed via CS techniques (see section 3.2). Finally, a state observer can be designed to estimate the global rotational state of the target. This procedure, whose details will be given next, is resumed by the flow chart in Fig.3.14

Characterizing finite rotations from the noisy positions of a homologous point set requires a consistent dimensionality of the set, at least for having an acceptable accuracy. The number of points that could be tracked with well-known optical flow techniques,

like the ones inspired by the work in [61], is typically very high. Moreover, the tracked points do not need to be matched with the features of the model. Thus, the 44 points shown in Fig. 1.6 do not have to correspond to natural features of the object for being realistically detected by a pair of cameras.

The rotational motion of the target could be characterized from the set of homologous feature by using some statements of the theory of rigid motions. As seen in chapter 2, The Mozzi-Chasles' theorem states that the most general rigid body movement is produced by a translation along an axis, called screw axis, and a rotation about that axis [33]. Then, the displacement of any set of features may be represented according to these two basic isometries:

$$ {}^{C}\boldsymbol{\rho}_i' = {}^{C}\boldsymbol{\rho}_i + {}^{C}\boldsymbol{t} + R_{\hat{\boldsymbol{e}},\alpha}\left({}^{C}\boldsymbol{\rho}_i - {}^{C}\boldsymbol{\rho}_g\right) \tag{3.101} $$

where ${}^{C}\boldsymbol{\rho}_g$ designates the position of the centroid of the set, while the symbol $(\prime)$ indicates that the entity refers to the displaced pose of the body. Equation (3.101) presents an optimization program in the variables ${}^{C}\boldsymbol{t}$, which is the translation vector aligned with the Euler's axis $\hat{\boldsymbol{e}}$, and $R_{\hat{\boldsymbol{e}},\alpha}$, which is the matrix representing the body rotation through the Euler's angle α about $\hat{\boldsymbol{e}}$.

It is evident that the parametrization consisting of ${}^{C}\boldsymbol{t}$ and $R_{\hat{\boldsymbol{e}},\alpha}$ is highly redundant. However, note that the actual values of these parameters are not dependent by the considered set of features, but they characterize the displacement of any possible sets.

A similar but more compact parametrization is obtainable by following the approach in [35]: the main idea that characterizes the latter part of the cited work is that finite displacements are the result of the sum of infinitesimal displacements. Thus, similarities between expressions that describe finite and infinitesimal motions should hold.

The so-called kinematic fundamental formula, which is shown below, is the generalization of Eq. (3.101) for infinitesimal displacements:

$$\dot{\boldsymbol{\rho}}_i = \dot{\boldsymbol{\rho}}_g + \boldsymbol{\omega} \times \left(\boldsymbol{\rho}_i - \boldsymbol{\rho}_g\right) = \dot{\boldsymbol{\rho}}_g + \boldsymbol{\omega} \times \boldsymbol{d}_i \tag{3.102}$$

where $\boldsymbol{d}_i$ is the vector connecting the centroid of the set to the i-th feature belonging to the set. Prescript C is removed for increasing readability. Indeed, Eq. (3.102) with all the following expressions will have a general validity in any reference frame.

Angular rate $\boldsymbol{\omega}$ is a very concise parameter for describing the infinitesimal rotational motion of the object. $\boldsymbol{\omega}$ does not depend on the velocity of the features but characterize their speed and position. There is no possibility of finding $\boldsymbol{\omega}$ directly from the location of the features, but also the knowledge of their velocity is necessary. However, Eq. (3.102) do not represent the unique source for identifying the angular rate.

The following equation gives the definition of the angular momentum of a set of unit point masses:

$$\sum_i \boldsymbol{d}_i \times \dot{\boldsymbol{\rho}}_i = J_g \boldsymbol{\omega} \tag{3.103}$$

where J_g is the inertia matrix of the feature set with respect to the centroid of the set. In particular, it holds:

$$J_g = \begin{bmatrix} \sum_i \left(d_{2_i}^2 + d_{3_i}^2\right) & -\sum_i d_{1_i} d_{2_i} & -\sum_i d_{1_i} d_{3_i} \\ -\sum_i d_{1_i} d_{2_i} & \sum_i \left(d_{1_i}^2 + d_{3_i}^2\right) & -\sum_i d_{2_i} d_{3_i} \\ -\sum_i d_{1_i} d_{3_i} & -\sum_i d_{2_i} d_{3_i} & \sum_i \left(d_{1_i}^2 + d_{2_i}^2\right) \end{bmatrix} \tag{3.104}$$

Hence, the angular rate of a rigid body may be obtained directly from Eq. (3.103), if positions and velocities of some features are known. Actually, if uncertainties affect the data, only an approximation of the real angular rate of the body will be provided. Indeed, due to the uncertainties, the detected features do not belong rigorously to a rigid body. Therefore, the higher the number of the detected features, the more the accuracy of the angular rate estimation. This statement has been demonstrated, for instance, in [62].

Nevertheless, it is needed to find similar expressions for finite displacements. Evidently, the composition of finite movement cannot be obtained via simple addition:

$$\Delta\boldsymbol{\rho}_i \neq \Delta\boldsymbol{\rho}_g + \alpha\hat{\boldsymbol{e}} \times \boldsymbol{d}_i \tag{3.105}$$

where $\Delta\boldsymbol{\rho}_i = \boldsymbol{\rho}'_i - \boldsymbol{\rho}_i$. However, one of the expressions of the famous Rodrigues's rotation formula [63] for spherical displacements states:

$$\boldsymbol{d}'_i - \boldsymbol{d}_i = \tan\left(\frac{\alpha}{2}\right)\hat{\boldsymbol{e}} \times \left(\boldsymbol{d}'_i + \boldsymbol{d}_i\right) \tag{3.106}$$

In a complete analogy with the fundamental formula in Eq. (3.102), the expression in Eq. (3.106) reveals the existence of an intrinsic description of the finite rotation of a rigid body between two poses. In Eq. (3.106), the *Gibbs representation* of the axis-angle parametrization $\boldsymbol{\Omega} = \tan(\alpha/2)$ do not depend on the features. Moreover, from the definition of the vector $\boldsymbol{d}_i$, it is possible to recast Eq. (3.106) in a form that is completely similar to both Eq. (3.105) and Eq. (3.102):

$$\Delta\boldsymbol{\rho}_i = \Delta\boldsymbol{\rho}_g + \boldsymbol{\Omega} \times \left(\boldsymbol{d}'_i + \boldsymbol{d}_i\right) \tag{3.107}$$

Therefore, it is possible to define a quantity that is very similar to the angular momentum vector defined by Eq. (3.103):

$$\sum_i \left(\boldsymbol{d}'_i + \boldsymbol{d}_i\right) \times \Delta\boldsymbol{\rho}_i = J''_g \boldsymbol{\Omega} \tag{3.108}$$

where J''_g have a similar structure to J_g in Eq. (3.104), but the components of the vector $\boldsymbol{d}_i$ are substituted by the components of the vector $\boldsymbol{d}'_i + \boldsymbol{d}_i$. The quantity $J''_g/2$ may be physically interpreted as the inertia matrix of a virtual body whose contour is defined by the midpoints of segments connecting the homologous points after and before the displacement. $\Delta\boldsymbol{\rho}_i/2$ is interpretable as a virtual displacement corresponding to the half of the real displacement of each feature. Thus, eventually, the quantity $\left(\boldsymbol{d}'_i + \boldsymbol{d}_i\right)/2$ is the vector from the centroid of the virtual body to the virtually displaced i-th feature.

With this interpretation, Eq. (3.107) for the virtual body is totally equivalent to Eq. (3.102) for the real body. Thus, the vector $\boldsymbol{\Omega}$ results aligned with the instantaneous rotation axis of the virtual body.

The vector $\boldsymbol{\Omega}$ is easily obtainable from Eq. (3.108) through the knowledge of the positions of homologous features at two adjacent time samples. An example of the evaluation of $\boldsymbol{\Omega}$ is given in Fig. 3.15; the relevant dynamic conditions of the target are the one illustrated in subsection 1.2.1. Occlusion periods having a duration of 60 seconds were introduced with a regular frequency.

The equations presented in this subsection showed the equivalence between the angular rate and the Gibbs representation of attitude. The sparsity of the angular rate was discussed in the previous subsection. Thus, it is considerably reasonable to assume that $\boldsymbol{\Omega}$ is sparse in the frequency domain. Indeed, Fig. 3.15 shows the periodicity of the signal $\boldsymbol{\Omega}$.

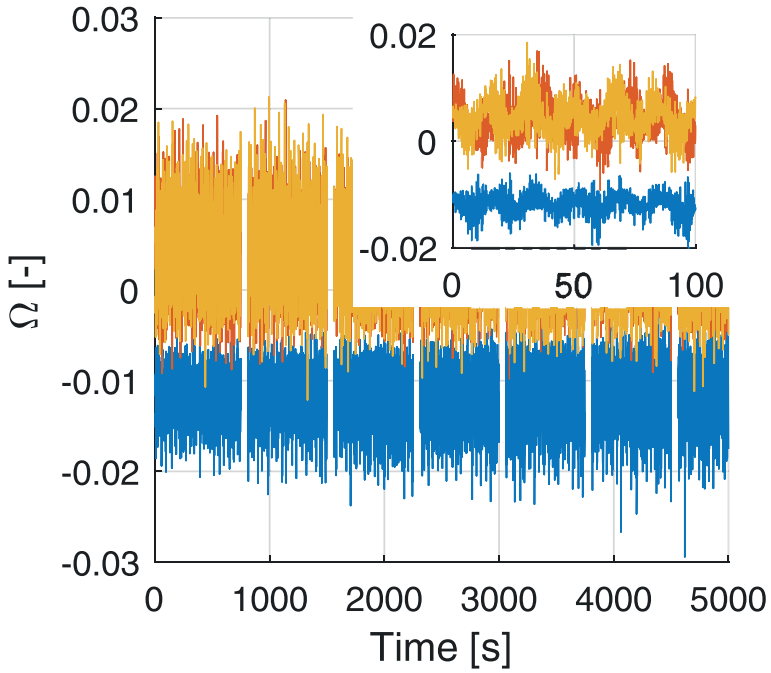

Figure 3.15 Raw $\boldsymbol{\Omega}$ from trajectories of features. A local zoom on the time axis reveals the periodicity and the sparsity of the signal

In the previous subsection, CS techniques were exploited to recover a partial and noisy attitude signal. In this case, $\boldsymbol{\Omega}$ do not represent the orientation of a body-fixed coordinate system. On the contrary, it represents finite rotations of a body-fixed coordinate system. These finite rotations are represented without ambiguity because only three parameters describe them. Hence, the recovery of the missing samples on the signal $\boldsymbol{\Omega}$ can be performed by directly applying the theory shown in section 3.2.

The recovery of the signal in Fig. 3.15 with SALSA (see subsection 3.2.2) is illustrated in Fig. 3.16

The recovered $\boldsymbol{\Omega}$ represents the rotational motion of the observed object. In particular, each sample of the signal represents an attitude change of any body-fixed reference frame. Both angular rate and mass distribution of the body influence the values of $\boldsymbol{\Omega}$.

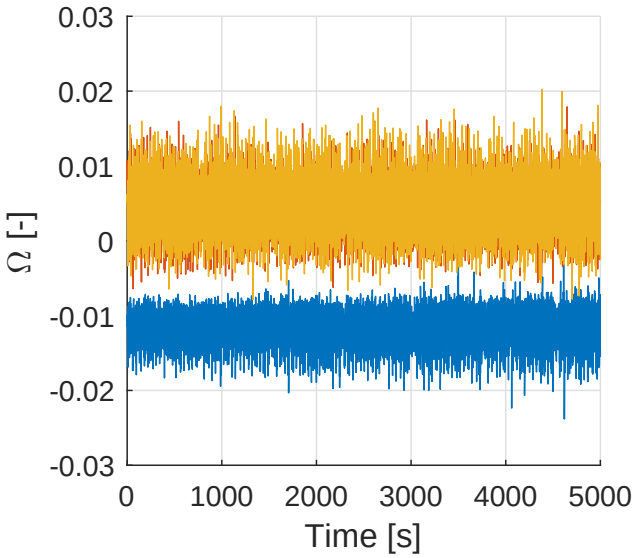

Figure 3.16 Recovered $\boldsymbol{\Omega}$: the amplitude of the signal is slightly decreased due to the reduction of the noise power. The signal does not present missing samples.

Thus, the state vector

$$x = \begin{bmatrix} {}^{I}\boldsymbol{\Omega}^{T} & {}^{B}\boldsymbol{\omega}^{T} & {}^{B}\boldsymbol{J}^{T} \end{bmatrix}^{T}$$

can be observed starting from the measured values of ${}^{I}\boldsymbol{\Omega}$. For that purpose, a UKF was designed. Note that the orientation of the frame C, in which the Gibbs representation of the Euler's axis and angle is evaluated, is the same of the frame I by construction.

The discrete nonlinear state-space model, which serves as the framework for the UKF, is introduced by the evaluation of the new finite rotation as a function of the angular rate. First of all, an attitude variation in terms of quaternions should be calculated:

$${}^{I}\delta q_k = \begin{bmatrix} \cos\left(\frac{\alpha_k}{2}\right) & e_{1_k}\sin\left(\frac{\alpha_k}{2}\right) & e_{2_k}\sin\left(\frac{\alpha_k}{2}\right) & e_{3_k}\sin\left(\frac{\alpha_k}{2}\right) \end{bmatrix} \tag{3.109}$$

Remember that ${}^{I}\boldsymbol{\Omega}_k = \tan(\alpha_k/2)\,{}^{I}\hat{\boldsymbol{e}}_k$. Considering the prior attitude of the body in terms of quaternions, it holds:

$$^{B}q_{I_k} = {}^{I}\delta q_k \otimes {}^{B}q_{I_{k-1}} \tag{3.110}$$

The prediction of the attitude at $k+1$ is performed by using a discretized form of Eq. (1.6):

$$^{B}q_{I_{k+1}} = {}^{B}q_{I_k} + \frac{1}{2}\Delta t\, {}^{B}W_k\, {}^{B}q_{I_k} \tag{3.111}$$

Then, one can obtain a predicted attitude variation:

$$^{I}\delta q_{k+1} = \left({}^{B}q_{I_k}\right)^{-1} \otimes {}^{B}q_{I_k+1} = \left({}^{B}q_{I_k}\right)^{-1} \otimes \left({}^{B}q_{I_k} + \frac{1}{2}\Delta t\, {}^{B}W_k\, {}^{B}q_{I_k}\right) \tag{3.112}$$

Because of the structure of ^{B}W in Eq. (1.6), it is straightforward to verify that it holds:

$$^{I}\delta q_{k+1} = \pm \begin{bmatrix} 1 \\ -\frac{\Delta t}{2}\, {}^{B}\boldsymbol{\omega}_k \end{bmatrix} \tag{3.113}$$

Thus, the predicted attitude variation $^{I}\delta q_{k+1}$ can be easily converted into its Gibbs representation:

$$^{I}\boldsymbol{\Omega}_{k+1} = \frac{{}^{I}\delta \boldsymbol{q}_{k+1}}{{}^{I}\delta q_{0k+1}} = -\frac{\Delta t}{2}\, {}^{B}\boldsymbol{\omega}_k \tag{3.114}$$

The prediction scheme of $^{I}\boldsymbol{\Omega}_{k+1}$ is resumed by the flow chart in Fig. 3.17

Equation (3.114) can be combined with a discretized form of Eq. (1.9) and with the conservation of the principal moments of inertia to form state equations for the target rotational dynamics:

$$x_{k+1} = x_k + \Delta t \begin{bmatrix} -\frac{1}{2}\,{}^{B}\boldsymbol{\omega}_k \\ \operatorname{diag}\left({}^{B}\boldsymbol{J}_k\right)^{-1}\left[{}^{B}\boldsymbol{\omega}_k \times \left(\operatorname{diag}\left({}^{B}\boldsymbol{J}_k\right){}^{B}\boldsymbol{\omega}_k\right)\right] \\ 0_{3\times 1} \end{bmatrix} + w_k \tag{3.115}$$

Then, the measurement equations:

$$z_k = {}^{I}\boldsymbol{\Omega}_k + v_k \tag{3.116}$$

complete the framework of the designed UKF. As mentioned in the previous subsection, it is advantageous that quaternions do not appear explicitly in the state vector. If quaternions represent the attitude, the classic update phase typically leads to a violation of their unit norm constraint. On the other hand, other constraint-free attitude representations are

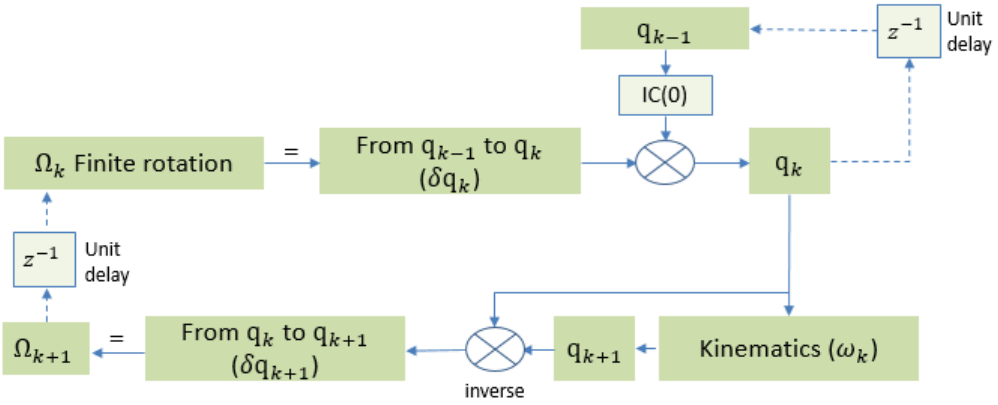

Figure 3.17 Prediction scheme of ${}^{I}\boldsymbol{\Omega}_{k+1}$.

not recommended due to the well-known *gimbal-lock* singularity (for instance, see Eq. (1.5)). [60] is one of the works that treat this topic in detail.

Actually, there is a condition in which the vector ${}^{I}\boldsymbol{\Omega}$ can assume values that are not finite. That is clearly the case of a rotation angle $\alpha = \pi/2$. However, if Δt is reasonably small, this opportunity seems to be inconsistent.

Concerning the current state of the art, the proposed framework for the UKF is original, and its strength lies in using finite rotations for representing attitude kinematics, instead of orientation parameters. Using finite rotations leads to avoiding singular attitude representations; moreover, there are no redundant attitude parameters, so it is not necessary to manage constraint violations. Besides, it is worth noticing that (Eq.3.114) is compact and in analogy with Eq.(1.5) when little rotations occur. Finally, the proposed approach allows to overcome the main limits of the other two shown methods:

- quaternions are redundant, and a normalization step has to be applied to the output of the filter, that produce singular state covariance matrix;
- Euler angles are not redundant but the solution of Eq.(1.5) can be singular; a linearized formulation would exclude singularities but is not applicable for tumbling objects due to the violation of small angles assumption.

The prediction and updating scheme of the UKF were detailedly described in section 3.1.2. As in the previous section, the chosen set of sigma points is the one in Eq. (3.50). Hence, the spherical simplex unscented transform was employed again.

An example of the final result of Kalman filtering the recovered Gibbs representation $\boldsymbol{\Omega}$ of the successive finite rotations of the target is depicted in Fig. 3.18: the components of the estimated angular rate are compared to the ones obtained via simulation of the target attitude dynamics (see Appendix B.2). The standard deviation of the noise added

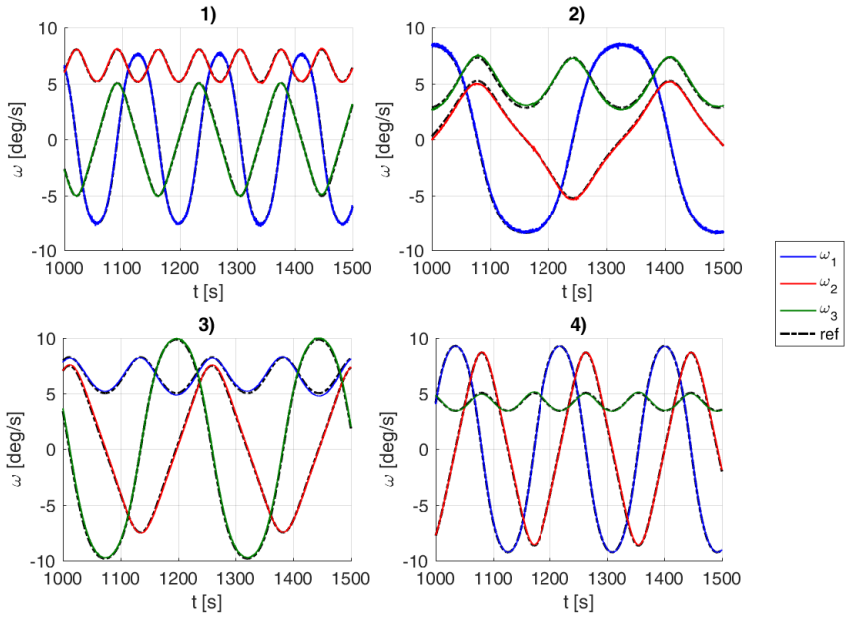

Figure 3.18 Final estimation of the angular rate after Kalman filtering the recovered Gibbs representation $\mathbf{\Omega}$ of the successive finite rotations. Reference values of the angular rate components are represented by dashed lines.

to the feature coordinates decreased to 10 mm. The latter value remains in the accuracy standards of existing passive sensors (see subsection 1.2.2 for details))

Actually, it is expected that raw $\mathbf{\Omega}$ signal is much more corrupted than quaternion signal, which is obtained assuming prior knowledge of the target shape. Indeed, $\mathbf{\Omega}$ is derived in Eq.(3.108) starting from a discrete set of points, and the quality of its estimation improves with the number of points. Ideally, the best estimation comes if all the points of the target are available. This reasoning does not apply in the quaternion approach, where the attitude signal is derived starting from the coordinates of only three points, and the availability of a higher number of points would not be exploitable.

Finally, note that the 44 points (see.Fig.1.6) are not always all visible at the same time; the minimum number of points that are visible at the same time is 9, which is a very low value. Nevertheless, as seen is subsection 1.2.2, 10mm at coordinate level corresponds

to 10^{-5} at the camera image plane level. Thus, the estimations given according to this second approach can be compared with the ones of the current state of art methods e.g. [64].

The four results refer to the scenarios listed in Tab. 3.1. The estimated values of the normalized inertia moments are shown in Fig. 3.19. Even in this case, the latter part of the figure puts in evidence the simulated time needed by the observer to approximately learn the actual inertia ratios. Notice that the mentioned time is different in each case, and goes from 30 s (case 3) to 1000 s (case 2, which seems to be the worst). The estimation error directly reflects into the accuracy in identifying the angular rate and attitude.

The estimation algorithm was also applied to scenarios in Tab. 3.2. To show the performances of the whole approach, the final RMSE about each component of the

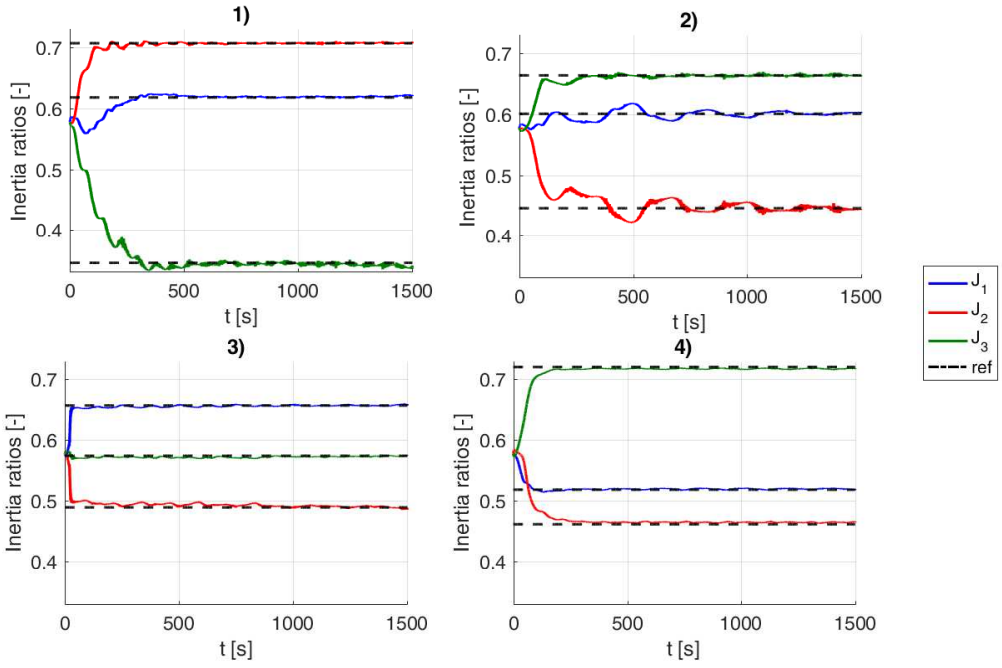

Figure 3.19 Final estimation of the relative values of the principal moments of inertia after Kalman filtering the recovered Gibbs representation $\boldsymbol{\Omega}$ of the successive finite rotations. Reference values are represented by dashed lines.

CaseID	ε_{ω_1}	ε_{ω_2}	ε_{ω_3}
1)	0.0988	0.1095	0.0702
2)	0.0944	0.1281	0.1286
3)	0.0749	0.1473	0.1769
4)	0.1053	0.0745	0.0551
5)	0.0743	0.0485	0.0928
6)	0.0235	0.0197	0.0216
7)	0.0867	0.1793	0.1268
8)	0.1255	0.0778	0.0842
9)	0.0380	0.0633	0.0718
10)	0.0515	0.0572	0.0337
M. unit:	[deg/s]	[deg/s]	[deg/s]

Table 3.5 Angular rate estimation error after Kalman filtering; standard deviation of the measurement noise is equal for each coordinate to 10 mm.

estimated rate, are listed in Tab. 3.5. These values were evaluated after the Kalman filter convergence.

Analyzing the data shown in Tab. 3.5 it appears that the errors in the angular rate estimation are approximately between 10^{-2} deg/s and 10^{-1} deg/s. As expected, the accuracy obtained with this second approach is similar to that of the first one, but the error on data is now lower, as a 10 mm noise amplitude were considered at coordinate level. Hence, the accuracy standards of the second approach slightly decrease, but this method required few assumptions, so it is more general than the first. Indeed, no prior information about the shape of the target is needed for the algorithm to be working. Moreover, the method shows to be robust against occlusions as the one in the previous section.

Nevertheless, the results obtained with the second approach are still comparable with those in [19], where the angular rate estimation error was assessed between 10^{-2} deg/s and 10^{-1} deg/s. These values were obtained starting from data affected by the minimum

CaseID	${}^{B}J_1$	${}^{B}J_2$	${}^{B}J_3$	$\Delta^{B}\bar{J}_1$	$\Delta^{B}\bar{J}_2$	$\Delta^{B}\bar{J}_3$
1)	0.6177	0.7068	0.3448	0.0028	0.0003	-0.0056
2)	0.6005	0.4462	0.6635	0.0015	-0.0020	-0.0000
3)	0.6570	0.4890	0.5738	-0.0002	-0.0007	0.0007
4)	0.5180	0.4614	0.7203	0.0034	0.0011	-0.0030
5)	0.2952	0.7806	0.5510	0.0035	-0.0025	0.0016
6)	0.5309	0.4729	0.7032	0.0040	0.0028	-0.0049
7)	0.7195	0.6575	0.2237	0.0000	-0.0004	0.0013
8)	0.7452	0.5123	0.4269	-0.0017	0.0007	0.0021
9)	0.7421	0.5215	0.4212	-0.0022	-0.0017	0.0059
10)	0.3714	0.7428	0.5571	-0.0010	-0.0002	0.0009
M. unit:	[-]	[-]	[-]	[-]	[-]	[-]

Table 3.6 Nominal normalized principal moments of inertia and difference beetwen nominal value and estimation after convergence

considered noise amplitude (10^{-5}) at the camera image plane level, corresponding to just 10mm at coordinate level.

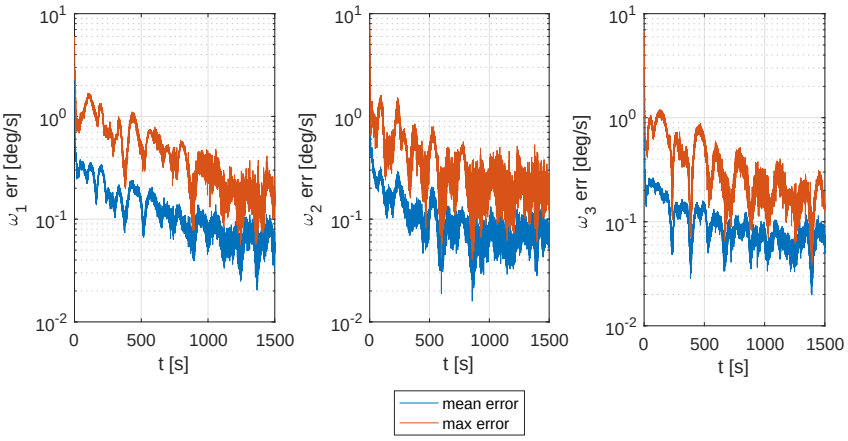

Figure 3.20 Mean and maximum estimation error for each angular rate component; the UKF converges at about 1000 seconds

.

The mean estimated normalized principal moments of inertia after convergence $\bar{J}$ are compared to the reference values in Tab. 3.6. The absolute value of error in the inertia moment estimation varies from 3×10^{-5} to 5.9×10^{-3}. The mean absolute error equals 2×10^{-3} .

Finally, to show the convergence properties of the designed unscented Kalman filter, the time behavior of mean and maximum angular rate estimation error in the considered scenarios is illustrated in Fig. 3.20. From the latter figure, note that the error level stabilizes at about 1000 s. Thus, the performances of the two unscented Kalman filters designed for the two approaches are comparable. Actually, the two schemes are fed with different indirect measurements, which come from the coordinates of the features. However, with the first approach the error in the calculation of the quaternions from the features is not amplified; on the other hand, for the second method, the error in the computation of $\boldsymbol{\Omega}$ is amplified by the fact the only a subset of points of the target is available. It is possible to conclude that the two approaches give comparable results starting with different noise amplitude at coordinate level (50mm in the first case, 10mm in the second).

Chapter 4

Experimental tests

Before thinking about a possible real application of any innovative technique for assisting debris removal missions, a laboratory test campaign is certainly essential. However, to perform optimal tests of the algorithms that were developed within this work, it is necessary to simulate, at least to some extent, the complex relative dynamics between two space objects.

It is quite evident that this is not an easy task. The most famous laboratories that simulate the relative dynamics between satellites are more focused on the orbital dynamics. Typically, the test-bed comprises a flat-floor or a granite table facility in which frictionless motion is achieved by releasing compressed air from appropriate tanks within the mock-ups of the satellites.

However, this kind of laboratories is quite rare in the world. Some examples are the Space System Lab at MIT [65], the Multivehicle Wireless Test-bed at Caltech [66], the Spacecraft Robotics Laboratory at the Naval Postgraduate School [67], and the Distributed Space Systems Laboratory at Technion [64].

There are also few other laboratories in which the mock-ups of the satellite are mounted on manipulators to better simulate the relative attitude dynamics. One example is the Spacecraft Formation Flying Hardware Simulator at CISAS [68], in which the air bearings for the two mock-ups support gimbals for allowing a 3 DOF attitude motion for the mock-ups. However, with that structure, the rotations of the mock-ups remain limited to few tens of degrees. In [69], the target mock-up is mounted on a 6 DOF Stewart platform, while a stereo rig is placed on a fixed support. Even in this case, the motion of the mock-up is severely restricted by the limited workspace of the supporting manipulator.

Hence, there are no laboratories in which the formation flying of two spacecraft is perfectly simulated for long time periods. However, it is possible to test state estimation algorithms on data coming from simulated relative dynamics, which have similar properties to the actual ones.

Politecnico di Torino does not own a specific facility for simulating spacecraft in formation flying. However, within the CADET program, Aviospace S.r.l. developed a test rig for the partial simulation of the relative motion between target and chaser satellites during a removal mission. The developed laboratory environment was called CADETLab [20]. This test-bed comprises the target mock-up mounted on a 3 DOF mechanical architecture, and the chaser mock-up consisting of a 5 DOF robotic arm.

The algorithm presented in this work were tested in this laboratory. Thanks to the respective work of Blue Engineering S.r.l. and of Eurix S.r.l., two sources of data were considered: the output of an infrared camera and a 3D stereo-rig system respectively. Both the two sensors were placed on the end-effector of the robotic arm. In particular, they were pointed toward the target mock-up, which was moved by the mentioned mechanical architecture.

The two different outputs were put in the form of trajectories of points fixed to the target mock-up. The mock-up was marker-free to simulate the non-cooperativeness between the satellites. The following section provides a complete description of the facility.

4.1 The CADETLab facility

The CADETLab facility consists of a control room and a series of ground test concepts aiming to host breadboards of the target and the chaser to simulate a non-cooperative rendezvous and capture in its major phases. The whole architecture was thought to maintain the layout as simple as possible, thereby optimizing the available resources.

The mock-up of the target is a scaled physical model of an Ariane 4 upper stage of the H10 family (see Fig. 1.2), whose virtual model were showed in Fig. 1.3. The

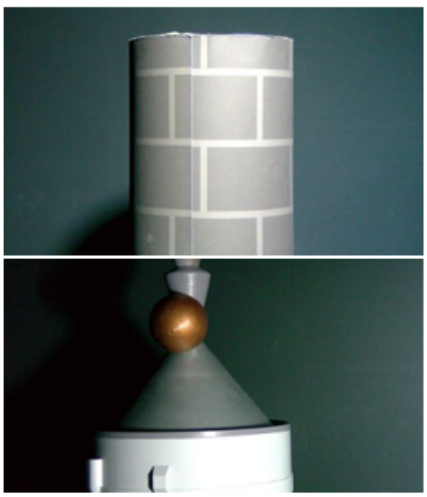

Figure 4.1 Scaled physical model of the H10 upper stage. The cylindrical part is approximately 1.2 m long and have a diameter of 330 mm. The texture formed by the external insulation layer is reproduced with decorative paper

chosen scale for the physical model, of which a photograph is shown in Fig. 4.1, was 1:8. The main body of the mock-up is of plastic material, and it was obtained via additive manufacturing techniques. The cylindrical part of the mock-up is hollow to accommodate a suitably set of actuated mechanisms, which are capable of rotating the cylinder around its axis of symmetry.

The operation of these mechanisms simulates the spin motion of an axisymmetric body on which no torques are exerted (see subsection B.2 for the concept of spin motion). A detail of this mechanism is in Fig.4.2 A second rotational degree of freedom is provided to the mock-up through an actuated revolute joint, which is installed on a cylindrical arm with one extreme connected to the mock-up surface, and the other to the base of the whole mechanism, comprising the mock-up itself. A detail of this part of the mechanism is shown in Fig.4.3.

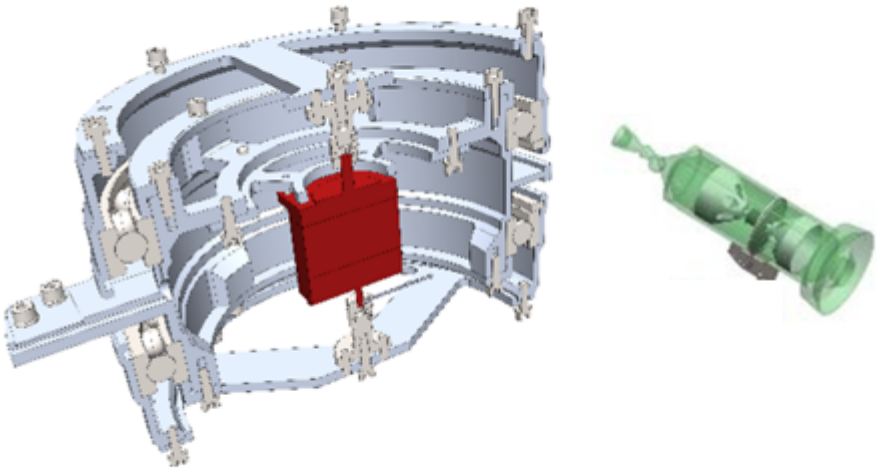

Figure 4.2 Mechanism for the simulation of the spinning motion of the mock-up. The mechanism is mounted inside the mock-up. A stepper motor allows the external structure rotating around its symmetry axis. Ball bearings support the rotating structure with respect to the frame of the motor.

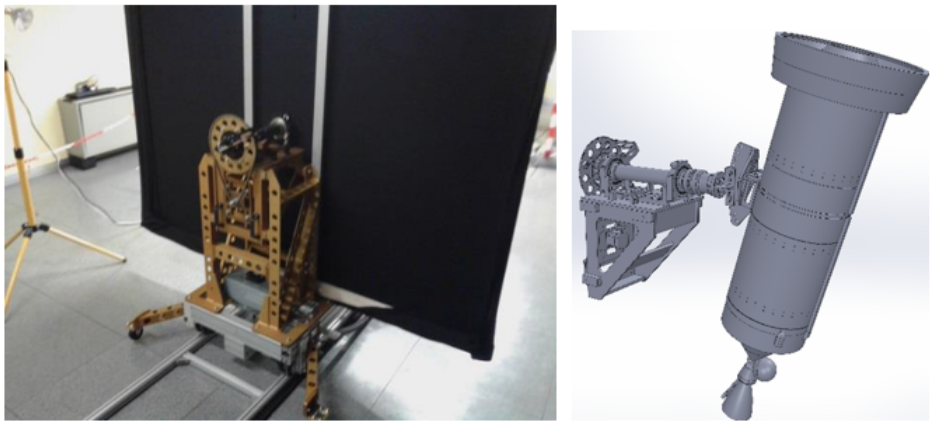

Figure 4.3 Mechanism for rotating the mock-up around a fixed axis in the inertial space. In the left image, one of the extremes of the visible cylindrical arm is hinged to a fixed platform welded to the base. The other extreme is hidden by a black panel. The right image shows the connection to the mock-up

The interface for connecting the mock-up surface to the rotating arm presents several bores as interface points. These bores allow the spin axis to have different inclinations with respect to the cylindrical arm. In particular, the inclination angle δ_{sp} can assume values from 60 deg to 120 deg.

Finally, a scheme of the rotational motion capability of the target mock-up is represented in Fig. 4.4

Notice from Fig. 4.4 that the rotation γ is about an axis that remains fixed in the inertial space. Thus, the spin axis performs a motion that develops on an inertially fixed plane. In other words, the axis of symmetry of the mock-up traces a circle instead of a cone. The latter fact leads to the result that also the resultant angular rate vector lays on the mentioned plane while tracing a closed curve, which is, in particular, a circle. In a body-fixed reference frame, the spin axis has a fixed direction even though it is not aligned with the angular rate vector because of the rotation γ. In particular, this constant

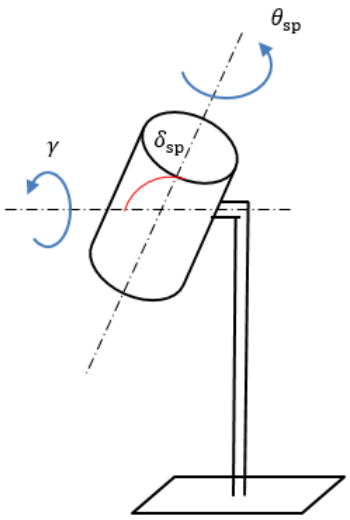

Figure 4.4 Scheme of the rotational degrees of freedom of the target mock-up. Note that θ_{sp} identifies the spin motion of an axisymmetric torque-free body.

direction forms an angle δ_{sp} equal to the inclination of the spin axis about the floor of the control room. Indeed, the cylindrical arm in Fig. 4.3 constantly remains parallel to that floor.

The above-mentioned properties of the planned mock-up motion are not consistent with the laws of spacecraft attitude dynamics (see Appendix B.2). The direction of the angular rate vector is not constant in the principal body-fixed reference frame. On the contrary, for an axisymmetric body, the angular rate vector traces a cone, and the Polhode is a circle. Due to the architecture of the laboratory, the angular rate vector of the mock-up traces a circle in an inertial frame.

The rotational degrees of freedom of the mock-up are both actuated by two commercial stepper motors. The maximum number of steps per revolution is equal to 400, while the maximum reachable velocity and absorbed current are equal to 5 rpm and 6 A respectively. No feedback control for both position and velocity are implemented. Thus, just a constant open-loop velocity set can be imposed for each mock-up axis. Thus, the

tracking sensors, of which the laboratory is equipped, should be appropriately displaced to obtain a realistic relative attitude dynamics. An additional difficulty is given by the fact that at low velocities (less than 1 rpm) the chosen stepper motors produce a visible discontinuous spin motion. This problem traduces in an additional source of noise on input data that serves to estimate the mock-up kinematics.

The entire mechanism for moving the target mock-up is mounted on a dolly platform, which is constrained to move along a linear guide. The dolly platform can be moved manually or employing a 24 V DC motor, which is controlled in position; moreover, the location of the dolly can be locked through a service brake. This structure, of which a detail is given in Fig. 4.5 is thought to regulate the distance between the target mock-up and the sensors, simulating a relative motion. Evidently, this system is not capable by itself of replicating the complex relative orbital dynamics between two close Earth's satellites. It is here reminded that, for unperturbed satellites, this dynamics is governed by Eq. (1.1).

As mentioned at the beginning of this chapter, the laboratory is equipped with a small 3D stereo rig and with an infrared camera. Both the sensors are integrated and fixed together to the end effector of a 5 DOF articulated robotic arm. In particular, the robot

Figure 4.5 A detail of the dolly platform and of the linear slider that constraints the motion of the platform

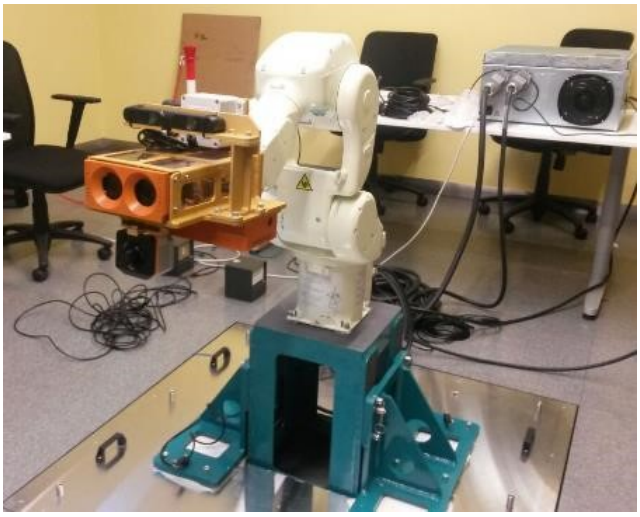

Figure 4.6 A photo of the 5 DOF Kawasaki RS05N robot. The end-effector is equipped with a plenty of sensors for the observation of the target mock-up.

is a Kawasaki RS05N. The total length of the robot in a fully stretched-out horizontal configuration is approximately equal to 770 mm. The base of the robot is fixed to the floor of the control room. In particular, the disposition of the elements in the control room is such that the plane of symmetry of the robot is parallel to the linear guide of the dolly platform of the mock-up. Moreover, the axis of symmetry of the mock-up belongs to that mentioned plane. A detail of the 5 DOF robot is in Fig. 4.6, while its characteristic dimensions and workspace are shown in Fig.4.7.

Finally, a real photographs of the complete layout of the CADETLab facility is shown in Fig. 4.8

As visible in Fig. 4.8 and in Fig. 4.6, the robot end effector is equipped with two different kinds of sensors for observing the motion of the target mock-up. In particular, there are a 3D stereo-vision system and a monocular infrared camera.

The first one is a commercial system called 3DOne (see Fig. 4.9). The main characteristic of this integrated system is a high resolution of 1920x1080, a fast acquisition rate of 30 Hz, and adjustable internal calibration parameters. However, the baseline between the

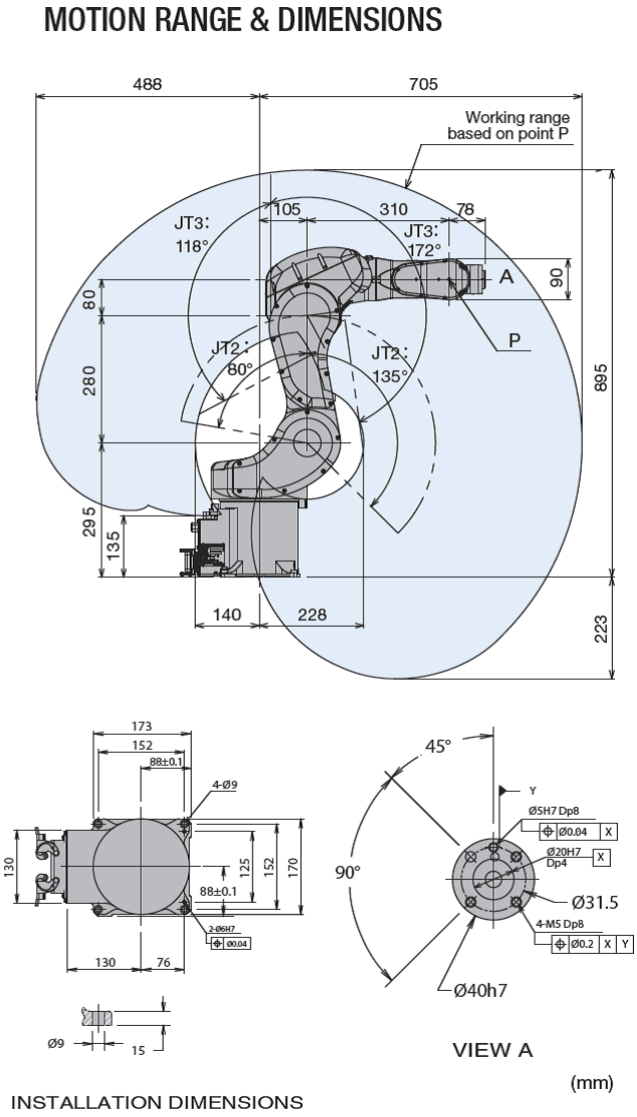

Figure 4.7 Characteristic dimensions and workspace of the Kawasaki RS05N robot.

two integrated cameras has a length of only 60 mm. Thus, to have a sufficient disparity between the images of the two cameras, it was necessary to consider a 0.9 m distance between the mock-up and the robot end effector. With that configuration, the resolution of the pixel became approximately equal to 1 mm, while the expected error in the depth coordinate amounted approximately to 25 mm (1-sigma). Hence, the noise conditions were similar to the ones of the simulated dataset in section 1.2.

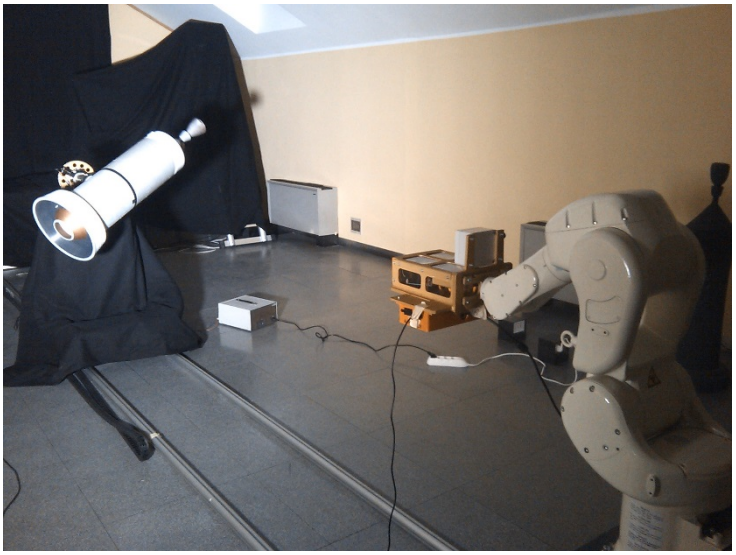

Figure 4.8 A photo of the CADETLab.

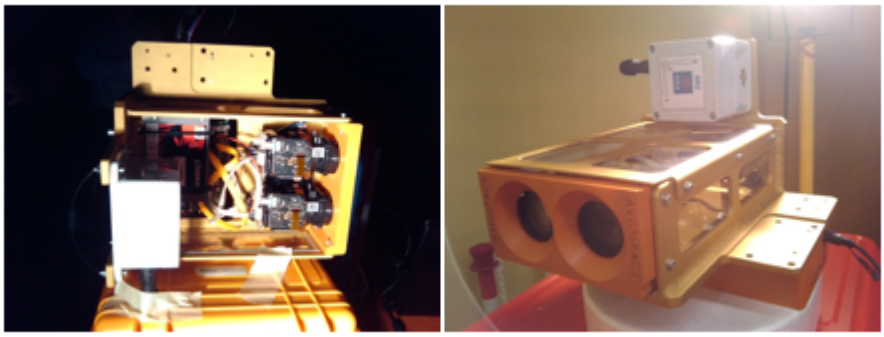

Figure 4.9 3DOne assembly and the case for tests

Actually, notice that the physical model of the target is eight times smaller than the virtual model used for simulations. In particular, given the layout of the laboratory and the architecture for rotating the target mock-up, the displacements in the depth direction of the mock-up features are particularly reduced. Hence, it is expected a higher incidence of the noise on the final results of the algorithms developed in this work.

Eurix s.r.l was responsible for the CADET research program of the feature-tracking employing the stereo-vision system depicted in Fig. 4.9. In particular, they created

Figure 4.10 Xenics uncooled silicon microbolometer with its case to form the monocular IR camera used for tests in CADETLab.

a novel tracking algorithm whose details can be found in [70]. The detection of the features exploits the classical Shi-Tomasi detector [71], which is combined with the Lucas-Kanade algorithm [61] to predict the future positions of the features.

Then, results are filtered to find outliers, which should be eliminated to increase usability of data. The underlying innovative idea consists of repeating the tracking procedure reversing the direction of time. An error for each feature can be evaluated as the distance between the *back-tracked* point and the same point at the original position. Once this distance is superior to a reasonable threshold, the relevant feature is treated as an outlier, and thus, it is discarded.

The monocular infrared camera, of which a photograph is given in Fig. 4.10, is produced by Xenics, and it is based on a *microbolometer* with spectral response within 8-14 μm. The resistive amorphous silicon focal plane array has a resolution of 384x288 pixel, with a pixel dimension of 25 μm. Thus, the expected performances concerning image definition are medium-low.

Blue Engineering s.r.l was responsible for the CADET research program of the target pose estimation employing the IR camera shown in Fig. 4.10. The performed coarse pose estimation was useful to be converted into the trajectory of three fictitious points.

Blue Engineering transmitted these data as inputs for the algorithms developed in this work for a strong refinement of the pose estimation.

Due to the low resolution of the camera, Blue Engineering was unable to use sophisticated algorithms like SIFT [72] to detect the features of the mock-up. However, relying on the expectable consistent difference between the temperature of the target and the environment, they exploited several known filtering algorithms to identify approximately the contour of the target. In the CADETLab environment, the target mock-up was appropriately heated by the usage of high-power lamps.

From the possession of a CAD model of the mock-up, which is equivalent to assuming the knowledge of prior information about the target shape, they performed a 3D rendering of the found contour. Thus, they attached three points to this rendered model evaluating their position for each time sample.

The necessity of producing 3D renderings of the detected contour led to a relatively slow algorithm capable of generating outputs with a frequency in the order of 1 Hz. However, this frequency is sufficient for an efficient refinement of the pose estimation via the algorithms developed in this work. Figure 4.11 give an illustration of the result of the rendering performed by Blue Engineering.

The described detection systems were useful to test with different kinds of inputs the algorithms for the identification of debris kinematics. Although the described laboratory does not reproduce exactly the formation flying of spacecraft, the provided data are the outputs of real sensing systems whose application can be feasibly extended to the space environment. Hence, the results of the algorithms in that context reveals with reasonable reliability the robustness of the pursued approach for debris dynamics estimation during a real removal mission.

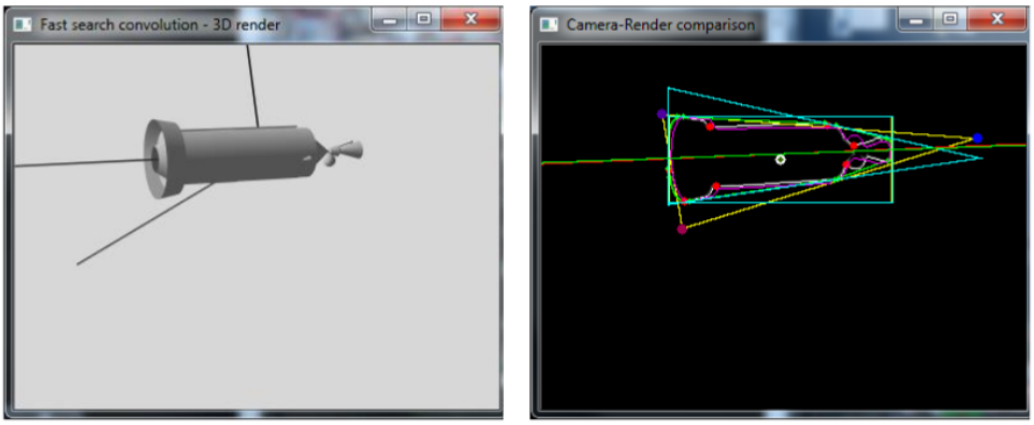

Figure 4.11 3D renedring of the object contour detected by Blue Engineering s.r.l. by Xenics IR camera.

4.2 Algorithms for laboratory conditions

The main difficulty in the application of the methods exposed in chapters 2 and 3 consists of the big difference between an approximate model of an Earth's orbiting satellite and the actual realizable motion of the mock-up in the depicted laboratory. In fact, as mentioned at the starting of this chapter, the attitude motion of the mock-up is characterized by an angular rate that behaves in an inertial frame in a similar way to the one of a satellite in its body-fixed frames.

Actually, the replication of the behavior of the angular rate of an axisymmetric satellite requires that the tumbling axis follows the spin motion while remaining fixed to the body, instead to the inertial frame. This replication requires complex mechanical architecture and high costs.

However, while the methodology exposed in chapter 2, independently from the actual kinematic behavior, can work until the body constantly rotates around the same point, the methods in chapter 3 are based on state observers. Thus, the latter methods are model-based. In particular, they cannot work if the kinematic behavior of the object is too far from the modeled kinematics.

An idea to overcome this problem could be linked to the movement of the robotic arm in Fig. 4.6 to simulate the realistic relative attitude dynamics accurately in a camera-fixed reference frame. However, this attempt results in a very fast dynamics for the robot. This dynamics is not consistent with the physical limits of the robot, though it would be possible to replicate the movement for a very short amount of time. This last way is not applicable with proficiency yet because of the relatively slow convergence rate of the UKF used for the inertia estimation (see Fig. 3.12 and Fig. 3.19). However, this last aspect is not critical for practical applications because the observation phase of a removal mission can have a long duration.

Then, excluding the above solutions, it is needed to consider algorithms based on a general kinematic model of the target that is suitable also for describing the attitude kinematics of the mock-up. In particular, a simple triple integrator model [73] is often exploited in practice to predict the motion of generic rigid bodies.

Because of the absence of singularities, quaternions are the most suitable parameters for modeling the attitude kinematics of a rigid body. Thus, the considered stochastic triple integrator model is the following:

$$x_{k+1} = \begin{bmatrix} {}^{\mathcal{F}}q_{Ik+1} \\ {}^{\mathcal{F}}\dot{q}_{Ik+1} \\ {}^{\mathcal{F}}\ddot{q}_{Ik+1} \end{bmatrix} = \begin{bmatrix} I_4 & \Delta t I_4 & \frac{\Delta t^2}{2} I_4 \\ 0_4 & I_4 & \Delta t I_4 \\ 0_4 & 0_4 & I_4 \end{bmatrix} \begin{bmatrix} {}^{\mathcal{F}}q_{Ik} \\ {}^{\mathcal{F}}\dot{q}_{Ik} \\ {}^{\mathcal{F}}\ddot{q}_{Ik} \end{bmatrix} + w_k \tag{4.1}$$

From the knowledge of the state in Eq. (4.1), Eq. (1.8), which is here resumed and rewritten in the generic body-fixed reference triad $\mathcal{F}$, allows the computation of the angular rate.

$${}^{\mathcal{F}}\boldsymbol{\omega} = 2\left({}^{\mathcal{F}}q_{0I}\,{}^{\mathcal{F}}\dot{\boldsymbol{q}}_I - {}^{\mathcal{F}}\boldsymbol{q}_I\,{}^{\mathcal{F}}\dot{q}_{0I}\right) - 2\,{}^{\mathcal{F}}\boldsymbol{q}_I \times {}^{\mathcal{F}}\dot{\boldsymbol{q}}_I \tag{4.2}$$

The estimation of the state in Eq. (4.1) requires the measurement of quantities that it directly affects. For instance, as treated in subsection 3.3.2, the computation of the vector ${}^{I}\boldsymbol{\Omega}$ from the positions of the target features is an indirect measurement of the body kinematics. Thus, the values of this vector are useful to evaluate the quaternions ${}^{\mathcal{F}}q_I$. This last evaluation would lead to the writing of the following measurement equation:

$$z_k = {}^{\mathcal{F}}q_{Ik} + v_k \tag{4.3}$$

Equation (4.1) and Eq. (4.3), which form a complete state-space model for the mock-up kinematics, are linear in the state variables. Among these variables, the quaternion derivative ${}^{\mathcal{F}}\dot{q}_I$ is necessary to compute the angular rate via Eq. (4.2). Optionally, after the estimation of the quaternion ${}^{\mathcal{F}}q_I$, one can compute the DCM ${}^{\mathcal{F}}A_I$ to express the angular rate in the inertial frame (${}^{I}\boldsymbol{\omega}$).

Since the state-space model of the system is linear, if the assumptions regarding the measurement and the process noise are approximately satisfied, the state can be observed by using a classic Kalman filter (see subsection 3.1.1)

In particular, Eq. (3.33) and Eq. (3.34), which are here resumed, are used for the prediction phase:

$$\bar{x}_{k+1}^{-} = F_k \bar{x}_k^{+} \tag{4.4}$$

$$P_{k+1}^{-} = F_k P_k^{+} F_k^T + Q_k \tag{4.5}$$

The Kalman Gain is computed via Eq. (3.27), here resumed:

$$K_{k+1} = P_{k+1}^{-} H_{k+1}^T \left(H_{k+1} P_{k+1}^{-} H_{k+1}^T + R_{k+1} \right)^{-1} \tag{4.6}$$

Finally, the updating phase is characterized by Eq. (3.28) and Eq. (3.29)

$$\bar{x}_{k+1}^{+} = \bar{x}_{k+1}^{-} + K_k \left(z_{k+1} - H_{k+1} \bar{x}_{k+1}^{-} \right) \tag{4.7}$$

$$P_{k+1}^{+} = P_{k+1}^{-} - K_{k+1} H_{k+1} P_{k+1}^{-} \tag{4.8}$$

Here, the matrices F and H are independent by the sample time k. In particular, they are the following ones:

$$F = \begin{bmatrix} I_4 & \Delta t I_4 & \frac{\Delta t^2}{2} I_4 \\ 0_4 & I_4 & \Delta t I_4 \\ 0_4 & 0_4 & I_4 \end{bmatrix} \tag{4.9}$$

$$H = \begin{bmatrix} I_4 & 0_4 & 0_4 \end{bmatrix} \tag{4.10}$$

The following part of this subsection explains how to evaluate quaternions from measurements, i.e. the trajectories of the features.

The outputs of the 3DOne stereo-vision system (see Fig. 4.9), appropriately elaborated by Eurix s.r.l, allows the effective evaluation of the vector ${}^{I}\boldsymbol{\Omega}$ (see section 3.3.2) for the target mock-up. Indeed, the used stereo-rig system is capable of tracking relatively dense clouds of points for several instants of time. The tracked features change significantly during the overall observation time. Thus, the resulting dataset has the same properties of the one used for simulations in subsection 3.3.2. In particular, the detected features are tracked for few time samples but once they disappear, they are definitively lost: no position information about those features is recoverable from the positions of other tracked points.

${}^{I}\boldsymbol{\Omega}$ describes the finite variation of the orientation between two different poses of the body. It was shown that this vector is not dependent on the particular group of points that are considered for its estimation, but it is a description of a motion property of the entire body.

If the motion of the object is regular, it is possible to assume that the components of ${}^{I}\boldsymbol{\Omega}$ are sparse in the frequency domain. This property permits the application of compressive sampling techniques to reduce noise in case of corrupted measurements of this vector (see section 3.2).

From one among all the infinite body-fixed reference triads, it is possible without any loss of generality to consider the one that at the initial time has the same orientation of the inertial frame. If this generic frame is indicated as $\mathcal{F}$, then the initial attitude of the mock-up is:

$$ {}^{\mathcal{F}}q_{I0} = \begin{bmatrix} 0 & 0 & 0 & 1 \end{bmatrix}^{T} \tag{4.11} $$

Then, for a general instant k, it holds:

$$ {}^{\mathcal{F}}q_{I_{k+1}} = {}^{I}\delta q_k \otimes {}^{\mathcal{F}}q_{I_k} \tag{4.12} $$

where ${}^{I}\delta q_k$ is the attitude variation whose relationship with ${}^{I}\boldsymbol{\Omega}$ can be found in Eq. (3.109), here resumed:

$$ {}^{I}\delta q_k = \begin{bmatrix} \cos\left(\frac{\alpha_k}{2}\right) & e_{1_k}\sin\left(\frac{\alpha_k}{2}\right) & e_{2_k}\sin\left(\frac{\alpha_k}{2}\right) & e_{3_k}\sin\left(\frac{\alpha_k}{2}\right) \end{bmatrix} \tag{4.13} $$

Again, remember that ${}^{I}\boldsymbol{\Omega} = \boldsymbol{e}\tan(\alpha/2)$.

For having an example of the result of these operations, a simulation of the motion of the mock-up was performed in a MATLAB-Simulink environment. A constant value of 1 rpm was set for both the angular rates $\dot{\theta}_{sp}$ and $\dot{\gamma}$ (see Fig. 4.4), which represent the spin motion and a pseudo-tumbling motion respectively. A set of unlabeled features were placed arbitrarily on a scaled CAD model of the target surface such to completely cover it.

The camera reference frame was assumed to be coincident with the inertial frame for all the duration of the simulation. The inertial frame I were built such that its first axis I^1 is parallel to the floor of the control room, its third axis I^3 is directed toward the roof, and the second axis I^2 completes a right-handed triad. The angle δ_{sp} between I^1 and the spin axis of the simulated target was set to 60 deg.

A Gaussian noise with 40 mm of standard deviation was added to each component of the simulated trajectories. The last value of standard deviation is consistent with the expected error level of the 3DOne in detecting depth coordinates of features.

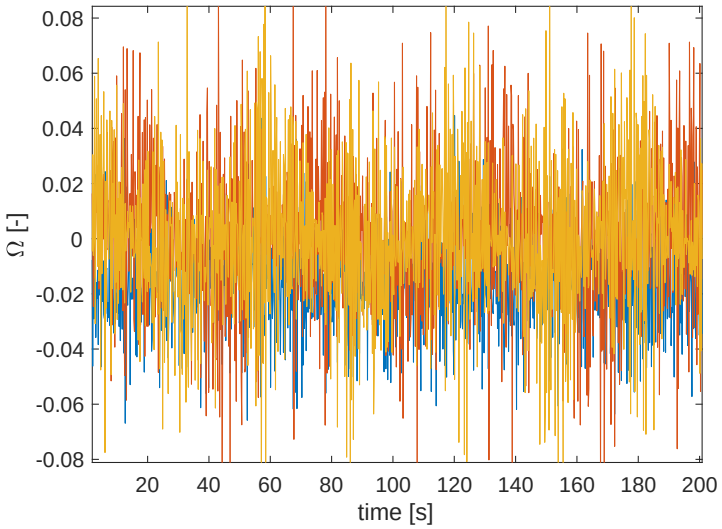

Figure 4.12 Raw ${}^{I}\boldsymbol{\Omega}$ from simulated trajectories of features in laboratory conditions.

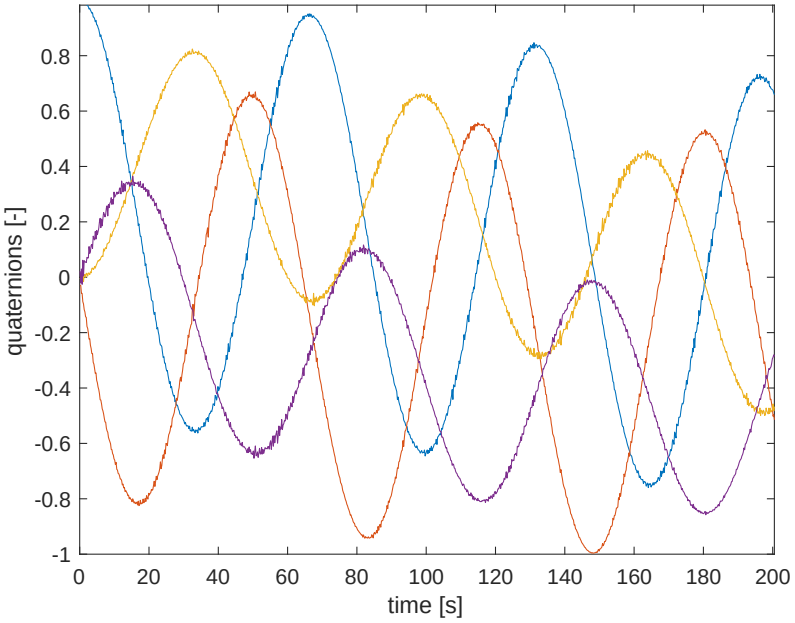

Figure 4.13 Attitude quaternions ${}^{\mathcal{F}}q_I$ from ${}^{I}\boldsymbol{\Omega}$ in Fig. 4.12 by means of Eq. (4.12).

The simulation of the trajectories of the considered features led to a ${}^{I}\boldsymbol{\Omega}$ that is illustrated in Fig. 4.12. Thus, after having performed a denoising of the signal via CS techniques, the quaternions obtained with Eq. (4.13) are shown in Fig. 4.13.

Note from Fig. 4.13 that Eq. (4.13) operates as a first order filter for the high-frequency noise contained in ${}^{I}\boldsymbol{\Omega}$. Indeed, the composition of quaternions is equivalent to summing-up all the finite rotations of the body. For time steps that tend to zero, the mentioned sum becomes equivalent to an integral, whose filtering properties are well known. The related undesired aspect consists in the typical drift of the integrated high-frequency noise. That is one of the reasons for which a state observer is needed for estimating the state vector x in Eq.(4.1).

The computation of the quaternions is necessary also when input data come from the IR camera. As seen in the previous subsection, Blue engineering s.r.l. developed

algorithms for extracting the trajectories of three features from the images taken by the used monocular microbolometer.

The tracked features are always the same for the whole observation period. Thus, the obtained dataset is practically equivalent to the one used to perform the simulations in subsection 3.3.1.

From the positions of three features at k in the frame I, one can define two connecting vectors, ${}^{I}\boldsymbol{\nu}_i$ and ${}^{I}\boldsymbol{\nu}_u$, whose cross product is the vector ${}^{I}\boldsymbol{\nu}_j$, which is perpendicular to both. A third column vector, ${}^{I}\boldsymbol{\nu}_k$, can be simply obtained through another cross product between ${}^{I}\boldsymbol{\nu}_i$ and ${}^{I}\boldsymbol{\nu}_j$. Then, the orientation of a body-fixed reference frame $\mathcal{F}$ is given by the following expression:

$$ {}^{I}A_{\mathcal{F}_k} = \left[\begin{array}{ccc} {}^{I}\hat{\boldsymbol{\nu}}_i & {}^{I}\hat{\boldsymbol{\nu}}_j & {}^{I}\hat{\boldsymbol{\nu}}_k \end{array} \right] \in SO(3) \tag{4.14} $$

As mentioned in Appendix B.1, a non-singular mapping between an element of the $SO(3)$ group and a unit quaternion always exists. This mapping has been shown in Eq. (1.7) for the orientation of I relative to B. However, the mapping mentioned above is valid for any considered reference frames.

Hence, the same Kalman filter that serves to estimate the derivatives of ${}^{\mathcal{F}}q_I$ can be fed indifferently with the mock-up attitude both in the case of data coming from stereo-vision than from thermal images.

In both cases, from the estimated derivatives of the quaternions, the angular rate is evaluated directly from Eq. (4.2) and transformed by means of ${}^{I}A_{\mathcal{F}}$.

Notice that, differently from the simulated dataset, it is tough to determine the principal inertia moments of the mock-up from data taken in the laboratory. Indeed, oppositely from the case of kinematics observation, it is not evident the possibility of finding a surrogate dynamic model that can approximate the actual dynamics of the

mock-up. This issue holds because the mock-up dynamics is far to be similar to the one of a torque-free body. On the contrary, it is sufficient that the mock-up motion is smooth such to have a so little jerk such that the triple integrator model well approximates the actual kinematics.

Hence, regarding the rotational state estimation, only the angular rate was estimated during the laboratory tests.

As regards the localization of the CoM, it is not necessary to make any adaptations to methods presented in chapter 3. Actually, during the whole motion, the angular rate vector of the mock-up passes always through one specific point in a body-fixed frame. In particular, this point is the intersection between the symmetry axis and the pseudo-tumbling axis, which remain fixed in the inertial frame.

Clearly, this fixed point was not thought to be coincident with the real CoM of the mock-up. However, this aspect does not require to modify algorithms because they rely on the assumption that the CoM coincides with the point around which the body rotates. The latter assumption is verified if the body is free from motion constraints. Although this is not true for the actual target mock-up, it would have been true if the mock-up had orbited the Earth. Thus, the laboratory tests of this method are reliable for proving their estimation capacity

The results of the CoM localization will be shown in the next section for both the kinds of data sources. Also, the results for the angular rate estimation will be illustrated.

4.3 Tests results

Data coming from the Xenics microbolometer (see Fig. 4.10) and from the 3DOne (see Fig.4.9) were respectively elaborated by Blue Engineering s.r.l and by Eurix s.r.l to provide suitable data in the form of 3D coordinates of points. During the tests, the

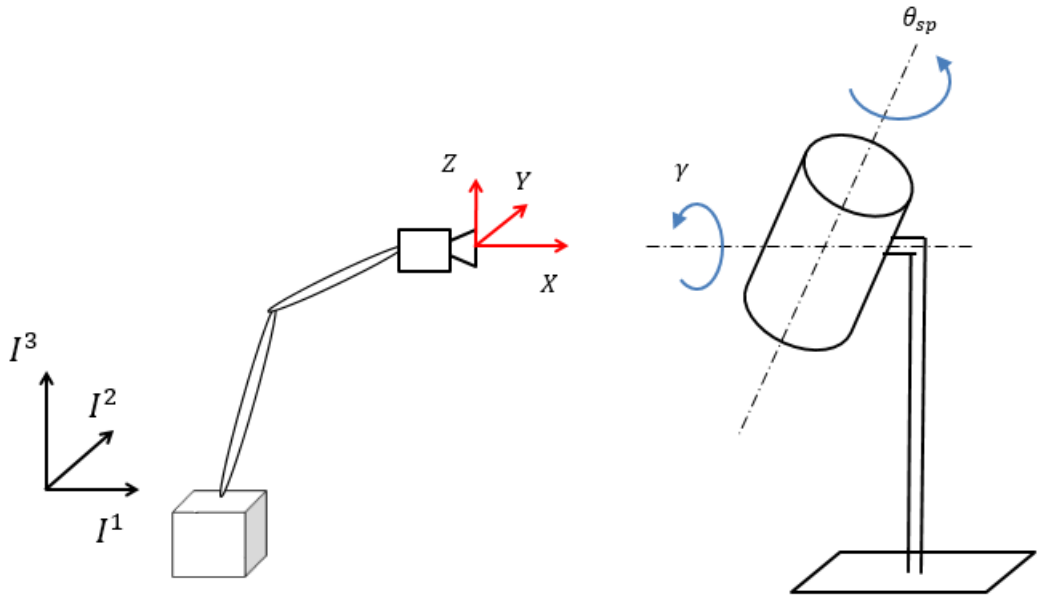

Figure 4.14 Layout of the CADETLab control room and reference coordinate system for input data

relative position between the cameras and the mock-up remained constant. Thus, the orientation of the cameras with respect to the control room was constant.

For those reasons, the camera-fixed reference frames for both the sensors were inertial. Hence, the achieved coordinates of the detected features were expressed in that frames, which were considered coincident because they were placed on the same robot end-effector. In particular, the same reference coordinate system was defined for both the frames: the first axis, namely X was defined as parallel to the floor of the control room; the third axis, namely Z was defined as directed toward the roof; the second axis, namely Y completed a right-handed coordinate triad.

Figure 4.14 illustrates the reference coordinate system for input data.

4.3.1 Data from infrared camera

The test of the algorithms on data from the IR camera was performed considering the following conditions:

- Nominal constant spin rate $\dot{\theta}_{sp} = 1$ rpm (counterclockwise)
- Nominal constant pseudo-tumbling rate $\dot{\gamma} = 1$ rpm (counterclockwise)
- Nominal inclination of the mock-up $\delta_{sp} = 76$ deg
- Nominal fixed position of the motor axes intersection $\boldsymbol{\rho} = \begin{bmatrix} 3.5 & 0 & 0 \end{bmatrix}$ m
- Acquisition time: 1200 s

Note that the above nominal set values are not actively controlled. For instance, no feedback is available to measure the actual angular rates of the two stepper motors. Figure 4.15 shows the coordinates of the three fictitious points coming from the rendered mock-up contour on the image of the IR camera.

As described in the previous section, the trajectories in Fig. 4.15 are exploited to find attitude quaternions of the mock-up. Then, the quaternions feed the Kalman filter, of

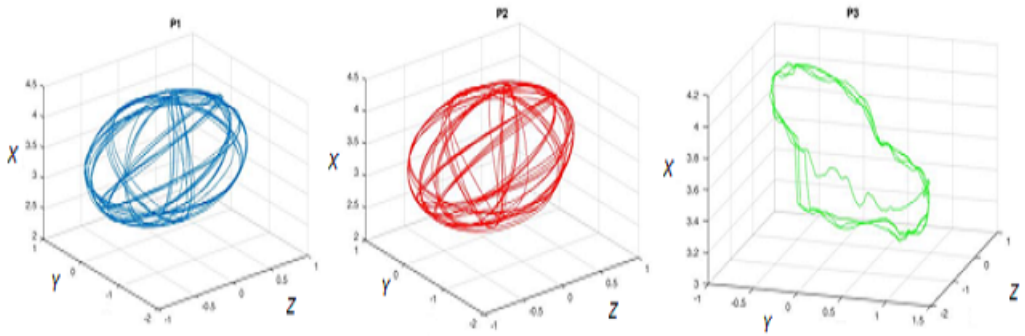

Figure 4.15 Trajectories of the three fictitious features from the elaboration of the data from the IR camera. The dimensions are expressed in m.

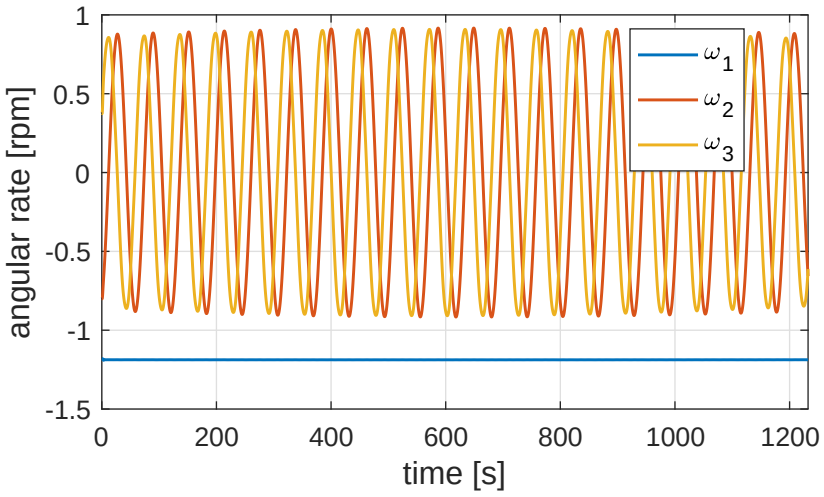

Figure 4.16 Estimated angular rate $\boldsymbol{\omega}$ of the mock-up in the camera-fixed frame shown in Fig.4.14. Notice the steadiness of the first component, which corresponds to the sum of the pseudo-tumbling rate $\dot{\gamma}$ and the constant component of the spin rate $\dot{\theta}_{sp}$ on the first axis

which Eq. 4.1 models the related process. The result is given in terms of the estimated angular rate expressed in the camera-fixed frame. Figure 4.16 illustrates this result; The output of the Kalman filter was further refined with a Savitzky-Golay filter [74].

The result in Fig. 4.16 does not give a direct idea of the accuracy of the taken approach. Thus, it is appropriate to use information about the architecture of CADETLab to decompose the estimated angular rate into the two fundamental components provided by the motors.

The two approximate sinusoidal components of the estimated angular rate in Fig. 4.16 reveals the circular motion of the mock-up symmetry axis. In particular, the mean period T_{ω_t} divided per 60 s gives an approximation of the pseudo-tumbling rate $\dot{\gamma}$. Thus the vector

$$\boldsymbol{\omega}_t = \begin{bmatrix} -\dot{\gamma} & 0 & 0 \end{bmatrix}^T$$

in the camera-fixed frame can be subtracted to the estimated angular rate $\boldsymbol{\omega}$ for each time sample. Hence, the direction of the mock-up symmetry axis is the unit vector corresponding to the last obtained vector.

The first direction cosine of the mentioned symmetry axis is evidently the angle δ_{sp}. Thus, an estimate of this angle is obtained for each time sample. The mean estimate of δ_{sp} from the angular rate in Fig. 4.16 is equal to 76.116 deg, which is quite similar to the nominal one.

Once an estimate of δ_{sp} is available, the estimated angular rate can be effectively decomposed. In particular, assuming positive and counterclockwise the velocities of the motors, it holds from simple kinematic considerations:

$$\dot{\theta}_{sp} = \sqrt{\omega_2^2 + \omega_3^2} - (1 - \sin\delta_{sp})\,\omega_1 \tag{4.15}$$

$$\dot{\gamma} = -\omega_1 - \dot{\theta}_{sp}\cos\delta_{sp} \tag{4.16}$$

The results of the application of Eq. (4.15) and of Eq. (4.16) are shown in Fig. 4.17 and in Fig. 4.18 respectively. To give a better idea of the committed relative errors, Fig. 4.19 shows the magnitude of the spin rate together with the pseudo-tumbling rate in the camera-fixed frame. In those figures, also the mean values are illustrated.

As shown in Fig. 4.17, the estimated spin rate presents a bias with respect to the nominal value of 1 rpm. It is visible that the estimation error is not perfectly centered, but it is evident that it remains bounded by two continuous curves whose curvature is quite low. This behavior could be attributed to different factors. First of all, the tracked features are fictitious: they come from the elaboration of thermal images, which are useful to a coarse estimation of the entire mock-up pose instead of the location of features. Secondly, CS techniques, which are applied to attitude quaternions, try to recover sparse

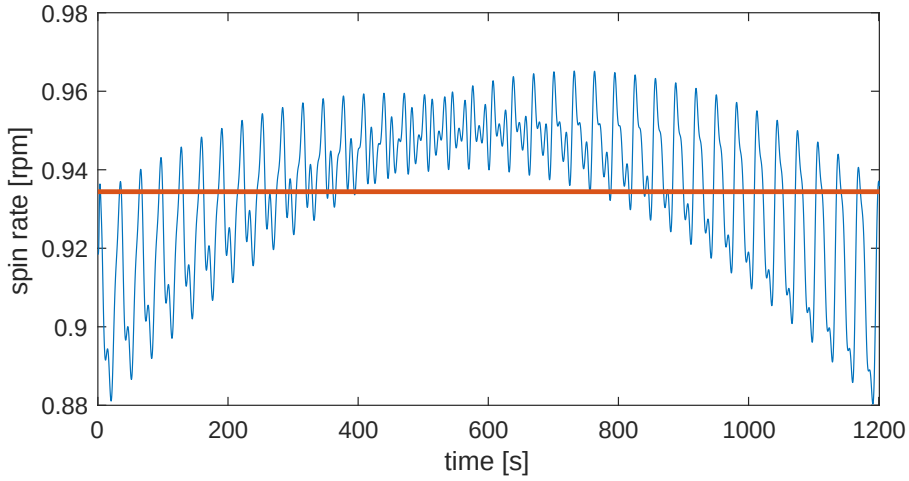

Figure 4.17 Estimated counterclockwise spin rate $\dot{\theta}_{sp}$ of the mock-up. The mean value is represented with a thick line

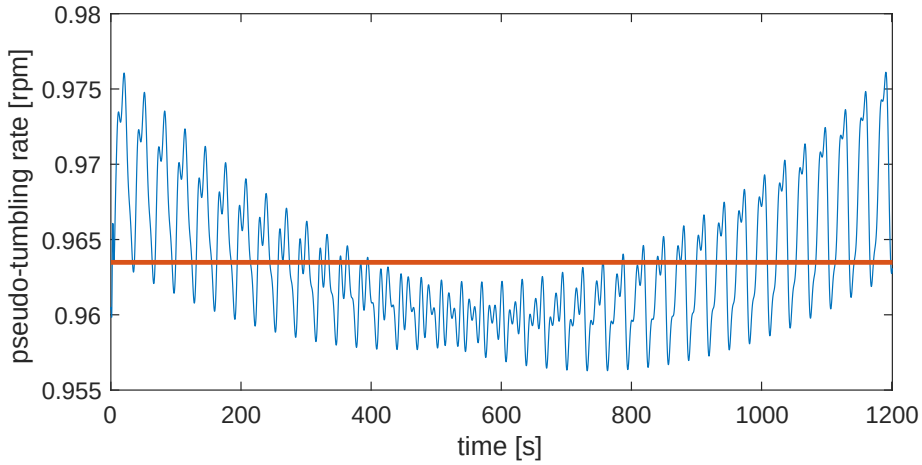

Figure 4.18 Estimated counterclockwise pseudo-tumbling rate $\dot{\gamma}$ of the mock-up. The mean value is represented with a thick line

signals; however, some minor residual frequency contributions to the spectrum of the quaternions could be not eliminated causing the introduction of systematic errors. In particular, the role of the parameter λ in Eq. (3.77) is fundamental: the higher its value, the sparser the output signal. Notwithstanding, the accuracy decreases: the magnitude of the coefficient vector c reduces globally due to the soft thresholding function in Eq.

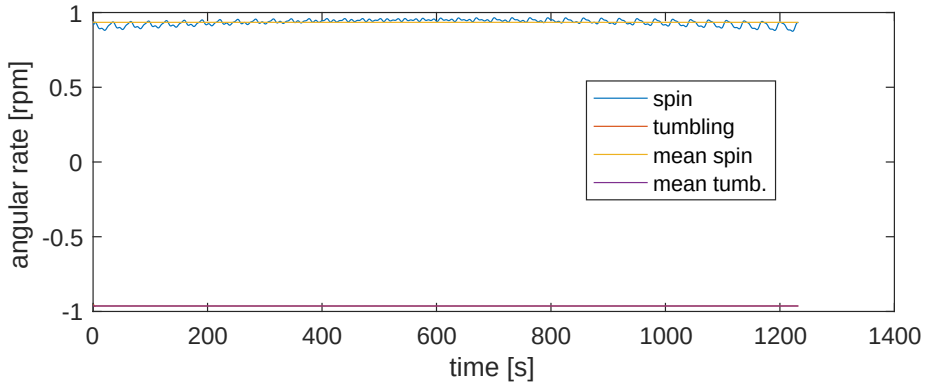

Figure 4.19 Estimated spin rate $\dot{\theta}_{sp}$ of the mock-up, and estimated pseudo-tumbling rate in camera frame. Notice the tiny differences between the mean values and the estimated signals

(3.87). Thus, the amplitudes of the recovered signal decrease incorrectly. Hence, it is better to accept the presence of low-amplitude residuals rather than losing accuracy in the estimation.

The mean value of the estimated spin rate is equal to 0.934 rpm, so a bias of 0.065 rpm, equal to 0.39 deg/s, exists with respect to the nominal value of 1 rpm. However, note that the nominal value is most probably different from the actual one. Indeed, the stepper motors used for moving the target are open-loop controlled. It is expected that the actual values of the angular rates are slightly inferior to the nominal one. This statement is also supported by the analysis of the images captured by the cameras. In fact, it emerged that after a minute of the mock-up motion, the object did not return exactly to its original position before the starting of the movement. In particular, the delay was about 2.5 s

For those reasons, it is probably more interesting to evaluate the bounds of the absolute deviations from the estimated mean. In particular, the difference between the maximum and the minimum deviations over all the long observation time is equal to 0.09 rpm, that is 0.54 deg/s. This is a quite good result if compared with the ones of other methods in the literature. For instance, in [19], experimental tests were conducted to determinate the relative yaw rate between two satellite mock-ups on a frictionless table.

In that work, the biggest estimation errors exceed 2 deg/s, which is approximately two times the sum of the bias and the maximum error found in this section.

The same considerations apply exactly for the estimation of the pseudo-tumbling rate, whose result is shown in Fig. 4.18. The mean value of $\dot{\gamma}$ is equal to 0.965 rpm while the nominal value was 1 rpm. Thus, it exists a bias of 0.037 rpm, that is 0.22 deg/s. The difference between the maximum and the minimum deviations from the mean value is equal to 0.021 rpm, whose corresponding value in deg/s is 0.12.

Hence, as visible from Fig. 4.19, the estimation of the pseudo-tumbling rate led to better results.

Regarding the localization of the intersection point of the two motion axes of the mock-up, all the methods exposed in chapter 2 were applied on data shown in Fig. 4.15. Using an analogous representation as in Fig. 2.19 The results of this test are shown in Fig. 4.20. The raw estimates are fitted with first order polynomials to avoid numerical problems due to singularities. An extremely high condition number of the matrix in the least-square fitting can be automatically detected. Thus there is no loss of generality: the starting order of the fitting polynomial is ten like in section 2.3, but it is decreased until the mentioned condition number is acceptable.

The constant values of the three components of the found position are 3.46 m, 0.03 m, and -0.04 m. Overall, an error in the order of 40 mm was made with respect to the nominal values. Looking to the experimental tests in [19], the CoM is identified with residuals that can be up to 0.1 m. Thus the quality of the achieved results is at least comparable with the one of the best methods known. However, the method developed in chapter 2 is free from hypothesis regarding the fixity of the detected set of features and the uninterrupted availability of measured data. This last aspect is an important point of novelty of the proposed method.

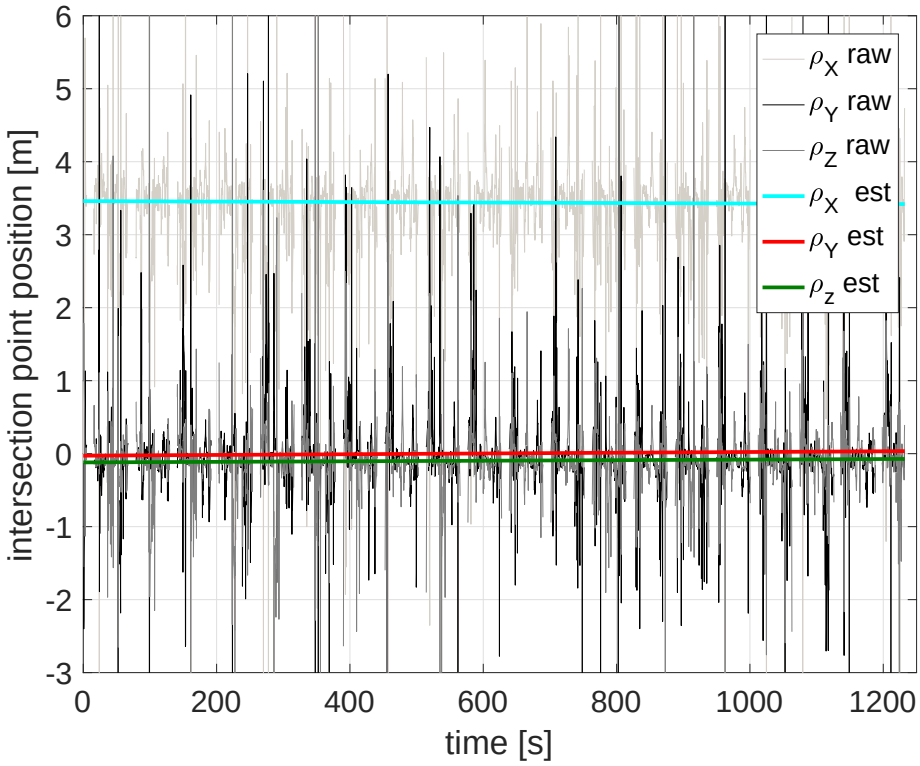

Figure 4.20 Localization of the intersection point of the spin axis with the pseudo-tumbling axis. The distance between this point and the camera was constant

4.3.2 Data from stereo-rig system

The test of the algorithms on data from the stereo-vision system was performed considering the following conditions:

- Nominal constant spin rate $\dot{\theta}_{sp} = 1.65$ rpm (counterclockwise)
- Nominal constant pseudo-tumbling rate $\dot{\gamma} = 1$ rpm (counterclockwise)
- Nominal inclination of the mock-up $\delta_{sp} = 90$ deg
- Nominal fixed position of the motor axes intersection $\boldsymbol{\rho} = \begin{bmatrix} 0.9 & 0 & 0 \end{bmatrix}$ m
- Acquisition time: 120 s

Again, note that the above nominal set values are not actively controlled. No feedback is available to measure the actual angular rates of the two stepper motors. As described in section 4.1, Eurix s.r.l. processed the images taken by the two cameras composing the system. Due to the very low baseline length between the two cameras (60 mm), it was necessary to bring the stereo rig near the mock-up. This operation led to a better accuracy in the definition of the depth map of the object. Although the mock-up was not included completely in the camera FOV, a huge number of features were detected: Figure 4.21 shows the tracked points for each time sample.

The detected features are not in any way correlated to prior knowledge about the mock-up shape. Once it is lost the tracking of a feature, there are not any possibilities of recovering information about the hidden feature. The tracking durations for each feature were collected into a histogram, which is in Fig. 4.22. From that histogram, note that most of the features are tracked for a few time samples. In particular, 98 features are tracked only for 7 time samples.

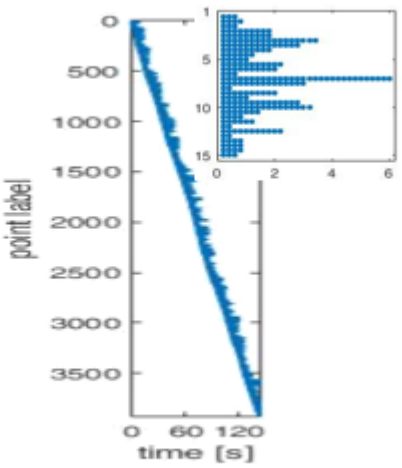

Figure 4.21 Tracked points from stereo-vision system by Eurix s.r.l. A total number of 3923 points were tracked with a 5 Hz frequency. A detail of the figure is offered to increase readability. No relationships can be extracted between the features and a CAD model of the mock-up.

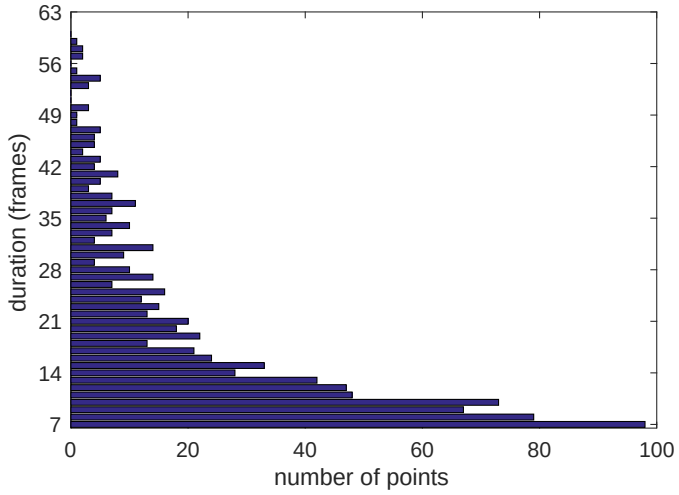

Figure 4.22 Number of time samples in which the features are continuously tracked. The horizontal axis shows the number of points associated to a specific tracking duration (in number of time samples)

The features in Fig. 4.21 are exploited to find through Eq. (3.108) the finite rotations of the mock-up in terms of the global parameter Ω. The Ω signal is filtered by using CS techniques. Then, as shown in the previous section, attitude quaternions are derived from Eq. (4.12) and Eq. (4.13). The obtained quaternions feed the Kalman filter, of which Eq.(4.1) models the related process.

The result is given in terms of the estimated angular rate expressed in the camera-fixed frame. Figure 4.23 illustrates this result; The output of the Kalman filter was further refined with a Savitzky-Golay filter [74].

As seen in the previous subsection, in which data from IR camera are treated, the result in Fig. 4.23 does not give a straightforward idea of the accuracy of the taken approach. Thus, it is appropriate to decompose the estimated angular rate into the two fundamental components provided by the motors.

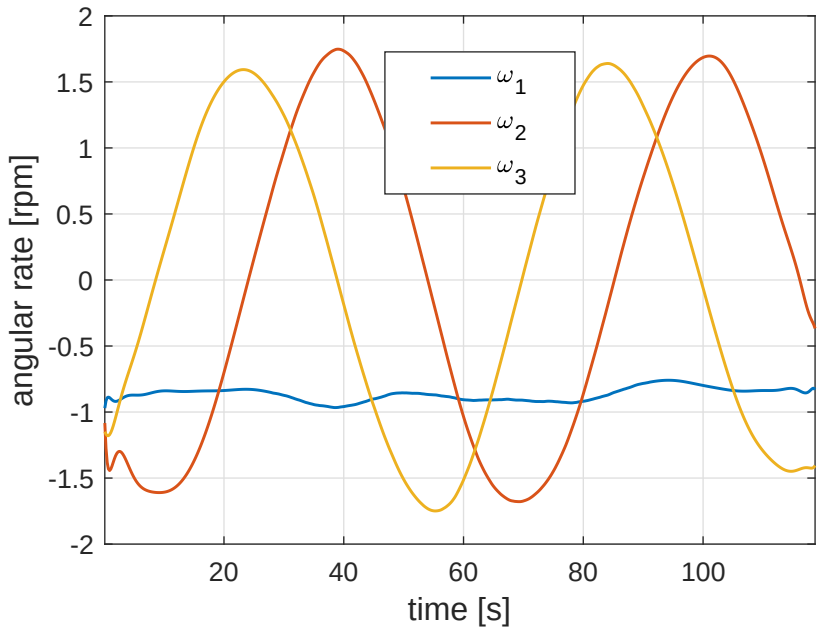

Figure 4.23 Estimated angular rate $\boldsymbol{\omega}$ of the mock-up in the camera-fixed frame shown in Fig.4.14. Notice the steadiness of the first component, which corresponds to the sum of the pseudo-tumbling rate $\dot{\gamma}$ and the constant component of the spin rate $\dot{\theta}_{sp}$ on the first axis

Following the same reasoning applied in the previous subsection, the mean estimate of δ_{sp} from the angular rate in Fig. 4.23 is equal to 91.268 deg, which is similar to the nominal one.

Once an estimate of δ_{sp} is available, the estimated angular rate can be effectively decomposed. The results of the application of Eq. (4.15) and of Eq. (4.16) are shown in Fig. 4.24 and in Fig. 4.25 respectively. To give a better idea of the committed relative errors, Fig. 4.26 shows the magnitude of the spin rate together with the pseudo-tumbling rate in the camera-fixed frame. In those figures, also the mean values are illustrated.

As visible in Fig. 4.17, the spin rate estimation is practically unbiased with respect to the nominal value of 1.65 rpm. This last aspect is explained by the increase of the angular rate. Indeed, the open-loop controlled step motors showed a poor behavior when

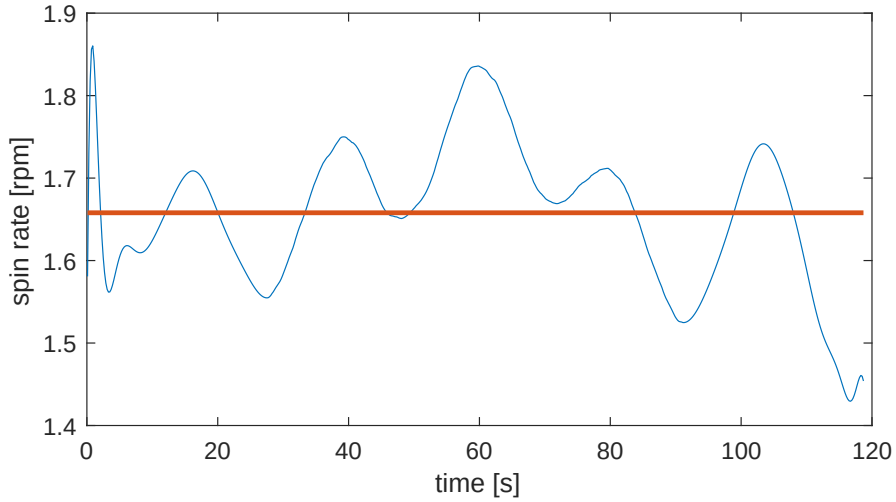

Figure 4.24 Estimated counterclockwise spin rate $\dot{\theta}_{sp}$ of the mock-up. The mean value is represented with a thick line

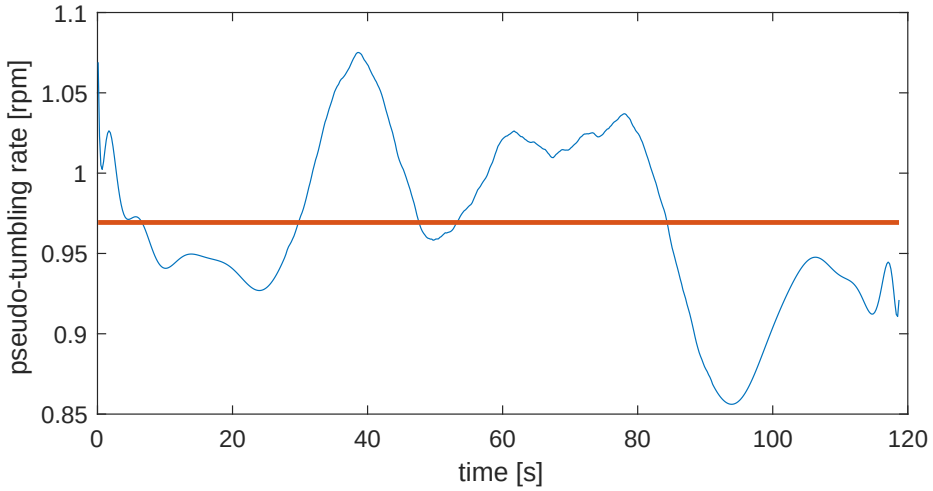

Figure 4.25 Estimated counterclockwise pseudo-tumbling rate $\dot{\gamma}$ of the mock-up. The mean value is represented with a thick line

working at low angular rates. In particular, at lower rates, step losses and vibrations seemed to occur.

The distribution of the estimation error seems to be regular and centered. Differently from the case of the elaboration of IR camera data (see Fig. 4.17), the raw data are directly

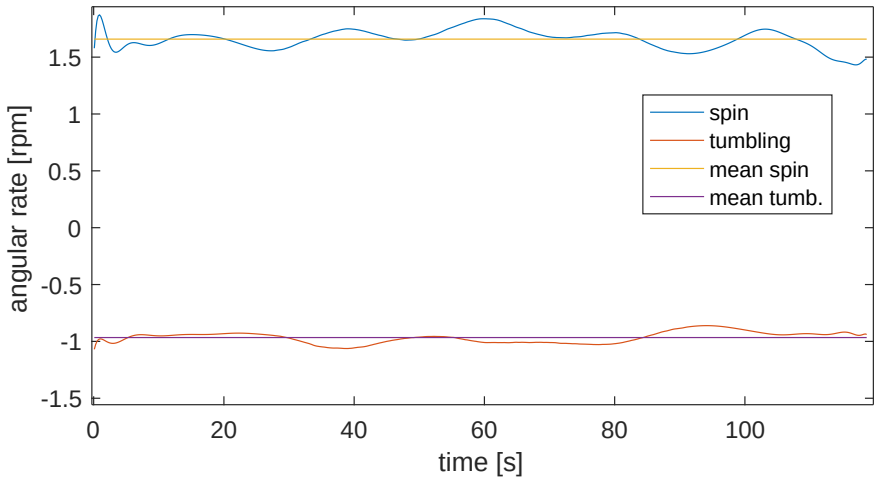

Figure 4.26 Estimated spin rate $\dot{\theta}_{sp}$ of the mock-up, and estimated pseudo-tumbling rate in camera frame. Notice that the quality of the estimation is not too bad.

exploited without any complex processing. This aspect helps CS sampling techniques in removing false residual frequency contributions to the Ω signal. In particular, this removal is performed without the need of increasing the parameter λ in Eq. (3.77). The role of this parameter has been extensively explained both in subsection 3.2.1 and in the previous subsection.

The mean value of the estimated spin rate is equal to 1.652 rpm, so there is no significant bias with respect to the nominal value of 1.65 rpm.

The difference between the maximum and the minimum deviations over all the observation time is equal to 0.43 rpm, that is 2.58 deg/s. This result shows that, although a well-distributed noise corrupts the data, the power of this noise is consistently higher than the ones of the noise affecting data from IR camera. After all, despite the good resolution of the cameras composing the 3DOne system (see Fig. 4.9), the very short baseline of 60 mm does not let optimism on the expected accuracy of the result.

However, in [19], the results of the experimental tests revealed estimation errors that exceed 2 deg/s. Thus, the results of the proposed methods are in-line with what can be

found in the literature. On the other hand, the proposed method showed a generality regarding assumptions that cannot be found in the state-of-art.

Same considerations apply exactly for the estimation of the pseudo-tumbling rate, whose result is shown in Fig. 4.25. The mean value of $\dot{\gamma}$ is equal to 0.969 rpm while the nominal value was 1 rpm. Thus, it exists a bias of 0.031 rpm, that is 0.186 deg/s. Actually, once the step motor works at low angular rates, a bias appear again. However, this bias should be attributed to the fact that the actual rate of the mock-up is slightly inferior to the nominal one. Again, from the analysis of the images captured by the cameras, it emerged that after a minute of the mock-up motion, the object did not return exactly to its original position before the starting of the movement. The delay was the same of the previous test (2.5 s).

The difference between the maximum and the minimum deviations from the mean value of the pseudo-tumbling rate is equal to 0.21 rpm, whose corresponding value in deg/s is 1.26.

Again, as visible from Fig. 4.26, the estimation of the pseudo-tumbling rate led to better results. Probably, this fact depends on the relative attitude between the mock-up and the cameras.

Regarding the localization of the intersection point of the two motion axes of the mock-up, all the methods exposed in chapter 2 were applied on data shown in Fig. 4.21. Using an analogous representation as in Fig. 2.19 The results of this test are shown in Fig. 4.27. The raw estimates are fitted with third order polynomials to avoid numerical problems due to singularities. An extremely high condition number of the matrix in the least-square fitting can be automatically detected. Thus there is no loss of generality: the starting order of the fitting polynomial is ten like in section 2.3, but it is decreased until the mentioned condition number is acceptable.

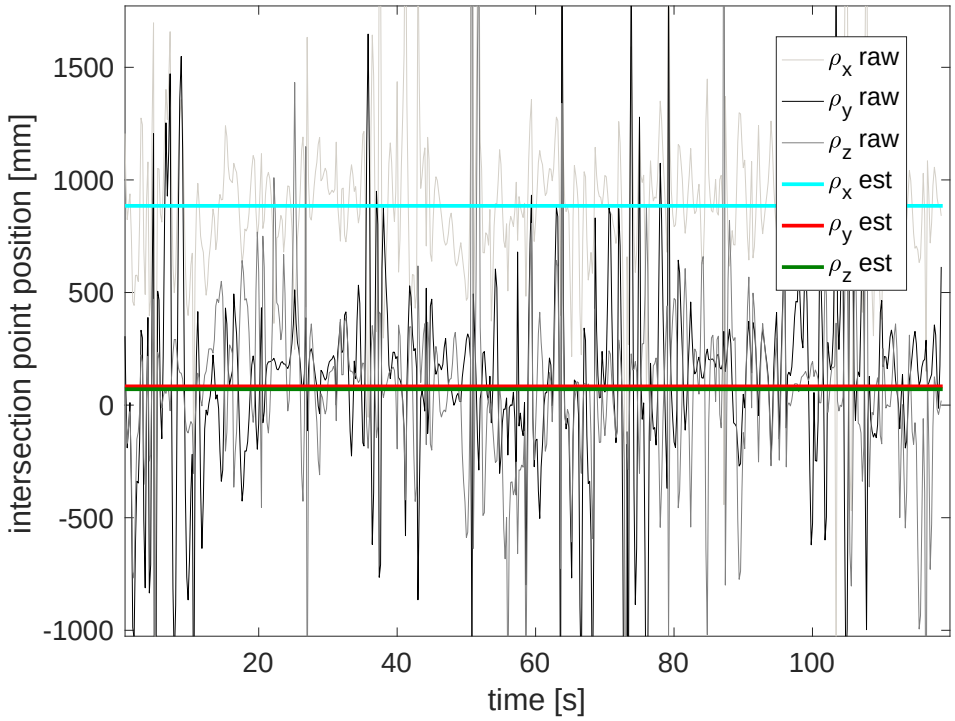

Figure 4.27 Localization of the intersection point of the spin axis with the pseudo-tumbling axis. The distance between this point and the camera was constant

The constant values of the three components of the found position are 893.8 mm, 83.2 mm, and 70.5 mm. Overall, an error in the order of 100 mm was made with respect to the nominal values. As expected, the quality of this result is worse than the one obtained with data from IR camera. The uncertainty on the depth coordinate due to the short stereo rig baseline is probably decisive. Moreover, the movement of the features in the depth direction is quite limited because of the particular architecture of the mock-up.

However, looking to the experimental tests in [19], the CoM is identified with errors that can be up to 0.1 m. Thus the quality of the achieved results remains comparable with the one of the best methods known. However, the method developed in chapter 2 is free from hypothesis regarding the fixity of the detected set of features and the uninterrupted

availability of measured data. This last aspect is an important point of novelty of the proposed method.

Conclusions

The main goal of this work was the investigation of methods and algorithms for estimating the dynamic state of non-cooperative spacecraft. Space debris mitigation is one of the most important topics that are currently discussed within the space community. An accurate knowledge of the CoM location and the rotational state of the target debris helps the capture and the removal of the object significantly. Indeed, the contact between two non-cooperative systems severely undermines the stability of the joint system.

One of the underlying assumption under which the methods were developed regards the possibility of tracking the positions of several features of the passive object. This operation has to be done through the exploitation of passive sensors only, which are placed appropriately on a chaser spacecraft. The latter satellite, in particular, is the one devolved to the capture and removal of the target.

The consideration that passive sensors should be preferred to active ones led to the necessity of making the methods robust to probable interruptions of the tracking, to which temporary unavailabilities of input data correspond. Moreover, part of the research work was spent to overcome one of the most common but restrictive assumptions in the literature, that is to consider the possibility of tracking one fixed set of features of the objects. However, it is quite evident that different poses of the objects during its tumbling motion correspond to diverse views of it from the sensors point of view. Hence, many different sets of features should be tracked during the whole observation period.

The answer to this need was differentiated for the estimation of the CoM location and the rotational state of the target. In particular, regarding the first mechanical property, it was developed a method that does not require the assumption of a specific dynamic model of the orbital motion of the target. This aspect differentiates the proposed method significantly from the other existing state-of-art methods. Typically, the coordinates of the CoM are estimated together with the ones of the features within a single state observer, which is also devolved to the estimation of the coupled rotational state of the target. This approach results unfeasible if the tracked features changes during the observation.

Given this non-feasibility, it was decided to put all the efforts in the development of a pure kinematic estimation approach. Despite the general mistrust that experts have against similar practices, it was proved through simulation results that the proposed estimator is capable of finding the CoM location with sufficient accuracy.

In particular, the combined usage of statistical shape analysis and Butterworth filters was decisive for guaranteeing similar accuracy in case of corrupted input data. The errors obtained, although distributed in a non-cataloged way, resulted bounded. The found accuracy is similar to one of the best methods known; however, the level of the necessary hypothesis was significantly lowered.

A similar approach could not be obtained to estimate the rotational state, which includes a normalized form of the inertia tensor. Indeed, the target dynamics characterize too much its actual movement, so that it is necessary to consider a model for state observation. At first, it was maintained the mentioned hypothesis of having a fixed set of features to detect. The problem of having missing data was faced by using compressive sampling techniques. In particular, an efficient patching of the available parts of the attitude information led to a complete recovery of the missing parts. Thus, attitude quaternions were restored as they were compressed images. That procedure allowed

an unscented Kalman filter to estimate the angular rate and the inertia moments of the object.

The level of accuracy and robustness reached by the method was slightly superior to the one of other known methods. Then, to remove all the restrictive assumptions, the attitude kinematics of the object were described through a succession of finite rotations. The chosen parametrization for this sequence of rotations was proven to be an intrinsic property of the motion, and so independent of the detected features. In this way, the assumption regarding the fixity of the detected set of features was dropped.

An original and compact state-space model was proposed for the rotational state observation. Another unscented Kalman filter was designed to be fed with rotation measurements. In particular, the measured signal regarding finite rotations of the body was preliminary treated with compressive sampling techniques to recover its missing samples.

The results of this second estimation approach were slightly worse than the ones of the first methodology, but still comparable to the ones of other state-of-art methods. Nevertheless, even in this case, the level of the necessary hypothesis was significantly lowered.

An important validation step to understanding the real applicability of the developed methods in the context of a removal mission was the laboratory tests. The work of the partners of the CADET research program allows us to collect data coming from two different kinds of sensors: a monocular infrared camera and a stereo-rig system. The tests produce satisfactory results, confirming the reliability of the proposed methods.

Finally, it is right to indicate some possible research directions for the improvement of this work. Up to the knowledge of the author of this dissertation, the proposed methods are the first ones that deal with the possibility of having missing input data. Much work can be done to have a real-time implementation of the estimation algorithms.

In particular, regarding the algorithms for the angular rate estimation, instead of applying compressive sampling techniques separately from Kalman filtering, it would be possible to include the few constant frequencies that characterize the sequence of body rotations into the state vector that has to be estimated. The assumption of sparsity of that signal would enhance the prediction capability of the filter in case of missing measurements

At the same time, with more challenges, even the estimator of the CoM location could be introduced in the context of a robust real-time state observer. In that case, there would also be the possibility of estimating the velocity of the CoM.

Doubtless, an experimental campaign in a microgravity laboratory could be planned for a final validation of all the proposed methods.

Bibliography

[1] A. Tan, T. X. Zhang, M. Dokhanian, Analysis of the iridium 33 and cosmos 2251 collision using velocity perturbation of the fragments, Advances in Aerospace Science and Applications 3 (2013) 13–25.

[2] M. Shan, J. Guo, E. Gill, Review and comparison of active space debris capturing and removal methods, Progress in Aerospace Sciences 80 (2016) 18–32.

[3] C. R. Phipps, A laser-optical system to re-enter or lower low earth orbit space debris, Acta Astronautica 93 (2014) 418–429.

[4] B. Barbee, S. Alfano, E. Pinon, K. Gold, D. Gaylor, Design of spacecraft missions to remove multiple orbital debris objects, in: Aerospace Conference, 2011 IEEE, 2011.

[5] C. J. Wetterer, C. C. Chow, J. L. Crassidis, R. Linares, M. K. Jah, Simultaneous position, velocity, attitude, angular rates, and surface parameter estimation using astrometric and photometric observations, in: Information Fusion (FUSION), 2013 16th International Conference on, IEEE, 2013, pp. 997–1004.

[6] R. Linares, M. K. Jah, J. L. Crassidis, F. A. Leve, T. Kelecy, Astrometric and photometric data fusion for inactive space object mass and area estimation, Acta Astronautica 99 (2014) 1–15.

[7] F. I. U. W. G.Kirchner, F.Koidl, Laser measurements to space debris from graz slr station, Advances in Space Research 51 (1) (2013) 21–24.

[8] Y. Xing, X. Cao, S. Zhang, H. Guo, F. Wang, Relative position and attitude estimation for satellite formation with coupled translational and rotational dynamics, Acta Astronautica 67 (3) (2010) 455–467.

[9] Z. Jun, H. He, L. Yingying, Spacecraft center of mass online estimation based on multi-accelerometers, in: Information Management and Engineering (ICIME), 2010 The 2nd IEEE International Conference on, IEEE, 2010, pp. 295–298.

[10] E. Wilson, D. W. Sutter, R. W. Mah, Motion-based mass-and thruster-property identification for thruster-controlled spacecraft, AIAA paper 6907 (2005) 2005.

[11] M. D. Lichter, S. Dubowsky, State, shape, and parameter estimation of space objects from range images, in: IEEE International Conference on Robotics and Automation (ICRA), Vol. 3, IEEE, 2004, pp. 2974–2979.

[12] F. Aghili, M. Kuryllo, G. Okouneva, C. English, Fault-tolerant position/attitude estimation of free-floating space objects using a laser range sensor, Sensors Journal, IEEE 11 (1) (2011) 176–185.

[13] J. Iqbal, M. Pasha, H. K. Riaz-un Nabi, J. Iqbal, Real-time target detection and tracking: A comparative in-depth review of strategies, Life Science Journal 10 (3) (2013) 804–813.

[14] S.-M. Lim, H.-D. Kim, J.-D. Seong, Vision-based ground test for active debris removal, Journal of Astronomy and Space Sciences 30 (4) (2013) 279–290.

[15] N. Li, Y. Xu, G. Basset, N. Fitz-Coy, Tracking the trajectory of space debris in close proximity via a vision-based method, Journal of Aerospace Engineering 27 (2) (2014) 238–248.

[16] N. W. Oumer, G. Panin, 3d point tracking and pose estimation of a space object using stereo images, in: 21st International Conference on Pattern Recognition (ICPR), IEEE, 2012, pp. 796–800.

[17] G. Fasano, M. Grassi, D. Accardo, A stereo-vision based system for autonomous navigation of an in-orbit servicing platform, in: Infotech aerospace conference, AIAA, 2009.

[18] F. Terui, H. Kamimura, S. Nishida, Motion estimation to a failed satellite on orbit using stereo vision and 3d model matching, in: 9th International Conference on Control, Automation, Robotics and Vision (ICARCV), IEEE, 2006, pp. 1–8.

[19] S. Segal, A. Carmi, P. Gurfil, Stereovision-based estimation of relative dynamics between noncooperative satellites: Theory and experiments, Control Systems Technology, IEEE Transactions on 22 (2) (2014) 568–584.

[20] A. Chiesa, F. Fossati, G. Gambacciani, E. Pensavalle, Enabling technologies for active space debris removal: the cadet project, in: Space Safety is No Accident, Springer, 2015, pp. 29–38.

[21] G. Biondi, A. Chiesa, S. Mauro, T. Mohtar, S. P. Pastorelli, M. Sorli, In-situ measurement of debris kinematics and inertial properties during active debris removal mission, in: AIDAA 2015 XXII International Conference.

[22] G. Biondi, S. Mauro, T. Mohtar, S. Pastorelli, M. Sorli, A geometric method for estimating space debris center of mass position and orbital parameters from features tracking, in: Metrology for Aerospace (MetroAeroSpace), 2015 IEEE, IEEE, 2015, pp. 265–270.

[23] G. Biondi, S. Mauro, T. Mohtar, S. Pastorelli, M. Sorli, Feature-based estimation of space debris angular rate via compressed sensing and kalman filtering, in: Metrology for Aerospace (MetroAeroSpace), 2016 IEEE, IEEE, 2016, pp. 215–220.

[24] G. Biondi, M. Stefano, S. Pastorelli, M. Sorli, Fault-tolerant feature-based estimation of space debris rotational motion during active removal missions, in: INTERNATIONAL ASTRONAUTICAL CONGRESS: IAC PROCEEDINGS, International Astronautical Federation, 2016.

[25] G. Biondi, S. Mauro, T. Mohtar, S. Pastorelli, M. Sorli, Attitude recovery from feature tracking for estimating angular rate of non-cooperative spacecraft, Mechanical Systems and Signal Processing 83 (2017) 321–336.

[26] B. Costic, D. Dawson, M. De Queiroz, V. Kapila, Quaternion-based adaptive attitude tracking controller without velocity measurements, Journal of Guidance, Control, and Dynamics 24 (6) (2001) 1214–1222.

[27] J. L. Junkins, H. Schaub, Analytical Mechanics of Aerospace Systems, Texas A&M University, 2001.

[28] M. Romano, Concise form of the dynamic and kinematicsolutions of the euler-poinsot proble, Advances in the Astronautical Sciences 145 (2012) 55–68.

[29] C. Bonnal, M. Sanchez, W. Naumann, Ariane debris mitigation measures, in: Second European Conference on Space Debris, Vol. 393, 1997, p. 681.

[30] J. D. Foley, A. Van Dam, S. K. Feiner, J. F. Hughes, R. L. Phillips, Introduction to computer graphics, Vol. 55, Addison-Wesley Reading, 1994.

[31] S. Soatto, R. Frezza, P. Perona, Motion estimation via dynamic vision, IEEE Transactions on Automatic Control 41 (3) (1996) 393–413.

[32] Z. Dang, Y. Zhang, Relative position and attitude estimation for inner-formation gravity measurement satellite system, Acta Astronautica 69 (7) (2011) 514–525.

[33] W. B. Heard, Rigid body mechanics: mathematics, physics and applications, John Wiley & Sons, 2008.

[34] F. Reuleaux, Kinematics of Machinery, MacMillan, London, 1876.

[35] Á. Page, H. de Rosario, V. Mata, C. Atienza, Experimental analysis of rigid body motion. a vector method to determine finite and infinitesimal displacements from point coordinates, Journal of Mechanical Design 131 (3) (2009) 031005.

[36] A. Tegopoulou, E. Papadopoulos, Determination of rigid-body pose from imprecise point position measurements, in: Intelligent Robots and Systems (IROS), 2011 IEEE/RSJ International Conference on, IEEE, 2011, pp. 2922–2927.

[37] D. Condurache, A. Burlacu, Dual tensors based solutions for rigid body motion parameterization, Mechanism and Machine Theory 74 (2014) 390–412.

[38] J. K. Eberharter, B. Ravani, Kinematic registration in 3d using the 2d reuleaux method, Journal of Mechanical Design 128 (2) (2006) 349–355.

[39] J. Angeles, Automatic computation of the screw parameters of rigid-body motions. part i: Finitely-separated positions, Journal of dynamic systems, measurement, and control 108 (1) (1986) 32–38.

[40] H. Benninghoff, F. Rems, T. Boge, Development and hardware-in-the-loop test of a guidance, navigation and control system for on-orbit servicing, Acta Astronautica 102 (2014) 67–80.

[41] I. Dryden, K. Mardia, Multivariate shape analysis, Sankhyā: The Indian Journal of Statistics, Series A (1993) 460–480.

[42] P. H. Schönemann, A generalized solution of the orthogonal procrustes problem, Psychometrika 31 (1) (1966) 1–10.

[43] M. B. Stegmann, D. D. Gomez, A brief introduction to statistical shape analysis.

[44] J. R. Norris, Markov chains, no. 2, Cambridge university press, 1998.

[45] J. S. Liu, R. Chen, Sequential monte carlo methods for dynamic systems, Journal of the American statistical association 93 (443) (1998) 1032–1044.

[46] A. Edwards, Likelihood', Cambridge Univ, Press, Cambridge, 1972.

[47] M. L. Eaton, Multivariate statistics: A vector space approach., 1983.

[48] S. J. Julier, J. K. Uhlmann, New extension of the kalman filter to nonlinear systems, in: AeroSense'97, International Society for Optics and Photonics, 1997, pp. 182–193.

[49] J. Uhlmann, Simultaneous map building and localization for real time applications, transfer thesis, Ph.D. thesis, Univ. Oxford, Oxford UK, 1 994 (1994).

[50] S. J. Julier, J. K. Uhlmann, Unscented filtering and nonlinear estimation, Proceedings of the IEEE 92 (3) (2004) 401–422.

[51] F. Wang, Grace cg offset determination by magnetic torquers during the in-flight phase, The University of Texas at Austin/Center for Space Research, Technical Memorandum, CSR-TM-00-01.

[52] S. J. Julier, The spherical simplex unscented transformation, in: American Control Conference, 2003. Proceedings of the 2003, Vol. 3, IEEE, 2003, pp. 2430–2434.

[53] D. S. S. Rodrigues, M. C. Zanardi, Spacecraft attitude propagation with different representation, Advances in Space Dynamics 4 (2004) 143–150.

[54] E. J. Candès, et al., Compressive sampling, in: Proceedings of the international congress of mathematicians, Vol. 3, Madrid, Spain, 2006, pp. 1433–1452.

[55] J. A. Tropp, Just relax: Convex programming methods for identifying sparse signals in noise, IEEE transactions on information theory 52 (3) (2006) 1030–1051.

[56] M. V. Afonso, J. M. Bioucas-Dias, M. A. Figueiredo, Fast image recovery using variable splitting and constrained optimization, IEEE Transactions on Image Processing 19 (9) (2010) 2345–2356.

[57] P. L. Combettes, V. R. Wajs, Signal recovery by proximal forward-backward splitting, Multiscale Modeling & Simulation 4 (4) (2005) 1168–1200.

[58] I. Selesnick, L1-penalized least squares with salsa, Tech. rep., Connexions (2014). URL http://cnx.org/content/m48933

[59] A. M. Sabatini, Kalman-filter-based orientation determination using inertial/magnetic sensors: Observability analysis and performance evaluation, Sensors 11 (10) (2011) 9182–9206.

[60] J. L. Crassidis, F. L. Markley, Unscented filtering for spacecraft attitude estimation, Journal of guidance, control, and dynamics 26 (4) (2003) 536–542.

[61] B. D. Lucas, T. Kanade, et al., An iterative image registration technique with an application to stereo vision., in: IJCAI, Vol. 81, 1981, pp. 674–679.

[62] A. Page, V. Mata, J. Hoyos, R. Porcar, Instantaneous screw axis experimental determination in human motions: error analysis, Mech. Mach. Theory 42 (2007) 429–441.

[63] O. Bottema, B. Roth, Theoretical kinematics, Courier Corporation, 1990.

[64] S. Segal, A. Carmi, P. Gurfil, Stereovision-based estimation of relative dynamics between noncooperative satellites: Theory and experiments, Control Systems Technology, IEEE Transactions on 22 (2) (2014) 568–584.

[65] V. I. Karlov, D. W. Miller, W. E. Vander Velde, E. F. Crawley, Identification of model parameters and associated uncertainties for robust control design, Journal of guidance, control, and dynamics 17 (3) (1994) 495–504.

[66] L. Cremean, W. B. Dunbar, D. van Gogh, J. Hickey, E. Klavins, J. Meltzer, R. M. Murray, The caltech multi-vehicle wireless testbed, in: Decision and Control, 2002, Proceedings of the 41st IEEE Conference on, Vol. 1, IEEE, 2002, pp. 86–88.

[67] R. Bevilacqua, T. Lehmann, M. Romano, Development and experimentation of lqr/apf guidance and control for autonomous proximity maneuvers of multiple spacecraft, Acta Astronautica 68 (7) (2011) 1260–1275.

[68] A. Valmorbida, F. Scarpa, M. Mazzucato, S. Tronco, S. Debei, E. C. Lorenzini, Attitude module characterization of the satellite formation flight testbed, in: Metrology for Aerospace (MetroAeroSpace), 2014 IEEE, IEEE, 2014, pp. 73–78.

[69] R. Li, Y. Zhou, F. Chen, Y. Chen, Parallel vision-based pose estimation for non-cooperative spacecraft, Advances in Mechanical Engineering 7 (7).

[70] W. Allasia, A. Bottino, Space debris motion reconstruction for removal, in: 23 rd Conference of the Italian Association of Aeronautics and Astronautics, 2015.

[71] J. Shi, C. Tomasi, Good features to track, in: Computer Vision and Pattern Recognition, 1994. Proceedings CVPR'94., 1994 IEEE Computer Society Conference on, IEEE, 1994, pp. 593–600.

[72] D. G. Lowe, Object recognition from local scale-invariant features, in: Computer vision, 1999. The proceedings of the seventh IEEE international conference on, Vol. 2, Ieee, 1999, pp. 1150–1157.

[73] F. Janabi-Sharifi, V. Hayward, C.-S. Chen, Discrete-time adaptive windowing for velocity estimation, IEEE Transactions on control systems technology 8 (6) (2000) 1003–1009.

[74] R. W. Schafer, What is a savitzky-golay filter?[lecture notes], IEEE Signal Processing Magazine 28 (4) (2011) 111–117.

[75] I. Newton, The Principia: mathematical principles of natural philosophy, Univ of California Press, 1999.

[76] D. Brouwer, G. M. Clemence, Methods of celestial mechanics, Elsevier, 2013.

[77] M. Capderou, Satellite in keplerian orbit, Satellites: Orbits and Missions (2005) 41–58.

[78] B. Cordani, The Kepler problem: group theoretical aspects, regularization and quantization, with application to the study of perturbations, Vol. 29, Birkhäuser, 2012.

[79] E. B. Wilson, J. W. Gibbs, Vector analysis: a text-book for the use of students of mathematics and physics, C. Scribner; E. Arnold, 1901.

[80] P. C. Hughes, Spacecraft Attitude Dynamics, John Wiley and Sons, 1986.

[81] B. Palais, R. Palais, S. Rodi, A disorienting look at euler's theorem on the axis of a rotation, American Mathematical Monthly 116 (10) (2009) 892–909.

[82] H. Goldstein, Classical mechanics, Pearson Education India, 1965.

Appendix A

Basics of orbital dynamics

The motion of the major natural satellites about the Sun has fascinated several scientists since the middle age. Very soon, they realized the importance of finding a compact equation for describing both the terrestrial mechanical phenomena and the celestial ones. In the book *The Principia* [75], Isaac Newton presented for the first time the law of universal gravitation, which states that given two masses m and M, an attraction force $\boldsymbol{F}$ is exerted on them:

$$\boldsymbol{F} = -G\frac{Mm}{|\boldsymbol{r}|^2}\hat{\boldsymbol{r}} \tag{A.1}$$

where $\boldsymbol{r}$ is the vector connecting the two masses, while

$$G = 6.672 \times 10^{-11} \ \ \mathrm{m\,s^{-2}\,kg^{-1}}$$

is the so-called *universal gravitational constant*. The notation $\hat{*}$ is used for indicating the unit vector corresponding to $*$.

Newton himself stated that in an inertial reference frame I, the sum of the forces on an object is equal to the product of its mass and its acceleration. According to this statement, if I has its origin in the center of the Earth and m is the mass of a relatively near satellite, equation (A.1) becomes:

$$ {}^{I}\ddot{\boldsymbol{r}} = -\mu \frac{1}{|\boldsymbol{r}|^2} {}^{I}\hat{\boldsymbol{r}} \tag{A.2} $$

considering that no other masses are sufficiently large and near to further significantly accelerate the satellite. The constant μ in Eq. (A.2), known as *planetary constant*, is the product of G and the mass of the Earth. The prescript I indicates that the relevant vector is expressed with respect to I; this kind of notation will have the same meaning for the entire document.

Clearly, the validity of the Eq. (A.2) is subject to assuming a uniform spherical mass distribution for both the Earth and the satellite. Altought this assumption is unrealistic, it is possible to correct Eq. (A.2) by the addition of tiny accelerations to take into account of the perturbation forces acting on the satellite. Other considerable environmental perturbations are due atmospheric drag or solar radiation pressure. However, in the short term, Eq. (A.2) is often a very reliable representation of the actual motion of a Earth orbiting satellite. Thus, in this work, perturbations are neglected.

A.1 Kepler's laws

Equation (A.1) reveals that the position and the acceleration of the satellite with respect to I have the opposite direction. Hence:

$$ {}^{I}\boldsymbol{r} \times {}^{I}\ddot{\boldsymbol{r}} = 0 \tag{A.3} $$

From which:

$$ \frac{d}{dt}\left({}^{I}\boldsymbol{r} \times {}^{I}\dot{\boldsymbol{r}}\right) = {}^{I}\dot{\boldsymbol{r}} \times {}^{I}\dot{\boldsymbol{r}} + {}^{I}\boldsymbol{r} \times {}^{I}\ddot{\boldsymbol{r}} = 0 \tag{A.4} $$

Thus, the first member of Eq. (A.4) is constant with respect to time.

From a graphical point of view, the magnitude of the result of a cross product is the area of the parallelogram defined by the two factors of the product. In that specific case, it holds:

$$ 2d\mathcal{A} = |{}^{I}\boldsymbol{r} \times {}^{I}\dot{\boldsymbol{r}}|dt \quad \Rightarrow \quad \dot{\mathcal{A}} = \frac{1}{2}|{}^{I}\boldsymbol{r} \times {}^{I}\dot{\boldsymbol{r}}| \tag{A.5} $$

where $d\mathcal{A}$ is the infinitesimal area defined by ${}^{I}\boldsymbol{r}$ and the displacement $d{}^{I}\boldsymbol{r}$

From Fig.A.1, the area spanned by the vector $\boldsymbol{r}$ is the difference betweeen the areas of the two triangles OPP'' and $PP''P'$. Hence:

$$ d\mathcal{A} = \frac{|{}^{I}\boldsymbol{r}| \cdot |{}^{I}\boldsymbol{r}|d\varphi}{2} - \frac{|{}^{I}\boldsymbol{r}|d\varphi \cdot d|{}^{I}\boldsymbol{r}|}{2} \tag{A.6} $$

The differentiation of the Eq. (A.6) with respect to time leads finally to the so called second Kepler's law:

$$ \dot{\mathcal{A}} = \frac{1}{2}|{}^{I}\boldsymbol{r}|^2\dot{\varphi} = \frac{1}{2}k_c. \tag{A.7} $$

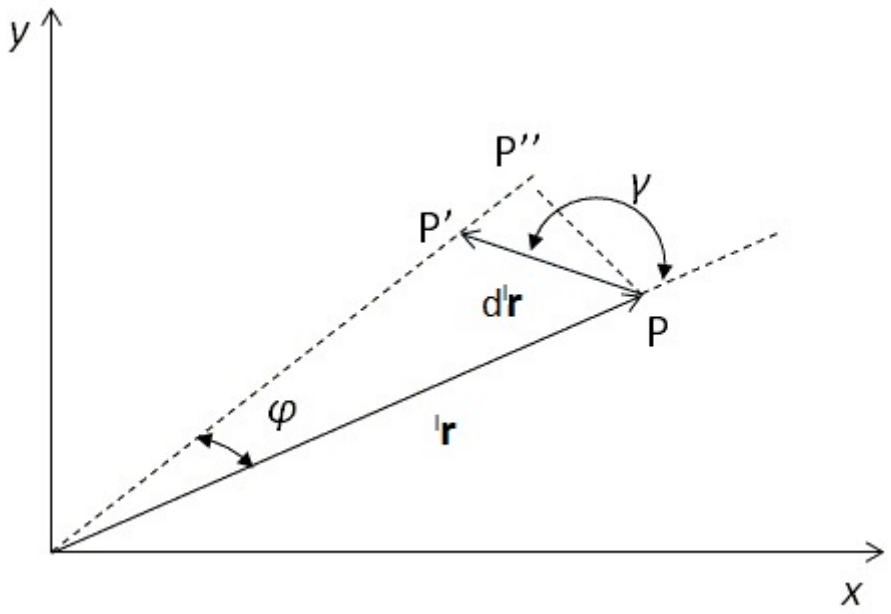

Figure A.1 Areas spanned by the moving vector ${}^I\boldsymbol{r}$. P' is the displaced point P and P'' is the projection of P on ${}^I\boldsymbol{r}$ after the displacement.

Equation (A.7) states that the position vector of a satellite sweeps out equal areas during equal intervals of time. Thus, the *areal velocity* is constant. On the other hand, $\dot{\varphi}$ is constant only if also $|{}^I\boldsymbol{r}|$ is constant, i.e. the position vector traces a circle. More in general, the position vector traces a curve on a plane.

The shape of the orbit of the satellite can be found by analyzing the factors of the areal velocity. Any vector that lies on a plane can always be expressed in exponential form as the product of its magnitude and a complex number $e^{i\varphi}$. φ represent the angle between the vector and the horizontal axis of the Argand plane. Thus, also the position of the satellite is representable in such form. For readability reasons, the magnitude of the position $|{}^I\boldsymbol{r}|$ will be indicated from now on as r (an analogous notation will be used for other vectors):

$$^{I}\boldsymbol{r} = re^{i\varphi} \tag{A.8}$$

Differentiating with respect to time, the following expression is obtained:

$$^{I}\dot{\boldsymbol{r}} = \dot{r}e^{i\varphi} + ir\dot{\varphi}e^{i\varphi} \tag{A.9}$$

Hence:

$$^{I}\ddot{\boldsymbol{r}} = \ddot{r}e^{i\varphi} + \dot{r}e^{i\varphi}i\dot{\varphi} + i\left[r\dot{\varphi}\cdot e^{i\varphi}i\dot{\varphi} + e^{i\varphi}\left(\dot{r}\dot{\varphi} + r\ddot{\varphi}\right)\right] \tag{A.10}$$

$$^{I}\ddot{\boldsymbol{r}} = \left(\ddot{r} - r\dot{\varphi}^2\right)e^{i\varphi} + i\left(2\dot{r}\dot{\varphi} + r\ddot{\varphi}\right)e^{i\varphi} \tag{A.11}$$

It can be easily demonstrated that multiplying the complex number i by a generic number corresponds to rotate the corresponding vector in the Argand plane by $\pi/2$. Thus, from Eq. (A.11) it is possible to identify two normal components of the satellite's acceleration:

$$a_r = \ddot{r} - r\dot{\varphi}^2 \qquad\qquad a_t = 2\dot{r}\dot{\varphi} + r\ddot{\varphi} \tag{A.12}$$

From Eq. (A.12) it can be observed that the tangential acceleration a_t is the time derivative of the quantity $r^2\dot{\varphi} = k_c$. Since this last quantity is constant with time, the tangential acceleration must be constantly null. Moreover, the radial component of the satellite's acceleration is given by:

$$a_r = \ddot{r} - \frac{k_c^2}{r^3} \tag{A.13}$$

Since the acceleration of the satellite is always directed toward the center of the Earth, Eq. (A.2) reveals the trend of the radial component of the acceleration:

$$\ddot{r} - \frac{k_c^2}{r^3} = -\frac{\mu}{r^2} \tag{A.14}$$

Equation (A.14) is an ordinary differential equation in the variable $r(t)$. An efficient way for solving the latter consists in making a change of the variable of integration:

$$\dot{r} = \frac{dr}{dt} = \frac{dr}{d\varphi}\dot{\varphi} = \frac{k_c}{r^2}\frac{dr}{d\varphi} = -k_c\frac{d}{d\varphi}\left(\frac{1}{r}\right) \tag{A.15}$$

Moreover:

$$\ddot{r} = \frac{d\dot{r}}{d\varphi}\dot{\varphi} = \frac{k_c}{r^2}\frac{d}{d\varphi}\left[-k_c\frac{d}{d\varphi}\left(\frac{1}{r}\right)\right] = -\frac{k_c^2}{r^2}\frac{d^2}{d\varphi^2}\left(\frac{1}{r}\right) \tag{A.16}$$

Replacing $1/r$ with an auxiliary variable u_a, it holds:

$$-k_c^2u_a^2\frac{d^2u_a}{d\varphi^2} - k_c^2u_a^3 = -\mu u_a^2, \tag{A.17}$$

and dividing by $-k_c^2u_a^2$:

$$\frac{d^2u_a}{d\varphi^2} + u_a = \frac{\mu}{k_c^2} \tag{A.18}$$

The solution of the associated homogeneous equation is: $u_{ac} = A\cos(\varphi + B)$, where A e B are two arbitrary constants. One particular integral of Eq. (A.18) is $u_{ap} = \mu/k_c^2$. Then:

$$u_a = A\cos(\varphi + B) + \frac{\mu}{k_c^2} \tag{A.19}$$

Substituting again for the original variable r, it holds:

$$r = \frac{1}{A\cos(\varphi + B) + \frac{\mu}{k_c^2}} = \frac{\mu/k_c^2}{1 + A\cos(\varphi + B)} \tag{A.20}$$

The arbitrariness of the constants A and B allows the imposition of

$$\vartheta = \varphi + B, \qquad \frac{k_c^2}{\mu} = p, \qquad \frac{Ak_c^2}{\mu} = e$$

That leads definitively to:

$$r = \frac{p}{1 + e\cos\vartheta} \tag{A.21}$$

Equation (A.21) represents a conic in polar form. The pole of the coordinate system coincides with a focus of the conic. A conic is the locus of all points having a distance from a focus that is a multiple of their distance from a line called directrix. The rate of these distances is the constant e, which is known as eccentricity.

Since the typical field of application of this work is restricted to satellites that have a closed orbit, it will be assumed $e < 1$, so that the conic is an ellipse.

The minimum and the maximum values of r correspond to $\vartheta = 0$ and $\vartheta = -\pi$ respectively:

$$r_{min} = \frac{p}{1 + e} \qquad r_{max} = \frac{p}{1 - e} \tag{A.22}$$

Referring to Fig. A.2, the sum of the values in Eq. (A.22) gives the major axis $2a$ of the ellipse:

$$\frac{p}{1-e}+\frac{p}{1+e}=2a \Rightarrow \frac{2p}{1-e^2}=2a \Rightarrow p=a\left(1-e^2\right) \tag{A.23}$$

From which:

$$r=\frac{a\left(1-e^2\right)}{1+e\cos\vartheta} \tag{A.24}$$

Equation (A.24) is better known as the first Kepler's law. This law states that satellites orbit their main attractor following an elliptic path, whose focus coincides with the attractor. The actual expression of the vector ${}^{or}\boldsymbol{r}$ with respect to the reference frame of Fig. A.2 is:

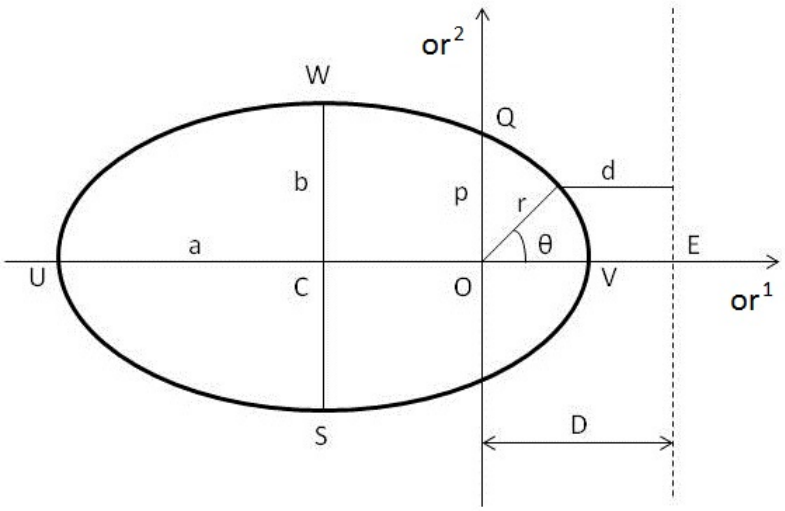

Figure A.2 Characteristic parameters of an ellipse

$$^{or}\boldsymbol{r} = \frac{a\left(1-e^2\right)}{1+e\cos\vartheta}\begin{bmatrix}\cos\vartheta\\ \sin\vartheta\\ 0\end{bmatrix} \tag{A.25}$$

the velocity vector of the satellite has a radial component $\dot{r}$ and a peripheral one $r\dot{\vartheta}$:

$$\dot{r} = \frac{a\left(1-e^2\right)e\sin\vartheta}{\left(1+e\cos\vartheta\right)^2}\frac{k_c}{r^2} = \sqrt{\frac{\mu}{a\left(1-e^2\right)}}e\sin\vartheta \tag{A.26}$$

$$r\dot{\vartheta} = \frac{1+e\cos\vartheta}{a\left(1-e^2\right)}\sqrt{\mu a\left(1-e^2\right)} = \sqrt{\frac{\mu}{a\left(1-e^2\right)}}\left(1+e\cos\vartheta\right) \tag{A.27}$$

remembering that $k_c = r^2\dot{\vartheta} = \sqrt{\mu a(1-e^2)}$ by definition.

Referring to the reference frame shown in Fig.A.2, the following is simply verifiable:

$$^{or}\dot{r}_1 = \dot{r}\cos\vartheta - r\dot{\vartheta}\sin\vartheta \qquad ^{or}\dot{r}_2 = \dot{r}\sin\vartheta + r\dot{\vartheta}\cos\vartheta \tag{A.28}$$

Finally:

$$^{or}\dot{\boldsymbol{r}} = \sqrt{\frac{\mu}{a\left(1-e^2\right)}}\begin{bmatrix}-\sin\vartheta\\ e+\cos\vartheta\\ 0\end{bmatrix} \tag{A.29}$$

From Eq. (A.29) and Eq. (A.24), it is possible to obtain a compact relationship between the magnitudes of $^{or}\dot{\boldsymbol{r}}$ and $^{or}\boldsymbol{r}$:

$$\dot{r}^2 = \mu\left(\frac{2}{r}-\frac{1}{a}\right) \tag{A.30}$$

Equation (A.7) has shown that the areal velocity $\dot{\mathcal{A}}$ is constant. From that statement it is possible to find the period of an elliptic orbit T_{or} as the time in which the position vector of the satellite sweeps out the entire area of the orbit:

$$\dot{\mathcal{A}} = \frac{\pi ab}{T_{or}} = \frac{1}{2}k_c = \frac{1}{2}\sqrt{\mu p} \tag{A.31}$$

From Eq. (A.22) it is straightforward to verify that the value of the parameter p is coincident with $\frac{b^2}{a}$. Hence:

$$2\pi\frac{ab}{T_{or}} = \sqrt{\frac{b^2}{a}\mu} \quad \Rightarrow \quad \frac{T_{or}^2}{a^3} = \frac{4\pi^2}{\mu} \tag{A.32}$$

This last result is the third Kepler's law, which states that the squared period of an orbit is proportional to the cube of its semi-major axis. That law is useful for calculating the orbital period from the geometrical characteristics of the orbit:

$$T_{or} = 2\pi\sqrt{\frac{a^3}{\mu}} \tag{A.33}$$

Finally the so-called *mean motion* n_m is introduced:

$$n_m = \frac{2\pi}{T_{or}} = \sqrt{\frac{\mu}{a^3}} \tag{A.34}$$

A.2 Parametrization for orbits

The Kepler's laws define the properties of the orbits of satellites by examining their kinematic behavior on the orbital plane. However, a correct modeling of the orbit of a space debris needs its characterization on an inertial reference frame I that has its origin coincident with the center of the Earth.

The ECI (Earth-centered inertial) frame is typically selectable for that purpose. The ECI frame is not rigorously inertial because a relative acceleration exists between the center of the Earth and the Sun. However, the effect of this very light acceleration is typically negligible. The first axis I^1 of the ECI frame points toward the vernal equinox, which is the ascending node of the ecliptic. The nodes are the intersection point between an orbit and the equatorial plane. The third axis I^3 of the ECI is directed toward the North pole, while the second axis I^2 completes a right-handed coordinate system.

The definition of I allows the identification of five parameters that characterize the geometry of the orbit, and of one parameter that describes the actual position of the satellite at the current epoch.

The eccentricity e and the semi-major axis a are the two parameters that identify the size and shape of the orbit. Three other parameters have to define its orientation. The first one is the right ascension of the ascending node (RAAN), which indicate the angle between the line segment connecting the nodes and the direction of the vernal equinox. This quantity is named with Ω_{an}. The second parameter is the inclination i_n, which is the vertical tilt of orbit with respect to the equatorial plane, measured at the ascending node. Finally, the argument of periapsis ω_p is an angle measured from the ascending node to the closest point reached by the satellite from the center of the Earth, i.e. the perigee. Figure A.3 gives an illustration of the depicted five parameters.

Typically, the sixth orbital parameter to complete the set of the so-called *two-line elements* is the mean anomaly at epoch $M_{\vartheta 0}$. This is a fictitious angle that describe the angular distance of the satellite from the perigee to the focus, assuming the satellite traveling along a circular orbit with the same period of the actual one. Since this parameter is fictitious, it is commonly converted into the true anomaly at epoch ϑ_0. The relationship between the two parameters is not straightforward; for low values of the

eccentricity e, one possible method for approximately obtaining ϑ_0 from $M_{\vartheta 0}$ consists of truncating the following series expansion [76]:

$$\vartheta_0 = M_{\vartheta 0} + 2\sum_{s=1}^{\infty}\frac{1}{s}\left\{J_s(se) + \sum_{w=1}^{\infty}\beta_e^w\left[J_{s-p}(se) + J_{s+p}(se)\right]\right\}\sin sM_{\vartheta 0} \tag{A.35}$$

where:

$$\beta_e = \frac{1}{e}\left(1-\sqrt{1-e^2}\right) \tag{A.36}$$

$$J_n(x) = \frac{1}{n!}\left(\frac{x}{2}\right)^n\sum_{m=0}^{\infty}(-1)^m\frac{\left(\frac{x}{2}\right)^{2m}}{m!\prod_{k=1}^{m}(n+k)} \tag{A.37}$$

A simpler way consists in an indirect evaluation trough the calculation of the eccentric anomaly $E_{\vartheta 0}$, that is the true anomaly of a satellite that is traveling along the auxiliary circle of its actual orbit. It can be demonstrated [77] that:

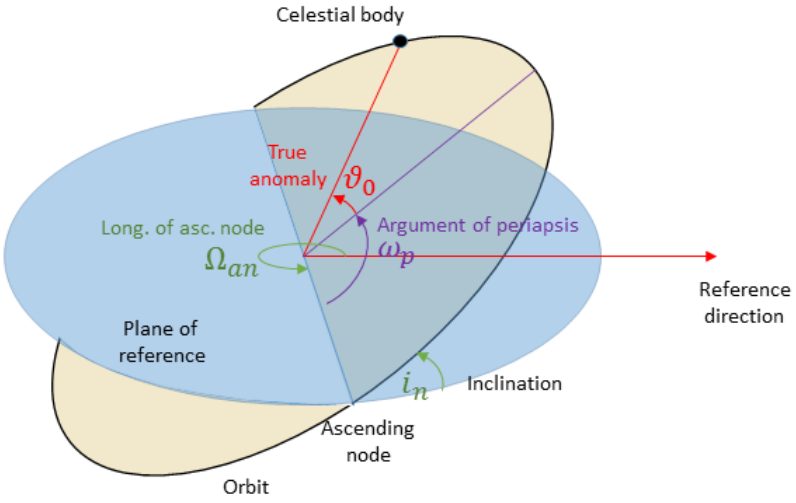

Figure A.3 Representation of the orbital parameters

$$M_{\vartheta 0} = E_{\vartheta 0} - e \sin E_{\vartheta 0} \tag{A.38}$$

$$\tan\left(\frac{\vartheta_0}{2}\right) = \sqrt{\frac{1+e}{1-e}} \tan\left(\frac{E_{\vartheta 0}}{2}\right) \tag{A.39}$$

Clearly, Eq. 1 has not a closed-form solution for $E_{\vartheta 0}$, but numerical methods can accurately solve it. However, in this work, there is no practical needing in considering the mean anomaly for characterizing orbits; thus, the true anomaly will be used for defining the initial position of the simulated target satellite.

Orbital parameters are a very convenient representation of the Keplerian motion of satellites, but solving Eq. (A.2) requires the knowledge of the initial position and velocity of the simulated satellite.

Equations (A.25) and (A.29) exploit the semi-major axis a, the eccentricity e, and the current value of the true anomaly ϑ for finding the position and velocity of the satellite in a reference frame that is represented in fig. A.2. Obviously, the initial position and velocity can be found using the initial value of the true anomaly ϑ_0. Between the reference frame in fig. A.2 and the ECI frame I an affine transform have to exist. In particular, it is a pure rotation that depends on the orientation of the orbit, which is completely described by the other three orbital parameters Ω_{an}, i_n, and ω_p. Affine transforms are linear maps between two vector spaces, so they can be represented by products between a transformation matrix and a vector.

In particular, three different rotation matrices can be defined:

- A first rotation by the angle Ω_{an} about the third axis I^3 of I

$$R_{I^3,\Omega_{an}} = \begin{bmatrix} \cos\Omega_{an} & \sin\Omega_{an} & 0 \\ -\sin\Omega_{an} & \cos\Omega_{an} & 0 \\ 0 & 0 & 1 \end{bmatrix} \tag{A.40}$$

- A second rotation by the angle i_n about the first axis I^1 of I

$$R_{I^1,i_n} = \begin{bmatrix} 1 & 0 & 0 \\ 0 & \cos i_n & \sin i_n \\ 0 & -\sin i_n & \cos i_n \end{bmatrix} \tag{A.41}$$

- A third rotation by the angle ω_p about the third axis I^3 of I

$$R_{I^3,\omega_p} = \begin{bmatrix} \cos\omega_p & \sin\omega_p & 0 \\ -\sin\omega_p & \cos\omega_p & 0 \\ 0 & 0 & 1 \end{bmatrix} \tag{A.42}$$

The appropriate multiplication of these rotation matrices gives:

$$^{or}\boldsymbol{r} = R_{I^3,\omega_p} R_{I^1,i_n} R_{I^3,\Omega_{an}} {}^{I}\boldsymbol{r} \tag{A.43}$$

$$^{or}\dot{\boldsymbol{r}} = R_{I^3,\omega_p} R_{I^1,i_n} R_{I^3,\Omega_{an}} {}^{I}\dot{\boldsymbol{r}} \tag{A.44}$$

Then, by simply inverting Eq. (A.43) and Eq. (A.44):

$$ {}^{I}\boldsymbol{r} = R^{T}_{I^3,\Omega_{an}} R^{T}_{I^1,i_n} R^{T}_{I^3,\omega_p} {}^{or}\boldsymbol{r} \tag{A.45} $$

$$ {}^{I}\dot{\boldsymbol{r}} = R^{T}_{I^3,\Omega_{an}} R^{T}_{I^1,i_n} R^{T}_{I^3,\omega_p} {}^{or}\dot{\boldsymbol{r}} \tag{A.46} $$

Equations (A.45) and (A.46), together with Eq. (A.25) and Eq. (A.29) define the forward transform from orbital to Cartesian parameters for the description of orbits.

For defining the inverse transform, it is convenient to preliminarily define some useful quantities:

- The *specific relative angular momentum vector*. Its direction is perpendicular to the orbital plane:
$$ {}^{I}\boldsymbol{h} = {}^{I}\boldsymbol{r} \times {}^{I}\dot{\boldsymbol{r}} \tag{A.47} $$
- The *nodal axis*. It has a magnitude that depends on ${}^{I}\boldsymbol{h}$; it is aligned with the line of nodes
$$ {}^{I}\boldsymbol{N}_a = \begin{bmatrix} 0 & 0 & 1 \end{bmatrix}^T \times {}^{I}\boldsymbol{h} \tag{A.48} $$
- The *eccentricity vector*. Its expression is such that its magnitude is equal to the eccentricity and its direction is aligned with the major axis of the orbit [78]:
$$ {}^{I}\boldsymbol{E} = \frac{1}{\mu}\left[\left(\dot{r}^2 - \frac{\mu}{r}\right){}^{I}\boldsymbol{r} - \left({}^{I}\boldsymbol{r}\cdot{}^{I}\dot{\boldsymbol{r}}\right){}^{I}\dot{\boldsymbol{r}}\right] \tag{A.49} $$

Banally, the eccentricity e is the magnitude of the vector ${}^{I}\boldsymbol{E}$. The semi-major axis can be found by exploiting Eq. (A.30):

$$ a = \left(\frac{2}{r} - \frac{\dot{r}^2}{\mu}\right)^{-1} \tag{A.50} $$

The three parameters that describe the orientation of the orbit are obtainable from simple trigonometric relations:

$$i = \arccos\left(\frac{{}^{I}h_3}{h}\right) \tag{A.51}$$

$$\Omega_{an} = \begin{cases} \arccos\left(\dfrac{{}^{I}N_{a_1}}{N_a}\right) & \text{if } {}^{I}N_{a_2} \geq 0 \\ 2\pi - \arccos\left(\dfrac{{}^{I}N_{a_1}}{N_a}\right) & \text{if } {}^{I}N_{a_2} < 0 \end{cases} \tag{A.52}$$

$$\omega = \begin{cases} \arccos\left(\dfrac{{}^{I}\boldsymbol{N}_a \cdot {}^{I}\boldsymbol{E}}{N_a E}\right) & \text{if } {}^{I}E_3 \geq 0 \\ 2\pi - \arccos\left(\dfrac{{}^{I}\boldsymbol{N}_a \cdot {}^{I}\boldsymbol{E}}{N_a E}\right) & \text{if } {}^{I}E_3 < 0 \end{cases} \tag{A.53}$$

Finally, the inverse transform is completed by the calculation of the true anomaly ϑ:

$$\vartheta = \begin{cases} \arccos\left(\dfrac{{}^{I}\boldsymbol{E} \cdot {}^{I}\boldsymbol{r}}{Er}\right) & \text{if } {}^{I}\boldsymbol{r} \cdot {}^{I}\dot{\boldsymbol{r}} \geq 0 \\ 2\pi - \arccos\left(\dfrac{{}^{I}\boldsymbol{E} \cdot {}^{I}\boldsymbol{r}}{Er}\right) & \text{if } {}^{I}\boldsymbol{r} \cdot {}^{I}\dot{\boldsymbol{r}} < 0 \end{cases} \tag{A.54}$$

A.3 Relative dynamics for two satellites

The target capturing involves a preliminary rendezvous with the chaser spacecraft such that it is capable of starting with the observation of the motion of the target. The most general meeting conditions are such that the chaser travels along an orbit that is sufficiently close to the one of the target. Clearly, for the facilitation of the observation, the relative range between the two bodies should not have a high variability, especially if sensors consists of stereo cameras.

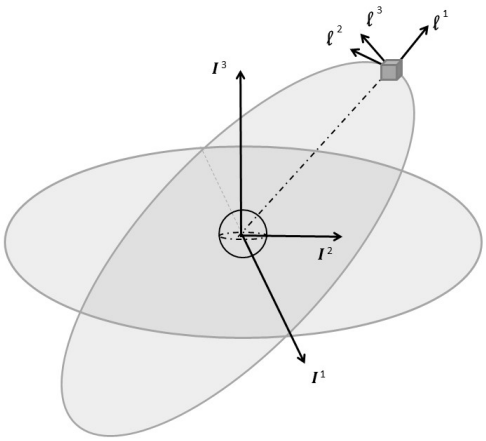

Figure A.4 Definition of the LVLH coordinate system of the target

One can simulate this condition mathematically by modeling the orbital dynamics of the chaser in the I frame. Then the relative position is computable by simple kinematic relationships.

However, to avoid a diverging range to the target, the orbital parameters of the chaser spacecraft should be selected appropriately. Typically, yet, the deviations from the orbital parameters of the target are too tiny for efficiently being interpreted. From that point of view, having the possibility of selecting the initial relative position and velocity is of higher impact in terms of intelligibility. Thus, it is common to model the Keplerian motion of one of the objects in a reference frame that has its origin in the center of gravity of the other one.

The most used reference frame for that purpose is the *local vertical-local horizontal* (LVLH) reference frame. The first axis of the LVLH frame ℓ^1 is directed along the radial direction, i.e. the corresponding unit vector to the position of the target ${}^I\boldsymbol{r}$. The third axis ℓ^3 has the same direction of the specific relative angular momentum vector ${}^I\boldsymbol{h}$ of the target. Finally the second axis ℓ^2 completes a right-handed coordinate system. Figure A.4 gives an illustration of these definitions.

Once an orbital reference frame has been defined, it is possible to derive the dynamic equations of motion of the chaser in that frame. Introducing ${}^{\ell}\boldsymbol{\rho}$ as the position of the chaser in the frame ℓ, it holds:

$$ {}^{\ell}\boldsymbol{r}_{ch} = \begin{bmatrix} r + {}^{\ell}\rho_1 & {}^{\ell}\rho_2 & {}^{\ell}\rho_3 \end{bmatrix}^T \tag{A.55} $$

Expressing the position of the target in the frame ℓ, it has only one component that is not null. In particular, its value is clearly equal to r. The LVLH frame rotates with an angular velocity and acceleration that are indicated as ${}^{\ell}\dot{\boldsymbol{\vartheta}}$ and ${}^{\ell}\ddot{\boldsymbol{\vartheta}}$ respectively. However, it is straightforward to verify that only the third component of these vectors is different from zero. In particular, they coincide respectively with the first and second derivative of the true anomaly ϑ. Thus, from kinematics:

$$ {}^{\ell}\ddot{\boldsymbol{r}}_{ch} = {}^{\ell}\ddot{\boldsymbol{r}} + {}^{\ell}\ddot{\boldsymbol{\vartheta}} \times {}^{\ell}\boldsymbol{\rho} + {}^{\ell}\dot{\boldsymbol{\vartheta}} \times \left({}^{\ell}\dot{\boldsymbol{\vartheta}} \times {}^{\ell}\boldsymbol{\rho} \right) + 2\,{}^{\ell}\dot{\boldsymbol{\vartheta}} \times {}^{\ell}\dot{\boldsymbol{\rho}} + {}^{\ell}\ddot{\boldsymbol{\rho}} \tag{A.56} $$

The vectorial Eq. (A.56) can be treated by considering each component:

$$ {}^{\ell}\begin{bmatrix} \ddot{r}_{ch_1} \\ \ddot{r}_{ch_2} \\ \ddot{r}_{ch_3} \end{bmatrix} = {}^{\ell}\begin{bmatrix} \ddot{r} - \ddot{\vartheta}\rho_2 - \dot{\vartheta}^2\rho_1 - 2\dot{\vartheta}\dot{\rho}_2 + \ddot{\rho}_1 \\ \ddot{\vartheta}\rho_1 - \dot{\vartheta}^2\rho_2 + 2\dot{\vartheta}\dot{\rho}_1 + \ddot{\rho}_2 \\ \ddot{\rho}_3 \end{bmatrix} \tag{A.57} $$

At any epoch, the Eq. (A.2) can be expressed in the frame ℓ. Hence, the position vector from the center of the Earth to the center of gravity of the target has one only non-null component:

$$ {}^{\ell}\ddot{r}_1 = -\frac{\mu}{r^2} \tag{A.58} $$

The same reasoning applies to ${}^{\ell}\ddot{\boldsymbol{r}}_{ch}$:

$$^{\ell}\ddot{\boldsymbol{r}}_{ch} = -\mu \frac{1}{r_{ch}^3} {}^{\ell}\boldsymbol{r}_{ch} \tag{A.59}$$

Thus, remembering Eq. (A.55), it is possible to obtain the following expression from Eq. (A.57):

$$^{\ell}\begin{bmatrix} \ddot{\rho}_1 \\ \ddot{\rho}_2 \\ \ddot{\rho}_3 \end{bmatrix} = {}^{\ell}\begin{bmatrix} 2\dot{\vartheta}\dot{\rho}_2 + \ddot{\vartheta}\rho_2 + \dot{\vartheta}^2\rho_1 - \frac{\mu(r+\rho_1)}{\left[(r+\rho_1)^2+(\rho_2)^2+(\rho_3)^2\right]^{3/2}} + \frac{\mu}{r^2} \\ -2\dot{\vartheta}\dot{\rho}_1 - \ddot{\vartheta}\rho_1 + \dot{\vartheta}^2\rho_2 - \frac{\mu\rho_2}{\left[(r+\rho_1)^2+(\rho_2)^2+(\rho_3)^2\right]^{3/2}} \\ -\frac{\mu\rho_3}{\left[(r+\rho_1)^2+(\rho_2)^2+(\rho_3)^2\right]^{3/2}} \end{bmatrix} \tag{A.60}$$

Equation (A.60) gives the full nonlinear equations of relative motion.

Appendix B

Basics of attitude dynamics

A possible definition of the attitude of a satellite could be the orientation of a right-handed Cartesian coordinate system, which is fixed to the satellite. The attitude of a satellite varies with time as a function of the angular rate of the body. For simulating the motion of the target body, the time variation of its attitude could come from solving proper kinematic equations, which are systems of ordinary differential equations whose independent variable is the angular rate. In particular, they often involve the time derivative of a set of redundant parameters representing the attitude.

In the same way, the angular rate is a fundamental property of the motion of the target; it depends on the mass distribution and the exerted torques. Thus, dynamic equations involving the derivative of the angular rate have to be identified for completing the simulation of the motion of the target.

The choice of an appropriate attitude parametrization has an important role for the purpose of simulating the motion of an object. The complexity of the kinematic equations increases with the number of parameters used for describing the attitude. On the other hand, the choice of a minimal set of parameters may lead to diverging solutions of the

equations. That occurs especially if the body performs large rotations or have a high angular rate.

B.1 Attitude kinematics and parameterizations

Given two arbitrary right-handed Cartesian coordinate systems F_a and F_b, it is possible to define a *direction cosines matrix* (DCM) as:

$$ {}^{F_b}A_{F_a} = \begin{bmatrix} \hat{\boldsymbol{b}}_1 \cdot \hat{\boldsymbol{a}}_1 & \hat{\boldsymbol{b}}_1 \cdot \hat{\boldsymbol{a}}_2 & \hat{\boldsymbol{b}}_1 \cdot \hat{\boldsymbol{a}}_3 \\ \hat{\boldsymbol{b}}_2 \cdot \hat{\boldsymbol{a}}_1 & \hat{\boldsymbol{b}}_2 \cdot \hat{\boldsymbol{a}}_2 & \hat{\boldsymbol{b}}_2 \cdot \hat{\boldsymbol{a}}_3 \\ \hat{\boldsymbol{b}}_3 \cdot \hat{\boldsymbol{a}}_1 & \hat{\boldsymbol{b}}_3 \cdot \hat{\boldsymbol{a}}_2 & \hat{\boldsymbol{b}}_3 \cdot \hat{\boldsymbol{a}}_3 \end{bmatrix} \tag{B.1} $$

where $\hat{\boldsymbol{b}}_i$ and $\hat{\boldsymbol{a}}_i$ are unit vectors aligned with the i-th axes F_a^i and F_b^i of the reference frames F_b and F_a respectively. According to the original definition of Gibbs [79], a vector is a directed line segment in a three-dimensional Euclidean space. So, a vector is a mathematical entity independent of any reference frame. The dot product of unit vectors is equal to the cosine of the angle formed by them, so each i-th column of the DCM in Eq. (B.1) contains the components of the vector $\hat{\boldsymbol{a}}_i$ in the reference frame F_b.

Hence, the DCM ${}^{F_b}A_{F_a}$ expresses the orientation of the triad F_a about the triad F_b. For that reason, a DCM gives a set of nine parameters for representing the attitude of a body. In particular, it is the only one that univocally expresses the orientation between two triads. For its particular structure, it is easy to demonstrate that it is orthonormal and has a determinant equal to one. Then, a DCM belongs to the *special orthogonal group* $SO(3)$. This belonging shows the constraints to which the nine parameters are subjected. Each column of a DCM have a unitary norm and the inner product between two different columns must be equal to zero. Thus, as expectable, only three of the nine parameters are independent. So, a DCM is a highly redundant attitude parametrization.

For instance, the orientation of the LVLH frame with respect to the ECI is given by:

$$ {}^{I}A_{\ell} = \begin{bmatrix} {}^{I}\hat{\boldsymbol{r}} & -{}^{I}\hat{\boldsymbol{r}} \times \frac{{}^{I}\boldsymbol{r} \times {}^{I}\dot{\boldsymbol{r}}}{\left|{}^{I}\boldsymbol{r} \times {}^{I}\dot{\boldsymbol{r}}\right|} & \frac{{}^{I}\boldsymbol{r} \times {}^{I}\dot{\boldsymbol{r}}_1}{\left|{}^{I}\boldsymbol{r} \times {}^{I}\dot{\boldsymbol{r}}\right|} \end{bmatrix} \tag{B.2} $$

The DCM allows performing the operation of vector basis transformation. For instance, it is possible to consider the position of the target about the center of the Earth:

$$ \boldsymbol{r} = {}^{\ell}r_1\hat{\boldsymbol{\ell}}_1 + {}^{\ell}r_2\hat{\boldsymbol{\ell}}_2 + {}^{\ell}r_3\hat{\boldsymbol{\ell}}_3 = {}^{I}r_1\hat{\boldsymbol{I}}_1 + {}^{I}r_2\hat{\boldsymbol{I}}_2 + {}^{I}r_3\hat{\boldsymbol{I}}_3 \tag{B.3} $$

where $\hat{\boldsymbol{\ell}}_i$ and $\hat{\boldsymbol{I}}_i$ are the unit vectors aligned with the i-th axes of the LVLH frame and the ECI frame respectively. However, it holds:

$$ \hat{\boldsymbol{\ell}}_i = \left(\hat{\boldsymbol{\ell}}_i \cdot \hat{\boldsymbol{I}}_1\right)\hat{\boldsymbol{I}}_1 + \left(\hat{\boldsymbol{\ell}}_i \cdot \hat{\boldsymbol{I}}_2\right)\hat{\boldsymbol{I}}_2 + \left(\hat{\boldsymbol{\ell}}_i \cdot \hat{\boldsymbol{I}}_3\right)\hat{\boldsymbol{I}}_3 \tag{B.4} $$

Thus, referring to Eq. (B.1) it is easy to verify that the following applies:

$$ {}^{I}\boldsymbol{r} = {}^{I}A_{\ell}\,{}^{\ell}\boldsymbol{r} \tag{B.5} $$

Although it comes with a particular case, it is evident that Eq. (B.5) has a general validity.

Due to its properties, a DCM is very similar to a rotation matrix, but there is a conceptual difference between the two entities. While the DCM is useful for expressing a vector in different reference frames, a rotation matrix transforms the orientation of one particular reference frame, also rotating the vectors fixed to it. Moreover, supposing that F_a is the rotated frame F_b, the generic vector ${}^{F_b}\boldsymbol{b}$ that is fixed to F_b is transformed as follows:

$$^{F_b}\boldsymbol{b}' = {}^{F_a}R_{F_b}\boldsymbol{b} \tag{B.6}$$

Nevertheless, due to the generality of Eq. (B.5), it holds:

$$^{F_a}\boldsymbol{b}' = {}^{F_a}A_{F_b}\,{}^{F_b}\boldsymbol{b}' \tag{B.7}$$

Since F_a is the rotated frame F_b, the entities $^{F_a}\boldsymbol{b}'$ and $^{F_b}\boldsymbol{b}$ are identical. Hence:

$$^{F_a}A_{F_b}\,{}^{F_a}R_{F_b} = I_3 \tag{B.8}$$

where I_3 identifies the 3×3 identity matrix. Equation (B.8), together with the orthogonality property of both DCM and rotation matrix, demonstrates that the matrix that rotates F_b into F_a is the transpose of the DCM from F_b to F_a.

Finally, for a complete description of the DCM parametrization, the following equation shows how the composition works:

$$^{F_a}A_{F_b}\,{}^{F_b}R_{F_c} = {}^{F_a}A_{F_c} \tag{B.9}$$

where F_c is a third generic reference frame.

For finding the kinematic equations, having chosen DCM as attitude representation, it is useful to introduce the concept of *vectrice* [80]: the vectors composing Euclidean coordinate systems are grouped into vectrices such that:

$$\begin{Bmatrix} \hat{\boldsymbol{b}}_1 \\ \hat{\boldsymbol{b}}_2 \\ \hat{\boldsymbol{b}}_3 \end{Bmatrix} = {}^{F_a}A_{F_b} \begin{Bmatrix} \hat{\boldsymbol{a}}_1 \\ \hat{\boldsymbol{a}}_2 \\ \hat{\boldsymbol{a}}_3 \end{Bmatrix} \tag{B.10}$$

Introducing the principal body-fixed frame B of the target, it is possible to write:

$$\left\{\hat{\boldsymbol{B}}\right\} = {}^{B}A_I \left\{\hat{\boldsymbol{I}}\right\} \tag{B.11}$$

Differentiating Eq. (B.11) in the ECI frame, it is possible to obtain the following:

$$\frac{d}{dt}\left\{\hat{\boldsymbol{B}}\right\} = \frac{d}{dt}\left({}^{B}A_I \left\{\hat{\boldsymbol{I}}\right\}\right) = {}^{B}\dot{A}_I \left\{\hat{\boldsymbol{I}}\right\} \tag{B.12}$$

Equation (B.12) holds because the axes of the frame I are obviously fixed in the same frame. Equation (B.12) and Eq. (B.10) yield to:

$$\frac{d}{dt}\left\{\hat{\boldsymbol{B}}\right\} = {}^{B}\dot{A}_I \, {}^{B}A_I^T \left\{\hat{\boldsymbol{B}}\right\} \tag{B.13}$$

If $\boldsymbol{\omega}$ is the absolute angular rate of the target, the derivative in the ECI frame of a generic unit vector $\boldsymbol{a}$ that is fixed to B is $-\boldsymbol{\omega} \times \boldsymbol{a}$. Thus:

$$\frac{d}{dt}\left\{\hat{\boldsymbol{B}}\right\} = -{}^{B}\boldsymbol{\omega}^{\times} \left\{\hat{\boldsymbol{B}}\right\} \tag{B.14}$$

Finally, comparing Eq. (B.14) to Eq. (B.13) it holds:

$${}^{B}\dot{A}_I = -{}^{B}\boldsymbol{\omega}^{\times} \, {}^{B}A_I, \tag{B.15}$$

that is the Darboux's equation. It is important to note that it is valid only if the angular rate is expressed in a body-fixed reference frame. The integration of Eq. (B.15) gives the attitude kinematics of the target. However, it is necessary to appropriately define nine initial dependent values such that the orthogonality property of ${}^{B}A_{I}$ is fulfilled.

The numerical integration of nine dependent variables is not computationally efficient. Moreover, the physical interpretation of the values of these variables is not immediate.

From that point of view, the best possible representation of attitude should consist of only three independent parameters. Indeed, any coordinate system can be made coincident with another one by three separate and independent rotations, each of them about a different axis. For reasons of simplicity, it is convenient to perform rotations about the axes of the moving coordinate system. Thus, twelve equivalent terns of axes can be considered: six permutations without repetition (3!) of the axes (e.g. 123-312-321) and six sequences for which the first and the third rotation develops about the same axis (e.g. 121-212-323).

The rotation angles take the name of *Euler angles*, namely ϕ, θ, and ψ. It is important to remark that the successive transformations apply to a moving coordinate system. Thus, although the rotation axes are aligned with the axes of one particular coordinate system, they are not perpendicular due to previous displacements of those axes. For that reason, the time derivatives of the Euler angles are not directly the components of the angular rate. Hence, the solution of the kinematic equations based on the Euler angles parameterization does not consist merely in the numerical integration of the angular rate.

It is worth mentioning that other twelve sequences come from considering the three rotations about a fixed coordinate system, instead of a moving one. The most famous sequence is undoubtedly the 123 one, known as the *roll-pitch-yaw* representation. This

choice simplifies the kinematic equations since the time derivatives of the angles are the components of the angular rate expressed in the fixed frame.

However, for space applications, the motion of rigid bodies is often described in body-fixed reference frames. For that reason, the usage of these alternative sequences will not be treated in detail.

Considering the 321 sequence, which is probably the most appreciated one, it holds:

$$^{B}A_{I} = R_{I^{1},\phi} R_{I'^{2},\theta} R_{I''^{3},\psi} \tag{B.16}$$

that is, explicitly:

$$^{B}A_{I} = \begin{bmatrix} \cos\theta\cos\psi & \cos\theta\sin\psi & -\sin\theta \\ \sin\phi\sin\theta\cos\psi - \cos\phi\sin\psi & \sin\phi\sin\theta\sin\psi + \cos\phi\cos\psi & \sin\phi\cos\theta \\ \cos\phi\sin\theta\cos\psi + \sin\phi\sin\psi & \cos\phi\sin\theta\sin\psi - \sin\phi\cos\psi & \cos\phi\cos\theta \end{bmatrix} \tag{B.17}$$

The problems in using Euler angles for representing attitude arise for some specific values of the angles. For instance, if $\theta = \pi/2$ the Eq. (B.17) becomes as follows:

$$^{B}A_{I} = \begin{bmatrix} 0 & 0 & -1 \\ \sin(\psi-\phi) & \cos(\psi-\phi) & 0 \\ \cos(\psi-\phi) & -\sin(\psi-\phi) & 0 \end{bmatrix} \tag{B.18}$$

From Eq. (B.18), note that if $^{B}A_{I}$ is known, the values of the Euler angles cannot be univocally determined. The nonlinear mapping between a DCM and any sequence of Euler angles can be singular for some attitude of the considered body.

One can find the kinematic equations recasting the following expression:

$$ {}^{B}\boldsymbol{\omega} = \dot{\phi} \begin{bmatrix} 1 \\ 0 \\ 0 \end{bmatrix} + R_{I^1,\phi}\dot{\theta} \begin{bmatrix} 0 \\ 1 \\ 0 \end{bmatrix} + R_{I^1,\phi}R_{I'^2,\theta}\dot{\psi} \begin{bmatrix} 0 \\ 0 \\ 1 \end{bmatrix} \tag{B.19} $$

where the rotation matrices align the rotation axes with the ones belonging to the body-fixed frame B. Hence:

$$ \begin{bmatrix} \dot{\phi} \\ \dot{\theta} \\ \dot{\psi} \end{bmatrix} = \frac{1}{\cos\theta} \begin{bmatrix} \cos\theta & \sin\phi\sin\theta & \cos\phi\sin\theta \\ 0 & \cos\phi\cos\theta & -\sin\phi\cos\theta \\ 0 & \sin\phi & \cos\phi \end{bmatrix} {}^{B}\boldsymbol{\omega} \tag{B.20} $$

Equation (B.20) reveals definitively that the Euler angle parametrization is not suitable for describing the motion of a tumbling space body. Once θ reaches values that are in the neighborhood of $\pi/2$, the time derivatives of the Euler angles become not finite. Obviously, the motion itself does not present any singularity, but its representation is not efficient.

Since the number of parameters cannot be minimum for the presented reason, a fourth dependent parameter should be introduced. One natural possibility of representing motion with four parameters consists into considering the *Euler axis and angle*.

The Euler's theorem [81] states that given two different coordinate systems, a unit vector $\hat{\boldsymbol{e}}$ exists such that its components are identical in both systems. In particular, an angle α exists such that one of the coordinate systems can be aligned with the other by rotating it by the angle about the vector $\hat{\boldsymbol{e}}$. Thus, the components of $\hat{\boldsymbol{e}}$ and the value of the angle α are a description of the orientation of a reference frame in another one.

However, for space applications, the most common parameters for representing attitude are the *quaternions*, which are directly related to the Euler axis and angle:

$$q = \begin{bmatrix} \cos\frac{\alpha}{2} \\ e_1 \sin\frac{\alpha}{2} \\ e_2 \sin\frac{\alpha}{2} \\ e_3 \sin\frac{\alpha}{2} \end{bmatrix} = \begin{bmatrix} q_0 \\ \boldsymbol{q} \end{bmatrix} \tag{B.21}$$

The first evident property of the quaternions is that their $l2$-norm must be equal to one. This constraint equilibrates the presence of a fourth redundant parameter.

Referring to the properties of the Euler axis and angle, it is interesting to observe that if both the signs of the vector $\hat{\boldsymbol{e}}$ and of the angle α change, the performed rotation is the same. For that reasons, looking to Eq. (B.21), two opposite quaternions q and $-q$ represent the same attitude information.

With a similar reasoning, if the sign of only one between the vector $\hat{\boldsymbol{e}}$ and the angle α changes, the new parameters represent an opposite rotation to the one represented by the original parameters. Thus, the inverse of the quaternion q is:

$$q^{-1} = \begin{bmatrix} -q_0 \\ \boldsymbol{q} \end{bmatrix} = \begin{bmatrix} q_0 \\ -\boldsymbol{q} \end{bmatrix} \tag{B.22}$$

The Euler's formula [81] shows the relationship between a DCM matrix and the corresponding Euler axis and angle:

$${}^{B}A_I = \cos\left({}^{B}\alpha_I\right) I_3 + \left[1 - \cos\left({}^{B}\alpha_I\right)\right] {}^{B}\hat{\boldsymbol{e}}_I \, {}^{B}\hat{\boldsymbol{e}}_I^T - \sin\left({}^{B}\alpha_I\right) {}^{B}\hat{\boldsymbol{e}}_I^{\times} \tag{B.23}$$

Equation (B.21), together with the application of the bisection formulas for $\cos\left({}^{B}\alpha_I\right)$ and for $\sin\left({}^{B}\alpha_I\right)$, give:

$$ {}^{B}A_I = \left({}^{B}q_{0I}^2 - {}^{B}\boldsymbol{q}_I^T\,{}^{B}\boldsymbol{q}_I\right) I_3 + 2\,{}^{B}\boldsymbol{q}_I\,{}^{B}\boldsymbol{q}_I^T - 2\,{}^{B}q_{0I}\,{}^{B}\boldsymbol{q}_I^{\times} \tag{B.24} $$

Equation (B.24) gives the way for transforming a quaternion into a DCM. The inverse transform is less straightforward because there is not a unique way for performing the conversion. In particular, four different ways come from the analysis of the explicit computation of the second member of Eq. (B.24):

$$ \begin{cases} {}^{B}q_{0I} = \pm\dfrac{1}{2}\sqrt{1+A_{11}+A_{22}+A_{33}} \\ {}^{B}q_{1I} = \dfrac{1}{4\,{}^{B}q_{0I}}(A_{23}-A_{32}) \\ {}^{B}q_{2I} = \dfrac{1}{4\,{}^{B}q_{0I}}(A_{31}-A_{13}) \\ {}^{B}q_{3I} = \dfrac{1}{4\,{}^{B}q_{0I}}(A_{12}-A_{21}) \end{cases} \quad \begin{cases} {}^{B}q_{0I} = \dfrac{1}{4\,{}^{B}q_{1I}}(A_{23}-A_{32}) \\ {}^{B}q_{1I} = \pm\sqrt{1+A_{11}-A_{22}-A_{33}} \\ {}^{B}q_{2I} = \dfrac{1}{4\,{}^{B}q_{1I}}(A_{12}+A_{21}) \\ {}^{B}q_{3I} = \dfrac{1}{4\,{}^{B}q_{1I}}(A_{13}+A_{31}) \end{cases} $$

$$ \begin{cases} {}^{B}q_{0I} = \dfrac{1}{4\,{}^{B}q_{2I}}(A_{31}-A_{13}) \\ {}^{B}q_{1I} = \dfrac{1}{4\,{}^{B}q_{2I}}(A_{12}+A_{21}) \\ {}^{B}q_{2I} = \pm\sqrt{1-A_{11}+A_{22}-A_{33}} \\ {}^{B}q_{3I} = \dfrac{1}{4\,{}^{B}q_{2I}}(A_{23}+A_{32}) \end{cases} \quad \begin{cases} {}^{B}q_{0I} = \dfrac{1}{4\,{}^{B}q_{3I}}(A_{12}-A_{21}) \\ {}^{B}q_{1I} = \dfrac{1}{4\,{}^{B}q_{3I}}(A_{13}+A_{31}) \\ {}^{B}q_{2I} = \dfrac{1}{4\,{}^{B}q_{3I}}(A_{23}+A_{32}) \\ {}^{B}q_{3I} = \pm\sqrt{1-A_{11}-A_{22}+A_{33}} \end{cases} \tag{B.25} $$

To conclude with the description of the properties of the quaternions, Eq. (B.24) and Eq. (B.9) can be exploited to define the composition of two quaternions:

$$ {}^{B}q_{I} \otimes {}^{I}q_{B} = \begin{bmatrix} {}^{B}q_{0I}\,{}^{I}q_{0B} - {}^{B}\boldsymbol{q}_{I}^{T}\,{}^{I}\boldsymbol{q}_{B} \\ {}^{B}q_{0I}\,{}^{I}\boldsymbol{q}_{B} + {}^{I}q_{0B}\,{}^{B}\boldsymbol{q}_{I} + {}^{B}\boldsymbol{q}_{I} \times {}^{I}\boldsymbol{q}_{B} \end{bmatrix} = \pm \begin{bmatrix} 1 \\ 0 \\ 0 \\ 0 \end{bmatrix} \tag{B.26} $$

Equation (B.26) defines the operator $\otimes$ as the quaternion multiplication. Clearly, the product between one quaternion and its inverse represent the null rotation, which is expressed by a null vectorial part.

B.2 Rotational dynamics in torque-free conditions

A particle with mass m have by definition a momentum that is given by:

$$ {}^{I}\boldsymbol{p}_{m} = m\,{}^{I}\boldsymbol{r} \tag{B.27} $$

where ${}^{I}\boldsymbol{r}$ is the position of the particle in the inertial frame I. The definition of angular momentum ${}^{I}\boldsymbol{L}$ is the following one:

$$ {}^{I}\boldsymbol{L} = {}^{I}\boldsymbol{r} \times {}^{I}\boldsymbol{p}_{m} \tag{B.28} $$

From the second Newton's law [75] and from the definition of torque, it holds:

$$ {}^{I}\dot{\boldsymbol{L}} = {}^{I}\mathcal{C} \tag{B.29} $$

where $\mathcal{C}$ is the sum of the torques applied on the particle. If the target satellite is treated as a simple particle, Eq. (B.29) leads to the definition of the orbital motion of the target as seen in the paragraph A.1.

However, after the rendezvous, when the target satellite is observed from a chaser spacecraft, it appears as a rotating continuous body. Since the target body is free from physical constraints, its rotation develops about the center of mass (CoM), which should not be confused with the application point of the gravity acceleration. The two points would have been coincident if the magnitude of the gravity acceleration had been uniform for each point of the space. However, the distance between the two points is often negligible. In [51] it is shown that typical values of this distance are under 1 mm.

By definition, the CoM of a continuous body is the result of the following volume integral:

$$ {}^{I}\boldsymbol{r} = \frac{1}{m} \iiint_{Q} \rho_d \left({}^{I}\boldsymbol{d} \right) {}^{I}\boldsymbol{d} \quad \mathrm{d}V \tag{B.30} $$

where ρ_d is the density of the body, Q is the volume of the body, and ${}^{I}\boldsymbol{d}$ is the position of the infinitesimal part of the volume $\mathrm{d}V$. Since the CoM is the pole of the rotation of the body, the angular momentum of the body relative to that point assumes the following form:

$$ {}^{B}\boldsymbol{L}_B = \iiint_{Q} {}^{B}\boldsymbol{d} \times \rho_d \left({}^{B}\boldsymbol{d} \right) {}^{B}\dot{\boldsymbol{D}} \quad \mathrm{d}V = {}^{B}J\,{}^{B}\boldsymbol{\omega} \tag{B.31} $$

where ${}^{B}\boldsymbol{D}$ is a vector from the origin of the frame I, i.e. the center of the Earth, to $\mathrm{d}V$. Moreover, J is the inertia matrix. By definition, the inertia matrix is symmetric and positive definite. Moreover, it holds $J_{ii} + J_{jj} > J_{kk}$ and $J_{ii} > J_{jk}$ for all $i \neq j \neq k$.

The quantities in Eq. (B.31) are expressed in the reference frame B without any loss of generality. Thus, ${}^{B}J$ is diagonal and constant with respect to time. The subscript B on the angular momentum vector indicates that the pole of the rotation is the origin of the reference frame B, i.e. the CoM of the target body.

Since the angular momentum vector is expressed in a moving frame, the application of the second Newton's law leads to:

$$ {}^{B}\dot{\boldsymbol{L}}_{B} + {}^{B}\boldsymbol{\omega} \times {}^{B}\boldsymbol{L}_{B} = {}^{B}\mathcal{C} \tag{B.32} $$

A tumbling space debris is not controlled; thus the only contributes to ${}^{B}\mathcal{C}$ would be tiny environmental torques and the gravity gradient torque due to the actual distance between the center of gravity and the CoM. However, considering the term ${}^{B}\mathcal{C}$ equal to zero is acceptable if the dynamics of the target is studied for short time periods [11]. Hence, environmental perturbation torques are neglected. Thus, it holds:

$$ {}^{B}J\,{}^{B}\dot{\boldsymbol{\omega}} + {}^{B}\boldsymbol{\omega} \times \left({}^{B}J\,{}^{B}\boldsymbol{\omega}\right) = \mathbf{0} \tag{B.33} $$

that is the *Euler's equation* for a torque-free rigid body. The explicit equations for each component of the angular rate are:

$$ \begin{cases} {}^{B}\dot{\omega}_1 + \dfrac{{}^{B}J_3 - {}^{B}J_2}{{}^{B}J_1}\,{}^{B}\omega_3\,{}^{B}\omega_2 = 0 \\ {}^{B}\dot{\omega}_2 + \dfrac{{}^{B}J_1 - {}^{B}J_3}{{}^{B}J_2}\,{}^{B}\omega_1\,{}^{B}\omega_3 = 0 \\ {}^{B}\dot{\omega}_3 + \dfrac{{}^{B}J_2 - {}^{B}J_1}{{}^{B}J_3}\,{}^{B}\omega_2\,{}^{B}\omega_1 = 0 \end{cases} \tag{B.34} $$

Notice that the solution of this system does not change if the principal inertia moments vector is multiplied by a positive scalar k.

Since the target body is considered free by torques, a first important consideration regards the conservation of two fundamental quantities, i.e. the magnitude of the angular momentum and the kinetic energy. The conservation is a direct consequence of the first Newton's law, which states that an object either remains at rest or continues to move at a constant velocity unless acted upon by a net torque. Thus, for a generic frame:

$$L_B^2 = J_1^2\omega_1^2 + J_2^2\omega_2^2 + J_1^3\omega_1^3 \tag{B.35}$$

$$2E_K^2 = J_1\omega_1^2 + J_2\omega_2^2 + J_3\omega_3^3 \tag{B.36}$$

where E_k indicates the kinetic energy of the target. Equations (B.35) and (B.36) are the analytical representations of two intersecting ellipsoids. The result of this intersection is a closed ellipse, which is traced by the angular rate vector during the body motion, and whose name is *Polhode*. So, the angular rate vector creates a surface that is called *body cone*. If the ellipsoids are seen from the reference frame B, they are fixed like the inertia matrix. On the contrary, from an inertial point of view, the values of the inertia moments variates during the motion of the body. Thus, the ellipsoids have a displacement in the inertial space. However, if ${}^I\mathcal{C} = 0$, Eq. (B.29) shows that the angular momentum vector is fixed in the inertial space. It is proved [82] that the endpoint of the angular rate moves on a plane, which is perpendicular to the angular momentum vector. In particular, that endpoint traces an open curve called *Herpoloid*.

The aforementioned curves are shown in Fig. B.1 and Fig.B.2. The graphic interpretation of Eq. (B.36) and Eq. (B.35) suggests that the angular velocity vector has a periodic behavior.

The solution of Eq. (B.33) becomes simple if the inertia matrix takes particular forms. Evidently, for a spherical mass distribution, the principal moments of inertia become all equal. Thus, the solution of Eq.(B.34) become straightforward: the components of the angular rate are constantly equal to their initial values.

A cylindrical mass distribution is a more interesting condition. It holds

$$^{B}\boldsymbol{J} = \left[^{B}J_{cy}, ^{B}J_{cy}, ^{B}J_{3}\right] \tag{B.37}$$

so $^{B}\omega_3 = const$ from (B.34). It is found using the energy conservation law that the angular velocity magnitude ω is constant, and then also $^{B}\omega_1^2 + {}^{B}\omega_2^2 = {}^{B}\omega_{12}^2$ will be constant. It is useful then to split angular velocity vector into two terms (with constant norm), usually known as *spin* (rotation around the symmetry axis) and *tumbling* (rotation around an axis orthogonal to the symmetry one). The spin and tumbling axes remain

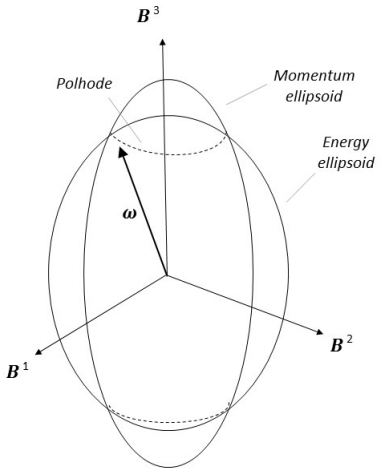

Figure B.1 Intersection of momentum and energy ellipsoid. The tip of the angular rate vector lies on the intersection curve, which is called Polhode

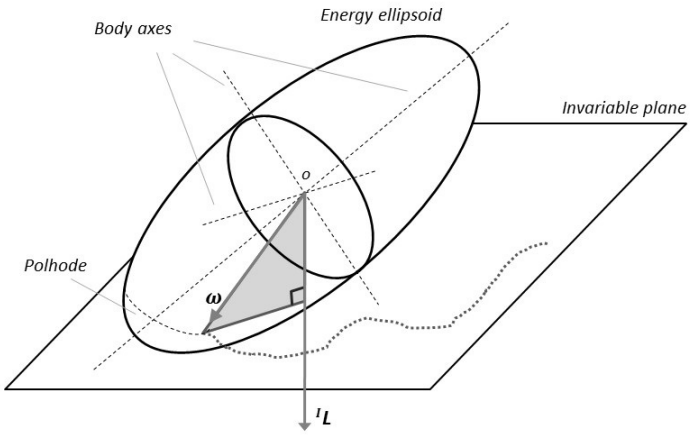

Figure B.2 The angular rate vector traces in the inertial frame an open curve, which is called Herpoloid. The energy ellipsoid rolls without sliding on the plane normal to the angular momentum vector

fixed in the frame B. The angular velocity vector traces a cone, from both a body-fixed point of view or from an inertial point of view. The exact solution of (B.34) is:

$$\begin{cases} {}^{B}\omega_3 = const \\ {}^{B}\omega_{12} = const = \sqrt{\omega^2 - {}^{B}\omega_3^2} \\ {}^{B}\omega_1 = {}^{B}\omega_{12}\cos\left(\dfrac{({}^{B}J_{cy} - J)\,{}^{B}\omega_3}{J}t + \Phi_{ph}\right) \\ {}^{B}\omega_2 = {}^{B}\omega_{12}\sin\left(\dfrac{({}^{B}J_{cy} - J)\,{}^{B}\omega_3}{J}t + \Phi_{ph}\right) \end{cases} \tag{B.38}$$